

**Investigations into Crystallization and Fundamental Thermal Properties of Semicrystalline  
Polymers by Conventional and Fast Scanning Calorimetry**

A dissertation submitted by:

**David Thomas**

In partial fulfillment of the requirements for the degree of:

Doctor of Philosophy

In

Physics

**Tufts University**

August 2017

Advisor: Prof. Peggy Cebe

## *Abstract*

This thesis presents new insights into the crystallization and fundamental thermal properties of semicrystalline polymers investigated by a combination of conventional thermal and structural analysis techniques and the recently developed chip based fast scanning calorimeters. The experiments performed and the results obtained fall into two categories. The first are investigations into the crystallization and fundamental thermal properties of the synthetic, semicrystalline polymer, polyvinyl alcohol (PVA) in bulk, in thin films, and in nanofibers. The second category includes the development and application of a new experimental technique for the preparation of electrospun fibers suitable for fast scanning calorimetry (FSC) chip based sensors.

PVA is hydrophilic, biocompatible, biodegradable, renewable, and possesses excellent mechanical and chemical resistance properties. It has been continuously studied since it was first synthesized nearly 100 years ago. Despite its frequent study, complete measurements of several fundamental thermal properties have been elusive due to thermal degradation which occurs within its melting range. Making use of both conventional DSC and FSC techniques it was possible to make the first, degradation free measurements of the following fundamental properties: 1. liquid phase specific heat capacity of PVA,  $c_p^{\text{Liquid}}(T)$ ; 2. Specific heat capacity increment at the glass transition for 100% amorphous material  $\Delta c_p^{\text{amor}}(T_g)$ ; 3. the critical cooling rate,  $|\beta_c|$ , required to quench the material and create an amorphous glass; and 4. the rigid amorphous fraction (RAF) of PVA.

Electrospun nanofibers are of interest for both applied and fundamental research. These fibers are light, “fluffy”, and delicate and must be handled with care. This poses a unique challenge for experimenters utilizing chip based calorimeters. Copper transmission electron microscope (TEM) grids provide a substrate both thermally conductive and mechanically durable. Directly

electrospinning fibers onto TEM grids allowed the fibers to be transferred to chip sensors and the presence of the grid ensured excellent sample to sensor contact. This technique was tested on the synthetic polymer, polyethylene terephthalate (PET). Cold crystallization experiments were performed on the fibers which were observed to break up into droplets following melting. These experiments yielded a new, and unexpected result in that the droplet confined PET showed a depression in the RAF.

### *Acknowledgements*

I would like to begin by acknowledging my advisor, Prof. Peggy Cebe, for everything she has done for me professionally and personally over these past five years. Without the opportunities and support she has provided, none of this would have been possible. One of the first things I was told by an undergraduate student in the lab after joining was something along the lines “Peggy believes in her students more than they believe in themselves”. There were plenty of days where I didn’t believe that I would get results in time or see success with a given experiment. Peggy would always begin by calmly reminding me that, I was in fact collecting useful data, and point out details I had overlooked before sending me on my way with new things to try or ideas to consider.

I am grateful to the members of my committee: Professors Peggy Cebe, Cristian Staii, Hugo Beauchemin, Austin Napier, and Christoph Schick. You have all played large roles in my development as I transitioned from a student simply taking classes to a research scientist. I would additionally like to thank Professor Schick and his research group for hosting us in his lab at the University of Rostock where many of the experiments discussed in this thesis were performed. I

thank Dr. Evgeny Zhuravlev for measuring my thin film samples with their custom-built calorimeter.

I would like to acknowledge the past department chair, Professor Roger Tobin, and the current chair, Professor Hugh Gallagher for their tireless efforts advocating for the students of this department. I would also like to extend my deep gratitude to Jean Intoppa, Gayle Grant, and Caroline Merighi for their help navigating all aspects of life at Tufts ranging from successfully filling out payroll paperwork, to juggling travel accommodations, or reminding me to enroll in classes before the cutoff date.

I thank the past and present members of the Cebe research group particularly, Matthew Peterson, Zach Pagel, John Merfeld, Emily Van Milligan, Benjamin Zager, Jonathan Minoff, Andrew Clarke, Nelaka Govinna, Yazhe Zhu, Bin Mao, and Wenwen Huang for their assistance in keeping equipment in working order, performing experiments, or providing much needed company during long hours in the lab. I thank the past members of the Staii research group particularly Derek Walkama and Peter Riley for their assistance during the summer internship program. Additionally, I thank Professor Timothy Atherton and his former post doc, Dr. Badel Mbanga for their guidance during my first research project studying liquid crystal elastomers and I thank Professor Sanchez-Ferrer at ETH Zurich for providing the elastomer samples.

I would also like to express my deep gratitude to Professors Michael Horne and Mevan Gunawardena who both generously gave of their time to develop the physics program at Stonehill College. These two exceptional teachers took on teaching additional courses to help me fill out my curriculum, provided undergraduate research opportunities, and hours of conversation aimed at helping me find my path towards graduate school.

Finally, I would like to thank my friends and family for the unwavering and limitless support which has enabled me to succeed in graduate school. Thanks also to my friends from Tufts, particularly Jeremy (Big Jerry) Wachter, Josh Cohen, Chris Burke, Eric Roebuck, Erin Fong, and Andrew DeBenedictis for every problem set, every practice talk, and every stress management session at the gym; my roommate of the past five years, Rob Colby, thanks for literally everything, you helped me keep my sanity more days than I can count; my siblings, Mary, Mikey, and Jack, thank you for keeping my perspective grounded and never losing sight of what is important in life; my parents, for all the sacrifices you two have made for the sake of our education and the excessive patience that was required to help all of us grow.

I acknowledge the funding sources which have supported my research. Financial support was provided by the National Science Foundation through the Polymer Program of the Division of Materials Research under DMR – 1206010 and DMR – 1608125. Support for the thermal analysis instrumentation was provided by the National Science Foundation through the MRI program under DMR – 020655. I also acknowledge the endowed Burlingame Fellowship for supporting me during my final year in the program.

## Table of Contents

|           |  |    |
|-----------|--|----|
| Chapter 1 | Introduction .....   | 1  |
| 1.0       | Polymers .....   | 1  |
| 1.1       | Polymer Basics .....   | 2  |
| 1.2       | Polymer Phases .....   | 6  |
| 1.3       | Crystallization .....  | 12 |
| 1.3.1     | General Theory of crystallization .....  | 12 |
| 1.3.2     | Polymer Crystals and Polymer Crystallization .....   | 16 |
| 1.3.3     | Spinodal Decomposition .....   | 25 |
| 1.4       | Rigid Amorphous Fraction .....   | 29 |
| 1.5       | Self-Nucleation .....  | 30 |
| 1.6       | Motivation for Experimental Work .....   | 33 |
| 1.6.1     | Polyvinyl Alcohol .....  | 34 |
| 1.6.2     | Fast Scanning Calorimetry .....  | 37 |
| 1.7       | References .....   | 39 |
| Chapter 2 | Experimental – Sample Preparation .....  | 55 |
| 2.1       | Sample Preparation with Experimental Constraints in Mind .....   | 55 |
| 2.2       | Solution Processing of Polymers .....  | 55 |
| 2.2.0     | Preparation of Solution Cast PVA Films for Self-Nucleation Experiments (Ch. 4) ..<br>.....                                   | 55 |
| 2.2.1     | Preparation of PVA Thin Films by Spin Coating (Ch. 5) .....  | 57 |
| 2.2.2     | Preparation of Polymers for Electrospinning (Ch. 6-7) .....  | 59 |
| 2.3       | Electrospinning of Polymers (Ch. 6-7) .....  | 60 |
| 2.3.0     | Electrospinning of PET for Development of Novel Technique to Study Fibers by<br>Fast Scanning Calorimetry (FSC) (Ch.6) ..... | 64 |
| 2.3.1     | Electrospinning of PVA – Nanofibers for Neural Tissue Scaffolds (Ch. 7) .....  | 65 |
| 2.3.2     | Electrospinning of PVA – Nanofibers for Nanofibers for Fast Scanning<br>Calorimetry (FSC) (Ch.7) .....                       | 66 |
| 2.4       | Electrospinning Fibers Suitable for Fast Scanning Calorimetry (FSC) Chip Sensors<br>(Ch.6-7) .....                           | 67 |
| 2.5       | Stabilization and Coating of PVA Nanofibers (Ch.7.1.2) .....   | 73 |
| 2.6       | Electrospun Fiber Sample Preparation for Differential Scanning Calorimetry (Ch.6-7)<br>.....                                 | 76 |
| 2.7       | Bulk PET Prepared for Symmetry Correction .....  | 78 |

|           |   |     |
|-----------|---|-----|
| 2.8       | References .....  | 78  |
| Chapter 3 | Experimental Techniques .....   | 84  |
| 3.0       | Theory and Methods .....  | 84  |
| 3.1       | Sample Imaging Techniques .....                                       | 85  |
| 3.1.1     | Polarizing Optical Microscopy (POM) .....                             | 85  |
| 3.1.2     | Scanning Electron Microscopy (SEM) .....                              | 88  |
| 3.2       | Structural Analysis Techniques .....                                  | 94  |
| 3.2.1     | Fourier Transform Infrared Spectroscopy (FTIR) .....                  | 94  |
| 3.2.2     | X-Ray Diffraction (XRD) .....   | 100 |
| 3.3       | Thermal Analysis Techniques .....                                     | 106 |
| 3.3.1     | Thermogravimetric Analysis (TGA) .....                                | 106 |
| 3.3.2     | Differential Scanning Calorimetry (DSC) .....                         | 107 |
| 3.3.2.1   | Power Compensated DSC .....   | 108 |
| 3.3.2.2   | Heat Flux DSC .....   | 109 |
| 3.3.2.3   | Temperature Modulated Differential Scanning Calorimetry (TMDSC) ..... | 119 |
| 3.3.2.4   | Experimental Methods Involving Temperature Modulated DSC .....        | 121 |
| 3.4       | Fast Scanning Calorimetry .....                                       | 122 |
| 3.4.1     | Custom-Built Chip Based Calorimeter .....                             | 122 |
| 3.4.2     | Mettler Toledo Flash DSC1 .....                                       | 126 |
| 3.4.3     | Experimental Methods for Quantitative FSC .....                       | 128 |
| 3.4.3.1   | FSC on Polymer Thin Films .....                                       | 128 |
| 3.4.3.2   | FSC on Electrospun Fibers .....                                       | 131 |
| 3.5       | Methods of Analyzing Fast Scanning Data .....                         | 133 |
| 3.6       | Assorted Equipment and Instruments - Mettler Hot Stage .....          | 139 |
| 3.7       | References .....  | 139 |
| Chapter 4 | Self Nucleation of PVA .....  | 147 |
| 4.0       | Sample Preparation Approaches .....                                   | 147 |
| 4.1       | Thermal Stability of PVA .....  | 148 |
| 4.2       | Self Nucleation of PVA by DSC .....                                   | 152 |
| 4.3       | Self Nucleation by FSC .....  | 161 |
| 4.4       | References .....  | 168 |
| Chapter 5 | Fundamental Thermal Properties of PVA by FSC .....                    | 170 |

|   |   |     |
|---|---|-----|
| 5.1   | Thermal Stability of PVA.....                               | 171 |
| 5.2   | Degree of Crystallinity of PVA.....                         | 174 |
| 5.3   | Liquid Phase Heat Capacity of PVA.....                      | 180 |
| 5.4   | Critical Cooling Rate for PVA.....                          | 181 |
| 5.5   | Glass Transition of PVA.....                                | 183 |
| 5.6   | Discussion of Fundamental Thermal Properties.....           | 190 |
| 5.7   | References.....   | 196 |
| Chapter 6 Novel Method for Fast Scanning Calorimetry of Electrospun Fibers: Polyethylene Terephthalate (PET) Nanofibers.....  |   |     |
| 6.0   | Introduction and Proof of Concept.....                      | 199 |
| 6.1   | Analysis of Electrospun PET Fibers.....                     | 200 |
| 6.2   | Fiber Integrity During Handling.....                        | 203 |
| 6.3   | Cold Crystallization and Melting of PET Fibers.....         | 206 |
| 6.4   | Conventional DSC on PET fibers.....                         | 212 |
| 6.5   | Melt Crystallization of PET confined to Droplets.....       | 215 |
| 6.6   | Empty TEM grids and Indium Loaded Grids.....                | 220 |
| 6.7   | References.....   | 224 |
| Chapter 7 Electrospun Polyvinyl Alcohol Nanofibers: Potential as Neural Tissue Scaffolds (PAT 2016 Internship) and Investigation into Fundamental Thermal Properties..... |   |     |
| 7.1   | Characterization of Electrospun PVA Fibers.....             | 230 |
| 7.1.1   | Assessment of “as spun” Fibers.....                         | 230 |
| 7.1.2   | 7.1.2 Stabilization of Nanofibers.....                      | 232 |
| 7.2   | Protein Coating and Creation of Neural Tissue Scaffold..... | 238 |
| 7.3   | Structural Analysis of PVA Nanofibers:.....                 | 240 |
| 7.4   | Thermal Analysis of Electrospun Nanofibers.....             | 243 |
| 7.4.1   | Conventional Thermal Analysis.....                          | 243 |
| 7.4.2   | FSC based Thermal Analysis of PVA Fibers.....               | 252 |
| 7.5   | References.....   | 255 |
| Chapter 8 Conclusions and Future Work.....  |   |     |
| 8.1   | Conclusions.....  | 262 |
| 8.2   | Future Work.....  | 266 |
| 8.3   | References.....   | 269 |

|            |  |     |
|------------|--|-----|
| Appendix A | Thermal Characterization of Thermotropic Nematic Liquid-Crystalline Elastomers ..... | 273 |
| Appendix B | MATLAB Code .....  | 302 |

## List of Tables

|            |  |     |
|------------|--|-----|
| Table 4.1: | % Sample mass loss per cycle and peak crystallization temperature .....  | 151 |
| Table 4.2: | Corrections to Initial Mass of PVA from Bound Water Removal and Degradation, at Various Self Nucleation Temperatures .....   | 154 |
| Table 5.1: | PVA sample properties: surface area, mass, enthalpy of crystallization, enthalpy of melting, and mass fraction crystallinity .....   | 179 |
| Table 5.2: | Short time isothermal melt crystallization .....   | 187 |
| Table 5.3: | Long time isothermal melt crystallization .....  | 188 |
| Table 5.4: | DSC isothermally crystallized samples .....  | 189 |
| Table 6.1: | Glass transition temperature, sample mass, mobile amorphous fraction, crystalline fraction, and rigid amorphous fraction for each cold crystallized fiber sample, as a function of crystallization conditions. ....  | 211 |
| Table 6.2: | Standard DSC results of glass transition temperature and heat capacity increment, melting peak temperatures and endotherm area, mobile amorphous, crystal, and rigid amorphous mass fractions for electrospun PET brought through the rate adjusted temperature-time profile. .... | 214 |
| Table 6.3: | Temperature series isothermal melt crystallization data on PET: heat capacity increment, peak melting temperature, temperature corrected heat of fusion, and crystalline, mobile amorphous, and rigid amorphous mass fractions.....  | 218 |
| Table 6.4: | Time series melt crystallization data on PET: glass transition temperatures, peak melting temperatures, and crystalline, mobile amorphous, and rigid amorphous mass fractions. ....  | 219 |
| Table 7.1: | Average fiber dimeters in nm corresponding to the data presented in Figure 7.5B ..   | 237 |
| Table 7.2: | Thermal properties of electrospun PVA fibers as measured by DSC .....  | 248 |
| Table 7.3: | Assessment of the thermal properties during heating of dried, “as spun” fibers and stabilized fibers: .....  | 251 |

## List of Figures

|             |  |   |
|-------------|--|---|
| Figure 1.1: | (A) Polyethylene and (B) the ethylene monomer, structures drawn with ChemDraw [3].....               | 2 |
| Figure 1.2: | (A) linear polyethylene and (B) branched polyethylene, structures drawn with ChemDraw Prime [3]..... | 3 |

Figure 1.3: Polymer tacticities: (A) isotactic, all functional groups lie in the same plane and orientation with respect to one another; (B) syndiotactic, every other functional group lies in plane and the other out of plane; (C) atactic, functional groups have random orientation with respect to one another. Solid and dashed wedges indicate bonds into and out of the page, respectively. Structures drawn with ChemDraw Prime [3]. ..... 5

Figure 1.4: The crystal structure is formed when atoms, ions, or molecules are placed at every point on a (A) space lattice. (B) A basis containing an ion pair is added to every point on the space lattice to form the (C) crystal structure. Figure reproduced from [45]. ..... 9

Figure 1.5: NaCl crystal structure and lattice example where chlorine is shown in purple and sodium in green. The unit cell vectors  $a$ ,  $b$ , and  $c$  are labelled. Original image annotated [46]... 10

Figure 1.6: The Miller indices ( $hkl$ ) define the set of planes across the unit cell. Figure reproduced from [47]. ..... 11

Figure 1.7: (A) Local thermodynamic phase,  $\beta$ , inside the parent phase,  $\alpha$ . (B) A critical nucleus,  $\beta_m$ , which is made from  $m$  particles formerly in the  $\alpha$  phase. .... 13

Figure 1.8: Free energy difference vs. number of particles in the nucleus, per Eqn. 1.3. The critical nucleus size,  $m$ , in terms of number of particles,  $i^*$ , is determined by the free energy maximum,  $\Delta G^*$  ..... 14

Figure 1.9: Bulk polymer crystal spherulites observed under crossed polarizers (see Section 3.1.1 for discussion of imaging technique) Scale bar is 200 microns and applies to both images. Figure reproduced from [61]. ..... 18

Figure 1.10: (A) Three-dimensional molecular structure of the PET monomer repeat unit seen in different views; (B) the crystalline unit cell of PET in dotted outline; and (C) the chemical structure of the PET molecule reproduced from [64, 65]. ..... 19

Figure 1.11: (A) Polymer nucleus formed from a series of adjacent polymer chain segments with amorphous chain segments not incorporated and (B) a general schematic of the stable polymer nucleus with dimensions  $a$ ,  $b$ , and  $l$  (where  $l$  is analogous to  $c$  in Figure 1.10). The surface free energy of the growth faces and fold face are denoted by  $\sigma$  and  $\sigma_e$ , respectively reproduced from [62]. ..... 20

Figure 1.12: A schematic of polymer crystallization from a nucleus. For the single crystal case, chains can attach at any surface other than the fold surface,  $\sigma_e$ . In this image the dimensions  $a$  and  $b$  correspond to the unit cell dimensions of the polymer crystal as shown in Figure 1.10 and  $l$  is the lamella thickness. Figure reproduced from [66]. ..... 22

Figure 1.13: Polymer crystal growth rate vs. lamella thickness. The solid black line is the kinetic barrier to nucleation and crystallization. The dashed, dotted line is the thermodynamic driving force. The dashed line is the resultant sum of these two competing forces. The minimum lamella thickness  $l_{min}$  is the minimum stable lamella thickness in Eqn. 1.10. The blue arrow indicates the kinetically favored lamella thickness. Figure reproduced from [68]. ..... 23

Figure 1.14: Formation of the bulk polymer crystal, the spherulite from (top left) a nucleus to (top middle and right) a bundle of growing lamella (bottom right) branching of lamella by secondary nucleation and crystal growth between lamella resulting in (bottom left) a fully formed polymer spherulite. Reproduced from [70] ..... 24

Figure 1.15: (A) Free energy of mixing vs. composition of the mixture. The composition boundaries for the stable, single phase mixture is determined from the local minima at a given

temperature. The composition boundary for the metastable mixture is determined by the inflection points between the local minima and the local maxima in the free energy. (B) Phase diagram as function of temperature and composition. The metastable and unstable regions are indicated by the blue and red arrows, respectively. .... 27

Figure 1.16: Schematic diagrams of microstructures formed by phase changes within the phase diagram shown in Figure 1.15B. (A) Nucleation and growth (N+G) of phase A within phase B, corresponding to the left hand metastable region in Figure 1.15B. (B) Spinodal decomposition (SD) into two, unmixed phases A and B corresponding to the unstable region in the phase diagram shown in Figure 1.15B. (C) Nucleation and growth (N+G) of phase B within phase A, corresponding to the right hand metastable region in Figure 1.15B. Figure adapted and reproduced from [72]. .... 28

Figure 1.17: Schematic of semicrystalline polymer phases. Lamella crystals are shown in the blue shaded regions. Mobile amorphous fraction (MAF) is shown in the yellow shaded region. The presence of crystals kinetically arrests the polymer chains and results in rigid amorphous fraction (RAF). .... 30

Figure 1.18: (A) Schematic of semicrystalline polymer; (B) Following melting seed nuclei or segments of aligned regions of polymer chains remain in the melt (shown in green); (C) Amorphous melt is recovered. .... 31

Figure 1.19: Optical micrograph images of crystals formed by self nucleation. (A) A pair of initial polymer spherulites before melting. (B) During melting, within radii of the spherulites, indicated by the green circle, an abundance of nuclei remain and trigger crystallization by self nucleation when the sample is cooled. Figure reproduced from [83]. .... 32

Figure 1.20: Chemical structure of (A) polyvinyl alcohol (PVA) and (B) polyvinyl acetate (PVAc) drawn using ChemDraw Prime [3]. .... 35

Figure 2.1: (A) Semi-crystalline PVA as received from PolySciences, Inc, (B) following solution processing into a 250  $\mu\text{m}$  thick film which has been cut to size using a hole punch to fit a standard DSC pan, and (C) spin coated onto a PTFE slide resulting in a film approximately 3  $\mu\text{m}$  thick. .... 57

Figure 2.2: (A) Sample cut from the thicker PVA film and loaded onto a Mettler Toledo UFSC11 sensor, imaged at 100x; (B) Sample from (A) digitally magnified for surface area determination and assessment of cut quality; (C) Sample mounted on a XI-390 chip sensor of the custom-built calorimeter [15, 16], imaged at 200x. .... 58

Figure 2.3: Electrospinning schematic reproduced from [23]. A syringe loaded with conductive polymer solution is placed in a syringe pump which pumps solution through the needle tip at constant rate. High voltage is applied to the needle tip and a rotating collector is grounded and serves as the counter electrode which is placed a fixed distance away. The electric field interacts with the solution and deforms the droplet creating the Taylor cone, pictured at the top, to the right of the syringe. With the proper electrospinning conditions a nanofibrous mat is deposited on collector. .... 61

Figure 2.4: (A) Single channel programmable syringe pump loaded with DGA syringe, also seen at the left side of (B) which shows the insulated PTFE lined box housing the counter electrode collector. The high voltage power supply is seen in the bottom right corner of the image. The

entire setup is run inside a larger vented cabinet which protects users from the volatile solvents used during the electrospinning process. .... 63

Figure 2.5: Example of an electrospun fiber mat next to a DGA syringe. The bulk tape is approximately 2.5 cm wide and has a thickness of about 100  $\mu\text{m}$ . .... 64

Figure 2.6: (A) Mettler Toledo UFSC1 chip sensor for use in the Mettler Flash DSC1. Example of a UFSC1 sensor with a penny for scale. The active sensor area is the light gray circle indicated by the arrow on the left side of the image. (B) A cross section of the sensor well from Mettler Toledo Product Literature [37]. Samples are manually lowered into the well using a fine wire and should be kept to heights less than 10  $\mu\text{m}$ . The components listed are: 1 – Ceramic Base, 2 – Silicon Frame, 3 – Connecting Wires, 4 – Resistance Heater, 5 – Aluminum Sample Area, 6 – Thermocouple. .... 67

Figure 2.7: Image of electrospun fibers manually deposited on sensor with silicone oil at 50x total magnification (A) and 100x total magnification (B). Getting fibers completely on top of the sensor is challenging as they move and spread out. The dark color of the fiber and oil indicates that the mass of material on top of the sensor is quite thick. .... 68

Figure 2.8: (A) Direct deposited electrospun PVA on a Mettler Flash UFSC1 sensor. (B) Cleaned reference side following water/ethanol solution rinse. (C) Fibers once melted show effective heating when samples are deposited on the underside of the sensor. The diameter of the silver, circular sensor is 500  $\mu\text{m}$ . .... 70

Figure 2.9: (A) TEM grid as received. (B) TEM grid through 10x objective, 100x overall magnification. The notched number “1” allowed for uniform alignment of the grids on the electrospinning drum. (C) TEM grids are aligned along the center of the electrospinning drum as indicated by the white arrow. Fibers are seen to be uniformly distributed across the width of the grid. The width of the foil wheel is approximately 1 inch. (D) Carefully unwrapping the foil from the rotating drum collector does not disturb the fibers or grids. White arrow indicates the TEM grid held in place between the conductive copper tape. .... 72

Figure 2.10: Thermally stabilized fibers are placed in the bottom of standard 24-well tissue culture plates and weighted down with FDA grade Viton™ rubber O-rings to prevent them from moving during sterilization, coating, and tissue plating. In this image, 9 wells contain fiber mats. .... 75

Figure 2.11: Example of how electrospun fibers are prepared for standard DSC experiments. (Left) Fibers are cut from the bulk tape and then rolled around a wire or the tip of a pair of tweezers. (Right) Rolled fibers are placed into DSC pans with the roll axis either parallel to the bottom of the pan (FXE) or perpendicular to the bottom of the pan (STD). Fibers placed loosely in the pan (FRE) can have poor sample to sensor contact as they contract during heating. Reproduced from [33]..... 77

Figure 3.1: (Left) Schematic of the basic principle behind polarized light microscopy and (right) an annotated image of the components of our Nikon E600 POL microscope. This image is reproduced from Nikon product literature [1]. .... 86

Figure 3.2: Polarizing optical microscopy image of melt crystallized polystyrene spherulites. Spherulites are the bright, circular structures highlighted by the green circles. The dark region surrounding the spherulites is the isotropic amorphous melt which appears dark between crossed

polarizers, whose fast axes directions are indicated by the white cross in the upper left corner. Image is reproduced from literature [2]. ..... 87

Figure 3.3: Schematic diagram of the components in a typical scanning electron microscope reproduced from [3]. The anode and alignment coil serve to collimate the electrons which are further focused by the condenser lens (CL) and the objective lens (OL). The entire system is under vacuum, typically in the range of 1-2 mb for tabletop SEM units. Secondary electrons which are emitted from the sample surface are recorded by the secondary electron detector. Additional components are added to detect backscattered electrons, X-rays, and photons emitted via cathode luminescence. .... 90

Figure 3.4: Example SEM micrographs of polyvinyl alcohol (PVA) fiber mats obtained with (A) Zeiss EVO MA10 SEM, and (B) Phenom G2 Pure Tabletop SEM. Differences in the fiber morphology are due to differences in the electrospinning conditions. Image quality and feature resolution are comparable at 4800x-5300x between the two instruments. .... 93

Figure 3.5: The various vibrational modes possible when a methylene molecule absorbs infrared radiation. Figure reproduced from [8]. + indicates rotations out of the page and – indicates rotation into the page. .... 95

Figure 3.6: (A) Michelson interferometer used inside a typical FTIR instrument reproduced from [9]. (B) Example of the baseline interferogram for an ideal system when no sample is present reproduced from [10]. The large peak in the center of the plot is the reference position at zero optical path difference. .... 97

Figure 3.7: Example of sample absorbance vs. wavenumber in  $\text{cm}^{-1}$  for a thermally stabilized PVA fiber mat. .... 99

Figure 3.8: Bragg's Law for constructive interference of X-rays scattered from a real space lattice. Constructive interference is only observed between atomic planes of spacing,  $d$ , when the path difference between the incident and scattered beam is equal to  $n\lambda$  where  $n$  is an integer. Image is reproduced from [14]. .... 102

Figure 3.9: Example of the Ewald Construction reproduced from [16]. The white dots on the right-hand side of the image are the reciprocal lattice points of the crystal. The white circle is the circle of radius  $2\pi/\lambda$  and the incident and scattered wavevectors are denoted  $k$  and  $k'$ , respectively. The incident X-rays are coming in from the left-hand side of the image in the direction  $k$  and strike the crystal located at the center of the white circle. The scattered X-rays move in the direction  $k'$ . If, for given  $\lambda$  and  $k$ ,  $k$  terminates on a point in the reciprocal lattice, then the Bragg condition is satisfied when the difference in the wavevectors,  $k' - k$ , has magnitude  $|G|$ , where  $G$  is a reciprocal lattice vector. Bragg's law is satisfied for reciprocal lattice points which lie on the circumference of the white circle. .... 104

Figure 3.10: X-ray diffraction pattern for as spun (blue) and isothermally crystallized (red) PVA electrospun fibers mounted on silicon (100) substrate. Substrate and background have been subtracted. .... 106

Figure 3.11: Reproduced diagram of a power compensated DSC [20]. Two independent furnaces are equipped with a heating element and temperature sensor. A sample (S) in a sealed pan is placed in one furnace and an empty reference pan (R) (nearly identical in mass to the sample pan) is placed in the other. The power required to bring each furnace through the temperature – time profile is recorded and the difference between these powers is measured. .... 108

Figure 3.12: (A) TA Instruments Q100 DSC in room 421 at 574 Boston Ave (B) Image of the open DSC cell (C) Cut away diagram of the Q100 Tzero™ DSC cell from the literature published by the manufacturer [24] The right hand side shows a cutaway of the sample post with a chromel wire thermopile under the sample (or reference). ..... 111

Figure 3.13: Heat flow rate vs. temperature curve for the heating of a quenched polyethylene terephthalate (PET) sample heated at 10 °C/min. Solid arrows with labels point to the various observed phase changes in the sample. Dashed arrows identify each heat flow rate baseline observed during heating. .... 114

Figure 3.14: (A) Schematic of the temperature profile during self nucleation experiments. First heating to  $T_s$  (black). Subsequent treatment (holding for 5 minutes at  $T_s$ , cooling, and reheating):  $T_s = 220$  °C (blue), 230 °C (red), 240 °C (green). The heating and cooling rates are  $\pm 10$  °C/min. The glass transition temperature,  $T_g$ , and endothermic peak melting temperature,  $T_m$ , are marked with dashed lines. The treatment stages are marked 1-4. [37-39] (B) Bounds on  $T_s$  values sampled are determined using the melting endotherm from first heating of PVA at 10 °C/min, and fall between the solid line and a temperature 10 °C above the dashed line which represents completion of the endotherm. Endotherm area was used to measure the initial crystallinity of the parent solution cast film. .... 118

Figure 3.15: Modulated temperature vs. time for a heating rate of 5 °C/min with temperature modulation amplitude of  $\pm 0.796$  °C over a period of 60 s. The solid blue curve is the TMDSC heating ramp and the dashed, orange line is the underlying, standard heating rate. This image is shown over a shorter range so that the modulated rate can be easily seen apart from the underlying heating rate. .... 120

Figure 3.16: (A) Images of the custom chip sensors manufactured by Xensor Integration designed for the custom-built calorimeter, figure reproduced from [50]. (B) Schematic of the chip sensor. Heating elements sit under the silicon nitride film supported on the silicon frame. Temperature sensors sit in between the heaters directly under the sample. A junction between the silicon frame allows the silicon nitride membrane to remain at the sensor support temperature. (C) Optical microscope image of a sample loaded onto the membrane shown in (A). Scale bar is 20  $\mu\text{m}$ . .... 123

Figure 3.17: Schematic of the entire custom-built chip based calorimeter [50]. The silver disk pictured at the bottom of the image is the temperature controlled oven where the individual chip sensors are loaded. In this image one sensor acts as the sample furnace and the other is the reference furnace. .... 124

Figure 3.18: Temperature vs. time schematic for the experiments performed on the custom-built calorimeter. Initial heating is shown in green at a heating rate of 10,000 K/s. The sample is then cooled at various rates between 1000 K/s and 200,000 K/s, shown in blue. The sample is reheated at 10,000 K/s, shown in red. .... 125

Figure 3.19: Reproduced image from paper detailing the design and testing of the MultiSTAR UFSC1 chip sensor [22]. Figure has been rearranged. (A) shows the chip upside down relative to how it is loaded into the Flash DSC1. Gold contacts on the ceramic base connect wires to the membrane sensor (B) with the Flash DSC1 base. (B) Individual membrane sensor. The bright circle in the middle is the aluminum layer on top of the primary and secondary heating elements. Black arrow points to one pair of the 8 total thermocouples which surround the sensor area. .. 127

Figure 3.20: Mettler Flash DSC1 being loaded with UFSC1 sensor, image is reproduced [55]. The left panel is the Flash DSC1 device, the middle panel is the sensor stage with gas purge lid open so the sample can be viewed through the overhead microscope. The right panel shows the UFSC1 chip lowered into the device without the holding collar in place. From this view the membranes are in recessed wells as diagrammed in Figure 2.6. .... 128

Figure 3.21: Temperature vs. time profile for the initial heat-cool-heat cycle applied to each sample. The blue segment is the first ramp to the melt which ejects solvents and flattens the sample, optimizing sample to sensor contact. The cool-heat segments, green segments above, are used for symmetry correction and mass determination, and then compiled for the second set of experiments. .... 129

Figure 3.22: The general temperature vs. time profile for isothermal melt crystallization experiments. Initial heat-cool-heat cycle segment is shown in green. Samples are cooled to  $T_c$  from the melt at 2000 K/s, crystallized isothermally for  $t_c$ . The crystallization step is shown as the orange segments in between the blue cooling and reheating ramps. .... 131

Figure 3.23: Temperature – time profile for the fast scanning methods used to measure electrospun fiber loaded grids. The purple segments at the beginning are first ramp and hold to a temperature above  $T_g$  where solvents are ejected. The blue segments that follow are the cold crystallization experiments where the fibers are crystallized and melted. Once melted the fibers are cooled at controlled rate to the sensor support temperature. The green segments represent various melt crystallization experiment which are appended following the initial fiber scan.... 132

Figure 3.24: Treatment of raw heat flow rate vs. temperature data. (A) Uncorrected raw sample data in heating (red) and cooling (blue); empty sensor data in heating (yellow) and cooling (purple). (B) Sample heat flow rate data after empty sensor subtraction in heating (red) and cooling (blue). Regions selected for symmetry line determination - heavy red and blue curves; Symmetry line - green. (C) Sample apparent heat capacity after subtraction of both the empty sensor and the symmetry line, in heating (red) and cooling (blue)..... 134

Figure 3.25: Optical microscope image of the five samples following the final heating collected using the Olympus microscope. Several samples were observed to curl up during the first ramp to the melt. .... 136

Figure 3.26: Raw heat flow rate vs. temperature curves for the five samples on a single sensor heated through the temperature – time profile shown in Figure 3.21. The curves in shades of blue correspond to cooling and the shades of red correspond to heating. As the number of samples (and subsequently the mass) increases the heat flow rate scales such that the curves are farther from the line of symmetry (i.e., the line at zero heat flow rate) between them. .... 137

Figure 3.27: Cases where the corrections applied and use of Eqn. 3.17 (A) does not require rotation and (B) requires rotation. The uncertainty in the mass is reported as the standard deviation of the mass about the straight line of best fit through masses as a function of temperature. .... 138

Figure 4.1: Heat flow rate vs. temperature curves over subsequent cycles (numbered 1-8 corresponding to cycle) of: (A) cooling “C” from  $T_s$ , showing loss of exotherm area and depression of peak crystallization temperature; (B) reheating “H”, showing loss of endotherm area and depression of peak melting temperature. Here, the same sample was used for all cycles of cooling and heating..... 149

Figure 4.2: %Weight remaining vs Temperature for (A) TGA scans over subsequent cycles of heating and cooling to 240 °C at 10 °C/min. Cycles 2-6 are numbered for clarity. (B) TGA scans at different self nucleation temperatures:  $T_s = 225$  °C (blue), 230 °C (red), and 235 °C (green). Each sample is heated to  $T_s$ , held 5 min (vertical section of the curves), then cooled and reheated. The arrows signify the range of mass lost due to water removal and to degradation..... 150

Figure 4.3: DSC heat flow rate vs. temperature, for (A) cooling and (B) reheating after thermal treatment at various self nucleation temperatures:  $T_s = 220$  °C (dark blue), 224 °C (red), 226 °C (yellow), 230 °C (purple), 234 °C (green), 238 °C (light blue). Curves have been vertically shifted for clarity..... 155

Figure 4.4: Melting onset temperatures as a function of  $T_s$  with low temperature onset plotted in circles and the second higher temperature onset (Domain III only) plotted in diamonds. Domain III - green symbols; Domain II - blue circles; Domain I - red circles. Domain boundaries are denoted by vertical dashed lines ..... 156

Figure 4.5: Crystallization peak temperatures as a function of  $T_s$ . Domain I (red), domain II (blue), domain III (green). ..... 158

Figure 4.6: Peak crystallization temperature against % Mass Loss for self nucleation experiments with each point representing a fresh sample (blue squares) and for multicycle experiments performed on a single sample (red circles). ..... 159

Figure 4.7: Domain II (blue circles) and Domain I (red circles) final crystallinity vs. self nucleation temperature with error bars  $\pm 0.004$ . The upper bound on the average initial crystallinity is indicated by the green dashed line. .... 160

Figure 4.8: Sampling of FSC heat flow rates vs. Temperature for (a) cooling and (b) reheating for various self nucleation temperatures,  $T_s$ . In order to highlight the recovery of glassy and melt baselines, curves have not been separated. .... 162

Figure 4.9: Melting peak temperatures as a function of  $T_s$  (red circles and purple squares) and cold crystallization peak temperatures (green diamonds) as a function of  $T_s$ . The domain III boundary is marked with a vertical, dashed line ..... 164

Figure 4.10: Crystallization peak temperatures as a function of  $T_s$ . Heterogeneously nucleated crystals (blue circles) and homogeneously nucleated crystals (green squares) formed non-isothermally during cooling. The vertical, dashed line marks the domain III boundary and the dashed and dotted line marks the shift from annealing to partial melting and annealing within domain III..... 165

Figure 4.11: Fast scanning heat flow rates vs. temperature for (A) cooling from  $T_s$  and (B) reheating, for three values of  $T_s$  near the domain III boundary. .... 166

Figure 5.1: Optical microscope images of PVA films at magnification of 100x before and after heating and cooling at  $|\beta| = 2000$  K/s. (A) As prepared on sensor and before heating; (B) after 5 meltings; (C) after 20 meltings; (D) 45 meltings. Sample can be seen to shrink between (A) and (B) indicating melting and bulk reorganization. Color changes from (B) through (D) indicate increasing sample degradation. .... 172

Figure 5.2: Heat flow rate from FSC as a function of temperature at  $|\beta| = 2000$  K/s after multiple meltings. Line styles are varied for clarity. (A) Cooling; (B) Heating. .... 173

Figure 5.3: Mass calculated per Eqn. 3.17 vs. sample surface area measured as described in Section 2.6..... 175

Figure 5.4: Enthalpy of melting,  $\Delta h_f$ , vs. mass calculated using Eqn. 1. Dashed, black line is the line of best fit. Intercept of 0.03  $\mu\text{J}$  indicates a systematic error and all reported enthalpies are adjusted accordingly. .... 177

Figure 5.5: Apparent specific heat capacity of PVA as a function of temperature at  $\beta = 2000$  K/s for 14 samples measured using the Mettler Flash DSC1. The literature values for the solid state heat capacity of PVA [6] are shown by the solid black line. The average experimental liquid phase heat capacity is extrapolated beyond the range of measurement, as shown by the dashed black line. .... 181

Figure 5.6: (A) Apparent specific heat capacity of PVA vs. temperature during heating at 10,000 K/s (colored curves), after cooling from the melt at the indicated rates using the custom calorimeter. Cooling at 20,000 K/s is overlaid (black line). (B) The overall change in enthalpy during heating at 10,000 K/s vs. prior cooling rate. Error bars are  $\pm 2.0$  J/g. The vertical dashed, black line indicates the upper limit of the cooling rate accessible for measurement in the Mettler Flash DSC1. Rates to the right of the dashed line are available only with the custom calorimeter. .... 182

Figure 5.7: Heat flow rate vs. temperature for PVA heated at 2000 K/s after isothermal melt crystallization for various short times at a temperature of: (A) 90 °C; (B) 95 °C; (C) 120 °C. Crystallization time increases as the color changes from blue to yellow. The glass transition temperature increases with crystallization time. .... 184

Figure 5.8: Heat flow rate vs. temperature for PVA heated at 2000 K/s after isothermal melt crystallization for various long times at a temperature of: (A) 140 °C; (B) 150 °C. Crystallization time increases as the color changes from blue to yellow. The glass transition temperature increases with crystallization time. .... 185

Figure 5.9: Apparent heat capacity vs. temperature and an example of the measurement of the heat capacity increment at the glass transition for PVA isothermally crystallized at 150 °C for 1 second. The dashed, green line is the tangent line of the glassy phase heat capacity taken below the glass transition (hollow, black square) and the dashed, red line is the tangent line of the semi-crystalline heat capacity taken above the glass transition. .... 186

Figure 5.10: Specific heat capacity increment at  $T_g$  vs. mass fraction crystallinity. Non-isothermally crystallized samples (blue x); Samples isothermally crystallized for short times at different temperatures: 90 °C (orange  $\square$ ), 95 °C (yellow  $\square$ ), 120 °C (red  $\square$ ). Samples isothermally crystallized for long times at different temperatures: 140 °C (green o), 150 °C (light blue o). Conventional DSC results are shown for comparison: PVA isothermally cold crystallized from 130-160 °C for various times or partially melted and annealed at 170 °C for various times (purple diamonds)..... 190

Figure 5.11: Recreation of Figure 5.10 with the addition of “less than gently degraded” data. Samples isothermally crystallized for short times at different temperatures: 100 °C (hollow pink  $\square$ ), 105 °C (hollow blue  $\square$ ), 110 °C (hollow red  $\square$ ), 115 °C (hollow black  $\square$ ), 125 °C (hollow fuchsia  $\square$ ), 130 °C (hollow green  $\square$ ). Conventional DSC Self Nucleation results are shown in dark blue diamonds for comparison, the meaning of other symbols can be found in the caption to Figure 5.10. The black dotted line is the best fit not including the newly added data..... 195

Figure 6.1: (A) SEM image of PET nanofibers taken from the aluminum foil between TEM grids. The spin direction is vertical. Images were collected at 5300X magnification where it was

possible to resolve the fiber diameter and assess fiber quality. (B) Fiber diameter distribution obtained using ImageJ [8] with the DiamterJ plugin [8]. The cluster of diameters between 800 nm and 1200 nm is the result of fiber mergers and fiber bundles which are not separated in ImageJ. .... 201

Figure 6.2: X-ray diffraction patterns for “as spun” (blue) and crystallized (orange) PET fibers. Fibers “as spun” are amorphous. The line segment at about  $33^\circ 2\theta$  replaces the silicon peak (100) peak from the sample holder. .... 202

Figure 6.3: (A) Optical image of ESPET loaded TEM grid though a 10X objective with 100x total magnification. Fiber bundles are observed to be running parallel to the spin direction. The alignment notch can be seen in the top left of the image. (B) Example of parent sample cut from the center of the ESPET loaded TEM grid. Fibers show no signs of being disturbed by the cutting process. (C) Oversized ESPET loaded TEM grid sample loaded onto Mettler UFSC1 sensor with fiber side up. Dark streaks running top to bottom are fiber bundles..... 204

Figure 6.4: (A) A typical example of a fiber loaded TEM grid loaded face down for FSC measurements. Here the jagged edges seen in the bottom left of the image show the last tolerable cut before a scalpel blade needs to be changed. (B) and (C) Cartoon schematics of fiber loaded sensor. The sensor is the gray oval, seen from an angled view. The orange polygon represents the TEM grid, the circular gray region represents the active sensor area on the UFSC1 chip, and the black lines represent the electrospun fibers. (B) Fibers loaded face down with minimal TEM grid impact. This sample has optimal contact with the sensor. (C) Grid cutting with a dull blade can result in crimping along the cut edges which prevents optimum sample to sensor contact. .... 205

Figure 6.5: Heat flow rate vs. temperature for a typical dry, isothermally cold crystallize, and melt experiment performed on electrospun fibers. The cold crystallization temperature,  $T_{CC}$ , is  $150^\circ\text{C}$  and the heating and cooling rate,  $\beta$ , is  $\pm 2000\text{ K/s}$ ..... 207

Figure 6.6: Example of a PET amorphous rescan following fiber melting. The curvature at high temperature seen here is due to the interaction between the tacky, liquid phase polymer and the thermal expansion and contraction of the TEM grid. The glass transition is fully expressed at  $84^\circ\text{C}$ , which is about  $15^\circ\text{C}$  above the equilibrium glass transition temperature,  $T_g = 69^\circ\text{C}$  [13]. 208

Figure 6.7: The rate adjusted temperature-time profile for replicating the FSC fiber drying and cold crystallization method (see Figure 3.23) in the Q100 DSC. Heating and cooling rates,  $\beta = \pm 0.5\text{ K/s}$ . The orange segments correspond to the drying step and the blue segments correspond to the cold crystallization and fiber melting steps. .... 212

Figure 6.8: Standard DSC heat flow rate vs. temperature for PET brought through the rate adjusted temperature-time profile. Non-isothermal cold crystallization is observed on the heating ramp to the crystallization temperature,  $T_{CC} = 150^\circ\text{C}$ . .... 213

Figure 6.9: Following a single heating fibers are observed to breakup into droplets (dark regions outlined with white ovals) or streams of continuous material (white arrow). As the fibers melt and coalesce into droplets regions of the TEM grid are left dry (black arrow). .... 216

Figure 6.10: Melt crystallization of PET confined to droplets following the complete melting of electrospun fibers. Moving from the bottom up the dashed, black curve is the first scan where the sample is quenched and reheated. Then the samples are melt crystallized between  $240^\circ\text{C}$  and  $100^\circ\text{C}$  in  $20^\circ\text{C}$  increments. Samples are isothermally melt crystallized at each temperature for 5

|  |     |
|--|-----|
| minutes and thermal history is completely erased by holding at 30 °C above the equilibrium melting temperature, $T_m^0 = 280$ °C, for 1 minute between each scan. ....   | 217 |
| Figure 6.11: Apparent heat capacity vs. temperature for a series of TEM grids of increasing area. Mass decreases from top to bottom in this image. Each curve comprises both the heating and cooling scans and shows nearly perfect overlap between heating and cooling following empty sensor subtraction and symmetry correction.....                                  | 221 |
| Figure 6.12: Average specific heat capacity of the copper TEM grids as measured from the five grids of increasing size. Black points are the NIST values [39] for the specific heat capacity of copper at various temperatures. ....   | 222 |
| Figure 6.13: Heat flow rate vs. temperature for indium loaded TEM grid. Inset shows the initial flake of indium loaded onto the rectangular section of TEM grid.....   | 223 |
| Figure 7.1: Images PVA fibers spun with various conditions obtained with the Phenom G2 SEM. (A) 8 wt.% PVA spun through a 26 gauge needle (B) and (C) 10 wt.% PVA spun through a 20 gauge needle. Green arrows indicate the prevailing fiber direction. Red circle highlights bead defects in the fiber mat. Electrospinning parameters can be found Section 2.3.1. .... | 230 |
| Figure 7.2: AFM topography scans of Electrospun PVA fiber mats over 50 $\mu\text{m}$ x 50 $\mu\text{m}$ area from (A) 30° tilt side view and (B) top down view. The fiber diameters are in agreement with the those observed in the SEM images. Data were taken by Derek Walkama and Peter Riley. ....   | 232 |
| Figure 7.3: Electron microscope images collected with the Zeiss SEM for (A) PVA “as spun” from mixed solvents and (B) following exposure to glutaraldehyde. Optical microscope images (obtained with the Zeiss internal microscope) of glutaraldehyde exposed dry fiber mats (C) after 1 hour in water and (D) after 16 hours in water.....                              | 233 |
| Figure 7.4: Images of PVA fiber mats at magnifications ranging between 4500-6000X collected with the Zeiss SEM for: (A) “as spun”, (B) following thermal stabilization treatment, (C) stabilized and soaked in water for 1 hour, (D) stabilized and soaked in water for 96 hours. ....   | 235 |
| Figure 7.5: (A) Example fiber diameter distribution for the “as spun” fiber mat, pictured in Figure 7.4A, and (B) average fiber diameters following each treatment where N is the “as spun” fiber, 0 received only thermal stabilization treatment with no water exposure, and each number corresponds to the number of hours fiber mats were soaked in water.....       | 236 |
| Figure 7.6: Neurons successfully plated and observed to be alive on the thermally stabilized, PDL, laminin, and fibronectin coated PVA tissue scaffold. The black and white arrow in the bottom left corner indicates the average fiber direction and one neuron is highlighted by the red circle. Image taken by Derek Walkama and Peter Riley. ....                    | 239 |
| Figure 7.7: X-ray diffraction patterns for (A) “as spun” (blue) and thermally stabilized (orange) PVA spun from DI water and (B) “as spun” (black) and thermally stabilized (green) PVA spun from 98/2 DI water/ acetic acid mixed solvent. ....   | 241 |
| Figure 7.8: Fourier Transform Infrared Spectroscopy absorbance spectra for (A) “as spun” (blue) and thermally stabilized (orange) PVA spun from DI water and (B) “as spun” (black) and thermally stabilized (green) PVA spun from 98/2 DI water/ acetic acid mixed solvent. The black arrow refers to the crystalline vibration at 1140 $\text{cm}^{-1}$ .....           | 242 |
| Figure 7.9: Thermogravimetric %mass remaining vs. temperature for “as spun” PVA spun from DI water (blue) and the 98/2 DI water/ acetic acid mixed solvent (orange). The glass transition is marked by the vertical, dotted line at $T_g = 85$ °C [31] and the equilibrium melting point is  |     |

marked by the vertical, dashed line at  $T_m^0 = 265 \text{ }^\circ\text{C}$  [31]. Both fibers show similar (6-7%) solvent retention and lose between 20-30% of their mass by  $T_m^0$ . ..... 244

Figure 7.10: Heat flow rate vs. temperature for (A) dried “as spun” (blue) and thermally stabilized (orange) PVA spun from DI water and (B) dried “as spun” (black) and thermally stabilized (green) PVA spun from 98/2 DI water/ acetic acid mixed solvent. Heating was performed at a rate of  $5 \text{ }^\circ\text{C}/\text{min}$ . ..... 246

Figure 7.11: Reversing and non-reversing heat flow rate vs. temperature. (A) PVA spun from DI water. Dried “as spun” is shown in blue and thermally stabilized shown in orange. The solid and dashed curves corresponding to the reversing and non-reversing heat rates, respectively. (B) PVA spun from mixed solvent. Dried “as spun” is shown in black and thermally stabilized shown in green. The solid and dashed curves corresponding to the reversing and non-reversing heat rates, respectively. .... 249

## *Chapter 1 Introduction*

### *1.0 Polymers*

Polymers are large molecules which can be either naturally occurring, or derived from natural sources, or derived synthetically. Naturally occurring biological macromolecules such as DNA, proteins, carbohydrates, and fatty acids are all polymers and essential to the function of living cells. Until the 1930s and the discovery of synthetic polymers, natural rubber sourced from tropical plantations was a critical strategic resource. The crosslinking of natural rubber (vulcanization) ushered in the modern polymer era. Modern synthetic polymers account for everything ranging from the polyester clothes we wear to the recyclable plastic cups that hold our morning iced coffee.

The incredible spectrum of applications and uses for polymers is due to favorable chemical and mechanical properties which allow light, durable, flexible, recyclable, and often biocompatible materials to be fabricated and processed at every scale ranging from laboratory research to industrial scale. This thesis presents research on both the fundamental structural and thermal properties of common, synthetic polymers as well as tuning their nano and microscale structures for novel applications.

This chapter serves to provide a basic overview of polymers, their molecular and microscale structure, and connect how the research conducted ties in with the greater body of polymer science. **Section 1.1** introduces polymer molecules; **Section 1.2** details polymer phases and provides a general overview of crystals; **Section 1.3** provides an overview of crystallization; **Section 1.4** provides an overview of the rigid amorphous fraction; **Section 1.5** introduces a special

case of polymer crystallization arising from self-nucleation; **Section 1.6** serves to introduce the following chapters and the motivation for the experiments performed.

### 1.1 Polymer Basics

A polymer is a macromolecule made up of hundreds to tens of thousands of repeating molecular units covalently bonded together. The base repeating unit is referred to as a monomer. Polymers which contain one repeat unit are referred to as homopolymers and those with two or more are referred to as copolymers. [1, 2] As an example, consider the simple polymer, polyethylene, shown in **Figure 1.1A**. This molecule is made of  $n$  repeating ethylene monomers, shown in **Figure 1.1B**. Each ethylene monomer is a pair of methylene ( $-\text{CH}_2$ ) groups.

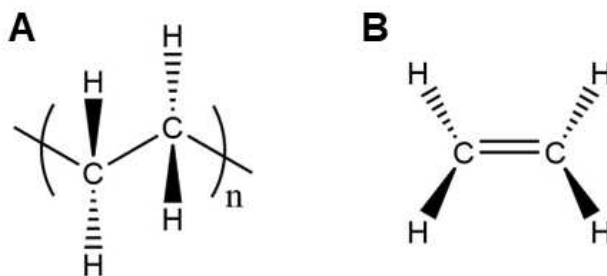


**Figure 1.1:** (A) Polyethylene and (B) the ethylene monomer, structures drawn with ChemDraw [3].

The sequence of carbon to carbon (C-C) bonds make up the backbone of this polymer with single hydrogen atoms forming the side groups of the polymer chain. The molecular weight of the macromolecule polyethylene is a function of the number of ethylene units it contains. In practice this is also referred to as the degree of polymerization,  $\text{DP}_n$  [2].

$$DP_n = X_n = M_w/M_0 \quad (1.1)$$

where  $M_w$  is the molecular weight of the polymer and  $M_0$  is the molecular weight of the monomer

Molecular weight is only directly proportional to the chain length of a polymer if the polymer is linear, meaning that all of the monomers are bonded end to end as in the example polyethylene in **Figure 1.2A**. The diameter of the polyethylene chain pictured **Figure 1.1A and 1.2A** is on the order of about 1 nm but a chain with 10,000 units would have an end to end length on the order of 1  $\mu\text{m}$ . It is also possible to have branched polymers where segments of polymer will be attached to the backbone, in the case of polyethylene this results in one hydrogen along the C-C backbone being replaced by a covalent bond to another carbon as shown in **Figure 1.2B**.

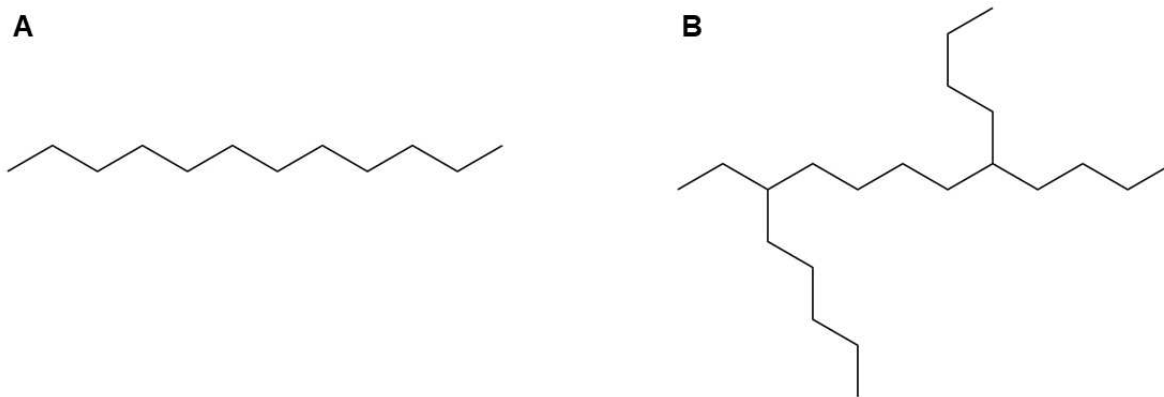


**Figure 1.2:** (A) linear polyethylene and (B) branched polyethylene, structures drawn with ChemDraw Prime [3].

Compared to linear polymers, the presence of branches typically reduces the crystallinity of the polymer and results in lower bulk density. In addition to branching, there are two chemical

structure (makeup/ chemistry) independent factors that impact the bulk behavior of a polymer, polydispersity and tacticity. In the bulk there are millions of millions of individual polymer chains which have various molecular weights. The polydispersity coefficient for a bulk polymer is the ratio of the weight average molecular weight,  $\overline{M}_w$ , and the number average molecular weight  $\overline{M}_n$  and serves as a useful measurement of the distribution of molecular weights. The polydispersity coefficient is given by the following relationship [2]:

$$U = \overline{M}_w / \overline{M}_n \quad (1.2)$$

The tacticity of a polymer refers to the spatial orientation of functional groups along the polymer backbone with respect to one another. These conformations are shown schematically in **Figure 1.3**. Tacticity plays an important role, particularly in polymers which have large functional groups along the backbone, or side groups which have particularly large dipole moments. In some polymers, polyvinylidene fluoride (PVDF) for example, the alignment of the fluorine atoms along the backbone gives rise to piezoelectric response in the bulk material [4]. Certain polymers cannot readily crystallize if they are atactic; polystyrene is typically only crystalline in the isotactic and syndiotactic conformations [5-7].

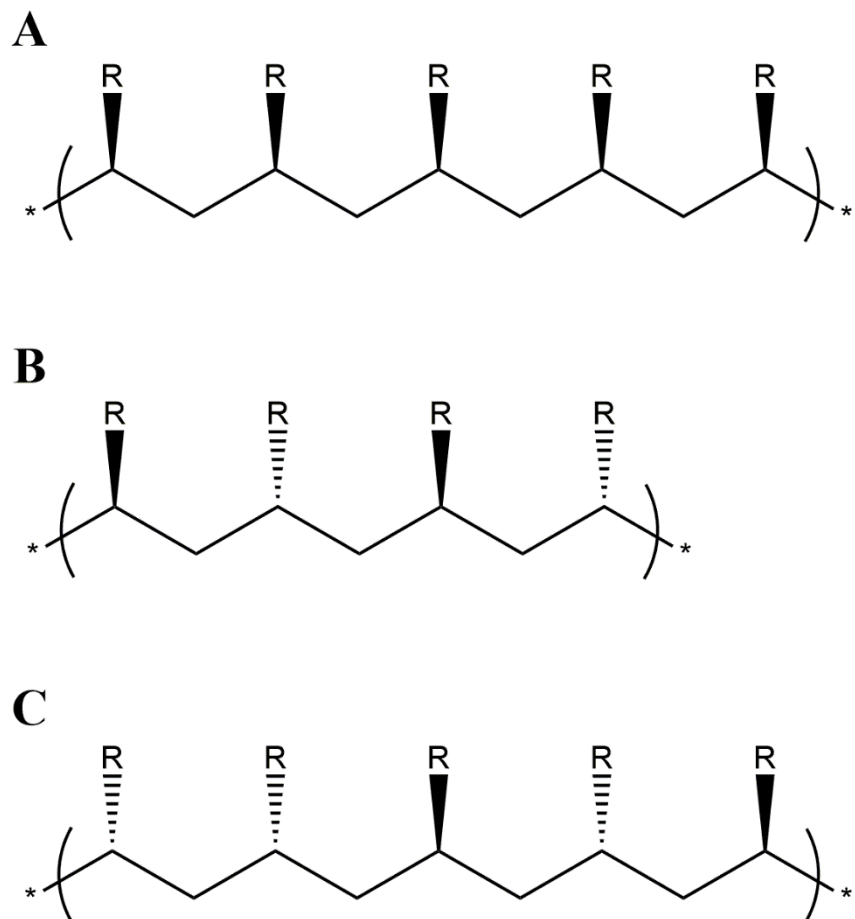


**Figure 1.3:** Polymer tacticities: **(A)** isotactic, all functional groups lie in the same plane and orientation with respect to one another; **(B)** syndiotactic, every other functional group lies in plane and the other out of plane; **(C)** atactic, functional groups have random orientation with respect to one another. Solid and dashed wedges indicate bonds into and out of the page, respectively. Structures drawn with ChemDraw Prime [3].

The molecular weight, polydispersity, and the tacticity all influence how a given polymer will crystallize as well as the optical, mechanical, and chemical properties of both the semicrystalline and amorphous material.

## 1.2 *Polymer Phases*

The unique molecular structure of polymers gives rise to a series of phase changes that are different from those typical for small molecule systems. At temperatures greater than the melting point a polymer is said to be in the melt. Here the long molecular chains will maximize their entropy by assuming a random coil conformation (as opposed to the highly ordered state pictured in **Figure 1.2A**). As the polymer melt is cooled below the melting point, regions of the polymer chain can crystallize. Because a bulk polymer is a network of millions of millions of individual chains there are regions in the melt where chains overlap and become entangled. These entanglements are regions of locally high viscosity and prevent all of the material from crystallizing and result in a mixture of crystalline and amorphous material – this is why polymers are said to be semicrystalline.

Continued cooling will bring the polymer into the glassy phase. In the glassy phase the only thermal motions of the polymer are those of bond vibrations. Depending upon the cooling rate, the stereochemistry, and polydispersity this can be either a semicrystalline or amorphous glass where there is no long range molecular order. In the glassy phase the solid polymer, as either an amorphous or a semicrystalline glass, will exhibit a solid state heat capacity that depends only on the bond vibrations. The glassy phase is well modeled and studied [8-10], however the relaxation behaviors, vitrification of the melt, and the glass transition are all active areas of research in the broad field of polymer physics [11-19].

The glass transition is a quasi second order phase change (quasi because it is a kinetic, i.e., heating rate dependent process) where the molecules along a polymer chain become free to rotate. The temperature where a polymer chain gains bond rotation degrees of freedom is called the glass transition temperature,  $T_g$ , and this transition is marked by an increase in the specific heat capacity,

$\Delta c_p(T_g)$ . Here the system can be reversibly cycled between a solid glass and rubbery high viscosity liquid by change of temperature, this is not the melting point, as any crystals present will remain solid until the crystalline melting point,  $T_m$ . Between these two temperatures the polymer chains can assume many conformations and ordered microstructures that depend upon thermal or mechanical stimuli.

While the heat capacity of a polymer in the solid state (below the glass transition) has been successfully modeled and shows agreement with experimental data [9], there has been limited success in modelling the liquid phase heat capacity [20-27]. Empirically, it has been found that the heat capacity of a liquid phase polymer is linear with respect to temperature in most cases [9, 20]. Some polymers, such as, polyethylene (PE), polypropylene (PP), and polystyrene (PS) the heat capacity of the liquid has been successfully modeled, however many cannot be easily predicted based on knowledge of their chemical bonds and their possible conformations in the melt. Because of this, precise empirical measurements of the specific heat capacity of the liquid phase are of fundamental importance.

A general three-phase model is used to describe the possible states accessible to chain segments within a semicrystalline polymer. The first component of this is the mobile amorphous fraction, MAF. These are the polymer chain segments which are not incorporated into a crystal and undergo the glass transition. There are no kinetic constraints on the polymer except for chain entanglements. The second component is the crystalline fraction; these are the regions of the polymer chains which have formed an ordered solid. Crystals in general are discussed in **Section 1.2** and polymer crystals are discussed in **Section 1.3.2**. The third component is the rigid amorphous fraction, RAF, which was proposed by Wunderlich [28-30] and has been heavily investigated in recent decades [11-14, 16, 29-41]. This accounts for the regions of the polymer

chain which are kinetically arrested by the presence of crystals or even by small crystalline fragment or nuclei [11-13, 29-34, 36, 37] and additives or fillers [40-44]. A more detailed discussion of the rigid amorphous fraction is found in **Section 1.4** following the discussion of polymer crystals and crystallization.

### *Crystals*

A crystal is a three dimensionally ordered solid built from atoms or molecules (referred to as the basis) which are spaced periodically along a lattice. This arrangement has both rotational and translational symmetry and moving in any direction along the lattice an identical structure is found. Mathematically this lattice is defined by the three translation vectors **a**, **b**, **c**. To build an ideal crystal from the basis a minimum arrangement of the basis, known as the unit cell, is infinitely repeated in for all possible integral translations along the lattice. The unit cell has the minimum volume  $\mathbf{a} \cdot \mathbf{b} \times \mathbf{c}$ . **Figure 1.4** shows the relationship between the lattice, the basis, and the crystal and this is diagramed in 2D for simplicity.

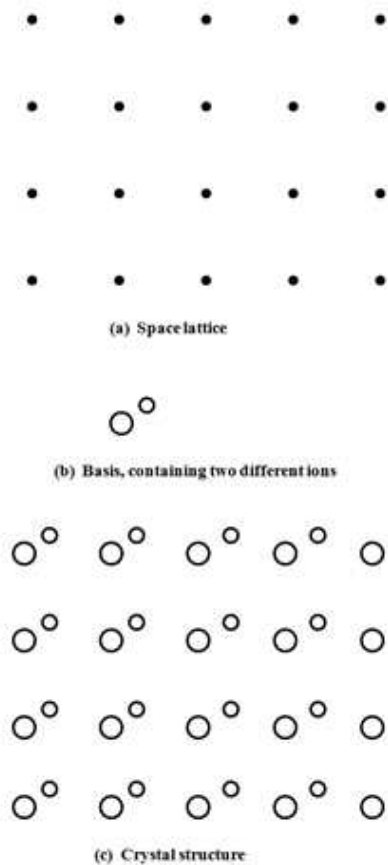


**Figure 1.4:** The crystal structure is formed when atoms, ions, or molecules are placed at every point on a **(A)** space lattice. **(B)** A basis containing an ion pair is added to every point on the space lattice to form the **(C)** crystal structure. Figure reproduced from [45].

To visualize this, consider the simple example of a crystal described by a cubic lattice. A common example of a cubic crystal structure is table salt, sodium chloride, shown in **Figure 1.5**. While the basis of the lattice is the ion pair sodium and chlorine the unit cell is made up of multiple ion pairs. The basic unit cell that forms the sodium chloride crystal is a cubic structure with ions placed along the corners of the lattice.

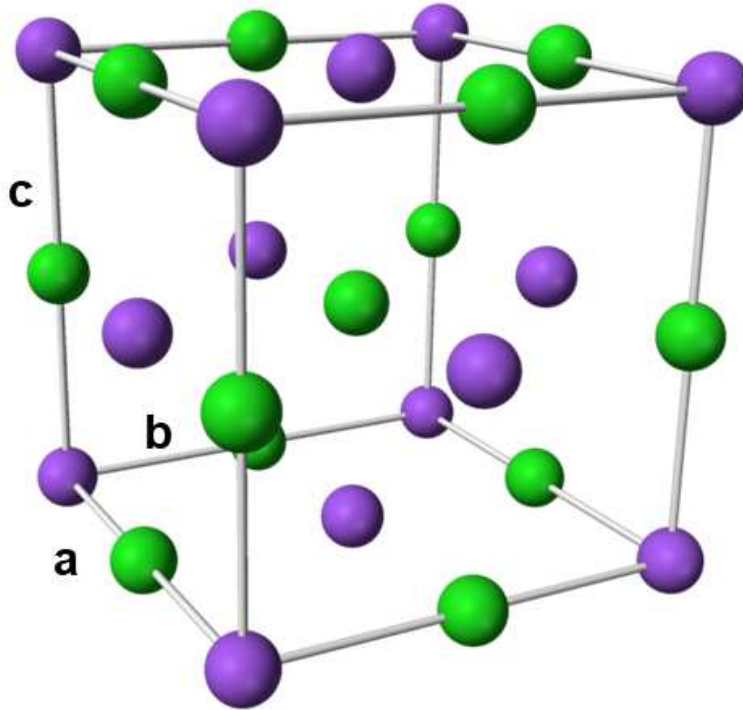


**Figure 1.5:** NaCl crystal structure and lattice example where chlorine is shown in purple and sodium in green. The unit cell vectors **a**, **b**, and **c** are labelled. Original image annotated [46].

During a scattering experiment (see **Section 3.2.2**) X-rays or electrons are scattered along directions corresponding to the set of planes defined with respect to the unit cell pictured above. These planes are defined by a set of indices,  $h$ ,  $k$ , and,  $l$ , known as the Miller indices. The Miller indices define sets of planes along the faces, or across the unit cell. For a simple cubic system, the sets of planes are shown in **Figure 1.6**.

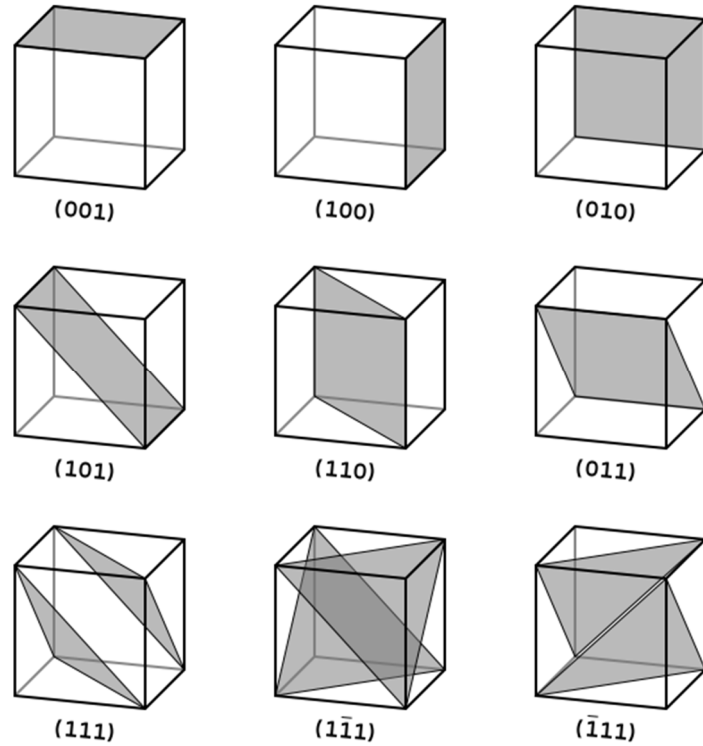


**Figure 1.6:** The Miller indices (hkl) define the set of planes across the unit cell. Figure reproduced from [47].

This is a general treatment, defining a mathematical lattice along which the basis of the crystal structure applies to any ordered solid. Unlike the simple example of a salt crystal where ions lie along the lattice, chain segments of a polymer and their functional groups serve as the basis and pack together along the lattice. The crystal is held together by either hydrogen bonding or Van der Waals forces. With a mathematical description of crystal structure attention is turned to a description of how a physical system changes phase from a disordered state to the ordered crystalline state. If the polymer melt or a polymer solution is metastable crystals will form by a process known as nucleation and by spinodal decomposition if the melt or solution is unstable at a given temperature. The modern theory of nucleation is grounded in the work done by Turnbull

and Fisher in the late 1940s [48, 49]. The modern theory of spinodal decomposition was laid out by Cahn and Hillard [50-54].

### ***1.3 Crystallization***

#### ***1.3.1 General Theory of crystallization***

Nucleation itself is the formation of a local thermodynamic phase,  $\beta$ , within a parent phase,  $\alpha$ . In the case of crystallization, nucleation is the formation of a local solid phase within the melt. In the absence of any impurities or any outside stimuli, nucleation is a spontaneous process driven by thermodynamics whenever a material is brought below its melting point. The degree to which a material is below its melting point is referred to as the undercooling (or supercooling, these terms are used interchangeably in the literature). At temperatures below the melting point a material will have lower free energy as a solid than as a liquid. This difference in free energy results in a thermodynamic driving force which increases with the undercooling. The further a system is brought below the melting point the more likely it will be to spontaneously reorganize into a solid.

Within the parent liquid phase, the individual atoms are free to move in all directions. Spontaneous nucleation occurs at temperatures below the melting point when a critical number of atoms move together, by random thermal fluctuations, such that they form a locally stable solid phase. This is referred to as homogenous nucleation. The formation of a local phase gives rise to a liquid – solid interface which has a free energy cost associated with it. A nucleus is only stable when the free energy cost to maintain this interface is less than or equal to the difference in free energy between the solid and liquid phase at a given temperature. The introduction of impurities or seed crystals, which will be discussed in more detail later, reduces the free energy cost of forming a local solid phase in the melt. When this occurs, the nucleation is referred to as

heterogeneous nucleation. The theory presented here is for the case of homogeneous nucleation.

**Figure 1.7** diagrams the local solid phase formation.

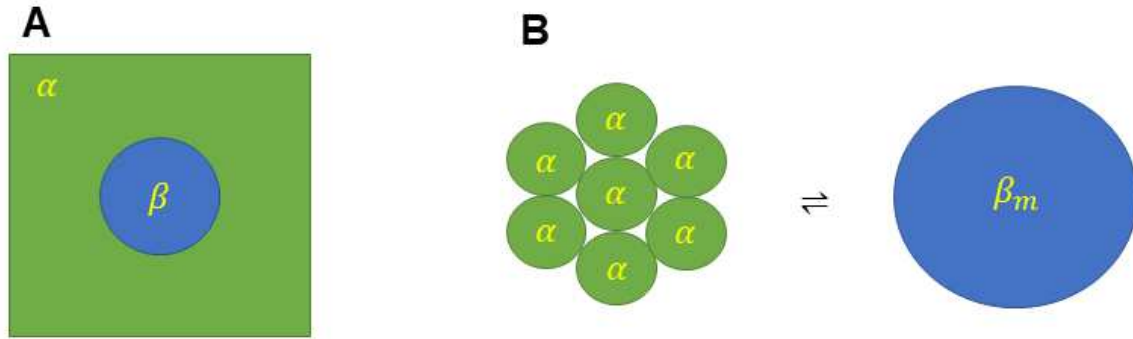


**Figure 1.7:** (A) Local thermodynamic phase,  $\beta$ , inside the parent phase,  $\alpha$ . (B) A critical nucleus,  $\beta_m$ , which is made from  $m$  particles formerly in the  $\alpha$  phase.

Formation of the local phase,  $\beta$ , in **Figure 1.7A** has a free energy,  $A$ , associated with the  $\alpha$ - $\beta$  interface (which is proportional to the surface energy between the liquid and solid phase). The free energy,  $B$ , is associated with the difference between the  $\alpha$  and  $\beta$  phase (the heat of fusion). The resulting free energy difference,  $\Delta G$  is given by the following relation [48, 49]:

$$\frac{\Delta G_i}{kT} = Ai^{2/3} - Bi \quad (1.3)$$

where  $i$ , is the number of atoms or molecules in phase  $\beta$ . The free energy difference as a function of number is plotted in **Figure 1.8**.

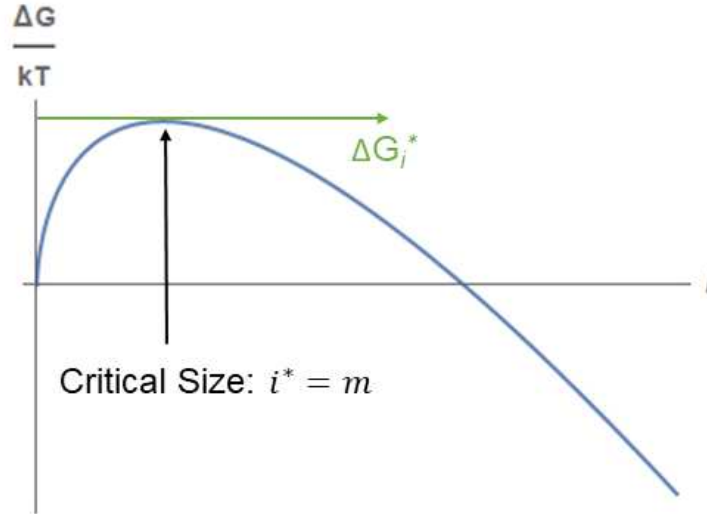


**Figure 1.8:** Free energy difference vs. number of particles in the nucleus, per Eqn. 1.3. The critical nucleus size,  $m$ , in terms of number of particles,  $i^*$ , is determined by the free energy maximum,  $\Delta G^*$ .

The critical free energy and critical nucleus size are determined from the free energy maximum,  $\Delta G^*$ . Once a critical number of particles (atoms or molecules) have aggregated into a nucleus by random thermal motion in the parent liquid phase the free energy decreases for each additional particle. A critical nucleus made from  $m$  (formerly  $\alpha$  phase) particles is shown in **Figure 1.7B**. Because the free energy is decreasing for each additional particle, the nucleus will remain stable and not dissociate by random thermal fluctuations that formed it. In the presence of a stable nucleus, any particles that attach to it will remain in the solid phase which allows the system to crystallize and form a single, solid phase material.

Taking the simple case of a homogeneously formed, spherical nucleus, the free energy to form a nucleus would be:

$$\Delta G = 4\pi r^2 \sigma - \frac{4\pi}{3} r^3 (\Delta H_{f0} \frac{\Delta T}{T_m^0}) \quad (1.4)$$

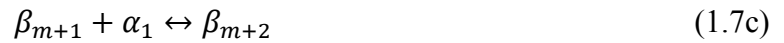
where  $\sigma$  is the surface free energy between the liquid and solid phase,  $\Delta H_{f0}$  is the equilibrium heat of fusion of the material, and  $\Delta T = T_m^0 - T$  is the undercooling. Minimizing this expression with respect to the critical radius,  $r^*$ , can be determined in terms of physically measurable parameters.

$$r^* = \frac{2\sigma T_m^0}{\Delta H_{f0}} \frac{1}{\Delta T} \quad (1.5)$$

substituting the critical radius into Eqn. 1.4 the critical nucleus size for a spherical nucleus is obtained:

$$\Delta G^* = \frac{16\pi\sigma^3 T_m^0{}^2}{3\Delta H_{f0}} \left(\frac{1}{\Delta T}\right)^2 \quad (1.6)$$

The kinetics of homogeneous nucleation were described in a manner analogous to chemical reaction rates. Treating each nucleus as a molecule made up of the particles moving from liquid to solid phase allows nucleation to be described by a chain of reactions in the following manner [49]:



where  $m$  is the critical number of particles to form a stable nucleus,  $\alpha_1$  is the addition of a single particle. This generalizes to the reaction for a nucleus,  $\beta_i$ , contains  $i$  particles.

This model for steady state rate of nucleation corresponds to the constant equal net forward rates for the reactions in Eqn. 1.7. The net forward rate is the difference in the rates at which a single particle can attach or detach from the nucleus. The individual forward and backward rate equations are worked out in detail in the original papers [49, 55]. This allows for the rate of nucleation,  $N^*$ , to be expressed in terms of the number of moles of material, the activation energy

for short range diffusion, and the critical free energy for the formation of a stable nucleus. The nucleation rate per mole per second is given by the following relationship [49]:

$$N^* = \left(\frac{NkT}{h}\right)e^{-(\Delta g^* + \Delta G^*)/kT} \quad (1.8)$$

where  $\Delta g^*$  is the activation energy for short range diffusion across the liquid solid interface. In this model of nucleation, the slowest diffusing component becomes the nucleation rate limiting factor.

This model of nucleation and crystallization has been successfully applied to modelling and predicating the rate of nucleation in simple atomic and molecular systems where the assumption of semi-spherical nuclei composed of individual particles holds. As detailed in **Section 1.1**, polymers are long chains of molecules and their unique molecular structure places constraints on nucleation driven by thermal fluctuations.

### ***1.3.2 Polymer Crystals and Polymer Crystallization***

Because polymers crystallize from a string of covalently bonded units the simple model for the minimum nucleus described above needs to be modified. Early investigations into the mechanisms of polymer crystallization were carried out by Keller and others in the late 1950s [56]. Their experiments involved the growth of single crystals from dilute polymer solutions. These solutions are dilute enough that the crystals formed entirely from as few as one single polymer chain. Transmission electron microscopy (TEM) allowed for both topographical micrographs and electron diffraction patterns to be collected. It was found that polymers crystallized into thin, plate like crystals which had thicknesses or step heights between layers which varied between 5 and 25 nm (larger undercooling results in thicker crystals). Electron diffraction revealed that the polymer backbone was aligned perpendicular to the flat surfaces of these plate like crystals [56]. Recall from **Section 1.1** that a polymer with 10,000 repeating units (a relatively low molecular weight

polymer) would be approximately 1  $\mu\text{m}$  end to end. The only way that the polymer could pack into such a thin plate like structure with their backbones perpendicular to the long axis of the plate is if the chain is folded by a series of “S” turns in a ribbon like manner. The ribbon folded plate like structures is known as a lamella crystal.

When bulk polymers crystallize, there is no single plate like crystal observed. Instead spherically symmetric crystal structures, known as spherulites, are observed. Polarized light microscopy (see **Section 3.1.1** for details on the technique) images of spherulites revealed the radial growth of an aggregate made up of individual blades which grew outwards from nucleation site [57-61]. Examples of polymer spherulites imaged with polarized light microscopy are shown in **Figure 1.9**. It was proposed that these individual blades within the spherulite were the same structure as the plate like crystals grown from dilute solutions. Electron micrographs of these spherulites revealed that the individual blades had thicknesses varying between 5 and 25 nm, corresponding to the same range as the solution grown plates [62]. This led to the conclusion that the polymer crystals, in both dilute solutions and in the bulk, were formed by the chain folding into a ribbon like lamella crystal structure.

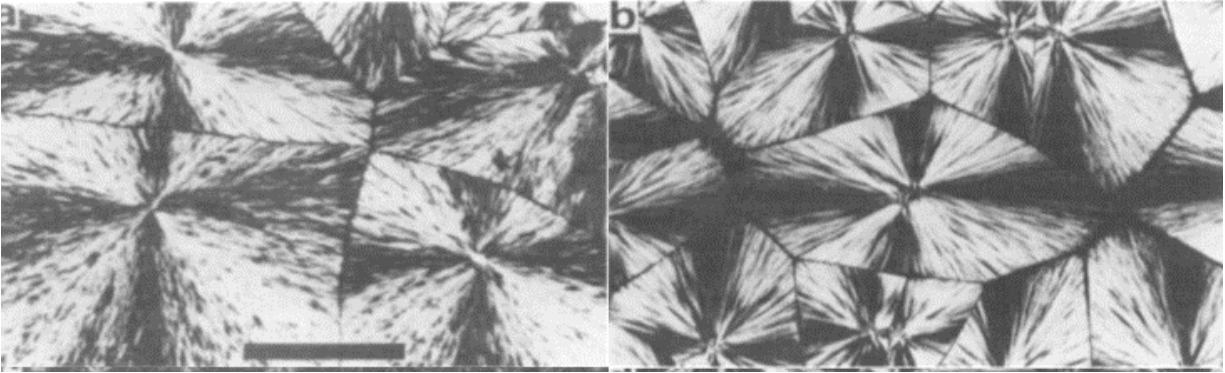


**Figure 1.9:** Bulk polymer crystal spherulites observed under crossed polarizers (see **Section 3.1.1** for discussion of imaging technique) Scale bar is 200 microns and applies to both images. Figure reproduced from [61].

As the polymer crystallizes from the melt, crystallization proceeds from nuclei and consumes available material from the adjacent melt. The pair of images in **Figure 1.9** show a series of spherulites crystallized from the melt which have become impinged by one another resulting in grain boundaries which appear as the dark outlines around each bright cross pattern (known as a Maltese cross). In these images the lamella all grow radially outward from the central nucleation site and grow nearly parallel to one another. With the knowledge that the polymer chains crystallize by folding first into lamella which then grow and aggregate to form spherical structures in the melt Hoffman and Lauritzen proposed a model for the nucleation and growth of polymer crystals [62]. The Hoffman-Lauritzen model for polymer nucleation and crystallization builds off of the approach laid out by Turnbull and Fisher and takes into consideration the long, chain like nature of polymers.

Electron diffraction [56] and X-ray scattering [63, 64] investigations had established that the unit cells of polymeric crystals were formed by the chain to chain packing of polymers with their functional groups interacting by van Der Waals forces or hydrogen bonding to stabilize the crystal [64]. For example, consider the crystal structure of polyethylene terephthalate (PET) shown

in **Figure 1.10**. The basic unit cell of the crystal is made up of four chain segments running parallel to one another forming a triclinic unit cell.

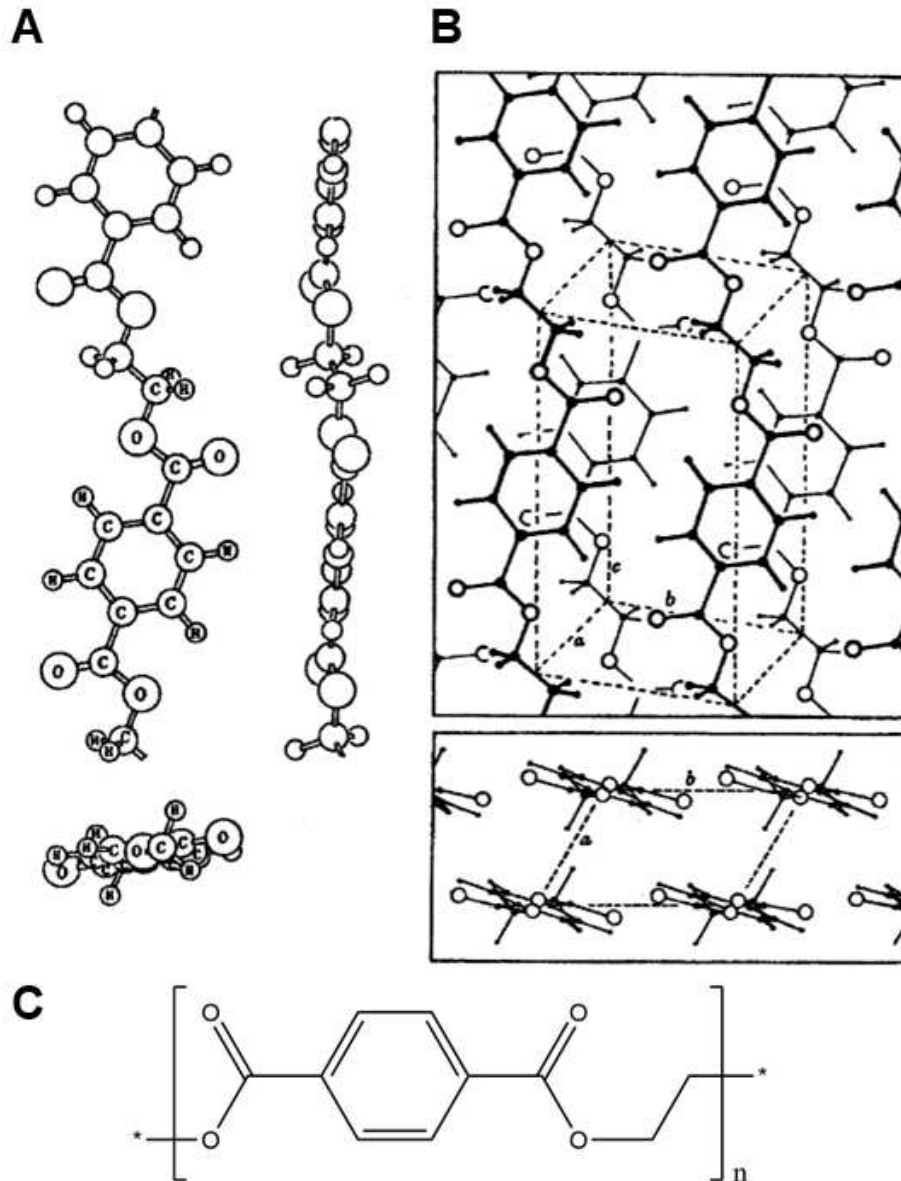


**Figure 1.10:** (A) Three-dimensional molecular structure of the PET monomer repeat unit seen in different views; (B) the crystalline unit cell of PET in dotted outline; and (C) the chemical structure of the PET molecule reproduced from [64, 65].

**Figure 1.10A** shows a three-dimensional drawing of the PET monomer unit alongside its crystalline unit cell in **Figure 1.10B**. The unit cell dimensions  $a$ ,  $b$ , and  $c$  (these correspond to the vectors  $\mathbf{a}$ ,  $\mathbf{b}$ , and  $\mathbf{c}$  in **Figure 1.5**) set the minimum volume which can be repeated to create a PET crystal [65]. Once brought below the melting point, random thermal motion of the chains can cause several segments of the polymer (either regions of the same long chain or adjacent chains) to pack side by side. If enough segments fall side by side, then it is possible for a stable nucleus to form. The general scheme for the structure of such a nucleus is shown in **Figure 1.11**.

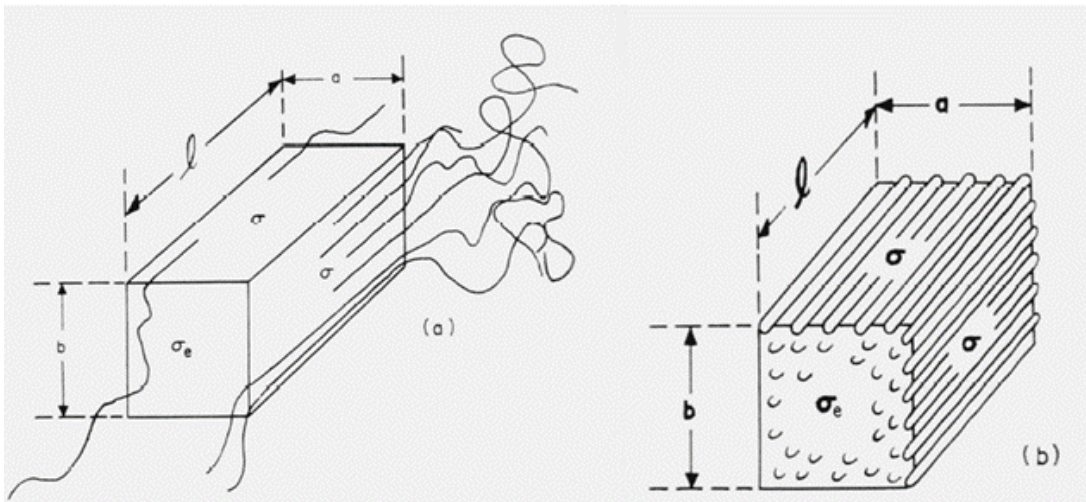


**Figure 1.11:** (A) Polymer nucleus formed from a series of adjacent polymer chain segments with amorphous chain segments not incorporated and (B) a general schematic of the stable polymer nucleus with dimensions  $a$ ,  $b$ , and  $l$  (where  $l$  is analogous to  $c$  in **Figure 1.10**). The surface free energy of the growth faces and fold face are denoted by  $\sigma$  and  $\sigma_e$ , respectively reproduced from [62].

A critical polymer nucleus requires the same condition as the simple spherical case, in that the free energy of the polymer in the local solid state is greater than or equal to the free energy cost of forming a liquid-solid interface. In contrast to the case of small molecules or single atoms

there are two surface free energy terms to consider in the case of polymers. Polymers crystallize by bond rotations which allow segments to fold into “S” shapes as they pack into a nucleus. This results in a high energy, fold surface,  $\sigma_e$ , in the direction perpendicular to the chains, denoted by  $l$  in **Figure 1.10**. Along the nuclei faces where polymer backbones are parallel there is one surface energy,  $\sigma$ , which is lower than the ends of the nucleus where chains fold. This energy difference arises from the energy required to bend the polymer chains and complete a fold. A single fold requires multiple bonds to rotate from their *trans* to *gauche* conformation. This increases the free energy and along that segment of the polymer backbone as compared to the regions where the chains lie parallel to one another creating an energy difference between the two surfaces. With these adjustments, the following expression for the free energy of a polymer nucleus is:

$$\Delta G = 2la\sigma + 2lb\sigma + 2ab\sigma_e - abl\Delta H_{f0} \quad (1.9)$$

where  $a$ , and  $b$  are the cross-sectional area of the nucleus, and  $l$  is the length of the nucleus.

Minimization of the free energy yields the critical dimensions of a polymer nucleus in terms of physically measurable parameters:

$$l^* = \frac{4\sigma_e T_m^0}{\Delta H_{f0} \Delta T} \quad (1.10)$$

$$a^* = b^* = \frac{4\sigma T_m^0}{\Delta H_{f0} \Delta T} \quad (1.11)$$

Once a nucleus has formed, crystallization will proceed as thermal motions of polymer chains near the nucleus will result in the layer by layer deposition of material along the lower energy surface,  $\sigma$ . A diagram of this is shown in **Figure 1.12**.

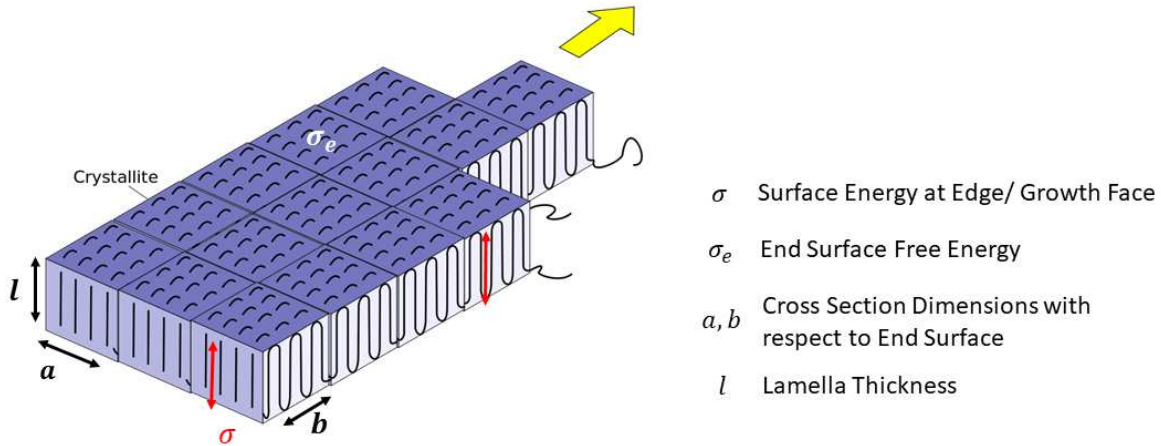


**Figure 1.12:** A schematic of polymer crystallization from a nucleus. For the single crystal case, chains can attach at any surface other than the fold surface,  $\sigma_e$ . In this image the dimensions  $a$  and  $b$  correspond to the unit cell dimensions of the polymer crystal as shown in **Figure 1.10** and  $l$  is the lamella thickness. Figure reproduced from [66].

While the conditions for nucleation set out the minimum dimensions which allow a stable crystal to form, the lamella thickness of the crystals are governed by the growth kinetics. The kinetic theory of polymer growth relies on the balance of the thermodynamic driving for crystallization which is a function of the undercooling,  $\Delta T$  [67, 68], and the kinetic barrier to nucleation and crystallization [67-69]. Thicker lamella are more thermodynamically stable as the total volume to surface area is such that fold surface is minimized. Because polymers crystallize by the random thermal motions allowing new chain segments to attach to the growth faces, the kinetics become increasingly unfavorable as lamella thicken. **Figure 1.13** shows a schematic of these two competing forces which govern polymer crystal growth.

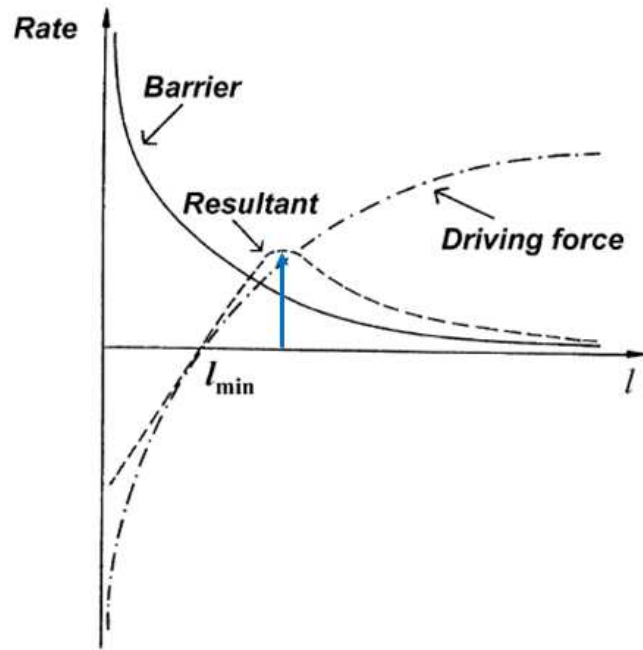


**Figure 1.13:** Polymer crystal growth rate vs. lamella thickness. The solid black line is the kinetic barrier to nucleation and crystallization. The dashed, dotted line is the thermodynamic driving force. The dashed line is the resultant sum of these two competing forces. The minimum lamella thickness  $l_{\min}$  is the minimum stable lamella thickness in Eqn. 1.10. The blue arrow indicates the kinetically favored lamella thickness. Figure reproduced from [68].

With this model for the crystallization of polymers, which results in sheet like crystals formed by the “S” folding of polymer chains in the melt, the formation of spherulites in the bulk can be explained. One nuclei will form a single lamella as shown in the top left of **Figure 1.14**. As other lamella form in the melt differences between the crystalline and melt density will drive the lamella together forming bundles as seen in upper middle of **Figure 1.14**. While this is occurring, the individual lamella sheets will continue to grow.

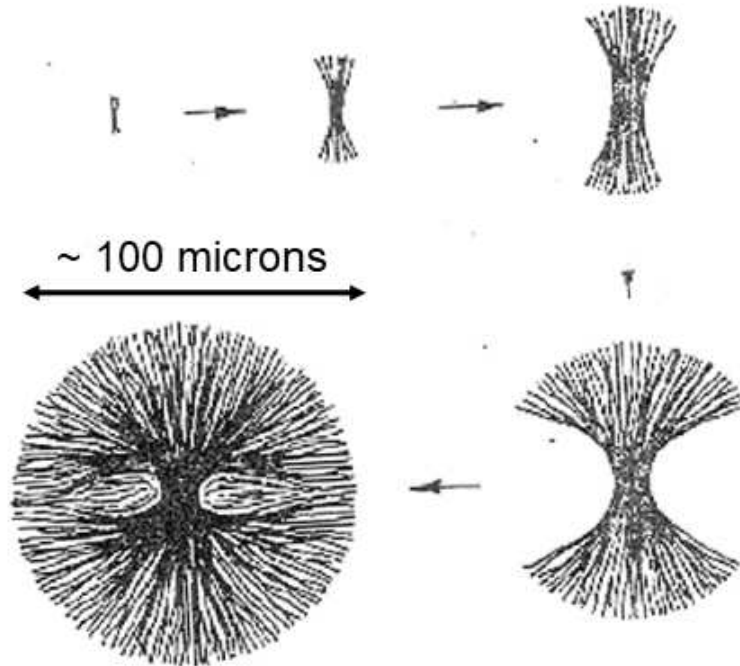


**Figure 1.14:** Formation of the bulk polymer crystal, the spherulite from **(top left)** a nucleus to **(top middle and right)** a bundle of growing lamella **(bottom right)** branching of lamella by secondary nucleation and crystal growth between lamella resulting in **(bottom left)** a fully formed polymer spherulite. Reproduced from [70]

As the individual lamella in each bundle continue to grow, defects can form which interrupt the crystallization along a growth direction for a given lamella. These defects can be due to random segments of chains entering the lamella not unlike wires on a switchboard, the end of a polymer molecule, or the growth front encountering polymers too entangled to allow the parallel alignment of backbone segments. When this occurs, new lamella will nucleate and grow in the space in between the bundles. This causes the bundles to branch out radially as seen in the right two panels of **Figure 1.14**. The abundance of nucleation sites provided by the lamella bundles enables the polymer in the melt to crystallize and fill in around the bundles.

### 1.3.3 Spinodal Decomposition

Another way that polymers can crystallize is by a process known as spinodal decomposition. This is a thermodynamically driven process by which liquids or solids can rapidly unmix from one thermodynamic phase into two coexisting ones. A common example of this would be a warm salad dressing of olive oil and vinegar which is well mixed until left on the table for some time. As the mixture cools, the oil and water rapidly unmix into separate oil and water phases. In the case of the polymer melt or a polymer solution this rapid unmixing can result in the formation of a solid phase. In contrast to nucleation spinodal decomposition does not have a kinetic barrier and only occurs if the parent thermodynamic phase is unstable. Nucleation occurs in a metastable melt and a solid phase can only form once a sufficiently large nucleus has formed.

The criteria for the thermodynamic stability was first laid out by Gibbs [71]. A metastable phase lies at local minimum in the free energy and is resistant to small fluctuations (either a small perturbation over a large area, or a large perturbation over a small area). If a mixture is unstable, any small changes in the local composition within the bulk are sufficient to trigger rapid phase change. Cahn and Hillard provide the mathematical framework for modelling this rapid unmixing as being driven by continuous fluctuations in local composition changes within a mixture (either a mixture of thermodynamic phases of the same material, a polymer and solvent, or two materials) [50-54]. The free energy of mixing was previously provided by Flory and his coworkers [22, 23, 27]:

$$\bar{F}_{mix} = \frac{f}{N_A} \ln(f) + \frac{(1-f)}{N_B} \ln(1-f) + \chi f(1-f) \quad (1.12)$$

where  $f$  is the fraction of species A (composition of the mixture),  $N_A$  and  $N_B$  are the number of particles of A and B, respectively.  $\chi$  is the Flory interaction parameter, a term which encapsulates

the interaction energies between species A and B. When this term is negative the two species are miscible, when it is positive mixing is not energetically favorable, and when it is zero mixing is driven by entropy alone.

The free energy of mixing as function of composition,  $f$ , is shown in **Figure 1.15A**. The binodal points are defined as the local free energy minima and determine the compositions which are energetically favorable. These points are the boundary between the stable, single phase mixture and the metastable region where phase change can only occur by nucleation. Here a kinetic barrier must be overcome before the mixture can change phase. The inflection points between these local minima and the local maxima are the spinodal points. The compositions at the spinodal points mark the transition between the metastable mixture and the unstable mixture. All compositions between the binodal and spinodal points sweep out the metastable region (the area between the blue and red curves) in the phase diagram shown in **Figure 1.15B**.

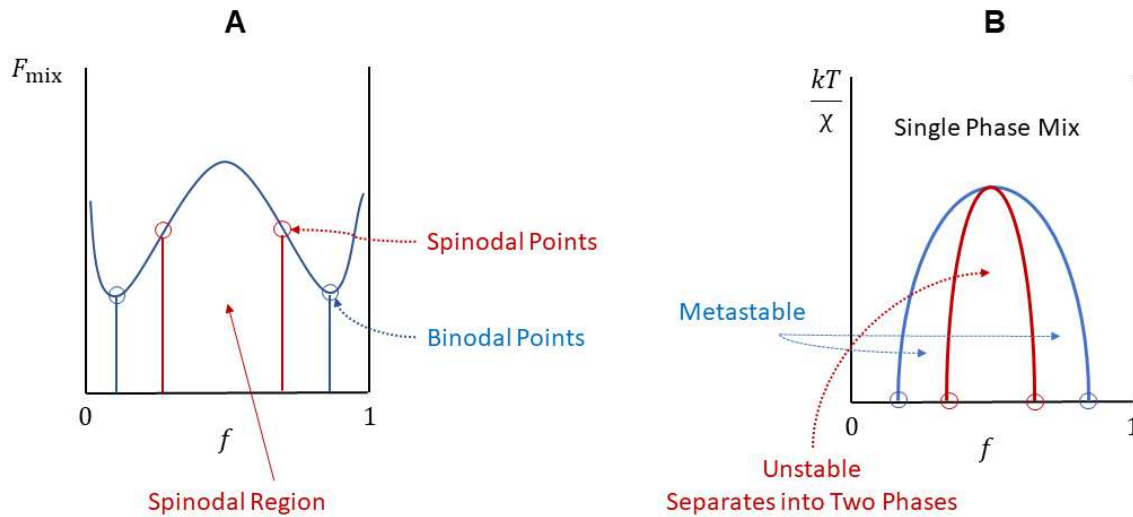


**Figure 1.15:** (A) Free energy of mixing vs. composition of the mixture. The composition boundaries for the stable, single phase mixture is determined from the local minima at a given temperature. The composition boundary for the metastable mixture is determined by the inflection points between the local minima and the local maxima in the free energy. (B) Phase diagram as function of temperature and composition. The metastable and unstable regions are indicated by the blue and red arrows, respectively.

Within the metastable region nucleation and growth governs phase change from the liquid to solid. The inner area of the red curve in **Figure 1.15B** sweeps out the unstable region. Any small thermal motions of the mixture result in composition changes which lower the free energy of the mixture. Each fluctuation increases the number and size of local regions which are dominated by a high concentration of phase A or phase B. This allows subsequent fluctuations to further separate the two phases.

Consider any composition,  $f$ , between the spinodal points shown in **Figure 1.15A**. A small fluctuation in local composition by random thermal motions will result in one region of locally higher concentration of phase A and lower concentration of phase B and another region which is lower in phase A and higher in phase B. These two new local compositions  $f_1$  and  $f_2$  will result in a lower free energy of mixing than the original which energetically penalizes the entropically

favoured diffusion towards a totally mixed A and B phase. Further fluctuations will result in these regions coalescing and driving the system towards separated regions which are rich in phase A or phase B. The resulting microstructure is shown in **Figure 1.16B**.

For the metastable region seen on the left-hand side of the phase diagram in **Figure 1.15B** phase A will be nucleated inside of phase B, as shown in **Figure 1.16A**. Similarly, the right-hand side of the phase diagram in **Figure 1.15B** results in phase B being nucleated inside of phase A, as seen **Figure 1.16C**. Because these regions are metastable, there is a kinetic barrier which must be overcome. This barrier is the kinetic nucleation barrier described in **Section 1.3.2**.

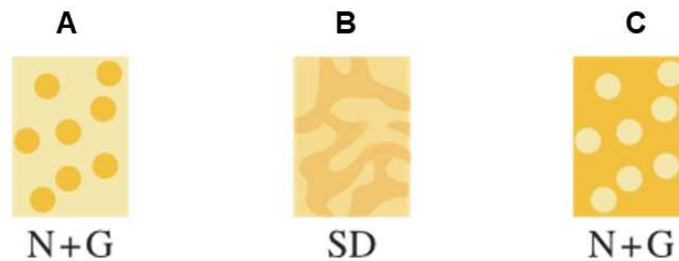


**Figure 1.16:** Schematic diagrams of microstructures formed by phase changes within the phase diagram shown in **Figure 1.15B**. **(A)** Nucleation and growth (N+G) of phase A within phase B, corresponding to the left hand metastable region in **Figure 1.15B**. **(B)** Spinodal decomposition (SD) into two, unmixed phases A and B corresponding to the unstable region in the phase diagram shown in **Figure 1.15B**. **(C)** Nucleation and growth (N+G) of phase B within phase A, corresponding to the right hand metastable region in **Figure 1.15B**. Figure adapted and reproduced from [72].

The small fluctuation driven, continuous separation of phases A and B which occurs in the unstable mixture (center of phase diagram **Figure 1.15B**) results in large domains of A and B as shown in **Figure 1.16B**. Unlike nuclei, which can be scattered throughout the melt, the phase separated domains which form by spinodal decomposition are uniformly distributed.

While this phenomenon is often observed in liquid-liquid mixtures it is also observed in polymer solutions or a polymer melt which is cooled below the melting point. Once a polymer solution or polymer melt is cooled below the polymer melting point small composition fluctuations, which can be either fluctuations in local polymer concentration in the case of the solution or density in the melt. It has been observed that spinodal decomposition like phase separation often precedes nucleation [73-76]. The spinodal decomposition of the polymer melt towards regions of higher and lower density provides regions which are rich in potential nucleation sites and can often precede homogenous nucleation.

#### ***1.4 Rigid Amorphous Fraction***

The third component of a semicrystalline polymer is the rigid amorphous fraction. This material is not incorporated into the crystal but it is kinetically arrested either by proximity to the crystal or entanglements with chain segments along the fold surface. The addition of nanoparticles such as clay [43, 44], graphene or carbon nanotubes [40], or mixing with other polymers can impact the total rigid amorphous fraction. For the minimal case of a homopolymer free of any inclusions, the relationship between the rigid amorphous fraction and the lamella crystal structure is shown in **Figure 1.17**.

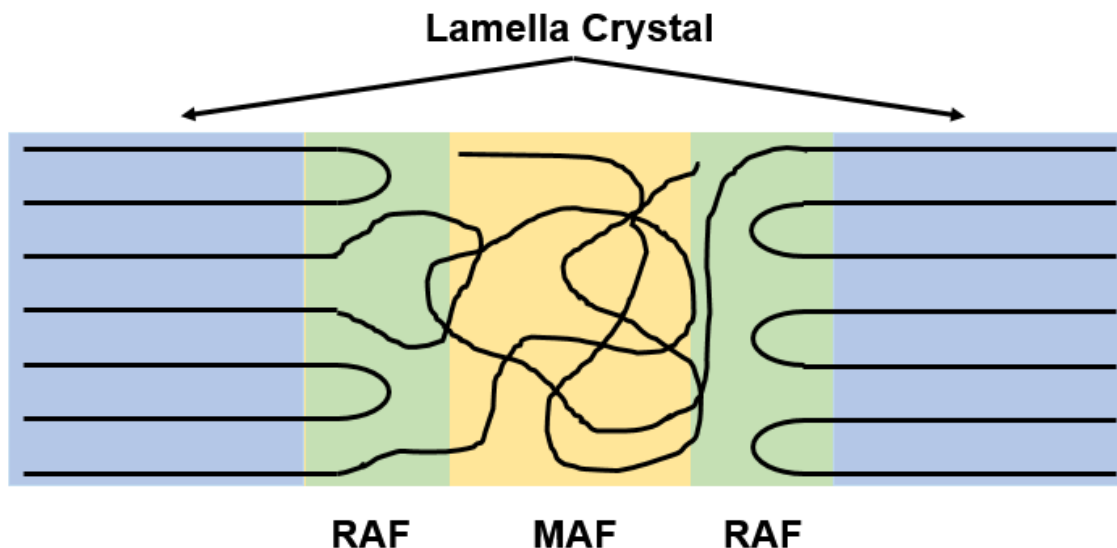


**Figure 1.17:** Schematic of semicrystalline polymer phases. Lamella crystals are shown in the blue shaded regions. Mobile amorphous fraction (MAF) is shown in the yellow shaded region. The presence of crystals kinetically arrests the polymer chains and results in rigid amorphous fraction (RAF).

The rigid amorphous fraction is known to vary with polymer chemistry and the conditions under which a polymer is crystallized. Polyethylene for example is known to contain very little rigid amorphous fraction. An investigation into the rigid amorphous fraction of polyvinyl alcohol (PVA) is one of the topics covered in **Chapter 5** of this work, and polyethylene terephthalate has been studied extensively [12, 14, 16, 29, 37, 39, 77].

### **1.5 Self-Nucleation**

Homogenous nucleation and crystallization rely on thermal fluctuations to create a stable nucleus from which crystallization proceeds. In contrast, heterogeneous nucleation is triggered by defects, additives, or the presence of crystals within the melt which allow the polymer to bypass

the kinetic barrier to nucleation [67, 78-82]. This allows polymers to crystallize at smaller undercoolings with a shorter crystallization onset time. Self nucleation is a special case of heterogenous nucleation where either embryonic/seed nuclei (very near or possibly below the minimum stable size), or regions with aligned chains, persist in the melt. Once cooled these sites rapidly trigger nucleation and crystallization. Because the locations of these seed nuclei or aligned regions of the melt depend upon the initial crystal locations this effect is also often referred to as “melt memory” [67]. This effect is diagrammed in **Figure 1.18**.

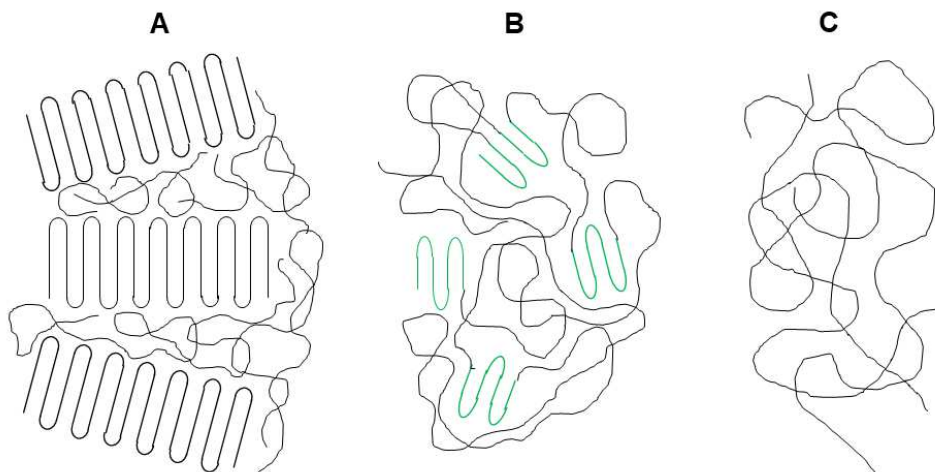


**Figure 1.18:** (A) Schematic of semicrystalline polymer; (B) Following melting seed nuclei or segments of aligned regions of polymer chains remain in the melt (shown in green); (C) Amorphous melt is recovered.

As the polymer crystal pictured in **Figure 1.18A** melts chains that have detached from the crystal will begin to return to their amorphous, random coil conformation. This return to the random coil conformation is a kinetic process. When a bulk polymer crystallizes the crystals that form are imperfect, finite crystals which melt at temperatures below the equilibrium melting point.

By heating to temperatures above the equilibrium melting point and holding in the melt all the polymer chains will eventually assume random coil conformation resulting in a fully amorphous melt as shown in **Figure 1.18B**. At an intermediate time between the onset of melting of the finite crystal and the return to the fully amorphous melt, there will remain both small crystal fragments and regions where crystals have melted but chains have not been able to fully return to their entropically favored, random coil conformation. These are diagrammed as the green regions in **Figure 1.18B**. An example of self nucleation in isotactic polypropylene is shown in **Figure 1.19**.

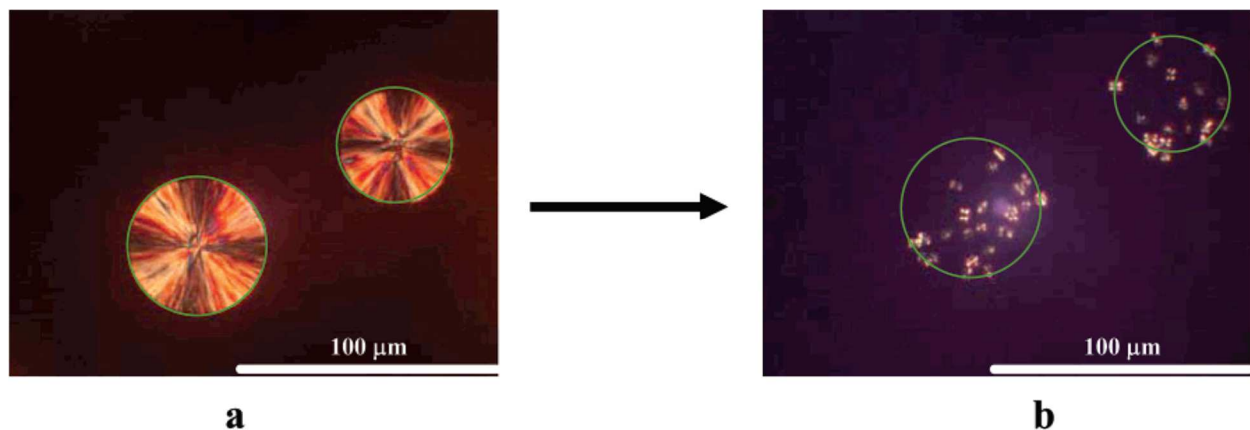


**Figure 1.19:** Optical micrograph images of crystals formed by self nucleation. **(A)** A pair of initial polymer spherulites before melting. **(B)** During melting, within radii of the spherulites, indicated by the green circle, an abundance of nuclei remain and trigger crystallization by self nucleation when the sample is cooled. Figure reproduced from [83].

Self-nucleation is an incredibly important technique for increasing the overall crystallinity and controlling the crystal grain size in polymeric materials during processing. Melting an initially crystalline sample such that only melt aligned regions remain allows for controlled cooling that drastically changes the distribution of crystalline, rigid amorphous, and mobile amorphous phase material in a bulk polymer. Beyond its practical, industrial applications this phenomenon allows

for the crystallization kinetics of a polymer to be carefully studied and the conditions necessary to obtain an amorphous molten state can be determined.

### ***1.6 Motivation for Experimental Work***

Despite the abundance of commercial polymers, there are many for which there is no literature consensus on their fundamental thermal properties, crystallization kinetics, or the impact of confinement of the polymer to nanofibers or nanocomposites. This has broad implications at both the industrial and research level. At the industrial level gaining insights into the fundamental thermal properties can improve efficacy during processing or minimize material lost to thermal degradation. The mechanical, optical, and electrical properties of polymeric materials are highly dependent on the microstructure of the polymer so it is critical that the crystallization kinetics and the conditions under which certain crystal structures can form. For example, the piezoelectric response of bulk polyvinylidene fluoride (PVDF) is only possible when polymer crystallizes with aligned beta phase crystals. Many polymers are transparent when amorphous but as they crystallize they can become cloudy or opaque. Semicrystalline polymers are often used in polarizing layers in display devices.

The combination of conventional differential scanning calorimetry (DSC) and more recently, fast scanning calorimetry (FSC) allows for complete measurements of both the fundamental thermal properties of polymers and their crystallization kinetics. This thesis focuses on the development of new data analysis techniques developed for and tested on the widely used commercial polymers, polyvinyl alcohol and polyethylene terephthalate. The successes of these experiments provide new avenues for the study of semicrystalline polymers that have been

difficult to study due to rapid phase change kinetics or undergo thermal degradation within their melting range.

### **1.6.1 Polyvinyl Alcohol**

Polyvinyl Alcohol (PVA) is a semicrystalline, hydrophilic, linear (typically atactic) synthetic polymer which is synthesized by hydrolyzing polyvinyl acetate (PVAc) [84]. PVA is water soluble above its glass transition, non-toxic, biodegradable, biocompatible, and its production does not rely on petroleum. It also possesses favorable mechanical properties and has excellent resistance to both vapors and organic solvents. Its unique chemical and vapor resistance properties coupled with its mechanical properties have led to many uses in textile and industrial applications including but not limited to: the production of glues and adhesives [85, 86], paper coatings [87], and food and medicine packaging [88-90]. Because of its nontoxicity, biodegradability [91, 92], and biocompatibility, PVA has found applications in the pharmaceutical and biomedical industries such as: drug delivery systems [93-95], fiber membranes and meshes for wound dressings [96-98], embolization particles for radiologic intervention [99], and hydrogels that are used in orthopedic medicine [100] or in the formation of contact lenses [101].

Beyond the widespread industrial and applied research applications, PVA is also used to generate a force field for computer simulation of polymer crystallization. A simplified version of a model for poly(vinyl alcohol) (PVA) was derived by a systematic coarse-graining procedure from fully atomistic simulations [102] and is still in use [103] even though the applied cooling rates in the simulations are orders of magnitude faster than the critical cooling rate determined in our work (see **Chapter 5**). PVA is a relatively simple polymer consisting of a hydrocarbon backbone with one hydroxyl group bonded to every other carbon, as shown in **Figure 1.20**.



well as the crystallization behavior of PVA hydrogels [105, 116], PVA nanofibers [94, 95, 97, 117, 118], and PVA blends and composites [93, 110, 111, 119]. A critical challenge to overcome when investigating the thermal properties and nucleation and crystallization behavior of PVA is that, at high temperatures, PVA will undergo thermal degradation within its melting range. This was recognized in some of the earliest studies on PVA [104, 115] and there have been conflicting reports [104, 105, 108, 110-112, 116] as to the impact degradation will have on the crystallization kinetics and fundamental thermal properties of PVA.

Early work done by Peppas reports that for 99% hydrolyzed PVA there was no evidence of degradation [116]. Subsequent investigations report it was only possible to observe equilibrium melting and melt crystallization of PVA free of degradation by using a high vacuum differential scanning calorimetry (DSC) technique [120]. Recent investigations into crystallization of PVA-carbon nanotube (CNT) composites [117, 118, 121, 122] and PVA-graphene composites [110, 111] have reported that thermal degradation of PVA occurs during non-isothermal crystallization. It is important to note that the addition of CNTs and graphene were reported to serve both as heterogeneous nucleation and degradation accelerators, while the polymer host was still being affected by degradation during the non-isothermal crystallization. Given the lack of consensus in the literature as to the degree and impact of degradation on the crystallization of PVA, studies are still being carried out on the crystallization mechanisms of PVA and PVA composites [110, 111, 123].

Self-seeded nuclei serve as the best possible heterogeneous sites which tend to increase both the crystallization onset temperature and the nucleation density throughout the melt. To better understand the crystallization behavior of PVA during the melt, self nucleation experiments are

performed. These experiments can be performed in a conventional DSC using a protocol developed by Fillion *et al.*, the details of which are outlined in **Section 3.3.2.2**.

To date, two of the fundamental thermal properties of PVA have remained elusive. These are the specific heat capacity of the liquid phase,  $c_p^{\text{Liquid}}(T)$ , and the specific heat capacity increment at the glass transition for 100% amorphous material,  $\Delta c_p^{\text{amor}}(T_g)$ . First, concerning the measurement of  $c_p^{\text{Liquid}}(T)$ , thermal degradation can set in at temperatures as low as 200 °C, a temperature which is typically within the melting range of semi-crystalline PVA [104, 108, 110-112]. To my best knowledge there are no accepted values for  $c_p^{\text{Liquid}}(T)$ . Second, measurement of  $\Delta c_p^{\text{amor}}(T_g)$  relies on being able to obtain PVA in its fully amorphous state, which is difficult to achieve because PVA crystallizes extremely rapidly upon cooling from the melt. To our knowledge there is no  $\Delta c_p^{\text{amor}}(T_g)$  value for PVA in literature.

### ***1.6.2 Fast Scanning Calorimetry***

Since the development of non-adiabatic chip based fast scanning calorimetry (FSC) [124-126] it has become possible to make complete, degradation free measurements of polymeric materials which are not possible in conventional differential scanning calorimeters (DSC). Both custom-made FSC systems [126, 127] and the commercial Mettler Flash DSC1 [128-130] allow for scanning rates four to six orders of magnitude greater than those accessible to conventional DSC systems [128]. The ultra-fast scanning rates accessible to these instruments have provided new insights into the crystallization kinetics of polymers such as: polyamide 6 [15, 131], polyethylene terephthalate [132, 133], polybutylene terephthalate [133, 134], polyvinylidene fluoride [135], isotactic polypropylene [136], and poly( $\epsilon$ -caprolactone) [137, 138], and polymers

in the presence of nucleating agents [133, 138]. With scanning rates on the order of 1000 K/s these instruments have been successfully utilized to measure the melting point and heat of fusion of silk fibroin [139-141], measurements which were not possible by standard DSC as silk fibroin, like PVA, undergoes thermal degradation within its melting range [104, 108, 110-112].

To make complete, degradation free measurements of these important properties, both fast scanning and conventional DSC were employed to provide thermal data on PVA over a range of heating rates from 5-20 K/min (DSC), 2000 K/s (FSC, using the Mettler Flash DSC1), and 1,000 K/s-600,000 K/s (FSC, using a custom-built chip based calorimeter [126, 127]).

In addition to the investigations into previously difficult to measure fundamental thermal properties of PVA, fast scanning calorimeters can be utilized to study the effects of confinement on electrospun fibers. Previous investigations by our group have utilized to study the effects of confinement [142, 143] on the crystallization of PET nanofibers [142]. Once brought above the equilibrium melting point the fibers begin to melt and break down into droplets. This is an interesting problem that can be tackled with fast scanning calorimeters, as both the effects of confinement on crystallization and melting can be studied simultaneously with fiber breakup. Furthermore, the ultra-fast scanning rates allow for the kinetics of fiber breakup to be studied.

To date there have been no successful experimental measurements on electrospun fibers by fast scanning calorimetry. This is due to the unique constraints on the sample preparation needed for chip based calorimeters. Sample sizes suitable for the chip sensors utilized in fast scanning calorimeters should be no larger than 150  $\mu\text{m}$  on a given edge with thickness no larger than 10  $\mu\text{m}$  [136, 144]. Electrospun fibers are light, fluffy, and delicate and physically handling them will readily damage the fibers and it is nearly impossible to manually deposit fibers on the chip sensor ensuring sufficient sample to sensor contact. This challenge motivated a new sample

preparation technique for studying electrospun fibers by fast scanning calorimetry. Because of the rich and well-studied phase behavior of semicrystalline PET, nanofibers of PET were prepared by electrospinning for the development and testing of a novel approach to obtaining fast scanning data on electrospun fibers, reported in **Chapter 6**.

### **1.7 References**

- [1] R.A. Jones, Soft condensed matter, Oxford University Press 2002.
- [2] R.J. Young, P.A. Lovell, Introduction to polymers, CRC press 2011.
- [3] ChemDraw Prime, PerkinElmer Informatics, Inc., Cambridge, MA, 2016.
- [4] H. Kawai, The piezoelectricity of poly (vinylidene fluoride), Japanese Journal of Applied Physics 8(7) (1969) 975.
- [5] S. Cimmino, E. Di Pace, E. Martuscelli, C. Silvestre, Syndiotactic polystyrene: crystallization and melting behaviour, Polymer 32(6) (1991) 1080-1083.
- [6] P. Maiti, M. Hikosaka, K. Yamada, A. Toda, F. Gu, Lamellar thickening in isotactic polypropylene with high tacticity crystallized at high temperature, Macromolecules 33(24) (2000) 9069-9075.
- [7] G.S. Yeh, S.L. Lambert, Crystallization kinetics of isotactic polystyrene from isotactic-atactic polystyrene blends, Journal of Polymer Science Part B: Polymer Physics 10(7) (1972) 1183-1191.
- [8] Y.V. Cheban, S.-F. Lau, B. Wunderlich, Analysis of the contribution of skeletal vibrations to the heat capacity of linear macromolecules in the solid state, Colloid and Polymer Science 260(1) (1982) 9-19.
- [9] B. Wunderlich, The ATHAS database on heat capacities of polymers, Pure and applied chemistry 67(6) (1995) 1019-1026.

- [10] B. Wunderlich, Motion in Polyethylene. I. Temperature and Crystallinity Dependence of the Specific Heat, *The Journal of Chemical Physics* 37(6) (1962) 1203-1207.
- [11] C. Schick, A. Wurm, A. Mohamed, Vitrification and devitrification of the rigid amorphous fraction of semicrystalline polymers revealed from frequency-dependent heat capacity, *Colloid and Polymer Science* 279(8) (2001) 800-806.
- [12] R. Androsch, B. Wunderlich, The link between rigid amorphous fraction and crystal perfection in cold-crystallized poly(ethylene terephthalate), *Polymer* 46(26) (2005) 12556-12566.
- [13] M.C. Righetti, E. Tombari, M. Angiuli, M.L.D. Lorenzo, Enthalpy-based determination of crystalline, mobile amorphous and rigid amorphous fractions in semicrystalline polymers, *Thermochimica Acta* 462(1) (2007) 15-24.
- [14] H. Chen, P. Cebe, Vitrification and Devitrification of Rigid Amorphous Fraction of PET during Quasi-Isothermal Cooling and Heating, *Macromolecules* 42(1) (2009) 288-292.
- [15] I. Kolesov, D. Mileva, R. Androsch, C. Schick, Structure formation of polyamide 6 from the glassy state by fast scanning chip calorimetry, *Polymer* 52(22) (2011) 5156-5165.
- [16] Q. Ma, M. Pyda, B. Mao, P. Cebe, Relationship between the rigid amorphous phase and mesophase in electrospun fibers, *Polymer* 54(10) (2013) 2544-2554.
- [17] M. Pyda, B. Wunderlich, Reversing and Nonreversing Heat Capacity of Poly(lactic acid) in the Glass Transition Region by TMDSC, *Macromolecules* 38(25) (2005) 10472-10479.
- [18] S. Gao, Y.P. Koh, S.L. Simon, Calorimetric Glass Transition of Single Polystyrene Ultrathin Films, *Macromolecules* 46(2) (2013) 562-570.
- [19] S.L. Simon, G.B. McKenna, Experimental evidence against the existence of an ideal glass transition, *Journal of Non-Crystalline Solids* 355(10) (2009) 672-675.

- [20] M. Pyda, B. Wunderlich, Computation of Heat Capacities of Liquid Polymers, *Macromolecules* 32(6) (1999) 2044-2050.
- [21] I.C. Sanchez, R.H. Lacombe, An elementary molecular theory of classical fluids. Pure fluids, *The Journal of Physical Chemistry* 80(21) (1976) 2352-2362.
- [22] P.J. Flory, R.A. Orwoll, A. Vrij, Statistical Thermodynamics of Chain Molecule Liquids. I. An Equation of State for Normal Paraffin Hydrocarbons, *Journal of the American Chemical Society* 86(17) (1964) 3507-3514.
- [23] P.J. Flory, R.A. Orwoll, A. Vrij, Statistical Thermodynamics of Chain Molecule Liquids. II. Liquid Mixtures of Normal Paraffin Hydrocarbons, *Journal of the American Chemical Society* 86(17) (1964) 3515-3520.
- [24] I.C. Sanchez, J. Cho, A universal equation of state for polymer liquids, *Polymer* 36(15) (1995) 2929-2939.
- [25] R. Simha, T. Somcynsky, On the Statistical Thermodynamics of Spherical and Chain Molecule Fluids, *Macromolecules* 2(4) (1969) 342-350.
- [26] R. Simha, Configurational Thermodynamics of the Liquid and Glassy Polymeric States, *Macromolecules* 10(5) (1977) 1025-1030.
- [27] P.J. Flory, Thermodynamics of high polymer solutions, *The Journal of chemical physics* 10(1) (1942) 51-61.
- [28] S.Z.D. Cheng, M.Y. Cao, B. Wunderlich, Glass transition and melting behavior of poly(oxy-1,4-phenyleneoxy-1,4-phenylenecarbonyl-1,4-phenylene) (PEEK), *Macromolecules* 19(7) (1986) 1868-1876.

- [29] S.Z.D. Cheng, R. Pan, B. Wunderlich, Thermal analysis of poly(butylene terephthalate) for heat capacity, rigid-amorphous content, and transition behavior, *Die Makromolekulare Chemie* 189(10) (1988) 2443-2458.
- [30] H. Suzuki, J. Grebowicz, B. Wunderlich, Heat capacity of semicrystalline, linear poly(oxymethylene) and poly(oxyethylene), *Die Makromolekulare Chemie* 186(5) (1985) 1109-1119.
- [31] P. Huo, P. Cebe, Effects of thermal history on the rigid amorphous phase in poly(phenylene sulfide), *Colloid and Polymer Science* 270(9) (1992) 840-852.
- [32] M. Song, D. Hourston, Temperature-Modulated Differential Scanning Calorimetry IX. Some comments on the rigid amorphous fraction in semi-crystalline poly(ethylene terephthalate), *Journal of Thermal Analysis and Calorimetry* 54(2) (1998) 651-657.
- [33] H. Xu, B.S. Ince, P. Cebe, Development of the crystallinity and rigid amorphous fraction in cold-crystallized isotactic polystyrene, *Journal of Polymer Science Part B: Polymer Physics* 41(23) (2003) 3026-3036.
- [34] B. Wunderlich, Reversible crystallization and the rigid–amorphous phase in semicrystalline macromolecules, *Progress in Polymer Science* 28(3) (2003) 383-450.
- [35] M. Pyda, R.C. Bopp, B. Wunderlich, Heat capacity of poly(lactic acid), *The Journal of Chemical Thermodynamics* 36(9) (2004) 731-742.
- [36] H. Xu, P. Cebe, Heat Capacity Study of Isotactic Polystyrene: Dual Reversible Crystal Melting and Relaxation of Rigid Amorphous Fraction, *Macromolecules* 37(8) (2004) 2797-2806.
- [37] M.C. Righetti, M.L. Di Lorenzo, E. Tombari, M. Angiuli, The Low-Temperature Endotherm in Poly(ethylene terephthalate): Partial Melting and Rigid Amorphous Fraction Mobilization, *The Journal of Physical Chemistry B* 112(14) (2008) 4233-4241.

- [38] J.D. Badia, E. Strömberg, S. Karlsson, A. Ribes-Greus, The role of crystalline, mobile amorphous and rigid amorphous fractions in the performance of recycled poly (ethylene terephthalate) (PET), *Polymer Degradation and Stability* 97(1) (2012) 98-107.
- [39] M.C. Righetti, M. Laus, M.L. Di Lorenzo, Temperature dependence of the rigid amorphous fraction in poly(ethylene terephthalate), *European Polymer Journal* 58 (2014) 60-68.
- [40] Q. Ma, P. Cebe, Phase structure of electrospun poly(trimethylene terephthalate) composite nanofibers containing carbon nanotubes, *Journal of Thermal Analysis and Calorimetry* 102(2) (2010) 425-434.
- [41] Q. Zia, D. Mileva, R. Androsch, Rigid amorphous fraction in isotactic polypropylene, *Macromolecules* 41(21) (2008) 8095-8102.
- [42] C.E. Corcione, A. Maffezzoli, Glass transition in thermosetting clay-nanocomposite polyurethanes, *Thermochimica Acta* 485(1) (2009) 43-48.
- [43] A. Sargsyan, A. Tonoyan, S. Davtyan, C. Schick, The amount of immobilized polymer in PMMA SiO<sub>2</sub> nanocomposites determined from calorimetric data, *European Polymer Journal* 43(8) (2007) 3113-3127.
- [44] H.E. Miltner, G.V. Assche, A. Pozsgay, B. Pukánszky, B.V. Mele, Restricted chain segment mobility in poly(amide) 6/clay nanocomposites evidenced by quasi-isothermal crystallization, *Polymer* 47(3) (2006) 826-835.
- [45] C. Kittel, *Introduction to solid state physics*, Wiley 2005.
- [46] Benjah-bmm27, Sodium Chloride Unit Cell, in: *Sodium-chloride-unit-cell-3D-balls.png* (Ed.) public domain, Wikimedia Commons, 2007.
- [47] Cdang, Miller Indices Cubes, in: *Indicies\_miller\_plan\_example\_cube.png* (Ed.) Creative Commons Attribution-Share Alike 3.0 Unported Wikimedia Commons, 2009.

- [48] J. Fisher, J. Hollomon, D. Turnbull, Nucleation, *Journal of Applied Physics* 19(8) (1948) 775-784.
- [49] D. Turnbull, J.C. Fisher, Rate of nucleation in condensed systems, *The Journal of chemical physics* 17(1) (1949) 71-73.
- [50] J.W. Cahn, J.E. Hilliard, Free energy of a nonuniform system. I. Interfacial free energy, *The Journal of chemical physics* 28(2) (1958) 258-267.
- [51] J.W. Cahn, Free energy of a nonuniform system. II. Thermodynamic basis, *The Journal of chemical physics* 30(5) (1959) 1121-1124.
- [52] J.W. Cahn, J.E. Hilliard, Free Energy of a Nonuniform System. III. Nucleation in a Two-Component Incompressible Fluid, *The Journal of chemical physics* 31(3) (1959) 688-699.
- [53] J.W. Cahn, On spinodal decomposition, *Acta metallurgica* 9(9) (1961) 795-801.
- [54] J.W. Cahn, Phase separation by spinodal decomposition in isotropic systems, *The Journal of Chemical Physics* 42(1) (1965) 93-99.
- [55] S. Glasstone, K.J. Laidler, H. Eyring, *The theory of rate processes; the kinetics of chemical reactions, viscosity, diffusion and electrochemical phenomena*, McGraw-Hill Book Company, 1941.
- [56] A. Keller, A note on single crystals in polymers: Evidence for a folded chain configuration, *Philosophical Magazine* 2(21) (1957) 1171-1175.
- [57] A. Keller, J.R.S. Waring, The spherulitic structure of crystalline polymers. Part III. Geometrical factors in spherulitic growth and the fine-structure, *Journal of Polymer Science* 17(86) (1955) 447-472.
- [58] A. Keller, The spherulitic structure of crystalline polymers. Part II. The problem of molecular orientation in polymer spherulites, *Journal of Polymer Science* 17(85) (1955) 351-364.

- [59] A. Keller, The spherulitic structure of crystalline polymers. Part I. Investigations with the polarizing microscope, *Journal of Polymer Science* 17(84) (1955) 291-308.
- [60] A. Keller, The morphology of crystalline polymers, *Die Makromolekulare Chemie* 34(1) (1959) 1-28.
- [61] D.R. Norton, A. Keller, The spherulitic and lamellar morphology of melt-crystallized isotactic polypropylene, *Polymer* 26(5) (1985) 704-716.
- [62] J.D. Hoffman, J.I. Lauritzen Jr, Crystallization of Bulk Polymers with Chain Folding: Theory of Growth of Lamellar Spherulites *Journal of Research of the National Bureau of Standards - A. Physics and Chemistry* 65A(4) (1961) 297-336.
- [63] C. Bunn, Crystal structure of polyvinyl alcohol, *Nature* 161(4102) (1948) 929-930.
- [64] R.d. Daubeny, C. Bunn, The crystal structure of polyethylene terephthalate, *Proceedings of the Royal Society of London A: Mathematical, Physical and Engineering Sciences*, The Royal Society, 1954, pp. 531-542.
- [65] Regular chains and crystallinity, in: D.I. Bower (Ed.), *An Introduction to Polymer Physics*, Cambridge University Press, Cambridge, 2002, pp. 87-116.
- [66] G. Menges, *Plastics Materials Science*, Hanser Verlag 2002.
- [67] B. Wunderlich, *Macromolecular physics*, Elsevier 2012.
- [68] S.Z.D. Cheng, B. Lotz, Enthalpic and entropic origins of nucleation barriers during polymer crystallization: the Hoffman–Lauritzen theory and beyond, *Polymer* 46(20) (2005) 8662-8681.
- [69] K. Armitstead, G. Goldbeck-Wood, A. Keller, *Polymer crystallization theories, Macromolecules: synthesis, order and advanced properties* (1992) 219-312.
- [70] D.C. Bassett, *Principles of polymer morphology*, Cambridge University Press, Oxford 1981.
- [71] J.W. Gibbs, *The collected works of J. Willard Gibbs*, Yale Univ. Press, 1948.

- [72] T. Dimiduk, Development of colour-producing beta-keratin nanostructures in avian feather barbs, 2010. (Accessed 07/12/2017 2017).
- [73] R.H. Gee, N. Lacevic, L.E. Fried, Atomistic simulations of spinodal phase separation preceding polymer crystallization, *Nature Materials* 5(1) (2006) 39-43.
- [74] G. Matsuba, T. Kanaya, M. Saito, K. Kaji, K. Nishida, Further evidence of spinodal decomposition during the induction period of polymer crystallization: Time-resolved small-angle x-ray scattering prior to crystallization of poly (ethylene naphthalate), *Physical Review E* 62(2) (2000) R1497.
- [75] K. Kaji, K. Nishida, T. Kanaya, G. Matsuba, T. Konishi, M. Imai, Spinodal crystallization of polymers: crystallization from the unstable melt, *Interphases and Mesophases in Polymer Crystallization III* (2005) 187-240.
- [76] P.D. Olmsted, W.C. Poon, T. McLeish, N. Terrill, A. Ryan, Spinodal-assisted crystallization in polymer melts, *Physical Review Letters* 81(2) (1998) 373.
- [77] J. Lin, S. Shenogin, S. Nazarenko, Oxygen solubility and specific volume of rigid amorphous fraction in semicrystalline poly(ethylene terephthalate), *Polymer* 43(17) (2002) 4733-4743.
- [78] D. Blundell, A. Keller, A. Kovacs, A new self-nucleation phenomenon and its application to the growing of polymer crystals from solution, *Journal of Polymer Science Part C: Polymer Letters* 4(7) (1966) 481-486.
- [79] B. Fillon, B. Lotz, A. Thierry, J.C. Wittmann, Self-Nucleation and Enhanced Nucleation of Polymers – Definition of a Convenient Calorimetric Efficiency Scale and Evaluation of Nucleating Additives in Isotactic Polypropylene (Alpha-Phase) *Journal of Polymer Science Part B-Polymer Physics* 31(10) (1993) 1395-1405.

- [80] B. Fillon, A. Thierry, J.C. Wittmann, B. Lotz, Self-Nucleation and Recrystallization of Polymers – Isotactic Polypropylene, Beta-Phase – Beta-Alpha-Conversion and Beta-Alpha-Growth Transitions, *Journal of Polymer Science Part B-Polymer Physics* 31(10) (1993) 1407-1424.
- [81] B. Fillon, J.C. Wittmann, B. Lotz, A. Thierry, Self-Nucleation and Recrystallization of Isotactic Polypropylene (Alpha-Phase) Investigated by Differential Scanning Calorimetry *Journal of Polymer Science Part B-Polymer Physics* 31(10) (1993) 1383-1393.
- [82] M.L. Arnal, V. Balsamo, G. Ronca, A. Sánchez, A.J. Müller, E. Cañizales, C. Urbina de Navarro, Applications of Successive Self-Nucleation and Annealing (SSA) to Polymer Characterization, *Journal of Thermal Analysis and Calorimetry* 59(1) (2000) 451-470.
- [83] A. Mamun, S. Umemoto, N. Okui, N. Ishihara, Self-Seeding Effect on Primary Nucleation of Isotactic Polystyrene, *Macromolecules* 40(17) (2007) 6296-6303.
- [84] W.O. Kenyon, G.P. Waugh, Preparation of polyvinyl alcohol, Google Patents, 1953.
- [85] T.G. Kane, W.D. Robinson, Polyvinyl alcohol adhesives, United States, 1972.
- [86] M. Sumi, J. Suenaga, M. Takenaka, I. Murano, M. Tanabe, K. Hirai, Cold-set adhesive compositions comprising polyvinyl alcohol for paper and paper board, United States, 1984.
- [87] E.A. Wolff, Method of making a waterproof polyvinyl alcohol coated paper, United States, 1970.
- [88] J.H. Han, 4 - Antimicrobial food packaging, in: R. Ahvenainen (Ed.), *Novel Food Packaging Techniques*, Woodhead Publishing 2003, pp. 50-70.
- [89] A. Musetti, K. Paderni, P. Fabbri, A. Pulvirenti, M. Al-Moghazy, P. Fava, Poly(vinyl alcohol)-Based Film Potentially Suitable for Antimicrobial Packaging Applications, *Journal of Food Science* 79(4) (2014) E577-E582.

- [90] H.M.C. de Azeredo, Nanocomposites for food packaging applications, *Food Research International* 42(9) (2009) 1240-1253.
- [91] E. Chiellini, A. Corti, S. D'Antone, R. Solaro, Biodegradation of poly (vinyl alcohol) based materials, *Progress in Polymer Science* 28(6) (2003) 963-1014.
- [92] H. Huang, L. Gu, Y. Ozaki, Non-isothermal crystallization and thermal transitions of a biodegradable, partially hydrolyzed poly(vinyl alcohol), *Polymer* 47(11) (2006) 3935-3945.
- [93] I. Arvanitoyannis, I. Kolokuris, A. Nakayama, N. Yamamoto, S.-i. Aiba, Physico-chemical studies of chitosan-poly(vinyl alcohol) blends plasticized with sorbitol and sucrose, *Carbohydrate Polymers* 34(1-2) (1997) 9-19.
- [94] J. Zeng, A. Aigner, F. Czubyko, T. Kissel, J.H. Wendorff, A. Greiner, Poly(vinyl alcohol) Nanofibers by Electrospinning as a Protein Delivery System and the Retardation of Enzyme Release by Additional Polymer Coatings, *Biomacromolecules* 6(3) (2005) 1484-1488.
- [95] E.-R. Kenawy, F.I. Abdel-Hay, M.H. El-Newehy, G.E. Wnek, Controlled release of ketoprofen from electrospun poly(vinyl alcohol) nanofibers, *Materials Science and Engineering: A* 459(1-2) (2007) 390-396.
- [96] P.K. Khanna, N. Singh, S. Charan, V.V.V.S. Subbarao, R. Gokhale, U.P. Mulik, Synthesis and characterization of Ag/PVA nanocomposite by chemical reduction method, *Materials Chemistry and Physics* 93(1) (2005) 117-121.
- [97] K.H. Hong, Preparation and properties of electrospun poly(vinyl alcohol)/silver fiber web as wound dressings, *Polymer Engineering & Science* 47(1) (2007) 43-49.
- [98] Y. Zhou, D. Yang, X. Chen, Q. Xu, F. Lu, J. Nie, Electrospun Water-Soluble Carboxyethyl Chitosan/Poly(vinyl alcohol) Nanofibrous Membrane as Potential Wound Dressing for Skin Regeneration, *Biomacromolecules* 9(1) (2008) 349-354.

- [99] S. Vaidya, K.R. Tozer, J. Chen, An Overview of Embolic Agents, *Semin Intervent Radiol* 25(03) (2008) 204-215.
- [100] M.I. Baker, S.P. Walsh, Z. Schwartz, B.D. Boyan, A review of polyvinyl alcohol and its uses in cartilage and orthopedic applications, *Journal of Biomedical Materials Research Part B: Applied Biomaterials* 100B(5) (2012) 1451-1457.
- [101] S.-H. Hyon, W.-I. Cha, Y. Ikada, M. Kita, Y. Ogura, Y. Honda, Poly(vinyl alcohol) hydrogels as soft contact lens material, *Journal of Biomaterials Science, Polymer Edition* 5(5) (1994) 397-406.
- [102] H. Meyer, F. Müller-Plathe, Formation of chain-folded structures in supercooled polymer melts, *Journal of Chemical Physics* 115(17) (2001) 7807.
- [103] C. Luo, M. Kröger, J.-U. Sommer, Molecular dynamics simulations of polymer crystallization under confinement: Entanglement effect, *Polymer* 109 (2017) 71-84.
- [104] R.K. Tubbs, Melting point and heat of fusion of poly(vinyl alcohol), *Journal of Polymer Science Part A: General Papers* 3(12) (1965) 4181-4189.
- [105] N.A. Peppas, E.W. Merrill, Differential scanning calorimetry of crystallized PVA hydrogels, *Journal of Applied Polymer Science* 20(6) (1976) 1457-1465.
- [106] U. Gaur, B.B. Wunderlich, B. Wunderlich, Heat Capacity and Other Thermodynamic Properties of Linear Macromolecules. VII. Other Carbon Backbone Polymers, *Journal of Physical and Chemical Reference Data* 12(1) (1983) 29-63.
- [107] H.S. Bu, W. Aycock, S.Z.D. Cheng, B. Wunderlich, Heat capacities of various solid linear macromolecules, *Polymer* 29(8) (1988) 1485-1494.
- [108] B.J. Holland, J.N. Hay, The thermal degradation of poly(vinyl alcohol), *Polymer* 42(16) (2001) 6775-6783.

- [109] N.A. El-Zaher, W.G. Osiris, Thermal and structural properties of poly(vinyl alcohol) doped with hydroxypropyl cellulose, *Journal of Applied Polymer Science* 96(5) (2005) 1914-1923.
- [110] C.P. Li, J. Vongsvivut, X.D. She, Y.Z. Li, F.H. She, L.X. Kong, New insight into non-isothermal crystallization of PVA-graphene composites, *Physical Chemistry Chemical Physics* 16(40) (2014) 22145-22158.
- [111] C.P. Li, T.T. Hou, X.D. She, X.Y. Wei, F.H. She, W.M. Gao, L.X. Kong, Decomposition properties of PVA/graphene composites during melting-crystallization, *Polymer Degradation and Stability* 119 (2015) 178-189.
- [112] D. Thomas, P. Cebe, Self-nucleation and crystallization of polyvinyl alcohol, *Journal of Thermal Analysis and Calorimetry* 127(1) (2017) 885-894.
- [113] K. Tsuboi, Solution-grown crystals of poly(vinyl alcohol), *Journal of Macromolecular Science, Part B* 2(4) (1968) 603-622.
- [114] S.K. Mallapragada, N.A. Peppas, Dissolution mechanism of semicrystalline poly(vinyl alcohol) in water, *Journal of Polymer Science Part B: Polymer Physics* 34(7) (1996) 1339-1346.
- [115] T. Hiroyuki, S. Syûzô, N. Isamu, The Crystallinity of Solid High Polymers. I. The Crystallinity of Polyvinyl Alcohol Film, *Bulletin of the Chemical Society of Japan* 28(8) (1955) 559-564.
- [116] N.A. Peppas, P.J. Hansen, Crystallization kinetics of poly(vinyl alcohol), *Journal of Applied Polymer Science* 27(12) (1982) 4787-4797.
- [117] A. Koski, K. Yim, S. Shivkumar, Effect of molecular weight on fibrous PVA produced by electrospinning, *Materials Letters* 58(3) (2004) 493-497.

- [118] N. Minoo, L. Tong, P.S. Mark, D. Liming, W. Xungai, Electrospun single-walled carbon nanotube/polyvinyl alcohol composite nanofibers: structure–property relationships, *Nanotechnology* 19(30) (2008) 305702.
- [119] J. Jang, D.K. Lee, Plasticizer effect on the melting and crystallization behavior of polyvinyl alcohol, *Polymer* 44(26) (2003) 8139-8146.
- [120] R. Endo, S. Amiya, M. Hikosaka, Conditions for Melt Crystallization Without Thermal Degradation and Equilibrium Melting Temperature of Atactic Poly(Vinyl Alcohol), *Journal of Macromolecular Science, Part B* 42(3-4) (2003) 793-820.
- [121] O. Probst, E.M. Moore, D.E. Resasco, B.P. Grady, Nucleation of polyvinyl alcohol crystallization by single-walled carbon nanotubes, *Polymer* 45(13) (2004) 4437-4443.
- [122] M.L. Minus, H.G. Chae, S. Kumar, Single wall carbon nanotube templated oriented crystallization of poly(vinyl alcohol), *Polymer* 47(11) (2006) 3705-3710.
- [123] C.P. Li, T.T. Hou, J. Vongsvivut, Y.Z. Li, X.D. She, F.H. She, W.M. Gao, L.X. Kong, Simultaneous crystallization and decomposition of PVA/MMT composites during non-isothermal process, *Thermochimica Acta* 618 (2015) 26-35.
- [124] A.A. Minakov, C. Schick, Ultrafast thermal processing and nanocalorimetry at heating and cooling rates up to 1 MK/s, *Rev. Sci. Instr.* 78(7) (2007) 073902-10.
- [125] S.A. Adamovsky, A.A. Minakov, C. Schick, Scanning microcalorimetry at high cooling rate, *Thermochimica Acta* 403(1) (2003) 55-63.
- [126] E. Zhuravlev, C. Schick, Fast scanning power compensated differential scanning nanocalorimeter: 1. The device, *Thermochimica Acta* 505(1-2) (2010) 1-13.
- [127] E. Zhuravlev, C. Schick, Fast scanning power compensated differential scanning nanocalorimeter: 2. Heat capacity analysis, *Thermochimica Acta* 505(1-2) (2010) 14-21.

- [128] V. Mathot, M. Pyda, T. Pijpers, G. Vanden Poel, E. van de Kerkhof, S. van Herwaarden, F. van Herwaarden, A. Leenaers, The Flash DSC 1, a power compensation twin-type, chip-based fast scanning calorimeter (FSC): First findings on polymers, *Thermochimica Acta* 522(1) (2011) 36-45.
- [129] E. Iervolino, A.W. van Herwaarden, F.G. van Herwaarden, E. van de Kerkhof, P.P.W. van Grinsven, A.C.H.I. Leenaers, V.B.F. Mathot, P.M. Sarro, Temperature calibration and electrical characterization of the differential scanning calorimeter chip UFS1 for the Mettler-Toledo Flash DSC 1, *Thermochimica Acta* 522(1–2) (2011) 53-59.
- [130] S. van Herwaarden, E. Iervolino, F. van Herwaarden, T. Wijffels, A. Leenaers, V. Mathot, Design, performance and analysis of thermal lag of the UFS1 twin-calorimeter chip for fast scanning calorimetry using the Mettler-Toledo Flash DSC 1, *Thermochimica Acta* 522(1–2) (2011) 46-52.
- [131] D. Mileva, R. Androsch, E. Zhuravlev, C. Schick, Morphology of mesophase and crystals of polyamide 6 prepared in a fast scanning chip calorimeter, *Polymer* 53(18) (2012) 3994-4001.
- [132] R. Androsch, C. Schick, A.M. Rhoades, Application of Tamman's Two-Stage Crystal Nuclei Development Method for Analysis of the Thermal Stability of Homogeneous Crystal Nuclei of Poly(ethylene terephthalate), *Macromolecules* 48(22) (2015) 8082-8089.
- [133] A. Wurm, A. Herrmann, M. Cornelius, E. Zhuravlev, D. Pospiech, R. Nicula, C. Schick, Temperature Dependency of Nucleation Efficiency of Carbon Nanotubes in PET and PBT, *Macromolecular Materials and Engineering* 300(6) (2015) 637-649.
- [134] R. Androsch, A.M. Rhoades, I. Stolte, C. Schick, Density of heterogeneous and homogeneous crystal nuclei in poly (butylene terephthalate), *European Polymer Journal* 66 (2015) 180-189.

- [135] A. Gradys, P. Sajkiewicz, E. Zhuravlev, C. Schick, Kinetics of isothermal and non-isothermal crystallization of poly(vinylidene fluoride) by fast scanning calorimetry, *Polymer* 82 (2016) 40-48.
- [136] J.E.K. Schawe, Analysis of non-isothermal crystallization during cooling and reorganization during heating of isotactic polypropylene by fast scanning DSC, *Thermochimica Acta* 603 (2015) 85-93.
- [137] E. Zhuravlev, J.W.P. Schmelzer, B. Wunderlich, C. Schick, Kinetics of nucleation and crystallization in poly( $\epsilon$ -caprolactone) (PCL), *Polymer* 52(9) (2011) 1983-1997.
- [138] E. Zhuravlev, A. Wurm, P. Poetschke, R. Androsch, J.W.P. Schmelzer, C. Schick, Kinetics of nucleation and crystallization of poly(epsilon-caprolactone) - Multiwalled carbon nanotube composites, *European Polymer Journal* 52 (2014) 1-11.
- [139] P. Cebe, X. Hu, D.L. Kaplan, E. Zhuravlev, A. Wurm, D. Arbeiter, C. Schick, Beating the Heat - Fast Scanning Melts Silk Beta Sheet Crystals, *Scientific Reports* 3 (2013) 7.
- [140] P. Cebe, B.P. Partlow, D.L. Kaplan, A. Wurm, E. Zhuravlev, C. Schick, Silk I and Silk II studied by fast scanning calorimetry, *Acta Biomaterialia*.
- [141] P. Cebe, B.P. Partlow, D.L. Kaplan, A. Wurm, E. Zhuravlev, C. Schick, Using flash DSC for determining the liquid state heat capacity of silk fibroin, *Thermochimica Acta* 615 (2015) 8-14.
- [142] H. Chen, Z. Liu, P. Cebe, Chain confinement in electrospun nanofibers of PET with carbon nanotubes, *Polymer* 50(3) (2009) 872-880.
- [143] Q. Ma, B. Mao, P. Cebe, Chain confinement in electrospun nanocomposites: using thermal analysis to investigate polymer–filler interactions, *Polymer* 52(14) (2011) 3190-3200.

[144] A. Toda, M. Konishi, An evaluation of thermal lags of fast-scan microchip DSC with polymer film samples, *Thermochimica Acta* 589 (2014) 262-269.

## ***Chapter 2 Experimental – Sample Preparation***

### ***2.1 Sample Preparation with Experimental Constraints in Mind***

Investigations into bulk polymer thermal properties can use materials as received from the chemical supplier, provided they are tolerant of being heated to their melting point without degradation. This is an important criterion since, materials as received have unknown and varied thermal histories which make them poor candidates as starting points for systematic investigations into nucleation and crystallization. A typical starting point for crystallization studies on as-received material involves heating past the equilibrium melting point,  $T_m^0$ , and holding for up to 30 minutes followed by a controlled cooling from the melt resulting in a well-defined initial state [1-3]. Depending upon the cooling rate this will result in either an amorphous glass or semi-crystalline material once the material has been cooled below the glass transition,  $T_g$  [4-7].

Experiments which probe nucleation, crystallization, and melting behavior of polymers confined to thin films, nanofibers, or containing additives require additional considerations when preparing samples. Subsequent chapters will deal with the polymer crystallization of solution cast film samples, thin films prepared by spin coating, and nanofibers prepared by electrospinning, in addition to measurements made on raw starting as-received materials.

### ***2.2 Solution Processing of Polymers***

#### ***2.2.0 Preparation of Solution Cast PVA Films for Self-Nucleation Experiments (Ch. 4)***

Self nucleation experiments involve heating samples from an initial semi-crystalline state to various self nucleation temperatures,  $T_s$ , and isothermally holding for various times,  $t_s$ , to

determine the conditions under which the melt will retain memory of prior crystallinity. [1-3] For polymers which do not degrade at temperatures near their melting point it is possible to fully erase thermal history by heating and then treat a single sample at multiple  $T_s$  and  $t_s$ . However, polyvinyl alcohol (PVA) begins to undergo thermal degradation around 200 °C which is within its melting range [8-13] and well below its equilibrium melting point ( $T_m^0 = 265$  °C) [14]. This necessitates the preparation and use of a fresh sample of PVA for each measurement and only one combination of self nucleation temperature,  $T_s$ , and time,  $t_s$ , can be tested per sample. To bypass the initial heating to temperatures greater than  $T_m^0$ , samples of PVA were cut from a parent film of uniform crystallinity. Solution casting was the preferred method for preparing the parent film as it only requires heating of semi-crystalline samples to temperatures above its glass transition ( $T_g = 85$  °C) [14] where it becomes water soluble.

Semicrystalline pellets of PVA (see **Figure 2.1A**),  $M_w$  78,000 and 98 mol% hydrolyzed, were obtained from PolySciences, Inc. Bulk films suitable for DSC were made by dissolving PVA at 8.0 wt.% in deionized water at 90 °C with continuous stirring. Once a homogenous solution was obtained the solution was poured onto PTFE (Teflon™) sheets. The solution coated sheets were placed in a vacuum oven at approximately 30 °C and kept for 72 hours. This allowed the water to evaporate leaving behind a thin, semicrystalline film of PVA approximately 250  $\mu\text{m}$  in thickness with an initial crystallinity,  $\phi_C$  of 39.2%  $\pm$  1.6% (calculated using Eqn. 3.14). Samples were cut from the parent film such that they filled standard aluminum DSC pans with uniform contact across the entire surface. Masses varied between 4.5 and 10.4 mg; a listing of these samples is found in **Table 4.1** where the experiment is discussed in greater detail. A typical example of a sample cut from the parent film can be seen in **Figure 2.1B**.

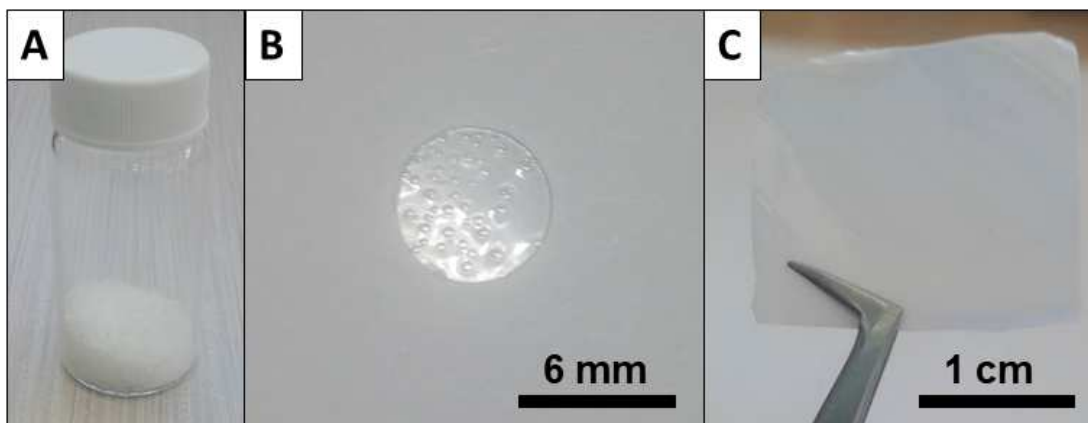


**Figure 2.1:** (A) Semi-crystalline PVA as received from PolySciences, Inc, (B) following solution processing into a 250  $\mu\text{m}$  thick film which has been cut to size using a hole punch to fit a standard DSC pan, and (C) spin coated onto a PTFE slide resulting in a film approximately 3  $\mu\text{m}$  thick.

### 2.2.1 Preparation of PVA Thin Films by Spin Coating (Ch. 5)

Semi-crystalline pellets of polyvinyl alcohol (PVA), MW 78,000 and 98 mol% hydrolyzed, were obtained from Polysciences, Inc. PVA pellets were dissolved at 3.0 wt.% in deionized water at 90 °C with continuous stirring for 2 hours resulting in a homogeneous solution. The solution was spun onto substrates (glass slides coated with PTFE) with a Headway research grade spin caster. To obtain thin film samples, 10 droplets of PVA solution was passed through a 0.8  $\mu\text{m}$  PTFE filter and sequentially deposited onto a PTFE coated glass slide spinning at 2000 rpm for 60 s. This resulted in films approximately 3  $\mu\text{m}$  thick which were easily removed from the PTFE coated slides prior to mounting on chip sensor membranes. The mass per unit area of this film was measured to be  $3.80 \times 10^{-12} \text{ g}/\mu\text{m}^2$ . An example of one of these films deposited on a PTFE coated slide can be seen in **Figure 2.1C**. This will be referred to as the “thicker film” and served as the parent film for 9 distinct samples discussed. A second set of thin films was prepared by passing the PVA solution through a 0.8  $\mu\text{m}$  PTFE filter and depositing 10 droplets on a PTFE coated slide

at rest. This slide was then set spinning at 2000 rpm for 60 s resulting in films approximately 1  $\mu\text{m}$  thick. This film will be referred to as the “thinner film” and was used as the parent film for one experiment. All films were placed in a vacuum oven at approximately 30  $^{\circ}\text{C}$  for 24 hours.

PVA thin films are easily peeled off the PTFE sheet and transferred to a clean glass slide. With the aid of surgical scalpel and a steady hand it is possible to cut these films to dimensions between 50  $\mu\text{m}$  and 100  $\mu\text{m}$  on edge. A binocular microscope with 2-10x magnification enables an operator to manually transfer cut samples from the glass slide to fast scanning chip sensors. Spin coating proved to be a reliable means of controlling sample thickness and allowed for an operator to easily produce high quality samples suitable for any chip based calorimeter sensor. These samples are easy to mount and image as seen in **Figure 2.2**.

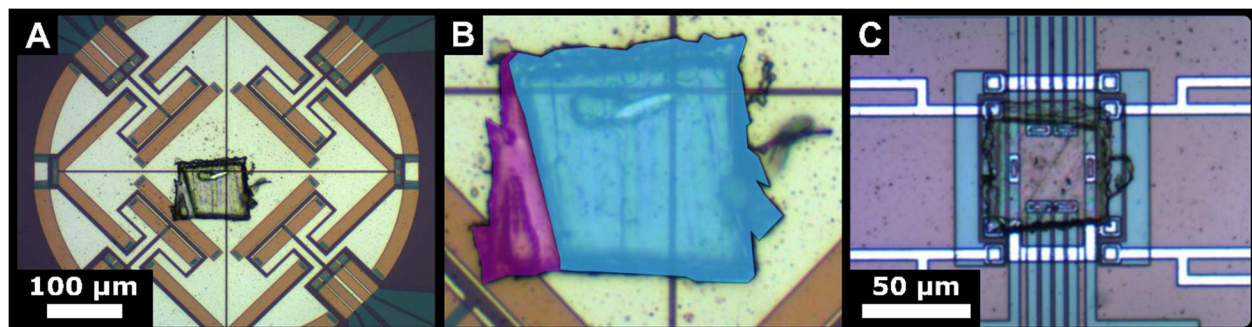


**Figure 2.2:** (A) Sample cut from the thicker PVA film and loaded onto a Mettler Toledo UFSC11 sensor, imaged at 100x; (B) Sample from (A) digitally magnified for surface area determination and assessment of cut quality; (C) Sample mounted on a XI-390 chip sensor of the custom-built calorimeter [15, 16], imaged at 200x.

Spin coating resulted in uniform, thin films. However, cutting did deform the edges and often partial cuts resulted in sheared regions which were not visible until the sample was imaged at magnifications  $\geq 50\times$ . The blue area seen in **Figure 2.2B** shows the region where the sample

retains the initial, uniform, thickness. The purple area in **Figure 2.2B** highlights regions damaged by handling which results in a reduction of thickness as material is sheared off during cutting. Despite these small issues in sample preparation the signal quality and sample to sensor contact was excellent and did not necessitate the use of silicone oil or gold foil.

### ***2.2.2 Preparation of Polymers for Electrospinning (Ch. 6-7)***

Semi-crystalline pellets of polyamide 6 (PA6), also known as Nylon 6, were dissolved at 8 wt.% in 1,1,1,3,3,3-Hexafluoro-2-propanol (HFIP), obtained from Oakwood Products, Inc. This PA6 was found in the chemical cabinet in a hand marked bag and these solutions were used for proof of concept work prior to the experiments on the two preselected polymers, polyethylene terephthalate (PET) and polyvinyl alcohol (PVA).

Semi-crystalline pellets of polyethylene terephthalate (PET), inherent viscosity 0.58, was obtained from Scientific Polymer Products, Inc. Trifluoroacetic acid (TFA) was obtained from Oakwood Products, Inc. Dichloromethane (DCM) was obtained from MilliporeSigma. PET was dissolved at 20 wt.% in 50/50 vol./vol. TFA/DCM with continuous stirring until a homogenous solution was obtained. These homogenous solutions are clear, with a very slight purple tint.

Semi-crystalline pellets of polyvinyl alcohol (PVA), MW 78,000 and 98 mol% hydrolyzed, were obtained from Polysciences, Inc. PVA was dissolved at both 8 wt.% and 10 wt.% in deionized water at 90 °C with continuous stirring until homogenous solutions were obtained. PVA was dissolved at 10 wt.% in 98/2 vol./vol. deionized water/ acetic acid. The 8 wt.% solution was used for electrospinning of fibers from the smallest diameter spinnerets and the 10 wt.% solutions were used for spinning fibers through larger diameter spinnerets. Homogenous solutions of PVA are clear and have a viscosity, when warm, similar to corn syrup.

### **2.3 *Electrospinning of Polymers (Ch. 6-7)***

Electrospinning is an experimental technique which has become widely used over the past 15 years to reliably produce polymer micro and nanofibers and fiber composites. [17-23] By confining polymer to fibers which have diameters between 100 nm and 800 nm unique bulk material properties can be obtained, novel materials that can promote tissue growth can be fabricated [23-31], and new insights into the fundamental effects of nanoconfinement on polymer crystallization can be gained [32, 33].

Semicrystalline pellets of various polymers are dissolved in volatile solvents from which micro and nanofibers are obtained by drawing the solution through a strong electric field. Once dissolved in a suitable solvent, the conductive polymer solution is loaded into a syringe (typically glass or chemically resistant plastic) equipped with conductive needle. Solution is flowed out of the syringe at a constant rate by either holding the syringe above the collector and allowing gravity to pull the solution out or by placing the syringe horizontally in a pump, as is done in our lab. An accelerating voltage, typically between 5-50 kV, is applied to the conductive needle. A conductive, grounded surface serves as the counter electrode and is placed some working distance, typically 10-20 cm, away from the opening of the needle tip. Between the needle tip and the counter electrode, the typical electric field strength is on the order of a kV/cm.

A polymer droplet is formed at the needle tip and will grow until gravity overcomes surface tension and the droplet falls off. For conductive solutions in the presence of an electric field the droplet is deformed and drawn towards the counter electrode. This deformation forms a Taylor cone [18], common to any hydrodynamic spray process where a charged solution is in the presence

of an electric field. For sufficiently viscous, flowing polymer solutions, a steady stream of solution is ejected from the tip of the Taylor cone and is pulled towards the counter electrode by the electric field. This stream is referred to as the jet. As the jet travel over the working distance the individual dipole moments along the polymer chains in the solution interact with the electric field. This interaction results in torques which drive the jet to move in a chaotic, whipping motion. As the jet whips through the air, solvent is ejected and the stream diameter is reduced. [18] A schematic of this process, reproduced from [23], can be seen in **Figure 2.3**.

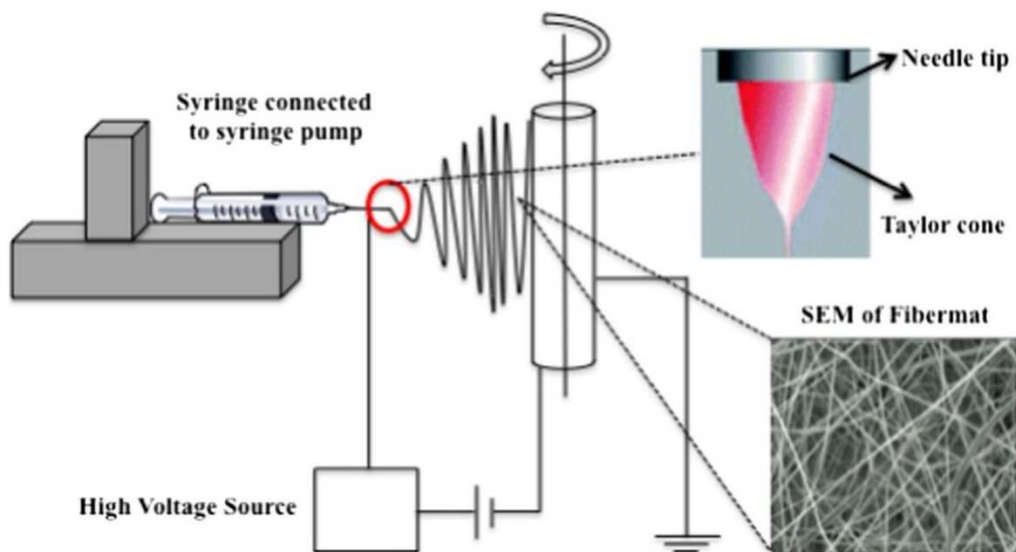


**Figure 2.3:** Electrospinning schematic reproduced from [23]. A syringe loaded with conductive polymer solution is placed in a syringe pump which pumps solution through the needle tip at constant rate. High voltage is applied to the needle tip and a rotating collector is grounded and serves as the counter electrode which is placed a fixed distance away. The electric field interacts with the solution and deforms the droplet creating the Taylor cone, pictured at the top, to the right of the syringe. With the proper electrospinning conditions a nanofibrous mat is deposited on collector.

Tuning the solution viscosity, either by varying the wt.% of polymer [17-19, 21, 22] or by addition of salts and surfactants [34], the diameter of the needle tip, working distance, and electric

field strength allow for reliable control over the fiber diameter. A stationary counter electrode results in a mat of randomly aligned fibers due to the chaotic whipping path of the fibers [21, 22]. If the counter electrode is set spinning at high speeds the fibers are stretched straight along the direction of rotation resulting in highly aligned fiber mats [21, 22].

The fibers produced were used for the development of a novel technique for preparing samples suitable for fast scanning calorimetry (FSC) and for neural tissue scaffolds. Both were produced using a rotating counter electrode which resulted in well aligned nanofibers. All the polymers studied here are readily electrospun and their preparations do not require the addition of surfactants or salts to produce suitable solutions. Solutions were loaded into glass syringes equipped with stainless steel needles and placed in a syringe pump as shown in **Figure 2.4A**. The needle tip is passed through a slot inside an insulated Teflon<sup>TM</sup> lined box and positioned in line with the rotating counter electrode collector. This insulated box prevents turbulence from the chemical hood duct work from disturbing the fibers during the electrospinning process. The complete experimental setup can be seen in **Figure 2.4B**. The specific glass syringes used were Cadence Science Dissolved Gas Analysis (DGA) 10 mL in ½ mL with (Luer) lock tip, obtained from the manufacturer or through Aldrich (depending upon price and order size). The syringe pump was obtained from New Era Pump Systems, Inc. Stainless steel needles with Luer lock were obtained from Hamilton Company.

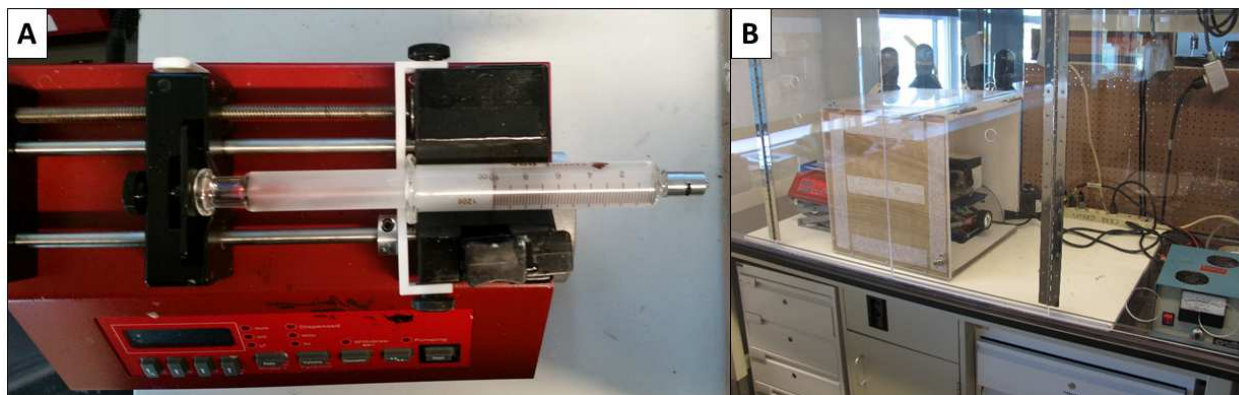


**Figure 2.4:** (A) Single channel programmable syringe pump loaded with DGA syringe, also seen at the left side of (B) which shows the insulated PTFE lined box housing the counter electrode collector. The high voltage power supply is seen in the bottom right corner of the image. The entire setup is run inside a larger vented cabinet which protects users from the volatile solvents used during the electrospinning process.

This process results in a non-woven mat of micro- or nanofibers. The thickness of this mat depends upon the spin time. Short spins result in rarefied fibers which are suitable for electron microscopy and fast scanning calorimetry, and are most often used when running high throughput tests to optimize the electrospinning parameters. Thick mats suitable for conventional differential scanning calorimetry, mechanical testing, or structural analysis such as X-ray diffraction or Fourier transform infrared spectroscopy are obtained using longer spin times ( $t_{\text{spin}} > 30$  minutes). An example of a typical fiber mat is shown in **Figure 2.5**.



**Figure 2.5:** Example of an electrospun fiber mat next to a DGA syringe. The bulk tape is approximately 2.5 cm wide and has a thickness of about 100  $\mu\text{m}$ .

### ***2.3.0 Electrospinning of PET for Development of Novel Technique to Study Fibers by Fast Scanning Calorimetry (FSC) (Ch.6)***

Polyethylene terephthalate solutions are stable with constant stirring when prepared in sealed containers and kept around room temperature. Electrospinning was performed at a flow rate of 0.02 mL/min through a 22 gauge ( $\text{\O} 0.717 \text{ mm}$ ) stainless steel needle with a working distance of 10 cm and 15 kV accelerating voltage. Aligned nanofibers are obtained by electrospinning onto a rotating drum collector coated in aluminum foil spinning at 2000 rpm. Fibers were electrospun for various times,  $t_{spin}$ , to prepare samples suitable for each experiment performed. Samples of fiber coated aluminum foil were cut free and set aside for scanning electron microscopy (SEM) analysis which will be discussed in the following chapter.

### ***2.3.1 Electrospinning of PVA – Nanofibers for Neural Tissue Scaffolds (Ch. 7)***

Once cooled, PVA solutions will transition from a homogenous, clear solution, first, to a blue tinted, clear solution before finally transitioning into a cloudy and clumpy solution. This has been described in the literature and is due to PVA hydrogen bonding to itself in solution which leads to the formation of a loose, gel like networks. [35, 36] As time increases, the ability to electrospin a cooled PVA solution decreases. It is best to use a fresh, warm solution when electrospinning PVA. All PVA solutions were kept on heat and stir and electrospinning was performed with an initially warm, homogenous solution. Time scales of electrospinning ( $t_{\text{spin}} < 4$  hours) are within in the range where PVA solutions are stable.

To obtain electrospun fibers suitable for neuronal tissue scaffolds PVA at 10 wt.% in deionized water and at 10 wt.% in deionized water/ acetic acid were electrospun with at a flow rate of 0.008 mL/min through an 18 gauge ( $\text{\O} 1.27$  mm) or 20 gauge ( $\text{\O} 0.9081$  mm) stainless steel needle at a working distance of 15 cm and 15 kV accelerating voltage. Aligned nanofibers are obtained by electrospinning onto a rotating drum counter electrode coated in aluminum foil spinning at 2000 rpm. Mats of fibers thick enough to serve as tissue scaffolds were formed by spinning for  $t_{\text{spin}} = 3$  hours. Once the spin is completed the aluminum foil is carefully unwrapped from the counter electrode and the fiber mats were placed in a vacuum oven at approx. 30 °C to dry.

Dried fiber mats were removed from the oven and the fibers could be removed from the aluminum foil substrate for additional treatments. PVA nanofibers adhered strongly to the aluminum foil and should be factored into decisions when electrospinning PVA for various applications. In the case of the tissue scaffold preparation the spin times were set such that the bulk of the mat which separated easily from the foil was thick enough that it could be studied with a

variety of instruments and was sufficiently thick for additional processing to create a tissue scaffold. The layer of fibers which remain on the aluminum foil are well suited for scanning electron microscopy (SEM) analysis following sputter coating.

### **2.3.2 *Electrospinning of PVA – Nanofibers for Nanofibers for Fast Scanning Calorimetry (FSC) (Ch. 7)***

Electrospun fibers suitable for fast scanning calorimetry (FSC) experiments were produced by electrospinning 8 wt.% PVA in deionized water. Solution was electrospun at a flow rate of 0.008 mL/min through a 26 gauge ( $\text{\O} 0.4636$  mm) stainless steel needle with a working distance of 15 cm with an accelerating voltage of 20 kV. Aligned nanofibers were obtained by electrospinning onto a rotating drum counter electrode coated in aluminum foil. Fibers were electrospun for various times,  $t_{spin}$ , to prepare samples suitable for each experiment performed. Samples of fiber coated aluminum foil were cut free and set aside for scanning electron microscopy (SEM) analysis which will be discussed in the following chapter.

Spinning PVA through a 26 gauge needle poses a unique challenge when  $t_{spin}$  is in excess of 30 minutes. Spin time for FSC experiments were short,  $t_{spin} = 4$  min. When preparing additional PVA samples for complimentary investigations it is necessary to change out the needle every 30 minutes as it becomes clogged easily. This clogging is a result of the occasional PVA aggregate in solution during long times which either jams up the needle or briefly interrupts the stream and exposes the interior of the needle to open air allowing the solution dry.

## 2.4 Electrospinning Fibers Suitable for Fast Scanning Calorimetry (FSC) Chip Sensors (Ch.6-7)

Fast scanning calorimeters utilize chip based sensors 500  $\mu\text{m}$  in diameter which allow for samples to be deposited into the well or coated to the bottom of the sensor, typical of masked vapor deposition sample preparation approaches. Thin film samples and tiny flakes of material shaved off a bulk sample are easy to manually lift and deposit into the well using a fine wire [ref]. The Mettler Toledo UFSC1 Chip sensor is shown in **Figure 2.6**.

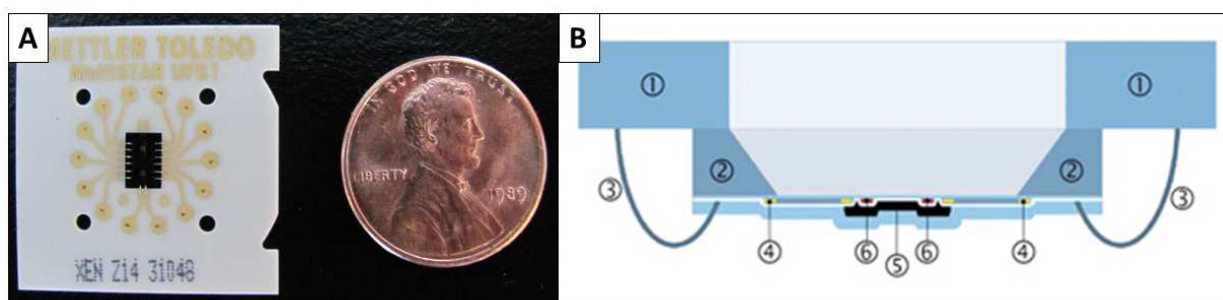


**Figure 2.6:** (A) Mettler Toledo UFSC1 chip sensor for use in the Mettler Flash DSC1. Example of a UFSC1 sensor with a penny for scale. The active sensor area is the light gray circle indicated by the arrow on the left side of the image. (B) A cross section of the sensor well from Mettler Toledo Product Literature [37]. Samples are manually lowered into the well using a fine wire and should be kept to heights less than 10  $\mu\text{m}$ . The components listed are: 1 – Ceramic Base, 2 – Silicon Frame, 3 – Connecting Wires, 4 – Resistance Heater, 5 – Aluminum Sample Area, 6 – Thermocouple.

Electrospun fibers are light, fluffy, and difficult to handle when cut to small sizes suitable for the chip sensors. Directly placing a cut portion of an electrospun fiber mat onto the sensor poses a challenge in that the fibers will cling to the walls of the well, stick to the wire, or become wadded up and exceed the 10  $\mu\text{m}$  height threshold for viable scans. Three early approaches taken to prepare electrospun fibers involved first, direct electrospinning onto the sensor; second placing the fibers into the well and adding a droplet of silicone oil; and last, an unsuccessful attempt to electrospin directly onto gold leaf was made.

When fibers are placed in the well and a droplet of silicone oil is added the fibers will clump up and act almost like a sponge for the oil. While there is sufficient sample to sensor contact through the oil, this approach leaves a mess of sample on the sensor which does not have a well-controlled sample thickness, nor is it possible to ensure that all the fibers remain in contact with sensor as they can slide and move along the sensor. An example of the mess of sample can be seen in **Figure 2.7**. This method did not yield high quality scans and was abandoned.

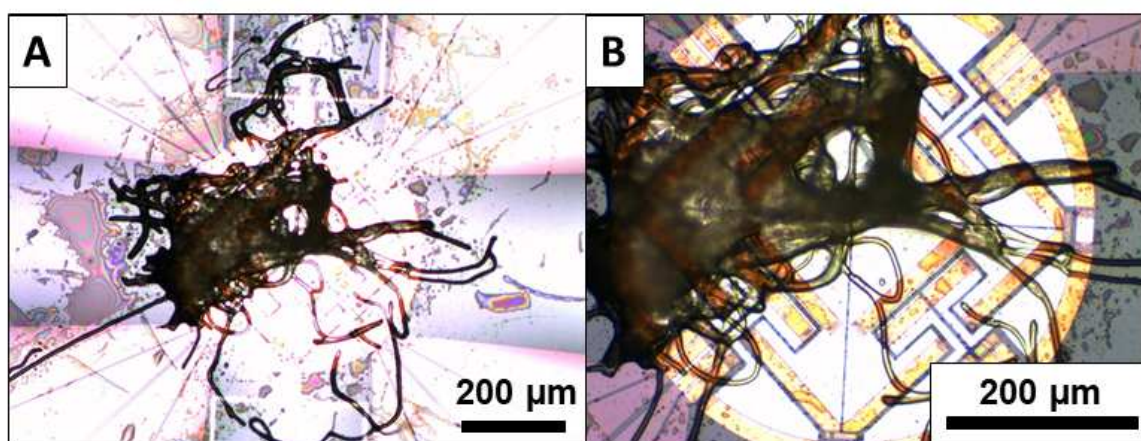


**Figure 2.7:** Image of elctropsun fibers manually deposited on sensor with silicone oil at 50x total magnification (**A**) and 100x total magnification (**B**). Getting fibers completely on top of the sensor is challenging as they move and spread out. The dark color of the fiber and oil indicates that the mass of material on top of the sensor is quite thick.

The next approach involved mounting the UFSC1 chip sensors on the rotating counter electrode collector. This sample preparation technique was informed by similar approaches used to vapor deposit [38] or spin coat directly onto the chip sensors where areas of the membrane sensor and reference side are masked off. The approach developed here was to prepare a sugar and water solution and deposit a droplet on top of the sensor on the reference side and allowed to dry. This results in small dome of solid sugar covering the sensor which can easily be rinsed off at the last stage of sample preparation. Once a batch of sensors has had their reference sensors covered

they are affixed to the rotating counter electrode. It is important that they are well adhered to the wheel using conductive tape. The rotation speed should be slowly brought up to 2000 rpm to prevent an accidental, violent ejection of a chip sensor. The sensor leads (part #3 in **Figure 2.6B**) and sensor support membrane are tolerant of the spinning process and no samples were damaged when care was taken to ensure all sensors were affixed to the drum.

Electrospinning is performed as described in the previous section. It was found that polymers such as PVA could be spun directly onto the sensor, although the fiber alignment was noticeably poorer across the sensor as compared to the neat aluminum foil. Polymers such as polybutylene terephthalate, PA6, and polyethylene terephthalate were found to be difficult to deposit on the sensors. During electrospinning, these fibers will crash into sensor leads (part #3 in **Figure 2.6B**) and bridge across them, preventing them making effective contact with the sensor. Attempting to cut these fibers loose and lowering them onto the sensor does not do an effective job of adhering to the sensor. For select polymers, where experiments do not rely on having highly aligned fibers, it is possible to directly electrospin onto the sensor.

Following electrospinning the entire chip is covered in nanofibers as seen in **Figure 2.8A**. A few droplets of a solution of deionized water with a small amount of ethanol is deposited on the reference side of the sensor. Within a few seconds the sugar coating is dissolved. Once dissolved the excess solution is pipetted off the reference side of the sensor and this effectively removes the fibers without disturbing the fibers deposited on the sample side, the cleaned reference sensor is seen in **Figure 2.8B**. To ensure the reference side is thoroughly cleaned it is rinsed several times with the water ethanol solution and allowed to dry before the chip sensor is loaded into the instrument.

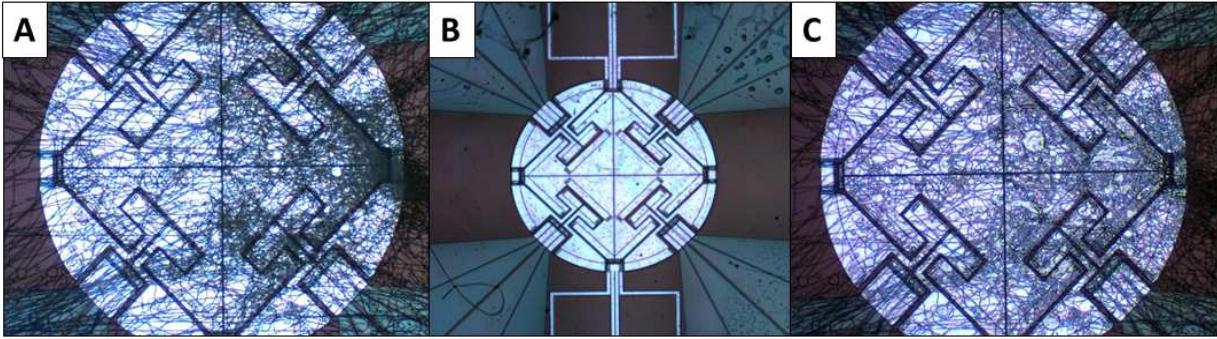


**Figure 2.8:** (A) Direct deposited electrospun PVA on a Mettler Flash UFSC1 sensor. (B) Cleaned reference side following water/ethanol solution rinse. (C) Fibers once melted show effective heating when samples are deposited on the underside of the sensor. The diameter of the silver, circular sensor is 500  $\mu\text{m}$ .

The method of direct spinning allowed for some fast scanning measurements of PVA, but the chip to chip variation was quite high and out of the 8 samples prepared only about half yielded usable data. Poor reproducibility and the inability to control the sample quality necessitated the development of a new method for delivering fibers onto the sensor area. Given that gold leaf is used to enhance sample to sensor contact in fast scanning calorimetry experiments [ref], electrospinning onto gold leaf was attempted. The gold leaf lacked the mechanical stability to serve as the sole substrate to electrospin fibers onto. Once gold leaf is laid flat on a surface it proved to be nearly impossible to remove it in any manner which did not damage the gold leaf or the fibers on top of it. While these methods all failed in so far as they did not provide a means to reliably deposit electrospun fibers spun onto chip sensors, they highlighted the exact challenges that need to be addressed when preparing electrospun fibers for FSC chip sensors.

The inability to transfer a section of bulk tape to the sensor, as shown in **Figure 2.7**, indicates the need for electrospun fibers need to be supported on a substrate. This substrate needs to be more durable than gold leaf yet still thermally and electrically conductive. In addition, the

combination of substrate and fibers needs to be light enough that they do not rupture the membrane when placed on the UFSC1 sensor.

Copper Gildar Extra Fine Bar Grids, 2000M were obtained from Ted Pella, Inc. These tunneling electron microscopy (TEM) grids provide a substrate that is mechanically durable enough to be handled but light enough that they can be cut to size and placed directly on Mettler Toledo UFSC1 chip sensors without damaging the membrane. The TEM grids have a solid region around the outer diameter as seen **Figure 2.9A**. This allows the grids to be affixed to aluminum foil wrapped around the rotating drum counter electrode with thin strips of conductive, copper tape. This hold the grids in place during electrospinning without masking off any of the mesh. There is a notch, as seen in **Figure 2.9B**, at the top of each grid which allows for alignment along the center of the drum as shown in **Figure 2.9C**. The drum is set rotating and fibers are electrospun for a preset spin time,  $t_{spin}$ . After electrospinning the aluminum foil can be removed by carefully unwrapping the drum leaving the fibers and grids undisturbed as seen in **Figure 2.9D**.

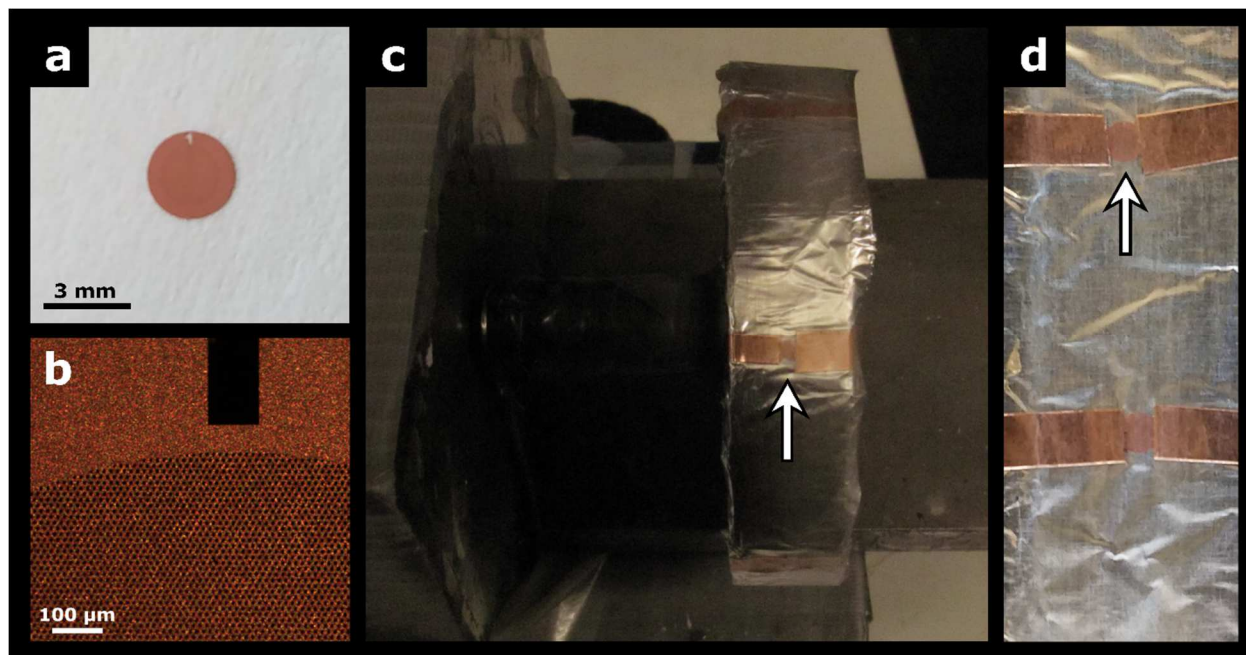


**Figure 2.9:** (A) TEM grid as received. (B) TEM grid through 10x objective, 100x overall magnification. The notched number “1” allowed for uniform alignment of the grids on the electrospinning drum. (C) TEM grids are aligned along the center of the electrospinning drum as indicated by the white arrow. Fibers are seen to be uniformly distributed across the width of the grid. The width of the foil wheel is approximately 1 inch. (D) Carefully unwrapping the foil from the rotating drum collector does not disturb the fibers or grids. White arrow indicates the TEM grid held in place between the conductive copper tape.

TEM grids loaded with electrospun fibers are easily removed from the aluminum foil by cutting along the taped edges of the TEM grids. The grids are transferred to clean glass slides where they can be cut to size before being loaded onto Mettler UFSC1 chip sensors. Using a fresh stainless steel surgical scalpel under 2-10x magnification, the copper ESPET loaded grids can be hand cut without disturbing the fibers. These grid sections are light enough that they can be lifted with a fine wire typical for fast scanning calorimetry (FSC) sample preparation and loaded onto the chip sensor.

Electrospun PET (ESPET) loaded grids were prepared by electrospinning under the conditions listed in section 2.3.0 for  $t_{\text{spin}} = 45$  seconds. Electrospun PVA (ESPVA) loaded grids were prepared under the conditions listed in **Section 2.3.2** for  $t_{\text{spin}} = 4$  minutes.

## **2.5 Stabilization and Coating of PVA Nanofibers (Ch. 7.1.2)**

For electrospun PVA fibers to serve as a viable nervous tissue scaffold they must be brought through a series of sterilization and surface treatments so that neurons can attach to the surface. These treatments require that fibers be rinsed in buffer and then soaked for 12-24 hours in various solutions of amino acids, proteins, and growth factors. While semi crystalline PVA is water soluble above the glass transition temperature, amorphous PVA or PVA with very low mass fraction crystallinity will dissolve in water at room temperature.

The first step in creating a tissue scaffold is to stabilize the electrospun PVA such that it does not dissolve in water. This was attempted in one of two ways, although only one of them was found to be successful. The first attempt involved chemically cross-linking PVA by exposing PVA to glutaraldehyde [36, 39, 40]. Glutaraldehyde, 50% aq., was obtained from Aldrich. The second approach was to isothermally cold crystallize the PVA fibers by heating to 150 °C and holding isothermally for 15 minutes [41, 42].

When electrospun from an acidic solution PVA can react with glutaraldehyde vapors. The acetal groups at each end of the symmetric glutaraldehyde react with the hydroxyl groups along the PVA polymer backbone and forms a hydrocarbon bridge between adjacent molecules [ref]. PVA fibers electrospun from the 98/2 deionized water/ acetic acid solution as outlined in **Section 2.3.1** were exposed to glutaraldehyde for several hours in an attempt to cross link the fibers to

prevent the fibers from dissolving when placed in water. Exposure was carried out by filling the bottom of a desiccator with glutaraldehyde and suspending fibers approximately 5 cm above the fluid and placing the lid over the desiccator. Exposure for times up to 48 hours did not show any signs of effectively crosslinking PVA and the fibers still dissolved in water.

Heat treatments have been shown to be effective in preventing PVA from dissolving at temperatures below its glass transition [41]. Sections of PVA fiber were heated to 150 °C and held isothermally for 15 minutes which crystallized PVA and prevented it from dissolving in water. Crystallized regions within the fibers effectively behave as staples which prevent the amorphous phase material from dissolving when exposed to water. After the fiber mats were crystallized samples were cut out using a #12 biopsy punch, manufactured by Acuderm, Inc., and placed in standard Falcon™ cell culture 24 well plates, an example of this can be seen in **Figure 2.10**. Because the sterilization protocol for plating with tissues involves rinsing the fiber mats with buffer solutions the mats are weighted down and held in place with FDA grade Viton™ rubber O-rings (Ø 12.7 mm) obtained from McMaster Carr.

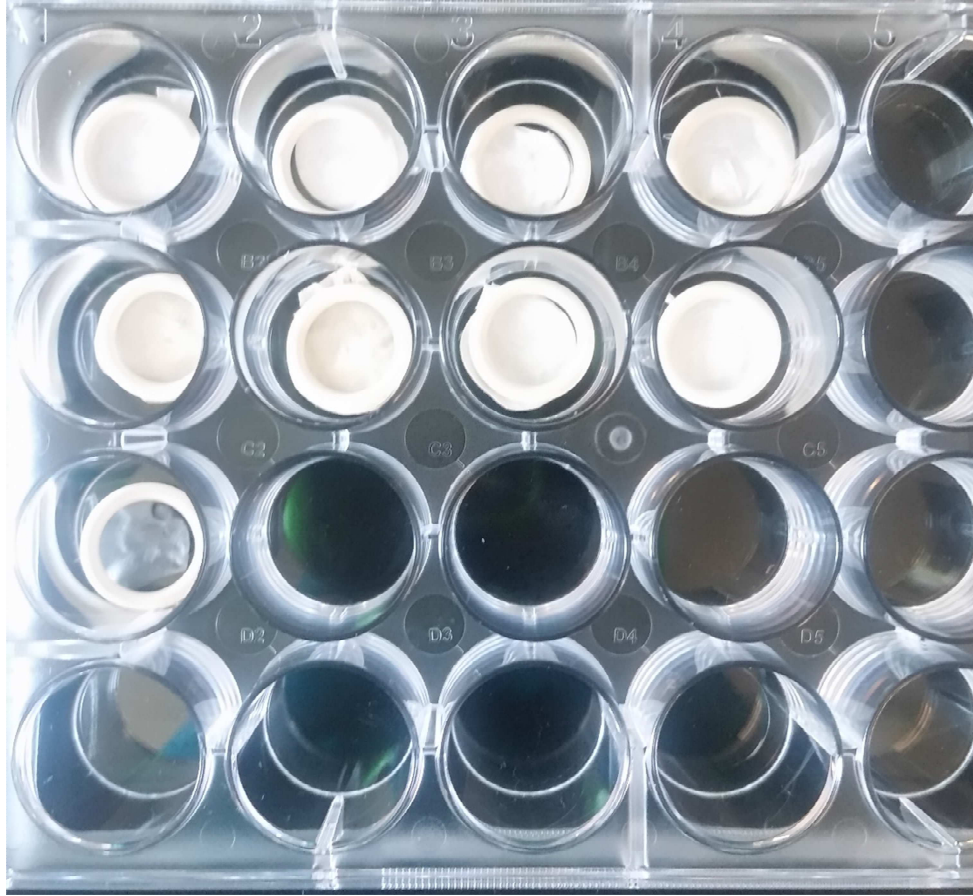


**Figure 2.10:** Thermally stabilized fibers are placed in the bottom of standard 24-well tissue culture plates and weighted down with FDA grade Viton™ rubber O-rings to prevent them from moving during sterilization, coating, and tissue plating. In this image, 9 wells contain fiber mats.

Poly-D-Lysine hydrobromide (PDL), mol wt. 70,000 – 150,000, was obtained as a lyophilized powder from Sigma-Aldrich. Laminin from EHS basement membranes, 1-2mg/mL in Tris buffered NaCl, was obtained from Sigma-Aldrich. Fibronectin, from rat plasma, was obtained in powdered form from Sigma-Aldrich. PDL was dissolved in standard phosphate buffered saline (PBS) at 0.1 mg/mL. Laminin was dissolved in PBS at 20 µg/mL and Fibronectin was dissolved in PBS at 50 µg/mL.

Following the rinse and sterilization protocol performed on the fibers they were soaked for 1 hour in PDL. The PDL solution is aspirated off and the fibers are rinsed again in PBS. Four groups of fibers are prepared for nerve scaffold testing. The first group received only the PDL coating. The second group was soaked in the fibronectin solution for 16 hours. The third group was soaked in laminin for 16 hours. The final group was soaked both fibronectin and laminin for 16 hours. Once coated, all samples were plated with rat neurons and solutions of growth factor, antibiotics, and PBS were added and the well plates were incubated for 12-36 hours.

## ***2.6 Electrospun Fiber Sample Preparation for Differential Scanning Calorimetry (Ch.6-7)***

Once heated above the glass transition electrospun fibers will shrink as the polymer chains within the fibers which have been stretched by the rotating counter electrode are able to return to their entropically favored random coil conformation. This results in a net contraction of the fiber mats in the direction(s) of the fiber orientation. While performing calorimetry experiments, maintaining consistent sample to sensor contact is essential. Techniques for preparing DSC samples from electrospun fibers were developed by previous group members [33] and were shown to be highly successful in yielding reproducible fiber data despite fiber contraction. By rolling along the fiber direction any contraction within the fiber mat will result in a tightening of the roll without causing sections of the sample to lose contact with the sensor. When the fiber roll is placed in the pan with the roll axis parallel to the bottom pan it is referred to as the *fixed-end* (FXE) orientation. When the roll axis is perpendicular to the bottom of the pan it is referred to as the *standard* (STD) orientation. [33] A diagram of this, reproduced from literature, is shown in **Figure 2.11**.

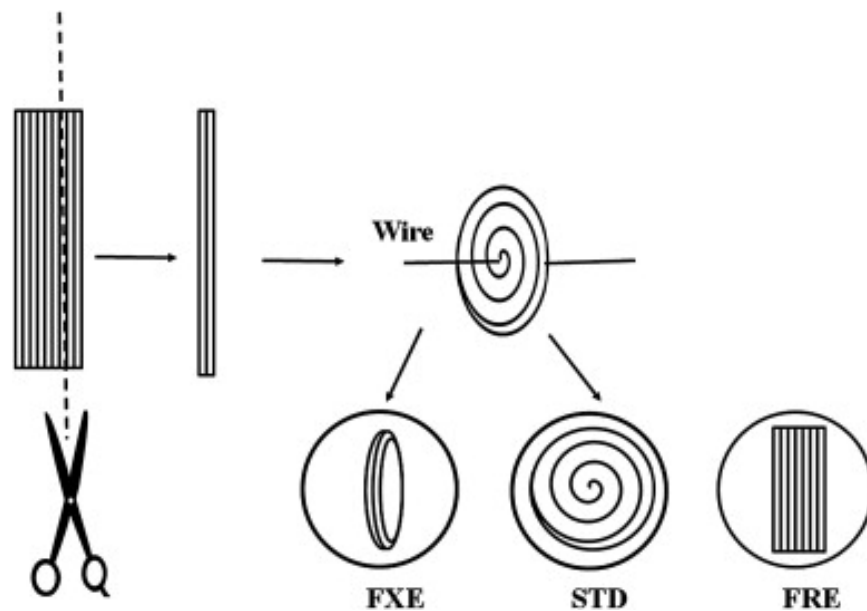


**Figure 2.11:** Example of how electrospun fibers are prepared for standard DSC experiments. **(Left)** Fibers are cut from the bulk tape and then rolled around a wire or the tip of a pair of tweezers. **(Right)** Rolled fibers are placed into DSC pans with the roll axis either parallel to the bottom of the pan (FXE) or perpendicular to the bottom of the pan (STD). Fibers placed loosely in the pan (FRE) can have poor sample to sensor contact as they contract during heating. Reproduced from [33]

The *free-end* method (FRE) is the basic method for preparing DSC samples from electrospun fibers. This involves placing the fibers freely in the DSC pan and loosely sealing the lid over the pan and sample with hand pressure [33]. This allows the fibers to contract freely by the relaxation of polymer chains within the fiber. The DSC used in our lab requires that sample masses greater than 1.5 mg to ensure high signal to noise ratio. Because of the low density of electrospun fibers, one or more layers of electrospun fibers are often required to obtain a sample of sufficient mass. This poses a challenge unique to the free-end method in that, as the bottom layer of fibers is heated and begins to contract, it can prevent uniform sample to sensor contact throughout the pan which leads to various thermal gradients which prevents high quality scans.

Previous work demonstrated that the STD and FXE orientations leads to high quality, reproducible data [33]. Unless otherwise stated, DSC samples prepared from both the bulk PET and PVA fiber mats were prepared in the FXE orientation.

## **2.7 Bulk PET Prepared for Symmetry Correction**

Semi-crystalline pellets of polyethylene terephthalate (PET), with inherent viscosity 0.58, were obtained from Scientific Polymer Products, Inc. In order to create samples of bulk PET small enough to be placed on UFSC1 chip sensors the pellets were filed down with a steel nail file over a glass slide. This resulted in a pile of flakes of various sizes, the smallest of which were ideal for being placed on the sensor. There is no processing of PET necessary with this approach and PET is tolerant of being heated and held above its equilibrium melting point.

## **2.8 References**

- [1] B. Fillon, B. Lotz, A. Thierry, J.C. Wittmann, Self-Nucleation and Enhanced Nucleation of Polymers – Definition of a Convenient Calorimetric Efficiency Scale and Evaluation of Nucleating Additives in Isotactic Polypropylene (Alpha-Phase) *Journal of Polymer Science Part B-Polymer Physics* 31(10) (1993) 1395-1405.
- [2] B. Fillon, J.C. Wittmann, B. Lotz, A. Thierry, Self-Nucleation and Recrystallization of Isotactic Polypropylene (Alpha-Phase) Investigated by Differential Scanning Calorimetry *Journal of Polymer Science Part B-Polymer Physics* 31(10) (1993) 1383-1393.
- [3] B. Fillon, A. Thierry, J.C. Wittmann, B. Lotz, Self-Nucleation and Recrystallization of Polymers – Isotactic Polypropylene, Beta-Phase – Beta-Alpha-Conversion and Beta-Alpha-

Growth Transitions, *Journal of Polymer Science Part B-Polymer Physics* 31(10) (1993) 1407-1424.

[4] B. Wunderlich, CHAPTER IX - Irreversible Melting, *Macromolecular Physics*, Academic Press, San Diego, 1980, pp. 128-253.

[5] B. Wunderlich, CHAPTER VIII - Equilibrium Melting, *Macromolecular Physics*, Academic Press, San Diego, 1980, pp. 1-127.

[6] B. Wunderlich, *Thermal Analysis Tools, Thermal Analysis of Polymeric Materials*, Springer Berlin Heidelberg, Berlin, Heidelberg, 2005, pp. 279-454.

[7] V.B.F. Mathot, *Calorimetry and Thermal Analysis of Polymers*, Hanser/ Gardner Publications, Cincinnati, Ohio, 1994.

[8] C.P. Li, T.T. Hou, X.D. She, X.Y. Wei, F.H. She, W.M. Gao, L.X. Kong, Decomposition properties of PVA/graphene composites during melting-crystallization, *Polymer Degradation and Stability* 119 (2015) 178-189.

[9] R.K. Tubbs, Melting point and heat of fusion of poly(vinyl alcohol), *Journal of Polymer Science Part A: General Papers* 3(12) (1965) 4181-4189.

[10] C.P. Li, J. Vongsivut, X.D. She, Y.Z. Li, F.H. She, L.X. Kong, New insight into non-isothermal crystallization of PVA-graphene composites, *Physical Chemistry Chemical Physics* 16(40) (2014) 22145-22158.

[11] D. Thomas, P. Cebe, Self-nucleation and crystallization of polyvinyl alcohol, *Journal of Thermal Analysis and Calorimetry* 127(1) (2017) 885-894.

[12] C.P. Li, T.T. Hou, J. Vongsivut, Y.Z. Li, X.D. She, F.H. She, W.M. Gao, L.X. Kong, Simultaneous crystallization and decomposition of PVA/MMT composites during non-isothermal process, *Thermochimica Acta* 618 (2015) 26-35.

- [13] B.J. Holland, J.N. Hay, The thermal degradation of poly(vinyl alcohol), *Polymer* 42(16) (2001) 6775-6783.
- [14] M. Pyda, Polyvinyl Alcohol (PVA) Heat Capacity, Enthalpy, Entropy, Gibbs Energy, 2014. [http://materials.springer.com/polymerthermodynamics/docs/athas\\_0147](http://materials.springer.com/polymerthermodynamics/docs/athas_0147). (Accessed 27-10-2015 2015).
- [15] E. Zhuravlev, C. Schick, Fast scanning power compensated differential scanning nano-calorimeter: 1. The device, *Thermochimica Acta* 505(1-2) (2010) 1-13.
- [16] E. Zhuravlev, C. Schick, Fast scanning power compensated differential scanning nano-calorimeter: 2. Heat capacity analysis, *Thermochimica Acta* 505(1-2) (2010) 14-21.
- [17] C.J. Thompson, G.G. Chase, A.L. Yarin, D.H. Reneker, Effects of parameters on nanofiber diameter determined from electrospinning model, *Polymer* 48(23) (2007) 6913-6922.
- [18] M.M. Hohman, M. Shin, G. Rutledge, M.P. Brenner, Electrospinning and electrically forced jets. I. Stability theory, *Physics of Fluids* 13(8) (2001) 2201-2220.
- [19] T. Subbiah, G.S. Bhat, R.W. Tock, S. Parameswaran, S.S. Ramkumar, Electrospinning of nanofibers, *Journal of Applied Polymer Science* 96(2) (2005) 557-569.
- [20] S. Mazinani, A. Ajji, C. Dubois, Fundamental study of crystallization, orientation, and electrical conductivity of electrospun PET/carbon nanotube nanofibers, *Journal of Polymer Science Part B: Polymer Physics* 48(19) (2010) 2052-2064.
- [21] W.E. Teo, S. Ramakrishna, A review on electrospinning design and nanofibre assemblies, *Nanotechnology* 17(14) (2006) R89.

- [22] Z.-M. Huang, Y.Z. Zhang, M. Kotaki, S. Ramakrishna, A review on polymer nanofibers by electrospinning and their applications in nanocomposites, *Composites Science and Technology* 63(15) (2003) 2223-2253.
- [23] R. Goyal, L.K. Macri, H.M. Kaplan, J. Kohn, Nanoparticles and nanofibers for topical drug delivery, *Journal of Controlled Release* 240 (2016) 77-92.
- [24] S.N. Alhosseini, F. Moztarzadeh, M. Mozafari, S. Asgari, M. Dodel, A. Samadikuchaksaraei, S. Kargozar, N. Jalali, Synthesis and characterization of electrospun polyvinyl alcohol nanofibrous scaffolds modified by blending with chitosan for neural tissue engineering, *Int. J. Nanomed.* 7 (2012) 25-34.
- [25] L. Binan, C. Tendey, G. De Crescenzo, R. El Ayoubi, A. Ajji, M. Jolicoeur, Differentiation of neuronal stem cells into motor neurons using electrospun poly-L-lactic acid/gelatin scaffold, *Biomaterials* 35(2) (2014) 664-674.
- [26] J.L. Bourke, H.A. Coleman, V. Pham, J.S. Forsythe, H.C. Parkinson, Neuronal Electrophysiological Function and Control of Neurite Outgrowth on Electrospun Polymer Nanofibers Are Cell Type Dependent, *Tissue Eng. Part A* 20(5-6) (2014) 1089-1095.
- [27] B. Carlberg, M.Z. Axell, U. Nannmark, J. Liu, H.G. Kuhn, Electrospun polyurethane scaffolds for proliferation and neuronal differentiation of human embryonic stem cells, *Biomed. Mater.* 4(4) (2009) 7.
- [28] J.M. Corey, C.C. Gertz, B.S. Wang, L.K. Birrell, S.L. Johnson, D.C. Martin, E.L. Feldman, The design of electrospun PLLA nanofiber scaffolds compatible with serum-free growth of primary motor and sensory neurons, *Acta Biomaterialia* 4(4) (2008) 863-875.

- [29] J.M. Corey, D.Y. Lin, K.B. Mycek, Q. Chen, S. Samuel, E.L. Feldman, D.C. Martin, Aligned electrospun nanofibers specify the direction of dorsal root ganglia neurite growth, *J. Biomed. Mater. Res. Part A* 83A(3) (2007) 636-645.
- [30] F. Huang, Y. Xu, B. Peng, Y. Su, F. Jiang, Y.-L. Hsieh, Q. Wei, Coaxial Electrospun Cellulose-Core Fluoropolymer-Shell Fibrous Membrane from Recycled Cigarette Filter as Separator for High Performance Lithium-Ion Battery, *ACS Sustainable Chemistry & Engineering* 3(5) (2015) 932-940.
- [31] S. Irani, M. Zandi, N. Salamian, S.M. Saeed, M.D. Joupari, S.M. Atyabi, The study of P19 stem cell behavior on aligned oriented electrospun poly(lactic-co-glycolic acid) nanofibers for neural tissue engineering, *Polym. Adv. Technol.* 25(5) (2014) 562-567.
- [32] H. Chen, Z. Liu, P. Cebe, Chain confinement in electrospun nanofibers of PET with carbon nanotubes, *Polymer* 50(3) (2009) 872-880.
- [33] Q. Ma, M. Pyda, B. Mao, P. Cebe, Relationship between the rigid amorphous phase and mesophase in electrospun fibers, *Polymer* 54(10) (2013) 2544-2554.
- [34] S.-P. Rwei, C.-C. Huang, Electrospinning PVA solution-rheology and morphology analyses, *Fibers and Polymers* 13(1) (2012) 44-50.
- [35] N.A. Peppas, P.J. Hansen, Crystallization kinetics of poly(vinyl alcohol), *Journal of Applied Polymer Science* 27(12) (1982) 4787-4797.
- [36] H.S. Mansur, C.M. Sadahira, A.N. Souza, A.A.P. Mansur, FTIR spectroscopy characterization of poly (vinyl alcohol) hydrogel with different hydrolysis degree and chemically crosslinked with glutaraldehyde, *Materials Science and Engineering: C* 28(4) (2008) 539-548.

- [37] I. Mettler Toledo International, Flash DSC 1 — Flash Differential Scanning Calorimeter from METTLER TOLEDO 2017. [http://www.mt.com/us/en/home/library/videos/lab-analytical-instruments/flash\\_dsc1.html](http://www.mt.com/us/en/home/library/videos/lab-analytical-instruments/flash_dsc1.html). (Accessed 6/12/2017 2017).
- [38] D. Bhattacharya, V. Sadtchenko, Enthalpy and high temperature relaxation kinetics of stable vapor-deposited glasses of toluene, *The Journal of Chemical Physics* 141(9) (2014) 094502.
- [39] A.G. Destaye, C.-K. Lin, C.-K. Lee, Glutaraldehyde Vapor Cross-linked Nanofibrous PVA Mat with in Situ Formed Silver Nanoparticles, *ACS Applied Materials & Interfaces* 5(11) (2013) 4745-4752.
- [40] Y. Wang, Y.-L. Hsieh, Crosslinking of polyvinyl alcohol (PVA) fibrous membranes with glutaraldehyde and PEG diacylchloride, *Journal of Applied Polymer Science* 116(6) (2010) 3249-3255.
- [41] M. Miraftab, A.N. Saifullah, A. Çay, Physical stabilisation of electrospun poly(vinyl alcohol) nanofibres: comparative study on methanol and heat-based crosslinking, *J. Mater. Sci.* 50(4) (2015) 1943-1957.
- [42] R.A. Franco, Y.-K. Min, H.-M. Yang, B.-T. Lee, On Stabilization of PVPA/PVA Electrospun Nanofiber Membrane and Its Effect on Material Properties and Biocompatibility, *Journal of Nanomaterials* 2012 (2012) 9.

## ***Chapter 3 Experimental Techniques***

### ***3.0 Theory and Methods***

This chapter serves to introduce the experimental techniques which were used to gain new insights into the bulk properties, microstructure, and fundamental thermal properties of polymers. The first thing an experimenter will encounter when working with commercially available polymers are powders, flakes, pellets, or larger sheets of raw material which must be handled and processed into useable forms. Processing and creation of samples suitable for experiments designed to probe their fundamental properties or create novel materials were outlined in the previous chapter. Here the various experimental techniques employed in probing these polymers are laid out. An overview of each instrument as a physical device built of measuring components and a short summary of the theories which support the measurement and analysis of the data are presented. For each measurement technique, the experimental protocols and methods for experiments performed with that instrument are outlined following the description of the technique. It is my hope this aids readers in understanding why experiments were designed as they were and will allow for smooth reference when the results are discussed in the subsequent chapters.

The introductory chapter laid out the motivation for study of polymers from their fundamental thermal properties and nanoscale structure up to the properties of the polymers in bulk at length scales where we interact with them in our day to day lives. Imaging techniques will be presented first as this is often the starting point of any study where the basic qualities of processed material are qualitatively and quantitatively studied. The techniques which allow structural information, i.e. the arrangement of the polymer molecules within the sample are presented next. The final topics presented in this chapter are the thermal analysis techniques which

provide a wealth of information on polymer phase change kinetics and fundamental material properties.

### ***3.1 Sample Imaging Techniques***

#### ***3.1.1 Polarizing Optical Microscopy (POM)***

Polarized light microscopy couples a standard optical microscope with a polarized light source, typically a linear polarizer where polarization angle can be varied by the operator, and a polarizer between the objective and ocular lenses. The second polarizer is referred to as the analyzer and is typically oriented  $90^\circ$  to the polarizer at the light source. Most modern polarizing light microscopy systems are equipped with cameras which allow for images, frame sequences, and in some systems high speed videos to be collected during experiments. Our lab is equipped with a Nikon Eclipse E600 Polarizing Optical Microscope. A diagram of this type of imaging system and annotated image of the instrument are shown in **Figure 3.1** [1]. It is worth noting that our microscope is not equipped with illuminators allowing for reflection mode imaging.

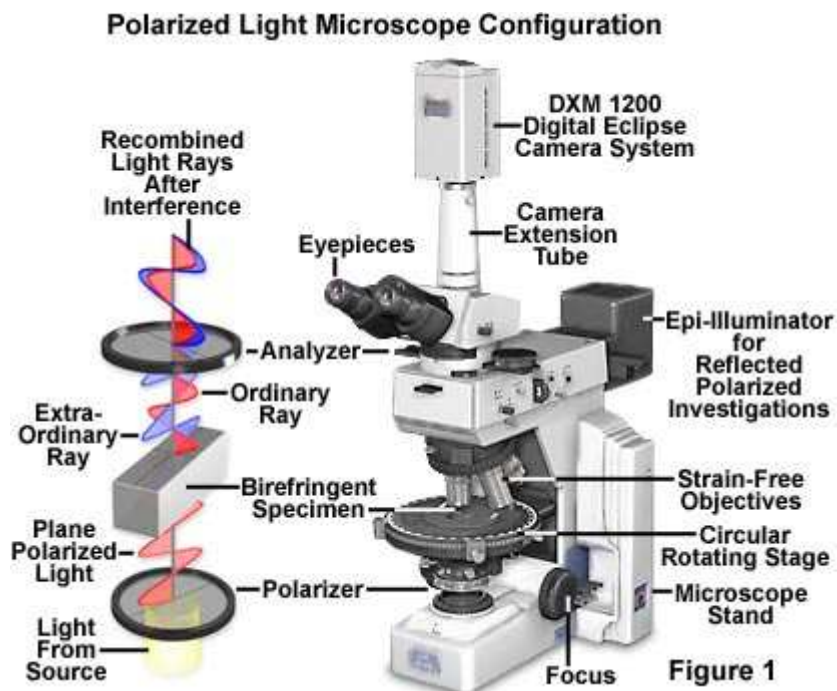


**Figure 3.1:** (Left) Schematic of the basic principle behind polarized light microscopy and (right) an annotated image of the components of our Nikon E600 POL microscope. This image is reproduced from Nikon product literature [1].

When no sample is present, or the sample is optically amorphous (it does not change the polarization state of light passing through) the analyzer will block all incoming light resulting in a black image. In an amorphous polymer, the molecules are randomly aligned which will result in a uniform index of refraction throughout the material. As the material crystallizes there are regions within the sample which have highly ordered molecules (see the description of polymer crystals in **Section 1.X**) resulting in areas within the sample which are birefringent. Birefringence occurs when a material exhibits two or three different, oriented indices of refraction. Birefringence,  $\Delta n$ , where  $n$  is the index of refraction of a material, and is defined, for a uniaxial material, in the following manner:

$$\Delta n = n_e - n_o \quad (3.1)$$

where  $n_e$  is the extraordinary index of refraction and  $n_o$  is the ordinary index of refraction. Along the direction of the extraordinary index of refraction, light moves through the medium at a different speed than in the direction along the ordinary index of refraction. The differences in the speed at which the light propagates through the material result in a phase difference between the ordinary and extraordinary rays from the incident polarized light once light has passed through the sample. This allows some portion of light to pass through the analyzer. In uniaxially birefringent samples the brightness is maximized at  $45^\circ$  to the incident polarization state. This allows for optical tracking of the formation of oriented, or crystalline material within an amorphous sample. A polarizing optical microscope image of polymer spherulites formed the amorphous melt is shown in **Figure 3.2**.

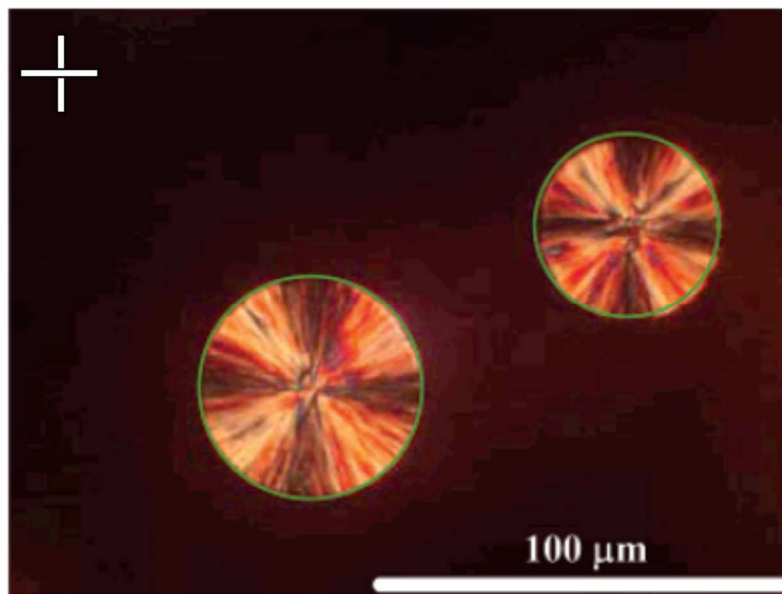


**Figure 3.2:** Polarizing optical microscopy image of melt crystallized polystyrene spherulites. Spherulites are the bright, circular structures highlighted by the green circles. The dark region surrounding the spherulites is the isotropic amorphous melt which appears dark between crossed polarizers, whose fast axes directions are indicated by the white cross in the upper left corner. Image is reproduced from literature [2].

As discussed in **Section 1.3.2** a polymer spherulite forms out of radially oriented lamellar sheets. These lamellar sheets result in the birefringence previously described. Moving in a circular path around the spherulite, bright and dark radial bands are seen. The dark bands (called the “Maltese cross”) are the result of birefringent regions which result in phase shifts aligned with the incident polarized light. The bright bands are regions where the transmitted light has been phase shifted such that it passes through the analyzer. Because spherulites are circularly symmetric there is one bright band per quadrant.

Beyond the polymer structure insights which can be gained using polarizing optical microscopes the the high-resolution cameras they are equipped with and varied magnifications accessible are useful for collecting images of samples used in fast scanning calorimetry experiments. Images of sensors loaded with samples as outlined in **Section 2.2.1** were collected with an Olympus BX41 microscope with 10x ocular magnification and DCM 510 camera. Images were collected with 5x, 10x, and 50x objectives. These images were collected in reflection mode with no analyzer as only magnified optical images of the samples on the membranes were needed.

These imaging systems allow for the measurements of polymer structures at 100-500x which corresponds to micron scale features.

### ***3.1.2 Scanning Electron Microscopy (SEM)***

When resolution down to nanometer scale features is necessary, optical microscopes are abandoned in favor of scanning electron microscopes (SEM). Electron microscopes focus a beam of high-energy electrons and scans across the surface sample. Just as an optical microscope uses lenses to focus light the SEM uses electromagnets to focus an electron beam. This allows for precise control over the focus allowing for high resolution images of sample surfaces over many

magnifications ranging from 20X up to 20,000X. The typical components of an SEM are shown in the schematic image in **Figure 3.3**. The typical components of an SEM are an electron gun which is collimated into a beam by an anode and then focused towards the sample by a series of electromagnetic lenses. Following the optics of the electron microscope there is a series of detectors which measure the signals generated by the interactions of the incident electrons and the sample. Nearly all scanning electron microscopes have a detector to measure the secondary electrons, or the electrons produced by inelastic scattering. These electrons provide topographical information about the specimen being imaged. Additionally, SEMs can be equipped with detectors for back scattered electrons, X-rays, and photons emitted by cathode luminescence.

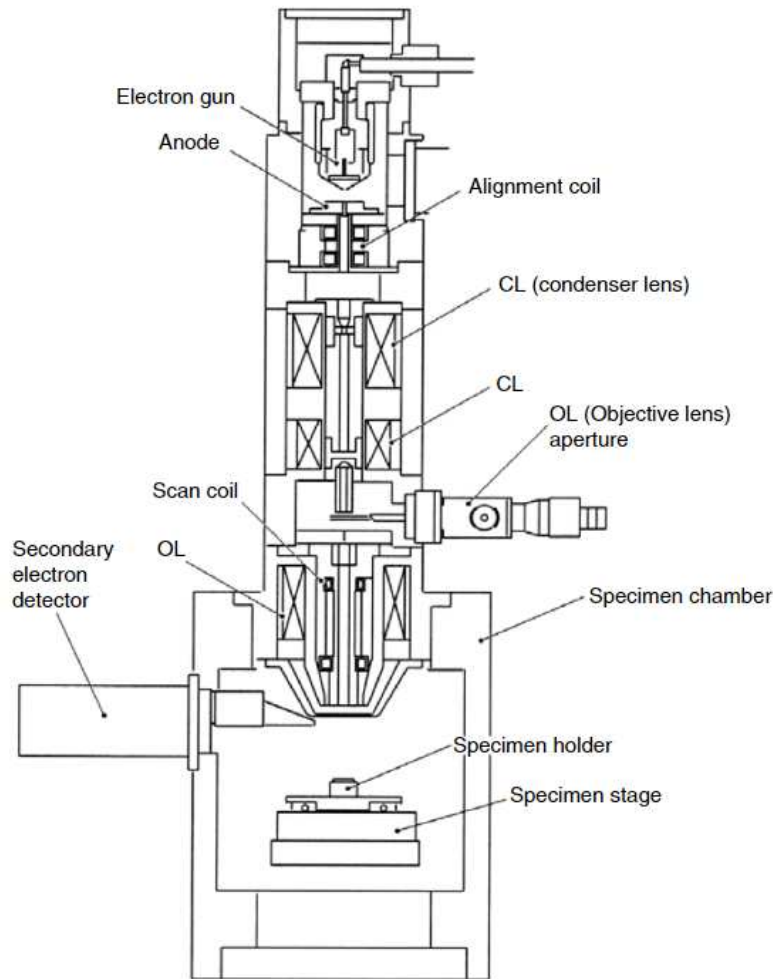


**Figure 3.3:** Schematic diagram of the components in a typical scanning electron microscope reproduced from [3]. The anode and alignment coil serve to collimate the electrons which are further focused by the condenser lens (CL) and the objective lens (OL). The entire system is under vacuum, typically in the range of 1-2 mb for tabletop SEM units. Secondary electrons which are emitted from the sample surface are recorded by the secondary electron detector. Additional components are added to detect backscattered electrons, X-rays, and photons emitted via cathode luminescence.

The electrons which collide with the sample are high in kinetic energy which will produce a variety of signals as the energy from the collision is dissipated by interactions with the solid sample surface. These interactions will result in the emission of: secondary electrons, backscattered electrons, characteristic X-rays, and photons by cathode luminescence. Secondary

electrons are emitted from very near the surface of the sample, usually within the first few nanometers, and provide the primary topographical information about the sample. Back scattered electrons, X-rays, and cathode luminescence are all produced from deeper within the sample. Back scattered electrons are the result of elastic scattering off of electrons within the sample. X-rays are emitted when the incident electron beam causes electrons from the sample to be ejected which are replaced by the high energy electrons from the beam. This results in the emission of X-rays as these electrons return to a lower energy state. The sample and all SEM components are typically operated under vacuum.

The back scattered electrons are useful for chemical analysis of specimens in the microscope as the intensity of these electrons is strongly correlated with the atomic number of the source. The characteristic X-rays are primarily used to identify the exact composition and measure the abundance of various elements within a sample.

Non-conductive samples must be coated in a thin layer of a conductive metal to prevent the buildup of charge on the surface. Any charge build up will obscure the detection of secondary electrons creating artifacts in the final image. Additionally, samples must be in the solid state or high viscosity liquid that will tolerate a high vacuum. Typical sample preparation involves sputter coating the samples in a thin layer of electrically and thermally conductive metal a few nanometers thick. This thin layer makes the surface of the samples electrically conductive and grounds the sample preventing charge build up. A secondary benefit of the sputter coating is that it increases the thermal conductivity of the surface of the material and prevents/ minimizes thermal expansion of the material which is particularly important when studying polymeric materials.

Samples presented in this work were sputter coated for times between 30 and 120 seconds under low vacuum using a gold-palladium target. A gold-palladium alloy is used as it provides

much smaller crystalline grain sizes than gold alone. Minimizing the grain size increases the quality of the topographical image obtained as small features are not masked over by the thin layer of metal. A Cressington Model 108 sputter coater (located in Sci-Tech 282) is operated under vacuum at 0.08 mb and sputtering is performed at 30 mA for times between 30 and 120 seconds.

Three scanning electron microscopes were used to image samples. The majority of fiber samples were imaged on a Phenom G2 Pure Tabletop SEM (owned and managed by Prof. Asetekin) and the Phenom G1 Tabletop SEM (partly owned by Prof. Cebe). The Phenom G1 and G2 SEMs are nearly identical, with the G2 being a slightly newer model of the same type as the G1. This SEM allows for magnification up to 15,000x which resolves features down to approximately 10 nm. Polyvinyl alcohol fiber mats used for the neural scaffold experiments were imaged using a Zeiss EVO MA10 Scanning Electron Microscope (owned and managed by Prof. Kaplan, located at 200 Boston Ave.). Electrospun fibers required various sputter coating times. It is often the case with electrospun fibers, which are hundreds of nanometers thick but many microns long, that they become heated by the electron beam. Small amounts of thermal expansion in these fibers translates to large movements within the field of view of the SEM. When fibers were observed to wiggle around under the field of view samples were ejected and sputter coated in 10 second increments until they remained still during imaging. Because fibers in the mats are loosely attached to one another and to the substrate it is essential that they are hit with small amount of compressed air prior to sputter coating and imaging. This removes any loose fibers which can get pulled up into the instruments when the sample is introduced to the vacuum.

Examples of images collected with each electron microscope are shown in **Figure 3.4**. **Figure 3.4A** shows an image collected with the Zeiss SEM (located at 200 Boston Ave). The Zeiss SEM is capable of obtaining high resolution images however the electron beam intensity in this

instrument must be carefully tuned for fiber samples as prolonged exposure damages the fibers and sputter coating reducing the image quality. During imaging the Zeiss takes a series of line averages across the sample and for publication quality images this process takes approximately 60 seconds. The Phenom G1 SEM (located in Sci-Tech room 219) and Phenom G2 Pure (located in Sci-Tech room 282) do not have the same high resolution imaging capacity that Zeiss does, but the images produced are publication quality and can be collected in less than 5 seconds. The high-speed operation and lack of sample damage made the Phenom SEM the instrument of choice for data collection.

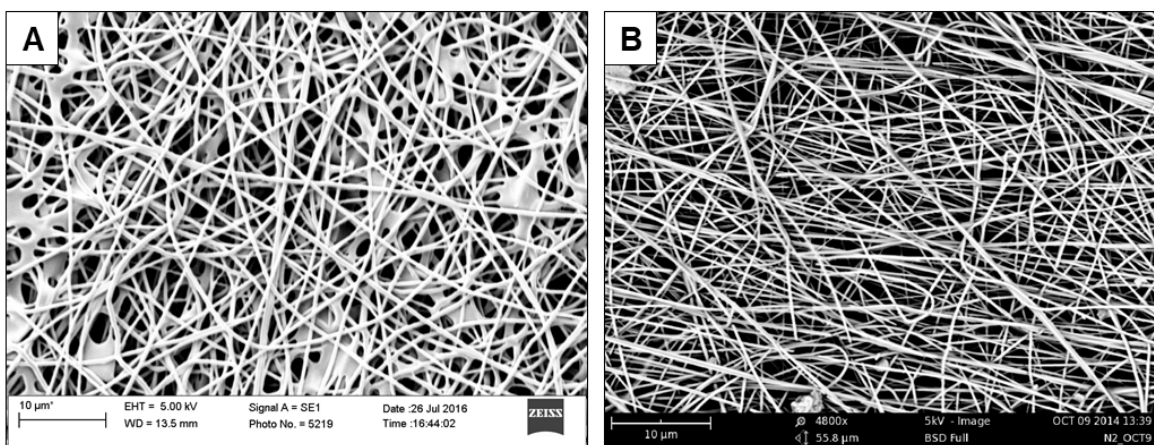


**Figure 3.4:** Example SEM micrographs of polyvinyl alcohol (PVA) fiber mats obtained with (A) Zeiss EVO MA10 SEM, and (B) Phenom G2 Pure Tabletop SEM. Differences in the fiber morphology are due to differences in the electrospinning conditions. Image quality and feature resolution are comparable at 4800x-5300x between the two instruments.

Images were analyzed using the open source software, ImageJ [4] equipped with analysis programs specifically designed for quantitative image analysis of fibers. The program DiameterJ [4] was used to obtain quantitative fiber diameters along all fiber segments in the image. This is accomplished by defining a contrast window for the image that allows for complete separation of fibers and their background. Fiber direction is measured and the image is segmented perpendicular

to each fiber direction detected. The output is a set of data tables which contain the frequency of each fiber diameter measured and this allows for diameter probability distributions to be calculated. It is worth noting that the distribution, Fiji [4], is ImageJ bundled with the many plugins, including DiameterJ.

### **3.2 *Structural Analysis Techniques***

The techniques presented in the previous section provide a means of investigating the mesoscale down to the microscale structure and properties of polymer samples. While SEM can resolve down to a few nanometers it does not allow for the investigation of the molecular scale structure of polymers which can often be tuned by processing, additives, and thermal treatments. Two techniques which are widely used to investigate the molecular scale structure and track structural changes due to different sample treatments are Infrared Spectroscopy (IR) and X-ray Scattering.

#### **3.2.1 *Fourier Transform Infrared Spectroscopy (FTIR)***

The general technique of infrared spectroscopy (IR) is used for the identification and characterization of the composition of given material and is a widely-used tool in the analysis of polymeric materials [5]. This instrument measures the differences in frequencies between the energy levels of photons absorbed by a molecule. Tracking the absorption of photons allows for the quantitative and qualitative analysis of polymers and yields insights into not only the chemical components of the polymer but also the conformational order and orientation of the molecules [6].

The basis behind infrared spectroscopy is that a polymer molecule can be viewed as nearly independently vibrating atomic groups within the larger molecule [7]. Infrared radiation is absorbed by the various atomic bonds within the material and this absorption is independent of the other bonds present as each bond will absorb different wavelengths of infrared radiation. Polymer chains have periodic structure as discussed in **Section 1.X** and this allows for vibrational analysis of entire polymer molecule. In addition to the specific chemical bond, the frequency of absorbed radiation corresponds to the type of vibrations [8]. For simplicity, these vibrations are shown for the case of methylene ( $\text{CH}_2$ ) in **Figure 3.5**

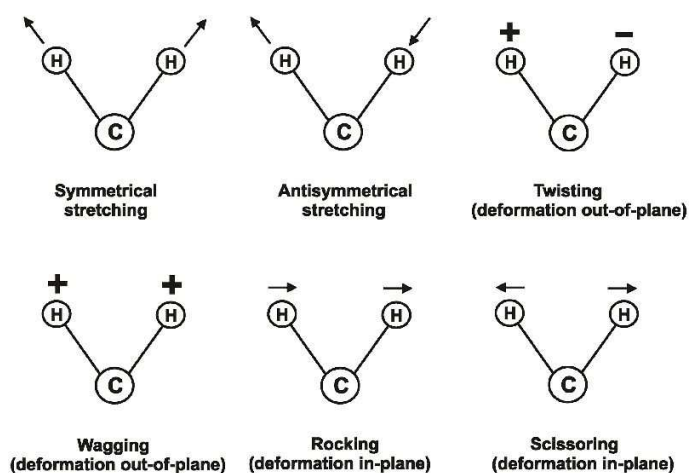


**Figure 3.5:** The various vibrational modes possible when a methylene molecule absorbs infrared radiation. Figure reproduced from [8]. + indicates rotations out of the page and – indicates rotation into the page.

Experimentally speaking it is only possible to measure the absorbance of sample,  $A$ , which is proportional to the radiation transmitted according to Beer’s Law [7]:

$$A = -\log(I/I_0) \tag{3.2a}$$

$$A = \sum_{i=1}^N \epsilon_i c_i l \tag{3.2b}$$

where  $I$  is the intensity of light which is transmitted and  $I_0$  is intensity of incident light. The absorbance is the sum over the concentration of attenuating species,  $c_i$ , weighted by the absorptivity of the species,  $\epsilon_i$ , over the path length of the radiation through the material,  $l$  [7]. For samples of finite thickness,  $dx$ , the sample will absorb a total fraction of photons,  $dI_x$ .

$$dI_x/I_x = -\alpha c dx \quad (3.3)$$

where  $\alpha$  is the absorption coefficient defined to be  $\alpha = \epsilon \ln(10)$ , with  $\epsilon$  being the total absorptivity of the sample. If the finite thickness ranges from  $x = 0$  to  $x = l$ , where  $l$  is the path length (sample thickness for thin samples), then:

$$\ln(I_0) - \ln(I) = \alpha l c \quad (3.4a)$$

Defining the transmittance,  $T$ , to be the ratio of  $I/I_0$  then:

$$T = e^{-\alpha l c} \quad (3.4b)$$

This allows the transmittance given by Eqn. 3.4b to be written in terms of total sample absorptivity, thickness, and total concentration of absorbing species.

$$T = 10^{-A} \quad (3.5)$$

The relationship in Eqn. 3.5 allows for conversion between absorbance and transmittance spectra and comparison of data collected between measurement modes. Experimentally, these measurements are made possible by using a Michelson Interferometer equipped with a moving mirror and multichromatic infrared source. A schematic of this is shown in **Figure 3.6A**. Collimated light from the source is directed at a partially reflective beam splitter where half of the intensity is reflected to the stationary mirror. The other half of the beam is directed at the moving mirror (perpendicular to the stationary mirror). Once reflected these beams are recombined by the beam splitter and directed towards a detector. The intensity of the beam is recorded as a function

of the position of the moving mirror resulting in an interferogram, an example of which is shown in **Figure 3.6B**.

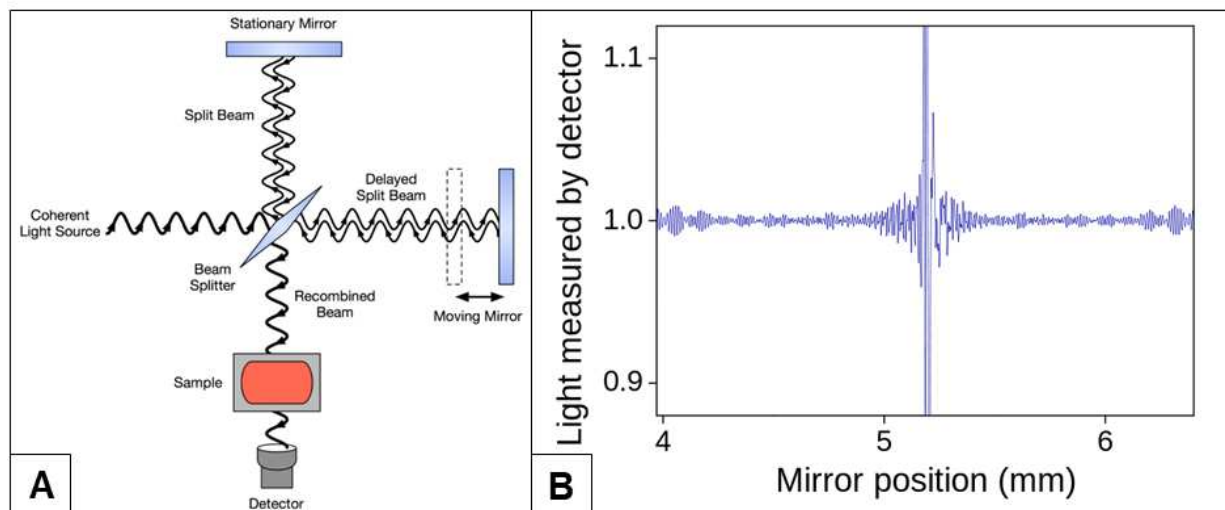


**Figure 3.6:** (A) Michelson interferometer used inside a typical FTIR instrument reproduced from [9]. (B) Example of the baseline interferogram for an ideal system when no sample is present reproduced from [10]. The large peak in the center of the plot is the reference position at zero optical path difference.

If the mirrors are equidistant from the beam splitter the optical path difference will be zero resulting in constructive interference. This is set as the reference point for the moving mirror. Displacements in the mirror from this point result in differences in the optical path length and result in interference patterns. In a Fourier Transform Infrared Spectrometer (FTIR) the intensity vs. mirror position interferogram is Fourier transformed by the computer running the instrument resulting in an absorption spectrum which is a function of frequency.

Background measurements are first made by collecting absorption spectra with the instrument as shown in **Figure 3.6A**. This allows for any background absorption due to the measuring device itself to be subtracted from data collected on samples. When a sample is placed between the source and the beam splitter, drawn as the orange block in **Figure 3.6A**, the sample

will preferentially absorb infrared radiation at frequencies corresponding to the various vibrations (shown in **Figure 3.5**) of each chemical group within the molecule.

A Jasco FT/IR – 6200 Fourier Transform Infrared Spectrometer was used in attenuated total reflection (ATR) mode to obtain the absorption spectra of the polyvinyl alcohol (PVA) and polyethylene terephthalate (PET) electrospun fibers for both the as spun fibers and following various thermal treatments. Because the electrospun fiber mats are thin, ATR mode was sufficient to obtain high signal to noise ratio.

Attenuated total reflection is achieved by placing the sample in contact with ZnSe crystal. ATR mode relies on the change in the total internal reflection of the infrared radiation within the ZnSe crystal as a sample in close contact will absorb energy from the effervescent waves passing through the crystal and attenuate the signal at the detector. This attenuation is due to the various wavelengths of infrared radiation absorbed by the characteristic vibrations shown in **Figure 3.5**. The measurement of the absorbance is made in the manner illustrated in **Figure 3.6**. Background and sample absorbance were measured between  $600\text{ cm}^{-1}$  and  $4000\text{ cm}^{-1}$  in  $0.964\text{ cm}^{-1}$  increments with a spectral resolution of  $4\text{ cm}^{-1}$ . Individual spectra are the result of averaging between 32 scans per sample. Data was collected for analysis using Spectra Manager 2.0 [11] and exported for further analysis using MATLAB [12].

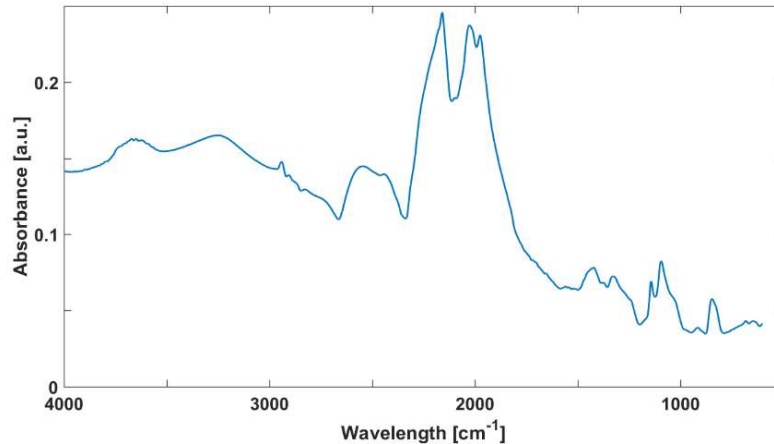


**Figure 3.7:** Example of sample absorbance vs. wavenumber in  $\text{cm}^{-1}$  for a thermally stabilized PVA fiber mat.

If the chemistry of a polymer is known the absorbance spectra can be used to identify the characteristic vibrations of its functional groups. Depending upon the molecular orientation of polymer chains or the functional groups within the polymer these vibrations can change or be frozen out entirely. This makes FTIR a useful tool for determine the presence of crystals within the sample as they will exhibit different molecular vibrations than the amorphous phase material. This is particularly useful in studying polyvinyl alcohol which will readily interact with bound water. The peak observed in **Figure 3.7** between  $3550 \text{ cm}^{-1}$  and  $3200 \text{ cm}^{-1}$  [13] is due to the hydrogen bonding interaction between hydroxyl groups along the polymer backbone. This peak is observed to increase when PVA contains bound water where the water can form hydrogen bonds both to itself and to the hydroxyl groups.

### 3.2.2 *X-Ray Diffraction (XRD)*

X-ray scattering is one of the most powerful tools in studying the structure of materials and is the primary method for studying crystal structure and molecular organization. The wavelength of X-rays ranges between 0.01 and 10 nanometers which allows them to resolve features down to atomic length scales. Typical wavelengths for X-rays used in diffraction measurements are on the order of 0.1 to 1 nanometers. This is the length scale of the interatomic distances within crystals and the interaction between the X-rays and the electrons within crystals. Analyzing the scattering patterns allows for measurements of the crystalline unit cell structure and parameters, long-range ordering within the material, phase changes, and measurements of crystallinity and molecular order.

There are three typical classes of X-ray scattering used. Wide angle X-ray Scattering (WAXS), small angle X-ray Scattering (SAXS), and X-ray powder diffraction (XRD). Theoretically these are identical in terms of the interactions between the X-rays and the material, however there are differences in the detectors and sample to detector distances involved. In WAXS measurements a two-dimensional detector is placed close to the sample so only X-rays scattered to large angles are observed as X-rays diffracted at small angles are obscured by the transmitted beam. In SAXS measurements the two-dimensional detector is placed far from the sample (typically with a vacuum flight path between the sample and detector to prevent any intermediate scattering). Here any X-rays scattered to wide angles do not hit the detector which has a finite radius. Finally, in a powder diffraction system (XRD) a one-dimensional detector is brought across a range of angles ( $5-50^\circ 2\theta$ ). In this case it is nearly impossible to measure orientational order, only the presence of known crystalline reflections and the average intermolecular spacing can be detected.

Because X-ray scattering is a recording of reciprocal space, wide angles correspond to the shortest real space distances and this is useful in making measurements of the unit cell, lattice parameters, intermolecular spacing (d-spacing), and short range molecular ordering. On the other hand, small angle measurements provide a means of measuring long-range order. This is one of the primary methods for measuring the periodicity of polymer crystals, lamellar thickness, and lamellar spacing.

Individual X-rays which scatter off individual electrons within a material do not produce a measurable signal. Instead a beam of monochromatic X-rays is directed at crystalline sample. The periodic order of the crystals allows for the constructive interference of the scattered X-rays and results in diffracted beam which can be measured. This constructive interference is dependent on a periodic geometry. The correlation of the relationship between constructive interference and the geometry is given by Bragg's Law:

$$n\lambda = 2d_{hkl}\sin(\Theta) \quad (3.6)$$

where  $n$  is the order of the reflection,  $\lambda$  is the wavelength of the incident X-rays,  $d$  is the interatomic distance between a given crystallographic plane (d-spacing), and  $\Theta$  is the half scattering angle. A real space schematic of diffraction as described by Bragg's Law is shown in **Figure 3.8**. Bragg's law allows for the determination of the real space d-spacing from the angle between the incident X-ray and the scattered X-rays.

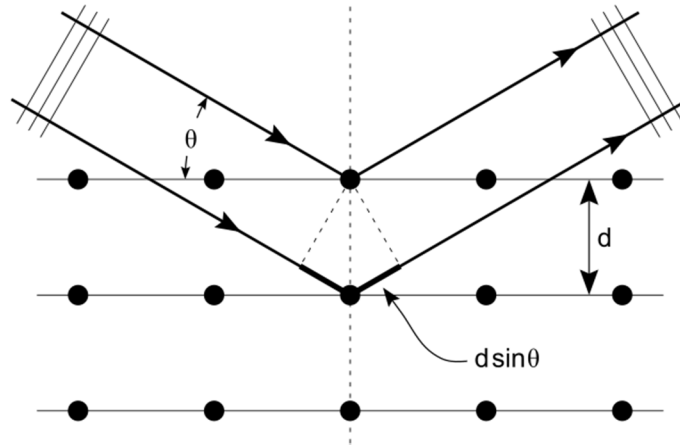


**Figure 3.8:** Bragg's Law for constructive interference of X-rays scattered from a real space lattice. Constructive interference is only observed between atomic planes of spacing,  $d$ , when the path difference between the incident and scattered beam is equal to  $n\lambda$  where  $n$  is an integer. Image is reproduced from [14].

For any possible real space crystal lattice, there exists a corresponding reciprocal space lattice. The reciprocal space lattice is scattering pattern obtained by X-ray diffraction and is related to the real space lattice by Fourier transformation. Modelling the scattering of X-rays off electrons in the lattice as elastic, it is possible to solve for real space parameters from the reciprocal space pattern. When incident X-rays with wavevector  $\mathbf{k}$  (length  $2\pi/\lambda$ ) are scattered, the diffracted X-ray has a wavevector  $\mathbf{k}'$ . Because the scattering is elastic the length of the wavevectors is the same.

The incident X-rays are a coherent beam of electromagnetic radiation which is being scattered by an array of atoms and as a result the phase relationship between scattered waves must be considered since only coherent waves produce constructive interference [15, 16]. The phase difference is given by the following relation:

$$\Phi = (2\pi/\lambda)(\mathbf{k}' - \mathbf{k}) \cdot \mathbf{r} \quad (3.7)$$

where  $(2\pi/\lambda)$  is the path difference,  $\mathbf{k}'$  and  $\mathbf{k}$  are the scattered and incident X-rays, respectively, and  $\mathbf{r}$  is the distance to the detector. The difference between  $\mathbf{k}'$  and  $\mathbf{k}$  is defined to be  $\Delta\mathbf{k}$ .

Constructive interference only occurs when  $\Phi$  is an integer multiple of  $2\pi$ . This requires that the  $(1/\lambda)(\mathbf{k}'-\mathbf{k})\cdot\mathbf{r}$  is equal to an integer,  $n$ . Further, the scattering vector,  $\mathbf{q}$ , is defined to be the difference between the scattered and incident wavevector,  $\Delta\mathbf{k}$ , divided by the wavelength. The magnitude of  $\mathbf{q}$  can be written as:

$$|\mathbf{q}| = 4\pi\sin(\Theta)/\lambda \quad (3.8)$$

Combining this with Bragg's Law (Eqn. 3.6) the d-spacing can be represented as function of the scattering vector. Any scattering vector,  $\mathbf{q}$ , which satisfies the Bragg condition is denoted by the reciprocal lattice vector,  $\mathbf{G}$  [16].

$$d_{hkl} = 2\pi/|\mathbf{q}| \quad (3.9a)$$

$$d_{hkl} = 2\pi/|\mathbf{G}| \quad (3.9b)$$

The geometrical construction of Ewald's sphere is used to determine which sets of crystal planes in a sample will result in diffraction that satisfies Bragg's Law. An example of the Ewald sphere construction is shown in **Figure 3.9**.

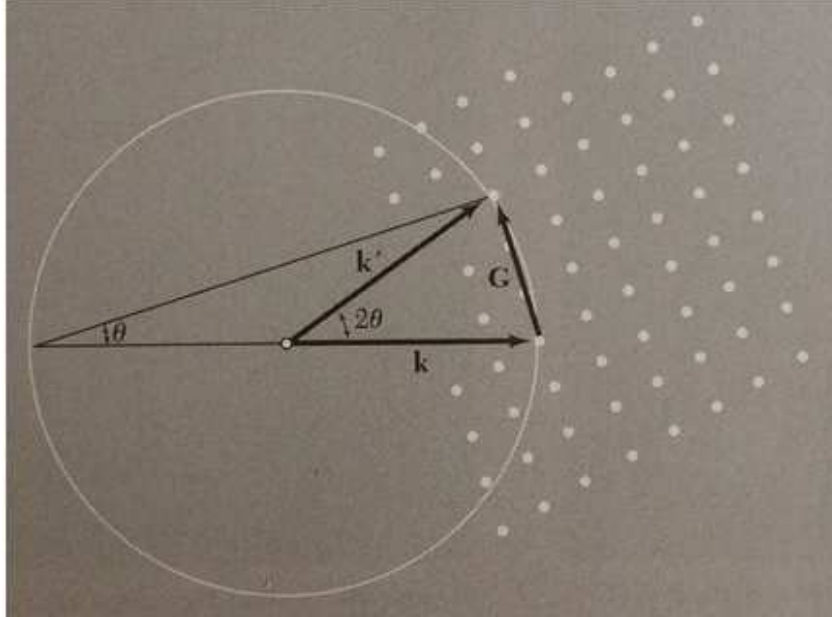


**Figure 3.9:** Example of the Ewald Construction reproduced from [16]. The white dots on the right-hand side of the image are the reciprocal lattice points of the crystal. The white circle is the circle of radius  $2\pi/\lambda$  and the incident and scattered wavevectors are denoted  $\mathbf{k}$  and  $\mathbf{k}'$ , respectively. The incident X-rays are coming in from the left-hand side of the image in the direction  $\mathbf{k}$  and strike the crystal located at the center of the white circle. The scattered X-rays move in the direction  $\mathbf{k}'$ . If, for given  $\theta$  and  $\lambda$ ,  $\mathbf{k}$  terminates on a point in the reciprocal lattice, then the Bragg condition is satisfied when the difference in the wavevectors,  $\mathbf{k}' - \mathbf{k}$ , has magnitude  $|\mathbf{G}|$ , where  $\mathbf{G}$  is a reciprocal lattice vector. Bragg's law is satisfied for reciprocal lattice points which lie on the circumference of the white circle.

This construction is an essential tool in extracting real space structure information from the reciprocal space scattering pattern. The sphere is swept out from the point in reciprocal space where the X-rays are scattered and has a radius of  $2\pi/\lambda$ . Only reciprocal space lattice points which lie on the sphere satisfy Bragg's Law. In the WAXS and SAXS systems the scattering pattern obtained by the two-dimensional detector is the projection of the 3-D sphere down into a 2-D circle. Our facility is equipped with an X-ray diffraction (XRD) system and this serves as the primary means of measuring the crystals present in our polymer samples.

Here X-rays are generated by sealed tube sources where high voltages are used to accelerate an electron beam into a metal target. This system measures a 1-D slice along the scattering angle,  $2\Theta$ . Crystal parameters can be directly extracted from this data by applying Bragg's law. Because PVA and PET are well studied [17-19] it is possible to identify each of the crystalline reflections and the amorphous material from the 1-D diffraction pattern.

For all experiments performed, we used a Phillips PW1830 X-ray generator operated at 40 kV and 45ma with an optically encoded diffractometer. The diffractometer is equipped with Cu  $K\alpha$  sealed tube X-ray source producing monochromatic X-rays  $\lambda = 0.1544$  nm. Scattering was investigated over a range of scattering angles from 5-40  $^{\circ}2\Theta$ . Fiber samples were investigated in  $\Theta/2\Theta$  mode with a scanning interval of 0.02  $^{\circ}$ /step with 2 s/step. An example of XRD data collected from PVA electrospun fibers is shown below in **Figure 3.10**. Gaussian peak fitting of the crystalline peaks and amorphous halos were performed with custom MATLAB programs written by previous members of the Cebe group [Matt Reveley, XRayFitGUI.m]. Fiber samples were mounted on a single crystal silicon (100) substrate. The silicon (100) scattering peak at 33  $^{\circ}2\Theta$  can be used to calibrate d-spacing measurements.

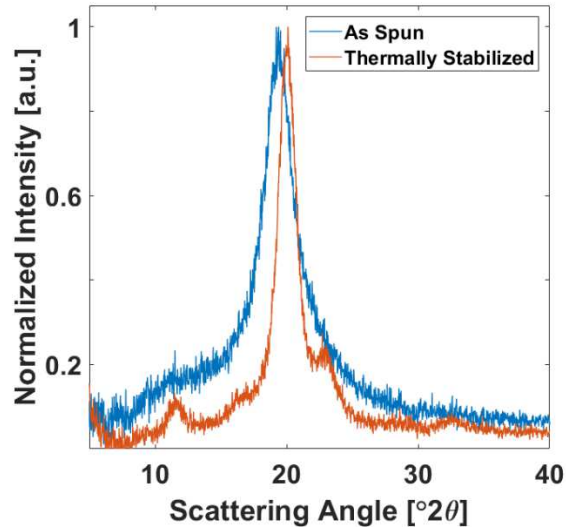


**Figure 3.10:** X-ray diffraction pattern for as spun (blue) and isothermally crystallized (red) PVA electrospun fibers mounted on silicon (100) substrate. Substrate and background have been subtracted.

### 3.3 Thermal Analysis Techniques

#### 3.3.1 Thermogravimetric Analysis (TGA)

Thermogravimetric analysis (TGA) is an experimental technique which makes use of a high precision balance seated inside a furnace which allows for the precise tracking of mass as a function of temperature and time. A TA Instruments Q500 Series TGA (New Castle, DE) was operated with a dried nitrogen purge for both the balance and the furnace at a rate of 50 mL/min. The TGA is seated on top of a Kinetic Systems KSI 9100 series vibration control workstation which isolates the balance during measurements from movements of the building from passing trains or from footsteps on the floor.

### 3.3.2 *Differential Scanning Calorimetry (DSC)*

Differential scanning calorimetry (DSC) is an experimental technique which allows for the precise measurement of the difference between the energy, in the form of heat, required to increase the temperature of a sample vs a reference as a function of temperature and time. This is a versatile instrument which allows for the measurement not only of the temperature dependent heat capacity of materials in a particular phase but also the temperatures and enthalpies of first order phase changes within materials. In the polymer specific case, it is extremely useful in gaining insight into the polymer glass transition, a quasi-second order transition (“quasi” because it is rate dependent), where the heat capacity increases as the polymer chains devitrify and gain rotational degrees of freedom.

There are various instrument designs, two of the most common being power compensated differential scanning calorimeters (commercial instruments made by Perkin-Elmer) [20] and heat flux differential scanning calorimeters (commercial instruments made by TA instruments and Mettler Toledo) [20]. The basic principle, monitoring the difference in the heat required to change the temperature of a sample compared to an empty reference, is the same but the physical construction of the instrument and means of measuring the signals are different. A brief overview of these two instrument designs are laid out as the TA Instruments Q100 DSC is a Heat Flux type calorimeter and the chip based fast scanning calorimeters are Power Compensated type calorimeters.

### 3.3.2.1 Power Compensated DSC

A power compensated DSC has two independent furnaces equipped with their own heating elements and temperature sensors. Both furnaces sit on a fixture (aluminum or another metal in conventional commercial calorimeters [21] and ceramic for the Mettler Flash DSC1 [22]) which is held at a constant temperature. Each furnace is heated individually through the programmed temperature – time profile. A schematic of this instrument is shown in **Figure 3.11** [20]. In the ideal case for two empty furnaces, the power required to bring each one through the programmed temperature – time profile is symmetric. During operation, a sample is loaded into one furnace and the other is left empty. Any endothermic or exothermic process which occurs in the sample results in a difference between the power draw for the furnace containing the sample when compared against the power draw of the empty reference furnace.

## Power-compensation DSC as Invented by the Perkin Elmer Co.

Types DSC 1-7 and Pyris

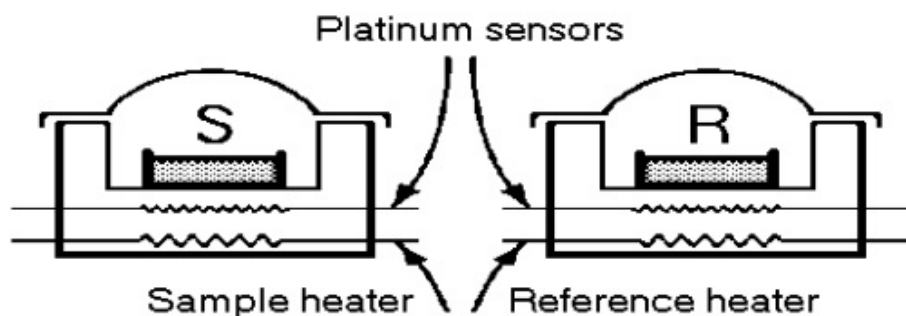


**Figure 3.11:** Reproduced diagram of a power compensated DSC [20]. Two independent furnaces are equipped with a heating element and temperature sensor. A sample (S) in a sealed pan is placed in one furnace and an empty reference pan (R) (nearly identical in mass to the sample pan) is placed in the other. The power required to bring each furnace through the temperature – time profile is recorded and the difference between these powers is measured.

Within the instrument a control circuit will deliver the same power to the heating elements in each furnace to change the temperature according to the programmed temperature – time profile. When a sample undergoes a phase change the symmetry between the furnaces is broken as the amount of energy required to change the temperature of the furnace has changed or the sample is actively exchanging heat with the furnace by an endothermic or exothermic process. The thermocouple(s) within the furnace containing the sample simultaneously measure the temperature deviations from the programmed temperature – time profile and signal to the control circuits. Control circuits will compensate for the phase change or reaction heat flow rate,  $\Delta\Phi$ , in the sample by increasing or decreasing the power supplied to the heating element,  $\Delta P$ . [20, 21]

$$\Delta P = K_1 \Delta T \quad (3.10a)$$

$$\Delta\Phi = K_2 \Delta T \quad (3.10b)$$

where the constant  $K_1$  is a fixed quantity within the control circuit and  $K_2$  is adjusted by calibrations within the instrument control software and against known standards.

### **3.3.2.2 Heat Flux DSC**

A heat flux DSC a sample and reference are placed on top of thermopiles inside of a single cavity which is connected to the furnace. Within this cavity are thermocouples which, in addition to the thermopiles under the sample and reference posts can measure the temperature of the sample

and the reference independently [20, 21]. An image of our heat flux DSC and schematic of this instrument are shown in **Figure 3.12**.

The cavity and the and the posts which house each thermopile are much larger than the reference and sample and result in an overall temperature field within the instrument dominated by the measuring system itself. This means that any temperature changes inside the cell due to the phase changes or reactions within the sample are quite small. High accuracy and high precision temperature measurements made by the thermopile under the sample and the adjacent thermocouples allow for the measurement of a differential temperature signal which is proportional to the heat flow rate,  $\Delta\Phi$ , [21]:

$$\Delta\Phi = \Phi_{\text{sample}} - \Phi_{\text{reference}} = -K \Delta T \quad (3.11)$$

where  $K$  is a cell constant related to the properties of the measuring system and can be dependent on the temperature – time profile. In an ideal case of an empty cell the heat flow rate should be flat for all temperatures. Any difference between the sample and reference sensor temperature,  $\Delta T$ , would indicate a thermal event (phase change or reaction) within the sample.

Practically speaking the cell must be run empty under various heating and cooling rates to assess the cell constant under the desired experimental conditions. This allows the thermal resistances of the empty cell to be corrected before samples are run. Further calibration requires collecting heat flow rate signals on standard materials. Pure metals such as indium and tin [20, 21] are used to calibrate for endotherm area and temperature accuracy and sapphire is used for heat capacity (equivalently heat flow) accuracy [20, 21]. In recent years, liquid crystals have been

shown to be useful tools in the calibration of DSCs [23]. The total heat flow rate measured by DSC is proportional to the total heat capacity of the material,  $C_p(T)$ , and the heating rate,  $\beta$ , according to the following relationship:

$$\Phi(T) = C_p(T) * \beta \quad (3.12)$$

A TA Instruments Q100 DSC (New Castle, DE) equipped with a TA Instruments Refrigerated Cooling System (RCS) was operated under a dried nitrogen purge at a flow rate of 50 mL/min for all conventional differential scanning calorimetry experiments performed. This is a heat flux type calorimeter with a DSC cell that operates generally as outlined above. An image of the instrument, as it sits in our lab now, and the manufacturer's schematic of the cell are seen in **Figure 3.12**.

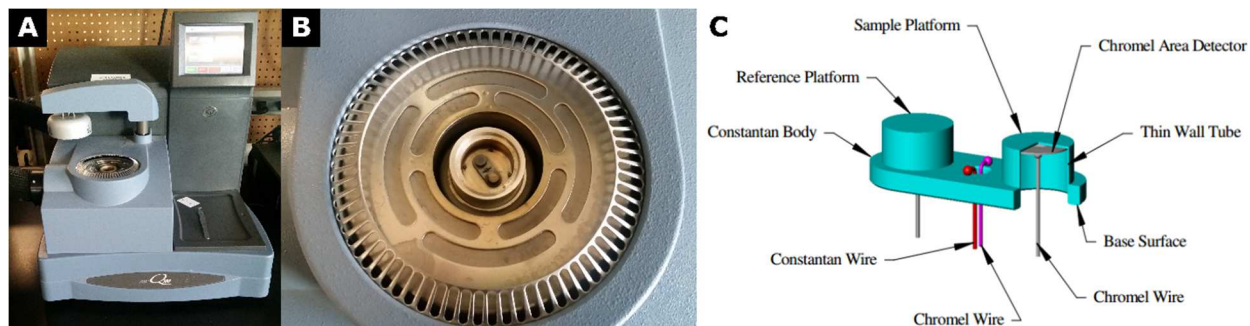


**Figure 3.12:** (A) TA Instruments Q100 DSC in room 421 at 574 Boston Ave (B) Image of the open DSC cell (C) Cut away diagram of the Q100 Tzero™ DSC cell from the literature published by the manufacturer [24] The right hand side shows a cutaway of the sample post with a chromel wire thermopile under the sample (or reference).

The temperature and heat flow measurement capabilities of this DSC allow for high precision and high accuracy measurements. It was designed such that the cell constants under many

conditions can be well calibrated providing highly repeatable data for carefully prepared samples. The design of this cell, pictured in **Figure 3.12C**, allows for careful measurement of the sample heat flow rate,  $\Phi$ , accounting for all the components within the cell.

This results in the following expression for the sample heat flow rate, as reported by the instrument manual [24, 25]:

$$\Phi = \frac{-\Delta T}{R_r} + \Delta T_0 \left( \frac{R_r - R_s}{R_r R_s} \right) + (C_r - C_s) \frac{dT_s}{dt} - C_r \frac{d\Delta T}{dt} \quad (3.13)$$

where  $\Delta T$  is the measured temperature difference between the sample and reference;  $\Delta T_0$  is the temperature difference between the measured base and the sample;  $R_r$  and  $R_s$  are the reference and sample sensor thermal resistances, respectively; and  $C_r$  and  $C_s$  are the reference and sample sensor heat capacities, respectively. The first term in this expression is the principle heat flow and is equivalent to Eqn. 3.11. The second and third terms correct for the imbalance between the thermal resistances of the reference and sample sensors and between the thermal capacitances of the reference and sample sensors, respectively. The final term corrects for any heating rate imbalances [24]. This relationship allows for the impact of the measuring system to be corrected when collecting data on a sample. TA Instruments control software in conjunction with indium and sapphire standards allow for the calibration of the cell and determination of the constants resulting in high precision and high accuracy heat scans at heating and cooling rates between 1 °C/min and 30 °C/min.

To ensure high accuracy measurements samples are prepared in sealed, aluminum pans. Within the pan samples should flat and dispersed evenly along the bottom of the pan. In addition to providing complete thermal contact between the sample and the thermopile the pan provides

uniform thermal contact with the furnace all around the sample. By placing an empty aluminum pan of nearly equal mass on the reference, any impact of the heat capacity of the aluminum pans on the measured signal is subtracted during the measurement. This means of sample preparation minimizes any thermal gradients within the sample and allows for complete measurements of phase changes or reactions within the sample where the accuracy of the heat flow measurement can be made within 1%.

*Theory and Data Analysis:*

When operated in standard mode (linear heating and cooling rates) the Q100 DSC provides the heat flow rate as a function of temperature (or time). This is converted to specific heat flow rate by independent measurements of the sample mass using an analytic balance. An example heat flow rate vs. temperature curve is plotted in **Figure 3.13** which allows for the measurement of various fundamental thermal properties.

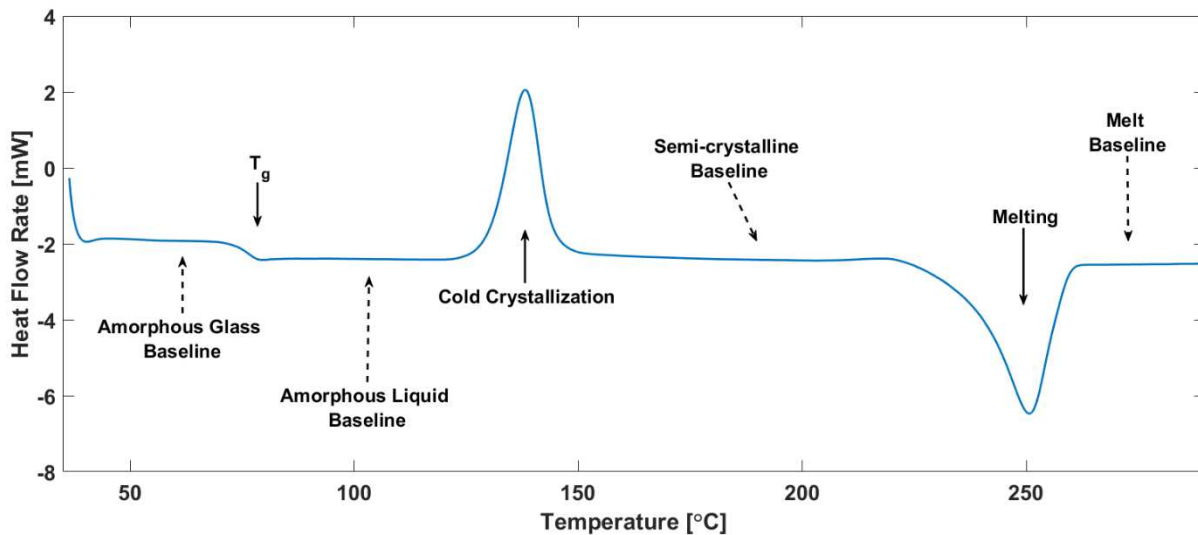


**Figure 3.13:** Heat flow rate vs. temperature curve for the heating of a quenched polyethylene terephthalate (PET) sample heated at 10 °C/min. Solid arrows with labels point to the various observed phase changes in the sample. Dashed arrows identify each heat flow rate baseline observed during heating.

Moving from left to right in **Figure 3.13** several important features are identified in the heat flow rate vs. temperature curve. At low temperature, the polymer is in a solid, glassy phase. As the temperature increases the sample transitions from a glassy phase to a high viscosity, rubbery, liquid phase. As the temperature continues to increase the polymer begins to crystallize during heating, known as cold crystallization. Crystallization (and melting) is a first order phase change and exhibits a latent heat. Under the conditions of the differential scanning calorimeter crystallization results in an upward pointing exothermic peak, seen in **Figure 3.13**, as the sample is releasing heat as it assumes the lower energy conformation of a solid. As the temperature is increased to the melting point of the polymer a downward pointing endothermic peak, seen in **Figure 3.13**, is observed as the sample takes in heat from the cell to assume the higher energy conformation of a liquid. At high temperature, the polymer is fully in the liquid phase where it can flow but does not undergo any spontaneous reorganization.

The solid state heat capacity is the same for an amorphous glass or crystalline polymer and has been successfully modeled [26-30]. As the temperature increases the polymer will undergo a quasi-second order phase change from the glassy solid characterized by vibrational motion to a high viscosity liquid (rubbery state) where the polymer chains can move by large scale rotation and translational motions. This results in an increase in the heat capacity. The glass transition temperature,  $T_g$ , is identified as the inflection point in this transition from a glassy solid to a rubbery liquid. The heat capacity increment,  $\Delta C_p(T_g)$ , is defined as the difference in heat capacity baselines at  $T_g$ . Studies have successfully modeled the increment of change in the heat capacity at  $T_g$  by quantifying the additional rotational energies of polymer chemical groups which become free to rotate at the glass transition. The specific solid state and specific liquid state heat capacities,  $c_p^{\text{solid}}$  and  $c_p^{\text{liquid}}$ , respectively, and the increment,  $\Delta c_p(T_g)$ , are fundamental thermal properties which are measured by DSC.

When measuring the heat capacity of an unknown material or when high accuracy measurements of the heat capacity are desired a general measurement protocol, often referred to as “the three runs method” performed. The first measurement is made on a pair of empty crucibles or pans across the temperature – time profile. This results in an empty pan line which is zero if the instrument has perfect symmetry between sample and reference sensors. In the second measurement, a material with a known heat capacity (typically sapphire) is encapsulated in a pan and placed on the sample sensor with an equal mass empty pan on the reference. This allows for any cell calibration constants to be determined. Finally, a sample is encapsulated in a pan and placed on the sample sensor with an empty pan on the reference sensor. This results in a measured  $\Delta T$  for the sample over the temperature – time profile. [21]

The specific enthalpy,  $\Delta h$ , of a given phase change or reaction within a sample can be measured from the heat flow rate vs. temperature curve by integrating the endothermic or exothermic peak against the heat flow baseline. Mass fraction crystallinity is then calculated by comparison of the measured specific enthalpy,  $\Delta h_f$ , to the equilibrium heat of fusion,  $\Delta H_{f0}$  with the following relation [20, 31]:

$$\phi_c = \Delta H_f / \Delta H_{f0} \quad (3.14)$$

where the equilibrium heat of fusion of polyvinyl alcohol is  $\Delta H_{f0} = 7.11$  kJ/mol [27, 32-34] and the equilibrium heat of fusion of polyethylene terephthalate is  $\Delta H_{f0} = 26.9$  kJ/mol [27, 32-34].

#### *Experimental Methods for Standard DSC:*

Standard DSC was employed to gain insight into the self nucleation and crystallization of polyvinyl alcohol. Sections of the solution cast PVA film (**Section 2.2.0**) were cut with a hole punch such that they filled standard aluminum DSC samples pans with uniform contact across the entire surface. The initial film has a thickness of 250  $\mu\text{m}$  and an average crystallinity of  $39.2\% \pm 1.6\%$ , calculated from the melting endotherm using Eqn. 3.14. Sample masses varied between 4.5 and 10.4 mg. Due to thermal degradation of PVA, it was deemed not possible to follow prior DSC experimental protocols, which erased thermal history by holding isothermally at 30 °C above the peak melting temperature for 30 min., a typical procedure for self nucleation experiments [2, 35-41]. Nor was it possible to hold the same sample at various values of the self nucleation temperature,  $T_s$ , as was done on other polymeric systems. [2, 37-39, 41-48] Therefore, to minimize thermal degradation of PVA, fresh samples cut from the same parent sheet were used for each experiment. The general procedure for our self nucleation experiment follows four steps:

1. Heat from 40 °C to a temperature,  $T_s$ , at a rate of 10 °C/min.
2. Hold isothermally at  $T_s$  for 5 minutes.
3. Cool at a rate of 10 °C min<sup>-1</sup> to 40 °C to create a semi-crystalline state.
4. Reheat from 40 °C to 240 °C at a rate of 10 °C min<sup>-1</sup> to assess the melting behavior of the crystals formed after steps 1-3.

The results of such an experiment will fall into three domains as defined by Fillon, *et al.* [37-39]:

*Domain I:* The complete melting domain. Here the self nucleation temperature,  $T_s$ , is sufficiently high that the crystalline memory of the system is lost.

*Domain II:* The exclusive self nucleation domain. Here the polymer will nucleate on crystal fragments, or on regions of the aligned polymer chain, with residual crystalline memory. There is no annealing of previously formed crystals and the crystallization is accelerated upon cooling, with the peak temperature of the crystallization exotherm shifted to higher temperatures.

*Domain III:* The self nucleation and annealing domain. Here the polymer crystals will undergo partial melting and annealing. The polymer exhibits similar crystallization temperatures to those observed in Domain II but manifests with a double melting peak upon subsequent heating, reflecting existence of two distinct populations of crystals.

**Figure 3.14A** shows the temperature – time profile for this procedure. The range of self nucleation temperatures,  $T_s$ , was determined by selecting a minimum value of  $T_s$  just below the peak melting temperature obtained by a first heating at a rate of 10 °C/min. The maximum value of  $T_s$  was selected to be approximately 10 °C above the endotherm foot, or the last point where

heat flow deviated from the linear baseline in the melt. The bounds selected from the melting endotherm are shown in **Figure 3.14B** where the solid black line shows the selection of the minimum  $T_s$  value and the dotted black line shows the endotherm foot. This procedure was performed on samples with values of  $T_s$  ranging from 220-230 °C in 1 °C intervals, and from 230-240 °C in 2 °C intervals. This procedure was repeated in the TGA with values of  $T_s$  ranging from 220 °C to 240 °C in 5 °C intervals, to assess the impact of  $T_s$  on thermal degradation and the results were used to account for mass loss during the DSC experiments.

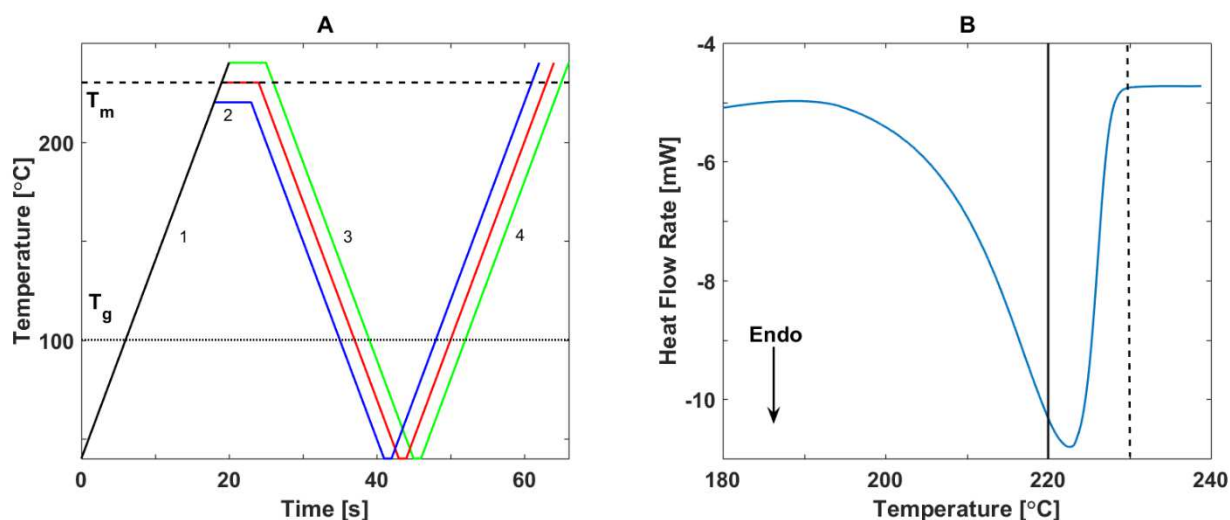


**Figure 3.14:** (A) Schematic of the temperature profile during self nucleation experiments. First heating to  $T_s$  (black). Subsequent treatment (holding for 5 minutes at  $T_s$ , cooling, and reheating):  $T_s = 220$  °C (blue), 230 °C (red), 240 °C (green). The heating and cooling rates are  $\pm 10$  °C/min. The glass transition temperature,  $T_g$ , and endothermic peak melting temperature,  $T_m$ , are marked with dashed lines. The treatment stages are marked 1-4. [37-39] (B) Bounds on  $T_s$  values sampled are determined using the melting endotherm from first heating of PVA at 10 °C/min, and fall between the solid line and a temperature 10 °C above the dashed line which represents completion of the endotherm. Endotherm area was used to measure the initial crystallinity of the parent solution cast film.

### 3.3.2.3 *Temperature Modulated Differential Scanning Calorimetry (TMDSC)*

When operating in standard mode the only signal measured is the total heat flow, which as discussed above, can provide insights into the fundamental thermal properties of polymers. One limitation of standard DSC is that the total heat flow is a composite signal of all thermal events in the sample occurring during heating. Certain processes, such as the glass transition, are completely reversible and contribute only to a change in the heat capacity whereas other processes such as crystal melting, shrinkage, or curing and aging of samples are kinetic and irreversible. As discussed in the introduction, polymer crystallization is a kinetic process which depends on the supercooling, heating or cooling rate, crystallization time, and the presence of nuclei in the melt. While it is possible to partially melt and recrystallize a polymer crystal, the complete melting of a crystal is generally irreversible and requires that the sample be cooled far below the melting point to nucleate and recrystallize.

In Temperature Modulated DSC (TMDSC) a sinusoidal temperature oscillation is applied on top of the standard DSC linear heating rate. The temperature – time relationship for TMDSC is given by the following equation [20, 24]:

$$dT/dt = \beta + A_r \omega \cos(\omega t) \quad (3.15)$$

where  $\beta$  is the standard linear heating rate,  $A_r$  is the amplitude of modulation,  $\omega$  is the angular frequency, and  $t$  is time. A typical temperature modulation is shown in **Figure 3.15**. This combination of a linear heating ramp and local heating and cooling with the linear behaves functionally like two independent experiments being run simultaneously.

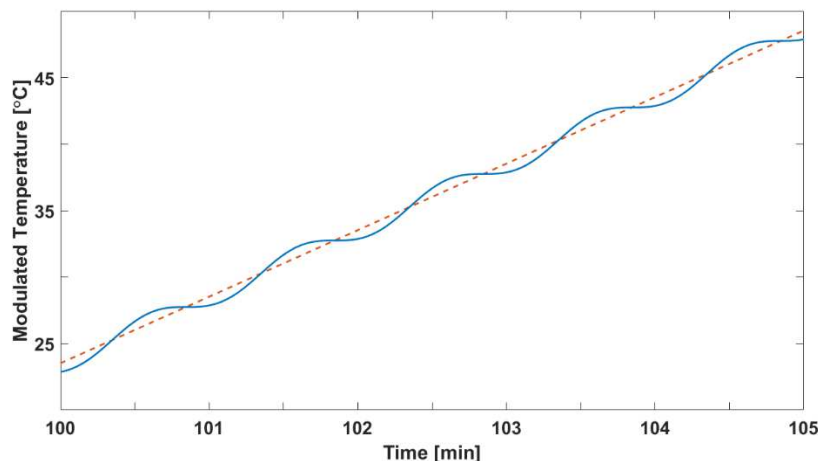


**Figure 3.15:** Modulated temperature vs. time for a heating rate of 5 °C/min with temperature modulation amplitude of  $\pm 0.796$  °C over a period of 60 s. The solid blue curve is the TMDSC heating ramp and the dashed, orange line is the underlying, standard heating rate. This image is shown over a shorter range so that the modulated rate can be easily seen apart from the underlying heating rate.

Performing a Fourier transform on the heat flow data collected allows for the heat flow data to be separated into two components in real time, the heat capacity component and the kinetic heat flow component. This is represented by the following relationship [20, 24]:

$$d\Phi(T)/dt = C_p(T) dT/dt + f(t,T) \quad (3.16)$$

In this relationship, the left-hand side yields the total heat flow. On the right-hand side of this relationship the first term provides the heat capacity component in the form of the reversing heat capacity and accounts for the portion of the signal which is the result of thermally reversible processes. The second term is the kinetic term which yields the non-reversing heat flow and accounts for all contributions to the total heat flow from thermally irreversible phase changes or reaction. This technique is quite powerful in that it allows complex thermal phenomena to be broken into individual components with a single experiment inside the calorimeter.

### 3.3.2.4 *Experimental Methods Involving Temperature Modulated DSC*

A hybrid program utilizing both standard DSC and TMDSC was employed to make measurements of the heat capacity increment at the glass transition and the total enthalpy of melting to measure crystallinity of stock PVA polymer. Fresh samples were prepared for each measurement. Two thermal treatments were used to crystallize these samples. The first treatment brought the samples from room temperature at 20 °C/min to 200 °C, just at the onset of melting, and then the sample was immediately cooled at 20 °C/min to  $T_c = 170$  °C and held for various times. The second treatment brought the samples from room temperature up to cold crystallization temperatures between 130 °C and 160 °C at 20 °C/min where they were held for various times. Sample and thermal treatment are listed with the discussion of results in **Table 5.4**.

Following the crystallization step, samples were cooled at 5 °C/min to -80 °C. Temperature modulation of  $\pm 0.796$  °C every 60 seconds was applied as the sample was heated at 5 °C/min from -80 °C to 120 °C, allowing for a precise measurement of the glass transition (observed to be between 75 °C and 80 °C) from the specific apparent reversing heat capacity. The sample is then cooled at 20 °C/min back to -80 °C and is reheated up to 270 °C at 20 °C/min (operating in standard DSC mode) allowing for a complete measurement of the melting endotherm. Crystallinity is determined per Eqn. 3.14.

In the case of solution processed polymers, a drying step is introduced where the polymer is heated to a temperature above the boiling point of the solvents used in processing and kept as near to the onset of the glass transition as possible. For PVA the primary solvent is deionized water which can be ejected between 80 °C – 120 °C and for PET the primary solvent is trifluoroacetic acid (TFA) which has a boiling point between 78-80 °C. Electrospun fibers are first heated to the drying temperature, isothermally held for one to five minutes to eject bound solvent and then

cooled to temperatures between -50 °C and -80 °C. Standard mode DSC is performed at scanning rates of 10 °C/min and 30 °C/min and TMDSC is performed at a scanning rate of 5 °C/min with an applied temperature modulation of  $\pm 0.796^\circ\text{C}$  every 60 seconds.

### **3.4 Fast Scanning Calorimetry**

#### **3.4.1 Custom-Built Chip Based Calorimeter**

In 2010 two papers were published detailing a new type of differential scanning calorimeter which was developed at the University of Rostock by Zhuravlev and Schick [49, 50]. Their device is a chip based, power compensated nano-calorimeter which allows for the measurement of nanogram and microgram sized samples at heating and cooling rates between 1 K/s and 600,000 K/s. The general principles of the power compensated DSC described in **Section 3.3.2.1** apply to this instrument as well but the development of membrane based sensors on a chip allow for the realization of an entirely new class of instrument.

The thin film chip based sensor is equipped with thermocouples for temperature measurements and heating elements. This chip based sensor functions as an individual furnace in a power compensated DSC system and is shown in **Figure 3.16A**. A sample is placed on top of the membrane, pictured schematically in **Figure 3.16B** and an image of a sample loaded is shown **Figure 3.16C**. These images are duplicated from the original publication [50].

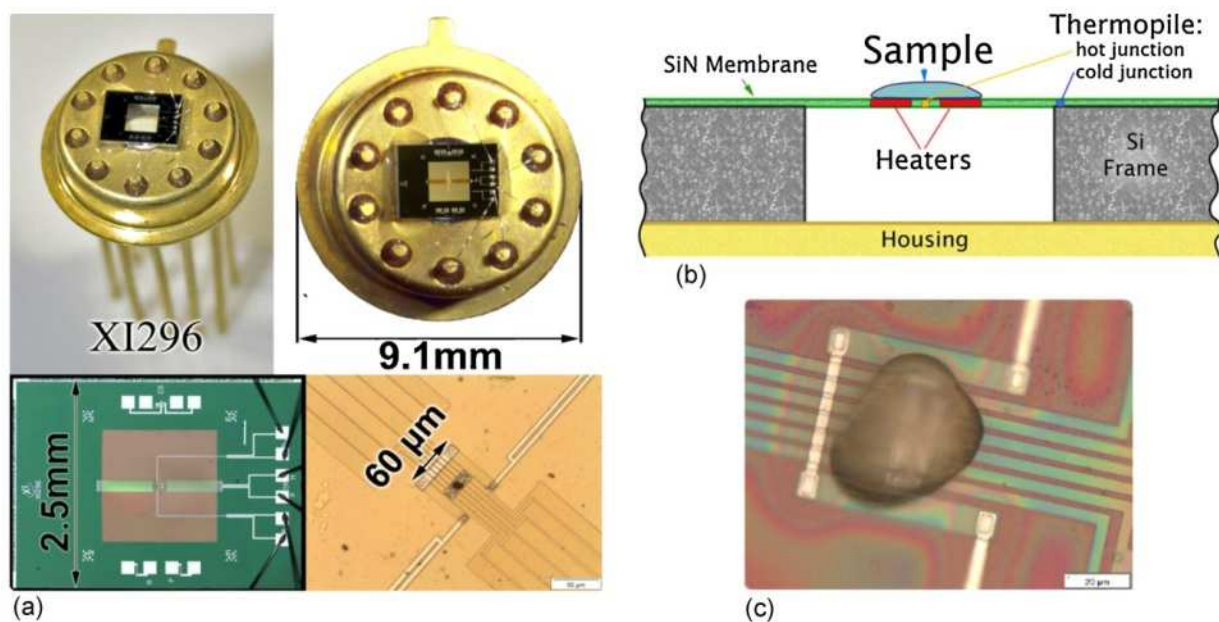


**Figure 3.16:** (A) Images of the custom chip sensors manufactured by Xensor Integration designed for the custom-built calorimeter, figure reproduced from [50]. (B) Schematic of the chip sensor. Heating elements sit under the silicon nitride film supported on the silicon frame. Temperature sensors sit in between the heaters directly under the sample. A junction between the silicon frame allows the silicon nitride membrane to remain at the sensor support temperature. (C) Optical microscope image of a sample loaded onto the membrane shown in (A). Scale bar is 20  $\mu\text{m}$ .

One of these chip based sensors is loaded with a sample as described in **Section 2.2.1** and another is left empty to serve as the reference sensor. Both sensors are loaded into an oven, pictured in **Figure 3.17**. The image of the oven and diagram of the instrument setup are duplicated from the original publication [50]. The oven is then placed at the bottom of a tube which is in a reduced pressure gas environment and surrounded by a liquid nitrogen reservoir. The oven is connected to temperature controllers which keep it at a constant, controlled temperature and data acquisition devices. The chip sensor and oven assembly are surrounded in liquid nitrogen which allows for heating from (and cooling to) low temperature. Additional details regarding the data acquisition device and control circuits are found in the papers detailing this custom-built instrument [50].

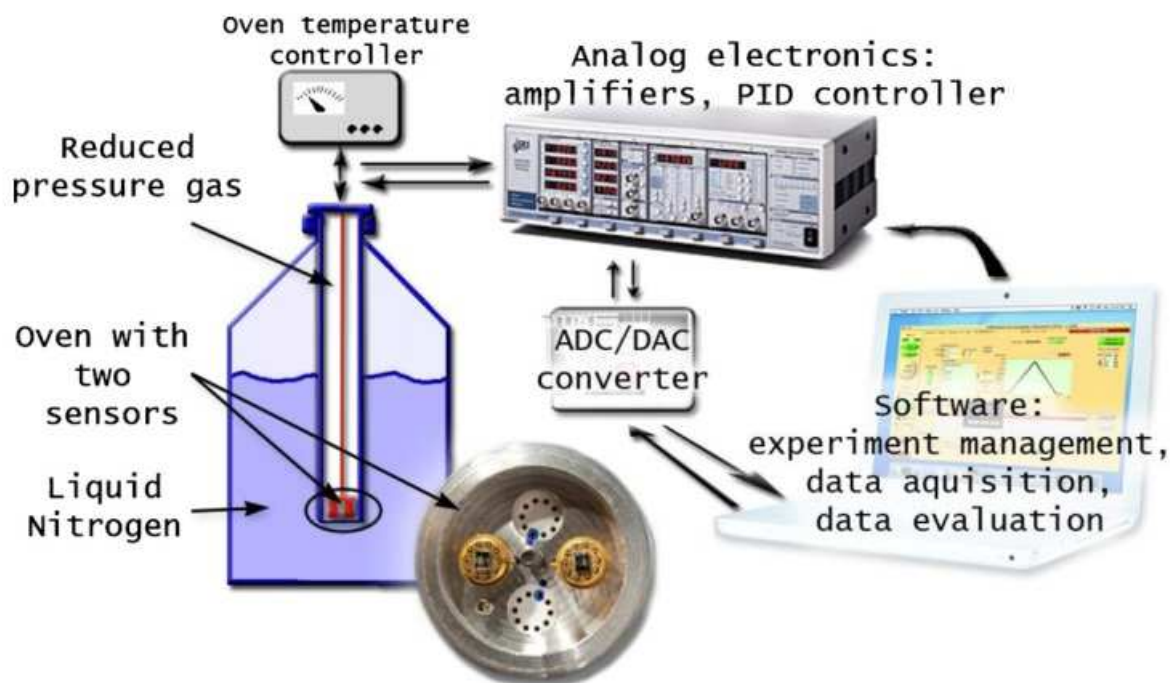


**Figure 3.17:** Schematic of the entire custom-built chip based calorimeter [50]. The silver disk pictured at the bottom of the image is the temperature controlled oven where the individual chip sensors are loaded. In this image one sensor acts as the sample furnace and the other is the reference furnace.

In the chip based system the membrane and support are held at sensor support temperature. When the oven is surrounded by a reservoir of liquid nitrogen this is around  $-196\text{ }^{\circ}\text{C}$ . Both the membrane and the reduced pressure gas purge are at this temperature and the sample is actively cooled by the gas flow which acts as the primary cooling agent. The sample is heated by the heating elements within the membrane, shown as the red block in **Figure 3.16B**. Because the sample masses are so small the gas purge is sufficient to achieve cooling rates in excess of  $100,000\text{ K/s}$ , even in the case of polymers which have poor thermal conductivity [49-51]. Thin film samples immersed in a helium environment can be cooled at rates up to  $600,000\text{ K/s}$ .

A sample was cut from the thicker spin coated film described in **Section 2.2.1** onto sensor XI-390 (not pictured but looks identical to the sensor in **Figure 3.16A**). The sample and sensor were encapsulated in a helium environment both to improve cooling performance and mitigate sample degradation. The sensor enclosure and reference were placed in the oven which was inserted into the tube surrounded by liquid nitrogen. PVA was heated to the melt at 280 °C and cooled to -170 °C at rates between 1,000 K/s and 600,000 K/s and reheated at a fixed rate of 10,000 K/s. The temperature – time profile for this experiment can be seen in **Figure 3.18**.

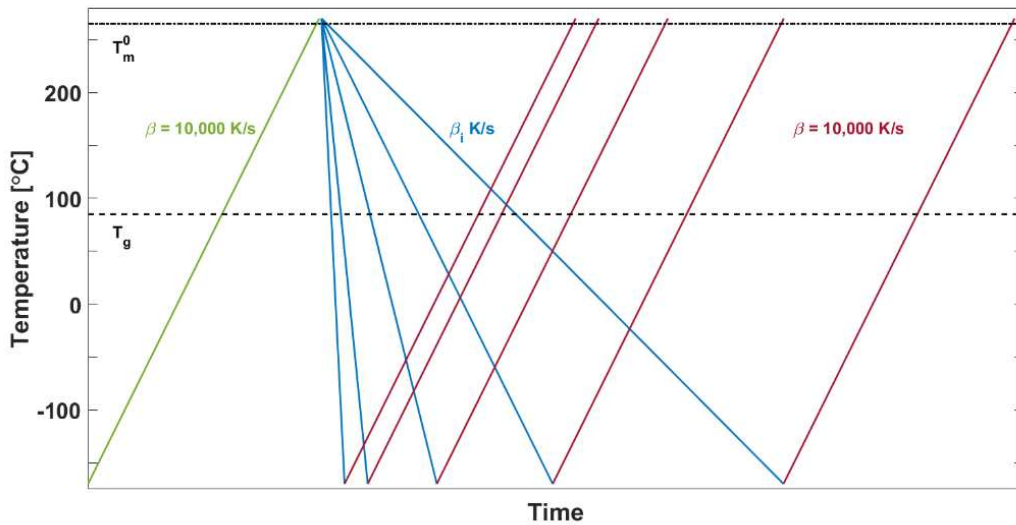


**Figure 3.18:** Temperature vs. time schematic for the experiments performed on the custom-built calorimeter. Initial heating is shown in green at a heating rate of 10,000 K/s. The sample is then cooled at various rates between 1000 K/s and 200,000 K/s, shown in blue. The sample is reheated at 10,000 K/s, shown in red.

### 3.4.2 *Mettler Toledo Flash DSC1*

Not long after the development of the custom- built calorimeter [49, 50] Mettler Toledo released a commercial instrument, the Flash DSC1, which makes use of similar membrane sensors [22] as the custom-built chip calorimeter described in the previous section. The major difference between these measuring systems is that instead of two chip sensors loaded into the oven, the Flash DSC1 utilizes a proprietary chip based sensor, the UFSC1 sensor [22] which contains both a sample and reference sensor on a single chip. Additionally the membrane sensors on the UFSC1 chip are slightly more robust and can tolerate larger samples, however they do not support heating and cooling rates as high as the custom-built system. Mettler Toledo reports cooling rates up to 4000 K/s and heating rates up to 40,000 K/s [52].

Every UFSC1 chip is functionally a pair of power compensated calorimeter furnaces and the device of the Mettler Flash DSC1 serves as the control module which provides the cooling, gas purge, and power control circuits for the chip sensors. Images of the UFSC1 sensor and the membrane are shown in **Figure 3.19** and are reproduced from the work published by the sensor manufacturer. The image in **Figure 3.19A** shows the underside of the UFSC1 sensor. The dark rectangular area inside the white ceramic support contains both the reference and sample membrane sensors, which are separated by thick silicon frame. This frame prevents any reaction or phase change in the sample from impacting the reference sensor.

The lower panel in **Figure 3.19B** shows an image of one membrane sensor. The circle in the middle of the image is the active sensor area. A pair of heaters are integrated into center of the membrane. The main heater is used for the general scan following the temperature – time profile and the secondary heater is used for power compensation. An aluminum layer covers the pair of heaters (this is the visible disk in the middle of the membrane) and ensures uniformity of

temperature within the sample area. A total of 8 p/n-type polysilicon thermocouples are used to measure the temperature across the sample area. A pair of thermocouples is housed inside the four rectangular bars, one of which is indicated by the black arrow in **Figure 3.19B**.

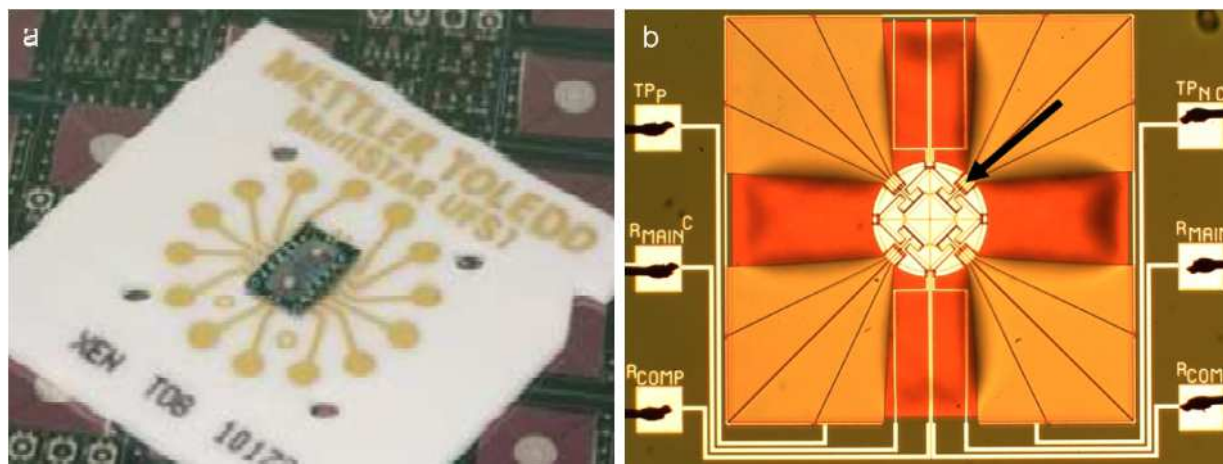


**Figure 3.19:** Reproduced image from paper detailing the design and testing of the MultiSTAR UFSC1 chip sensor [22]. Figure has been rearranged. **(A)** shows the chip upside down relative to how it is loaded into the Flash DSC1. Gold contacts on the ceramic base connect wires to the membrane sensor **(B)** with the Flash DSC1 base. **(B)** Individual membrane sensor. The bright circle in the middle is the aluminum layer on top of the primary and secondary heating elements. Black arrow points to one pair of the 8 total thermocouples which surround the sensor area.

The chip is placed into the Flash DSC1 “face down” with respect to the image in **Figure 3.19b**. An image of the UFSC1 chip being loaded into the Flash DSC1 is shown in **Figure 3.20**. Once loaded the membrane sensors are wells which samples can be lowered into in the manner described in **Section 2.2.1** and according to the diagram seen in **Figure 2.2A**. Samples loaded onto the sensors must not exceed 10  $\mu\text{m}$  in thickness [53, 54] for the heat transfer from the primary heater to uniformly heat the sample and prevent thermal gradients from obscuring measurements.



**Figure 3.20:** Mettler Flash DSC1 being loaded with UFSC1 sensor, image is reproduced [55]. The left panel is the Flash DSC1 device, the middle panel is the sensor stage with gas purge lid open so the sample can be viewed through the overhead microscope. The right panel shows the UFSC1 chip lowered into the device without the holding collar in place. From this view the membranes are in recessed wells as diagrammed in **Figure 2.6**.

### **3.4.3 Experimental Methods for Quantitative FSC**

#### **3.4.3.1 FSC on Polymer Thin Films**

A Mettler Flash DSC1 (Mettler-Toledo, Switzerland) was used to measure heat flow rate vs. temperature for PVA at a scanning rate,  $\beta$ , of  $\pm 2000$  K/s. Experiments were performed under a nitrogen gas flow of about 50 mL/min with the ceramic sensor base temperature set to  $-100$  °C. Empty Mettler Toledo UFSC1 chip sensors were conditioned following the manufacturer's procedure four to five times (this thermal protocol is built in to the instrument control software) then cooled and reheated between  $-90$  °C and  $270$  °C at 2000 K/s to obtain the baseline empty sensor signal. Samples from the parent films were hand cut with a surgical scalpel, with the assistance of a binocular microscope, carried on a fine wire and then placed onto the sensors.

PVA films contain bound water from processing [56] and, along with wrinkles and folds from handling, require an initial heating ramp to the melt to eject bound water and flatten the film.

This optimizes the sample-to-sensor thermal contact, and as such, all methods begin with an initial heat-cool-heat cycle. This cycle brings the sample between -80 °C and 270 °C at 2000 K/s with 0.01 s holding time between heating and cooling segments. The temperature – time profile for the initial sample conditioning is shown in **Figure 3.21**. Furthermore, this initial thermal cycle allows for the symmetry correction of the data, a necessary step in obtaining quantitative data from fast scanning calorimeters. [49, 57-59]

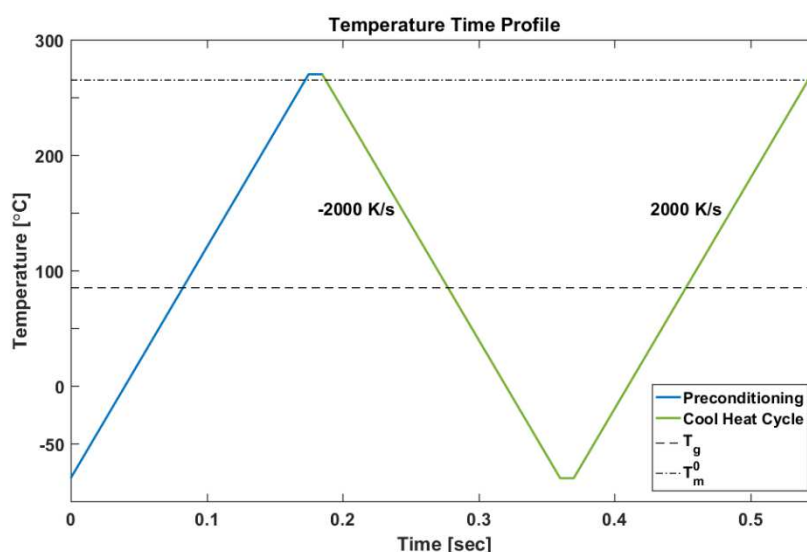


**Figure 3.21:** Temperature vs. time profile for the initial heat-cool-heat cycle applied to each sample. The blue segment is the first ramp to the melt which ejects solvents and flattens the sample, optimizing sample to sensor contact. The cool-heat segments, green segments above, are used for symmetry correction and mass determination, and then compiled for the second set of experiments.

After the drying and flattening stage two distinct experiments were performed with the Mettler Flash DSC1 on PVA films. The first experiment performed was to assess the thermal stability of PVA by cyclically heating and cooling between -80 °C and 270 °C at  $\beta = \pm 2000$  K/s with 0.01 s holding time between segments. The sample was removed after various numbers of

meltings and imaged under the Olympus Reflection microscope to visually check for signs of degradation.

The next set of experiments combined isothermal melt crystallization performed in the Mettler Flash DSC1 and isothermal cold crystallization performed with a conventional DSC (TA Instruments Q100 DSC) as outlined in **Section 3.3.2.3**. A summary of samples tests performed in the Mettler Flash DSC1 can be found in **Tables 5.2 and 5.3** where results are discussed.

Three samples were prepared for isothermal melt crystallization at temperatures between 90 °C and 150 °C for crystallization times,  $t_c$ , between 1 and 10,000 seconds. Following the initial heat-cool-heat cycle the sample is cooled at 2000 K/s to the isothermal melt crystallization temperature,  $T_c$ , and held isothermally, and then cooled to -80 °C. The sample is reheated at 2000 K/s to 270 °C. The glass transition temperature, the heat capacity increment at  $T_g$ , mass fraction crystallinity,  $\phi_c$ , and melting peak temperatures are measured on the reheating scan. The sample is then cooled back to the crystallization temperature and crystallized for the next crystallization time. A single sample was used for isothermal melt crystallization experiments at temperatures of 90 °C, 95 °C, and 120 °C with isothermal hold times,  $t_c$ , between 1 and 500 seconds. A fresh sample was used for each of the two sets of isothermal melt crystallizations temperatures of 140 °C and 150 °C for times between 1 and 10,000 seconds. A schematic of the temperature time profile is shown in **Figure 3.22**. The crystallization temperatures, isothermal hold times and thermal properties measured for the short and long isothermal times are found in **Tables 5.2 and 5.3**, respectively.

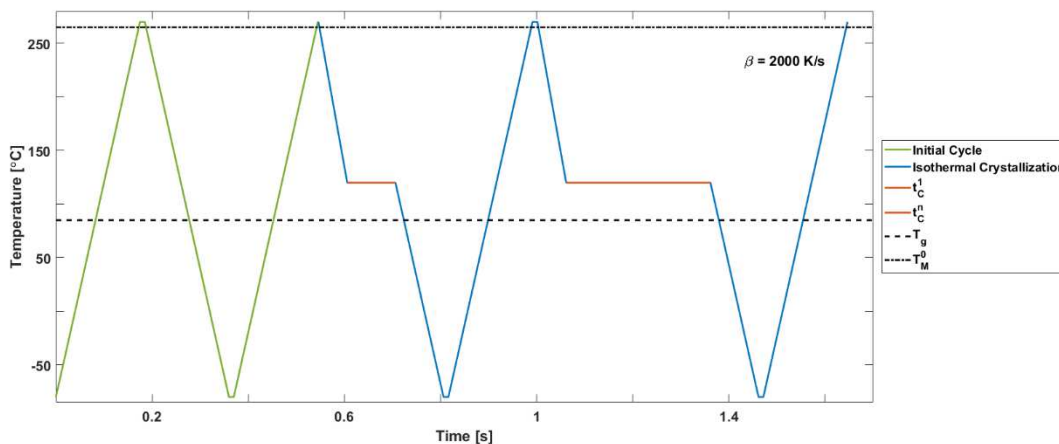


**Figure 3.22:** The general temperature vs. time profile for isothermal melt crystallization experiments. Initial heat-cool-heat cycle segment is shown in green. Samples are cooled to  $T_c$  from the melt at 2000 K/s, crystallized isothermally for  $t_c$ . The crystallization step is shown as the orange segments in between the blue cooling and reheating ramps.

Empty sensor and sample scans were collected and exported for further analysis via Mettler Toledo STARE<sup>®</sup> software. [60] Data analysis was performed with custom programs written in MATLAB<sup>®</sup>. [12] Details of the custom analysis programs can be found in the **Appendix B**.

### 3.4.3.2 FSC on Electrospun Fibers

New sensors are brought through the manufacturer’s conditioning treatment four to five times and then empty sensor scans are performed at  $\beta = \pm 2000$  K/s between -100 °C and 400 °C. Following the empty sensor scans, cut grid sections were carried on a fine wire and hand loaded onto the sensor. A select few scans were performed with grids loaded “fiber side up” for imaging following measurements; otherwise samples were loaded “fiber side down”.

Electrospun fibers typically contain residual solvents from the spinning process and must be dried prior to measurements. Sample treatments which have been previously used to eject

residual solvents during FSC experiments rely on heating the samples to high temperatures where the polymer can crystallize or melt, which will destroy the fiber structure. A short isothermal hold just above the glass transition was found to be sufficient to eject the solvent without crystallization. The general thermal protocol adopted involved heating the fibers at 2000 K/s to  $T_{dry} = 80\text{ }^{\circ}\text{C}$  and holding isothermally for 60 s. The sample is then cooled at 2000 K/s to  $-80\text{ }^{\circ}\text{C}$ , held isothermally for 0.01 s, before heating to a preset cold crystallization temperature,  $T_{cc}$ , where it is isothermally crystallized for 15 min. Following the crystallization step the sample is then cooled 2000 K/s to  $-80\text{ }^{\circ}\text{C}$  and reheated at 2000 K/s to  $310\text{ }^{\circ}\text{C}$ .

After this first ramp to the melt the fiber structure is lost but leaves behind confined droplets of polymer. Various isothermal melt crystallization experiments can then be appended following this thermal protocol. Details of these isothermal melt crystallization thermal protocols can be found in **Tables 6.2** where the data are discussed. An example schematic of this is shown in **Figure 3.23**.

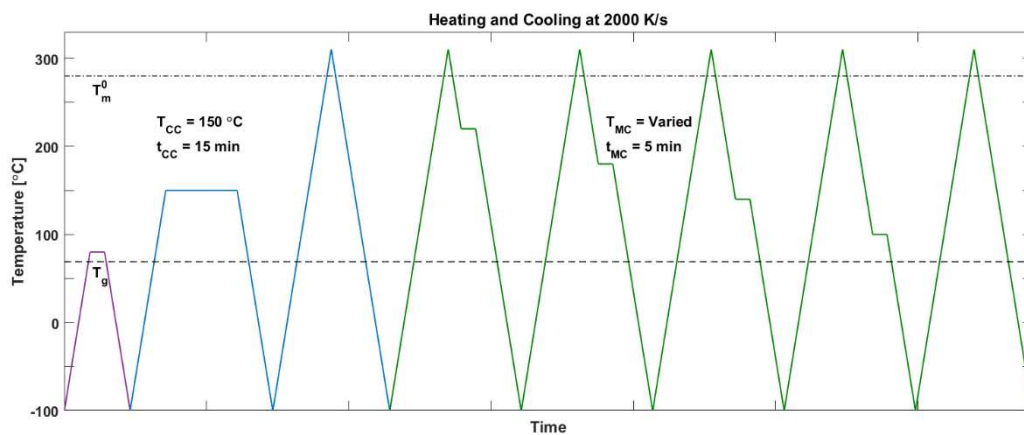


**Figure 3.23:** Temperature – time profile for the fast scanning methods used to measure electrospun fiber loaded grids. The purple segments at the beginning are first ramp and hold to a temperature above  $T_g$  where solvents are ejected. The blue segments that follow are the cold crystallization experiments where the fibers are crystallized and melted. Once melted the fibers are cooled at controlled rate to the sensor support temperature. The green segments represent various melt crystallization experiment which are appended following the initial fiber scan.

### 3.5 *Methods of Analyzing Fast Scanning Data*

To obtain quantitative and repeatable measurements of heat capacity by fast scanning calorimetry, several steps must be taken to correct the raw heat flow vs. temperature data. In a manner similar to other studies [59, 61] the first step is to subtract the empty sensor heat flow rate from the sample heat flow rate shown in **Figure 3.24A**. An example after subtraction is shown in **Figure 3.24B**. Unlike a conventional scanning calorimeter where samples are encapsulated with a covered pan, typically aluminum [21], the samples in a Flash DSC are directly exposed to the nitrogen purge which serves as the primary cooling agent for the system [51]. This results in thermal losses which vary with the physical state of the sample, and creates asymmetries between the heating and cooling scans with respect to the line of zero heat flow rate as a function of temperature. To address this, a line of symmetry is determined by comparing the heating and cooling heat flow rates as a function of temperature for two ranges, one when the sample is glassy, and the other when the sample is in the melt. [49, 59, 61] The symmetry line is constructed by first averaging the heat flow at each temperature within the two sampling regions and then fitting the entire temperature range with a 3<sup>rd</sup> order polynomial. This 3<sup>rd</sup> order polynomial serves as our symmetry line and is subtracted from both the heating and cooling scans. This results in a pair of curves which are symmetric about the line of zero heat flow. An example of the symmetry line determination is shown in **Figure 3.24B** and a final, corrected apparent heat capacity vs. temperature cycle is shown in **Figure 3.24C**.

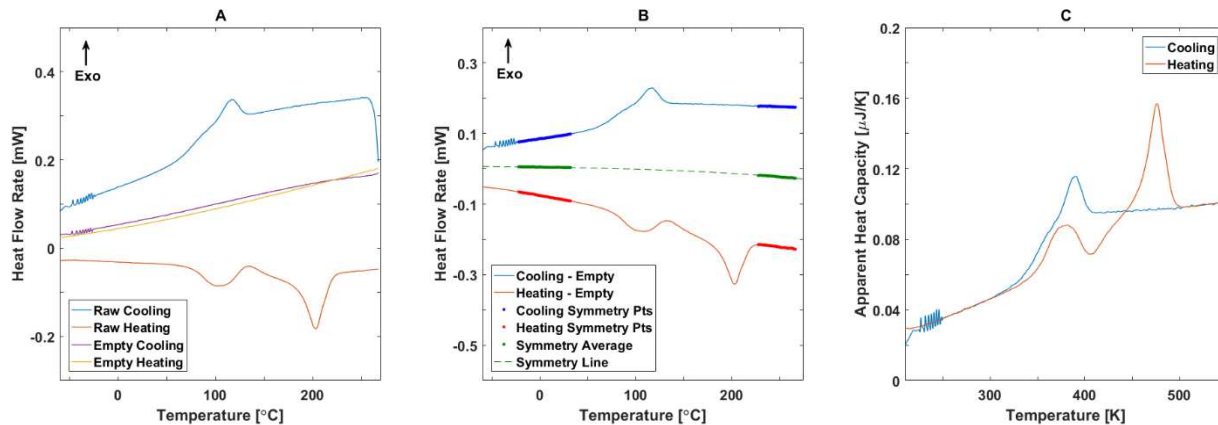


**Figure 3.24:** Treatment of raw heat flow rate vs. temperature data. (A) Uncorrected raw sample data in heating (red) and cooling (blue); empty sensor data in heating (yellow) and cooling (purple). (B) Sample heat flow rate data after empty sensor subtraction in heating (red) and cooling (blue). Regions selected for symmetry line determination - heavy red and blue curves; Symmetry line - green. (C) Sample apparent heat capacity after subtraction of both the empty sensor and the symmetry line, in heating (red) and cooling (blue).

To convert the symmetry corrected data into specific heat flow and specific heat capacity as functions of temperature, the sample mass needs to be known. The issue of mass determination in fast scanning calorimetry is not new [49-51, 59, 61-64] and several approaches have been developed to address it. When literature values for the specific heat capacity increment at the glass transition,  $\Delta c_p^{\text{amor}}(T_g)$  in J/(gK), are well known, and the 100% amorphous phase sample is available for testing, the measured heat capacity increment at  $T_g$ ,  $\Delta C_p^{\text{meas}}(T_g)$  in J/K, can be used to determine sample mass. [59] For cases where polymer is semi-crystalline [PE paper] or is known to possess rigid amorphous phase material, this method cannot be used unless the solid fraction is known. Instead, the apparent heat capacity,  $C_p^{\text{meas}}(T_1)$  in J/K, is sampled over a temperature range for  $T_1$  in the melt and divided by the literature value of the specific heat capacity of the liquid phase at  $T_1$ ,  $c_p^{\text{Liquid}}(T_1)$  in J/(gK), to determine the sample mass. [58, 62]

As mentioned above there is no literature consensus on the liquid phase heat capacity of PVA since thermal degradation sets in prior to the completion of crystal melting when using slow scan DSC. With the ultra-fast scanning rates accessible by FSC, thermal degradation can be avoided over a wider range of temperatures allowing for a careful measurement of the liquid phase heat capacity. Without literature values of either the specific heat capacity increment at  $T_g$  for 100% amorphous PVA or the liquid phase specific heat capacity of PVA, a new approach relying on the heat capacity of glassy PVA was developed, and is described below.

Before a method to determine the mass of sample in contact with sensor can be developed a simple experiment is performed to verify that the signal scales with sample mass. This was accomplished by cutting small pieces from the thinner film described in **Section 2.2.1**. A single sample was cut and placed on the sensor and brought through the preconditioning treatment outlined in **Section 3.4.3** and **Figure 3.21**. On this same sensor another sample was added adjacent to, but not in direct contact with the first and they are both brought through the same cycle. This was repeated until there were five samples on the sensor. A microscope image of the five samples on the single sensor was collected following the treatments and is shown in **Figure 3.25**.

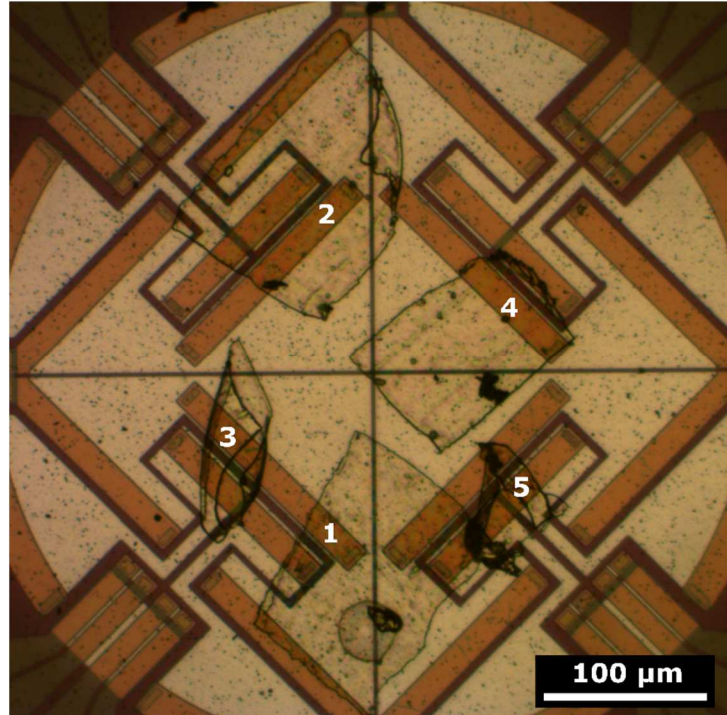


**Figure 3.25:** Optical microscope image of the five samples following the final heating collected using the Olympus microscope. Several samples were observed to curl up during the first ramp to the melt.

The heat flow rate vs. temperature for each preconditioning cycle was collected and is plotted in **Figure 3.26**. The mass on the sensor was increased by the addition of another identical sample each cycle and this resulted in an increase in the apparent heat flow rate under heating and cooling for sample added. This verifies that the measured signal is scaling with mass and a quantitative approach to determining the mass in contact with the sensor can be developed.

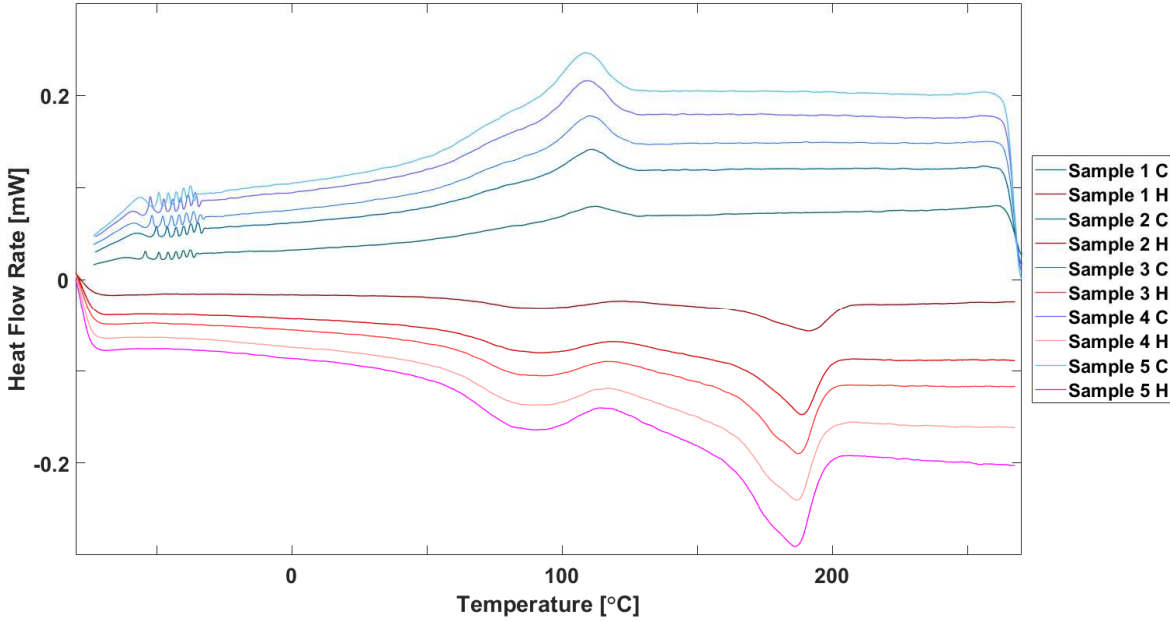


**Figure 3.26:** Raw heat flow rate vs. temperature curves for the five samples on a single sensor heated through the temperature – time profile shown in **Figure 3.21**. The curves in shades of blue correspond to cooling and the shades of red correspond to heating. As the number of samples (and subsequently the mass) increases the heat flow rate scales such that the curves are farther from the line of symmetry (i.e., the line at zero heat flow rate) between them.

Literature values from experimental data for the solid state specific heat capacity of PVA,  $c_p^{\text{Solid}}(T)$ , are obtained from the ATHAS databank. [65] Apparent heat capacity data,  $C_p^{\text{meas}}(T)$ , are selected from the corrected heating scan and compared to the literature value. The sampling temperature ranges from approximately 30 °C above the starting temperature, which is typically between -78 to -75 °C, up to 20 °C below the onset of the glass transition. Thus, heat capacity data over a temperature range between -45 °C and 40 °C are used for determination of the mass. Equation 3.17 is the relationship used to determine the mass at each temperature:

$$\text{Mass}(T) = C_p^{\text{meas}}(T) / c_p^{\text{Specific}}(T) \quad (3.17)$$

The mass is calculated as a function of temperature and is assumed to be constant in the glassy phase since there is no possibility of degradation at the temperatures sampled. If the mass is found to vary with temperature, a simple rotation about  $T = 273 \text{ K}$  ( $T = 0 \text{ }^\circ\text{C}$ ) is applied to the apparent heat capacity curves to bring the glassy phase heat capacity data into agreement with the literature values. The angle of rotation is calculated by determining the angle between the linear fits of the literature and experimental heat capacities over the temperature range used in the solid state. This approach allows for the calculation of the sample mass in contact with the sensor for any symmetry corrected data set.

There is sample to sample variation in the rotation necessary to correct the curves. Examples of two cases are shown below in **Figure 3.27**. In **Figure 3.27A** the empty sensor subtraction and symmetry correction were sufficient to obtain a constant mass as a function of temperature. Other samples require rotation as seen in **Figure 3.27B**.

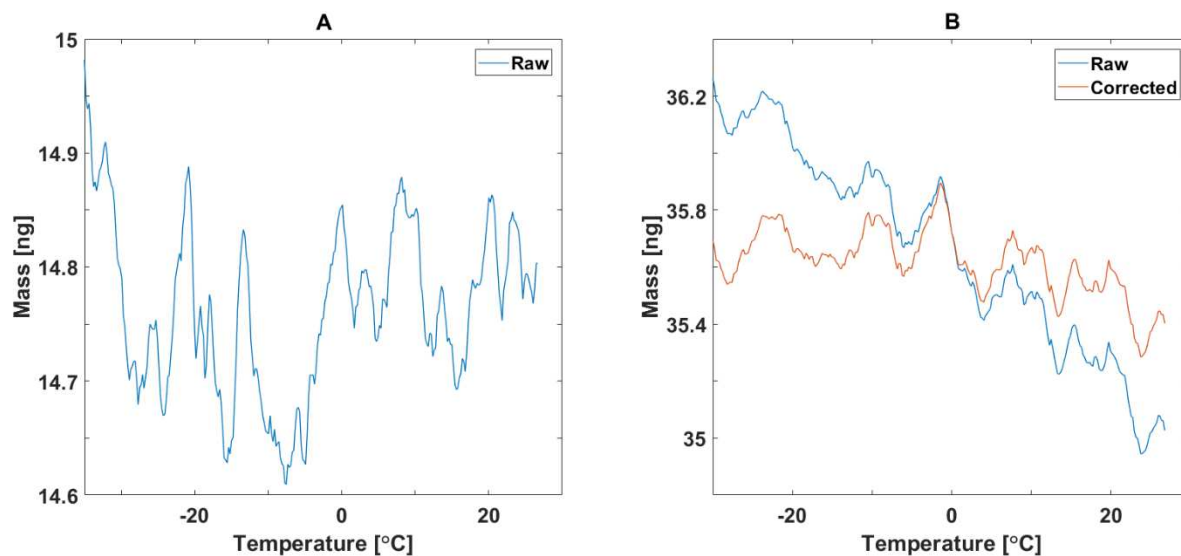


**Figure 3.27:** Cases where the corrections applied and use of Eqn. 3.17 (A) does not require rotation and (B) requires rotation. The uncertainty in the mass is reported as the standard deviation of the mass about the straight line of best fit through masses as a function of temperature.

### **3.6 Assorted Equipment and Instruments - Mettler Hot Stage**

A Mettler Toledo FP82HT hot stage equipped with a Mettler Toledo FP90 controller was used to replicate thermal treatments on bulk samples. Isothermal cold crystallization of electrospun fibers was performed at the same rates, temperatures, and crystallization times as their counterparts analyzed by DSC. This resulted in samples suitable for analysis in the Phillips Diffractometer (XRD) and the Jasco FTIR.

All thermal stabilization treatments on electrospun PVA fiber mats were performed with this hot stage. Samples were heated to 160 °C and held isothermally for 15 minutes to crystallize the samples. The hot stage was outfitted with an argon gas purge to displace any humid air from the room and sweep away any ejected solvents released during the isothermal crystallization.

### **3.7 References**

- [1] P.C. Robinson, M.W. Davidson, Polarized Light Microscopy, 2016. <https://www.microscopyu.com/techniques/polarized-light/polarized-light-microscopy>. (Accessed 6/12/2017 2017).
- [2] A. Mamun, S. Umemoto, N. Okui, N. Ishihara, Self-Seeding Effect on Primary Nucleation of Isotactic Polystyrene, *Macromolecules* 40(17) (2007) 6296-6303.
- [3] W. Zhou, R. Apkarian, Z.L. Wang, D. Joy, Fundamentals of Scanning Electron Microscopy (SEM), in: W. Zhou, Z.L. Wang (Eds.), *Scanning Microscopy for Nanotechnology: Techniques and Applications*, Springer New York, New York, NY, 2007, pp. 1-40.
- [4] J. Schindelin, I. Arganda-Carreras, E. Frise, V. Kaynig, M. Longair, T. Pietzsch, S. Preibisch, C. Rueden, S. Saalfeld, B. Schmid, J.-Y. Tinevez, D.J. White, V. Hartenstein, K. Eliceiri, P.

Tomancak, A. Cardona, Fiji: an open-source platform for biological-image analysis, *Nat Meth* 9(7) (2012) 676-682.

[5] R.S. McDonald, Review: Infrared Spectrometry, *Analytical Chemistry* 54(8) (1982) 1250-1275.

[6] J.L. Koenig, Chapter 1 - Theory of polymer characterization, *Spectroscopy of Polymers* (Second Edition), Elsevier Science, New York, 1999, pp. 1-33.

[7] J.L. Koenig, Chapter 2 - Vibrational spectroscopy of polymers, *Spectroscopy of Polymers* (Second Edition), Elsevier Science, New York, 1999, pp. 35-76.

[8] J.L. Agnieszka Nawrocka, Determination of Food Quality by Using Spectroscopic Methods, *Advances in Agrophysical Research*, INTECH2013.

[9] Sanchonx, Interferometer for FTIR, in: F. Interferometer.png (Ed.) Creative Commons Attribution-Share Alike 3.0 Unported Wikimedia Commons, 2011.

[10] Sbyrnes321, FTIR Interferogram, in: FTIR-interferogram.svg (Ed.) Origin, Creative Commons Attribution-Share Alike 3.0 Unported Wikimedia Commons, 2011.

[11] Spectra Manager, JASCO, 2008.

[12] MATLAB R2017a, The Mathworks, Inc, Natick, MA, 2017.

[13] H.S. Mansur, C.M. Sadahira, A.N. Souza, A.A.P. Mansur, FTIR spectroscopy characterization of poly (vinyl alcohol) hydrogel with different hydrolysis degree and chemically crosslinked with glutaraldehyde, *Materials Science and Engineering: C* 28(4) (2008) 539-548.

[14] Hydrargyrum, Bragg diffraction, in: B. diffraction2.svg (Ed.) Inkscape, Creative Commons Attribution-Share Alike 3.0 Unported Wikimedia Commons, 2011.

[15] J.E. Spruiell, E.S. Clark, 6.1 Unit Cell and Crystallinity, in: R.A. Fava (Ed.), *Methods in Experimental Physics*, Academic Press 1980, pp. 1-127.

- [16] C. Kittel, Introduction to solid state physics, Wiley 2005.
- [17] K. Tsuboi, Solution-grown crystals of poly(vinyl alcohol), Journal of Macromolecular Science, Part B 2(4) (1968) 603-622.
- [18] H.E. Assender, A.H. Windle, Crystallinity in poly(vinyl alcohol). 1. An X-ray diffraction study of atactic PVOH, Polymer 39(18) (1998) 4295-4302.
- [19] D.E. Bosley, X-ray determination of crystallinity in poly(ethylene terephthalate), Journal of Applied Polymer Science 8(4) (1964) 1521-1529.
- [20] B. Wunderlich, Thermal Analysis Tools, Thermal Analysis of Polymeric Materials, Springer Berlin Heidelberg, Berlin, Heidelberg, 2005, pp. 279-454.
- [21] V.B.F. Mathot, Calorimetry and Thermal Analysis of Polymers, Hanser/ Gardner Publications, Cincinnati, Ohio, 1994.
- [22] E. Iervolino, A.W. van Herwaarden, F.G. van Herwaarden, E. van de Kerkhof, P.P.W. van Grinsven, A.C.H.I. Leenaers, V.B.F. Mathot, P.M. Sarro, Temperature calibration and electrical characterization of the differential scanning calorimeter chip UFS1 for the Mettler-Toledo Flash DSC 1, Thermochemica Acta 522(1-2) (2011) 53-59.
- [23] S. Neuenfeld, C. Schick, Verifying the symmetry of differential scanning calorimeters concerning heating and cooling using liquid crystal secondary temperature standards, Thermochemica Acta 446(1-2) (2006) 55-65.
- [24] Q Series Thermal Analyzers, TA Instruments, New Castle, DE, 2006.
- [25] Q Series™ Getting Started Guide, N ed., TA Instruments, New Castle, DE, 2007.
- [26] S.Z.D. Cheng, S. Lim, L.H. Judovits, B. Wunderlich, Heat capacities of high melting polymers containing phenylene groups, Polymer 28(1) (1987) 10-22.

- [27] H.S. Bu, W. Aycock, S.Z.D. Cheng, B. Wunderlich, Heat capacities of various solid linear macromolecules, *Polymer* 29(8) (1988) 1485-1494.
- [28] M. Pyda, R.C. Bopp, B. Wunderlich, Heat capacity of poly(lactic acid), *The Journal of Chemical Thermodynamics* 36(9) (2004) 731-742.
- [29] M. Pyda, B. Wunderlich, Reversing and Nonreversing Heat Capacity of Poly(lactic acid) in the Glass Transition Region by TMDSC, *Macromolecules* 38(25) (2005) 10472-10479.
- [30] M. Pyda, X. Hu, P. Cebe, Heat Capacity of Silk Fibroin Based on the Vibrational Motion of Poly(amino acid)s in the Presence and Absence of Water, *Macromolecules* 41(13) (2008) 4786-4793.
- [31] A.P. Gray, Polymer crystallinity determinations by DSC, *Thermochimica Acta* 1(6) (1970) 563-579.
- [32] B. Wunderlich, CHAPTER VIII - Equilibrium Melting, *Macromolecular Physics*, Academic Press, San Diego, 1980, pp. 1-127.
- [33] B. Wunderlich, CHAPTER IX - Irreversible Melting, *Macromolecular Physics*, Academic Press, San Diego, 1980, pp. 128-253.
- [34] U. Gaur, B.B. Wunderlich, B. Wunderlich, Heat Capacity and Other Thermodynamic Properties of Linear Macromolecules. VII. Other Carbon Backbone Polymers, *Journal of Physical and Chemical Reference Data* 12(1) (1983) 29-63.
- [35] M.L. Arnal, V. Balsamo, G. Ronca, A. Sánchez, A.J. Müller, E. Cañizales, C. Urbina de Navarro, Applications of Successive Self-Nucleation and Annealing (SSA) to Polymer Characterization, *Journal of Thermal Analysis and Calorimetry* 59(1) (2000) 451-470.
- [36] J. Chau, J. Teh, Successive self-nucleation and annealing in the solvated state of ethylene copolymers, *Journal of Thermal Analysis and Calorimetry* 81(1) (2005) 217-223.

- [37] B. Fillon, B. Lotz, A. Thierry, J.C. Wittmann, Self-Nucleation and Enhanced Nucleation of Polymers – Definition of a Convenient Calorimetric Efficiency Scale and Evaluation of Nucleating Additives in Isotactic Polypropylene (Alpha-Phase) *Journal of Polymer Science Part B-Polymer Physics* 31(10) (1993) 1395-1405.
- [38] B. Fillon, A. Thierry, J.C. Wittmann, B. Lotz, Self-Nucleation and Recrystallization of Polymers – Isotactic Polypropylene, Beta-Phase – Beta-Alpha-Conversion and Beta-Alpha-Growth Transitions, *Journal of Polymer Science Part B-Polymer Physics* 31(10) (1993) 1407-1424.
- [39] B. Fillon, J.C. Wittmann, B. Lotz, A. Thierry, Self-Nucleation and Recrystallization of Isotactic Polypropylene (Alpha-Phase) Investigated by Differential Scanning Calorimetry *Journal of Polymer Science Part B-Polymer Physics* 31(10) (1993) 1383-1393.
- [40] C. Marco, G. Ellis, M.A. Gómez, J.M. Arribas, Analysis of the Dynamic Crystallisation of Isotactic Polypropylene/ $\alpha$ -Nucleating Agent Systems by DSC, *Journal of Thermal Analysis and Calorimetry* 68(1) (2002) 61-74.
- [41] A.J. Müller, M.L. Arnal, Thermal fractionation of polymers, *Progress in Polymer Science* 30(5) (2005) 559-603.
- [42] I. Arandia, A. Mugica, M. Zubitur, A. Arbe, G. Liu, D. Wang, R. Mincheva, P. Dubois, A.J. Müller, How Composition Determines the Properties of Isodimorphic Poly(butylene succinate-ran-butylene azelate) Random Biobased Copolymers: From Single to Double Crystalline Random Copolymers, *Macromolecules* 48(1) (2015) 43-57.
- [43] X.J. Chen, A. Mamun, R.G. Alamo, Effect of Level of Crystallinity on Melt Memory Above the Equilibrium Melting Temperature in a Random Ethylene 1-Butene Copolymer, *Macromol. Chem. Phys.* 216(11) (2015) 1220-1226.

- [44] Z. Horváth, A. Menyhárd, P. Doshev, M. Gahleitner, J. Varga, C. Tranninger, B. Pukánszky, Chain regularity of isotactic polypropylene determined by different thermal fractionation methods, *Journal of Thermal Analysis and Calorimetry* 118(1) (2014) 235-245.
- [45] A. Jalali, M.A. Huneault, S. Elkoun, Effect of thermal history on nucleation and crystallization of poly(lactic acid), *J. Mater. Sci.* 51(16) (2016) 7768-7779.
- [46] A.T. Lorenzo, M.L. Arnal, J.J. Sánchez, A.J. Müller, Effect of annealing time on the self-nucleation behavior of semicrystalline polymers, *Journal of Polymer Science Part B: Polymer Physics* 44(12) (2006) 1738-1750.
- [47] B.O. Reid, M. Vadlamudi, A. Mamun, H. Janani, H.H. Gao, W.B. Hu, R.G. Alamo, Strong Memory Effect of Crystallization above the Equilibrium Melting Point of Random Copolymers, *Macromolecules* 46(16) (2013) 6485-6497.
- [48] M.Q. Ren, X.J. Chen, Y. Sang, R.G. Alamo, Effect of Heterogeneous Short Chain Branching Distribution on Acceleration or Retardation of the Rate of Crystallization from Melts of Ethylene Copolymers Synthesized with Ziegler-Natta Catalysts, *Macromol. Symp.* 356(1) (2015) 131-141.
- [49] E. Zhuravlev, C. Schick, Fast scanning power compensated differential scanning nanocalorimeter: 2. Heat capacity analysis, *Thermochimica Acta* 505(1-2) (2010) 14-21.
- [50] E. Zhuravlev, C. Schick, Fast scanning power compensated differential scanning nanocalorimeter: 1. The device, *Thermochimica Acta* 505(1-2) (2010) 1-13.
- [51] A.A. Minakov, C. Schick, Ultrafast thermal processing and nanocalorimetry at heating and cooling rates up to 1MK/s, *Review of Scientific Instruments* 78(7) (2007) 073902.
- [52] I. Mettler Toledo International, Flash DSC 1 — Flash Differential Scanning Calorimeter from METTLER TOLEDO 2017. [http://www.mt.com/us/en/home/library/videos/lab-analytical-instruments/flash\\_dsc1.html](http://www.mt.com/us/en/home/library/videos/lab-analytical-instruments/flash_dsc1.html). (Accessed 6/12/2017 2017).

- [53] A. Toda, M. Konishi, An evaluation of thermal lags of fast-scan microchip DSC with polymer film samples, *Thermochimica Acta* 589 (2014) 262-269.
- [54] J.E.K. Schawe, Analysis of non-isothermal crystallization during cooling and reorganization during heating of isotactic polypropylene by fast scanning DSC, *Thermochimica Acta* 603 (2015) 85-93.
- [55] V. Mathot, M. Pyda, T. Pijpers, G. Vanden Poel, E. van de Kerkhof, S. van Herwaarden, F. van Herwaarden, A. Leenaers, The Flash DSC 1, a power compensation twin-type, chip-based fast scanning calorimeter (FSC): First findings on polymers, *Thermochimica Acta* 522(1) (2011) 36-45.
- [56] D. Thomas, P. Cebe, Self-nucleation and crystallization of polyvinyl alcohol, *Journal of Thermal Analysis and Calorimetry* 127(1) (2017) 885-894.
- [57] M. Chen, M. Du, J. Jiang, D. Li, W. Jiang, E. Zhuravlev, D. Zhou, C. Schick, G. Xue, Verifying the symmetry of ultra-fast scanning calorimeters using liquid crystal secondary temperature standards, *Thermochimica Acta* 526(1) (2011) 58-64.
- [58] I. Kolesov, D. Mileva, R. Androsch, C. Schick, Structure formation of polyamide 6 from the glassy state by fast scanning chip calorimetry, *Polymer* 52(22) (2011) 5156-5165.
- [59] P. Cebe, B.P. Partlow, D.L. Kaplan, A. Wurm, E. Zhuravlev, C. Schick, Using flash DSC for determining the liquid state heat capacity of silk fibroin, *Thermochimica Acta* 615 (2015) 8-14.
- [60] STARe Evaluation, Mettler Toledo GmbH, Analytical, Schwerzenbach, Switzerland, 2016.
- [61] P. Cebe, X. Hu, D.L. Kaplan, E. Zhuravlev, A. Wurm, D. Arbeiter, C. Schick, Beating the Heat - Fast Scanning Melts Silk Beta Sheet Crystals, *Scientific Reports* 3 (2013) 7.
- [62] A.A. Minakov, S.A. Adamovsky, C. Schick, Non-adiabatic thin-film (chip) nanocalorimetry, *Thermochimica Acta* 432(2) (2005) 177-185.

- [63] G.V. Poel, D. Istrate, A. Magon, V. Mathot, Performance and calibration of the Flash DSC 1, a new, MEMS-based fast scanning calorimeter, *Journal of Thermal Analysis and Calorimetry* 110(3) (2012) 1533-1546.
- [64] P. Cebe, B.P. Partlow, D.L. Kaplan, A. Wurm, E. Zhuravlev, C. Schick, Fast Scanning Calorimetry of Silk Fibroin Protein: Sample Mass and Specific Heat Capacity Determination, in: C. Schick, V. Mathot (Eds.), *Fast Scanning Calorimetry*, Springer International Publishing, Cham, 2016, pp. 187-203.
- [65] M. Pyda, Polyvinyl Alcohol (PVA) Heat Capacity, Enthalpy, Entropy, Gibbs Energy, 2014. [http://materials.springer.com/polymerthermodynamics/docs/athas\\_0147](http://materials.springer.com/polymerthermodynamics/docs/athas_0147). (Accessed 27-10-2015 2015).

## *Chapter 4 Self Nucleation of PVA*

### *4.0 Sample Preparation Approaches*

In order to further the understanding of the crystallization behavior of PVA an investigation into the self nucleation behavior has been conducted. This chapter is based largely on publication [1] Typically these experiments rely on an amorphous starting material [2-4] which is then brought into a semi-crystalline state by carefully cold or melt crystallizing the sample. Several unsuccessful attempts were made to create an amorphous PVA film from which samples could be cut. The first approach involved simple solution casting of a film from an 8% solution as described in **Section 2.2.1** which resulted in a semi-crystalline film. The next approach involved slowly dripping 8% PVA solution into a vigorously stirring bath of acetone. Acetone is a non solvent for PVA and will cause the polymer to rapidly precipitate out of solution. The mixture of acetone and solid PVA flakes were passed through a filter and placed in the vacuum oven to dry at room temperature overnight. The final attempt involved dropping PVA solution into a bath of acetone and dry ice, a solution with a temperature of -78 °C, in order to allow for both an ejection of water and a quenching of the polymer into an amorphous glass. Again, the flakes of solid material were collected by filtering and then placed in the vacuum oven to remove any surface acetone. Upon DSC measurements of both acetone precipitated flakes there was no apparent crystallization exotherm yet a melting endotherm was observed indicating the presence of crystals. This indicates that the polymer was able to crystallize as solvent was ejected. With this inability to produce amorphous PVA films it was decided that the best approach would be to take a solution cast film, which were the easiest to prepare, and use the semi-crystalline state, as cast, as the starting crystalline state for any self nucleation investigations.

#### **4.1 Thermal Stability of PVA**

It is well established that PVA degrades at temperatures in excess of 200 °C [5-12], with recent attention paid to the connection between non-isothermal crystallization and non-isothermal degradation that PVA, and PVA composite systems, undergo. [9-11] In general, the transition from the crystalline solid to the amorphous liquid is reversible in polymers. However once PVA becomes an amorphous liquid at high temperature, PVA is free to undergo a thermal degradation reaction resulting in random chain scission. [7] Multiple heating and cooling cycles result in a reduction of both the crystallization and melting enthalpies, as well as reduction in the observed melting peak temperature. [9, 11, 12] A cast film of PVA was treated through 10 cycles of cooling from the melt (**Figure 4.1A**) and reheating (**Figure 4.1B**) between 40 °C and 240 °C at 10 °C min<sup>-1</sup>. Thermogravimetric measurements were made with the same protocol to assess the degradation per cycle as well as to assess the degradation during various self nucleation conditions (**Figure 4.2**). The results presented in **Figure 4.1** show the same reduction of enthalpy and peak temperature as reported in the literature. [9, 11, 12] This depression in both peak temperature and peak area indicates that not only is the driving force for crystallization reduced, but the stability of crystallizable domains is decreased as well. [9, 13] This reduction is caused by thermal degradation between cycles and as a result, it was not possible to study just one sample treated at various self nucleation temperatures, nor was it possible to hold PVA isothermally at temperatures beyond the observed peak melting point without occurrence of degradation.

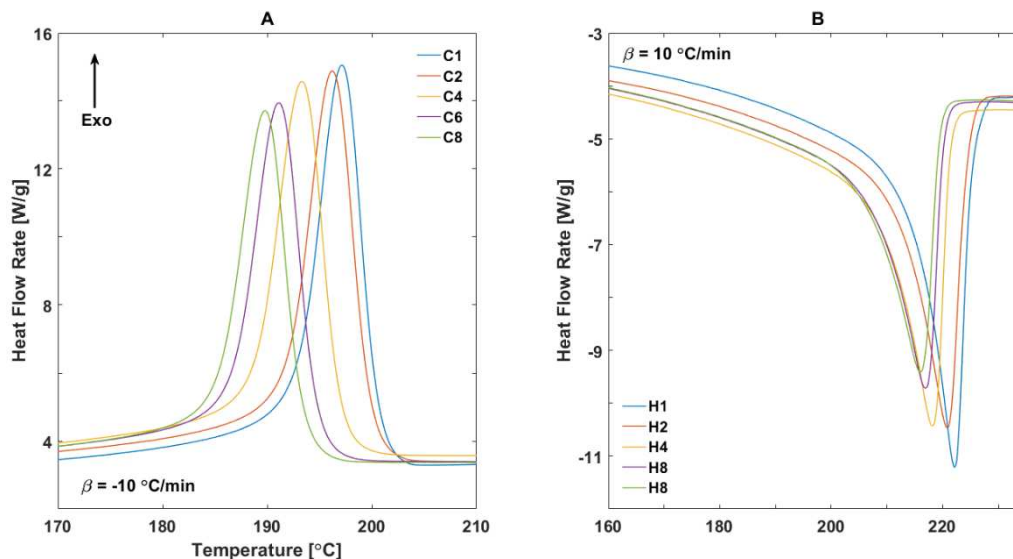


**Figure 4.1:** Heat flow rate vs. temperature curves over subsequent cycles (numbered 1-8 corresponding to cycle) of: **(A)** cooling “C” from  $T_s$ , showing loss of exotherm area and depression of peak crystallization temperature; **(B)** reheating “H”, showing loss of endotherm area and depression of peak melting temperature. Here, the same sample was used for all cycles of cooling and heating

Recent studies on the non-isothermal crystallization and the degradation of PVA during melting and crystallization have reported on the weight loss per melting-cooling cycle as well as the weight loss as a function of time for various temperatures approaching the equilibrium melting point. [9, 11] It was reported that PVA samples with  $M_w \sim 145,000$  and 98-99 mol% degree of hydrolysis would lose up to 5% of the mass after one cycle of heating at  $30 \text{ }^\circ\text{C min}^{-1}$  to  $245 \text{ }^\circ\text{C}$ , holding for 5 minutes, and cooling at  $30 \text{ }^\circ\text{C min}^{-1}$ . Isothermal thermogravimetric experiments at  $240 \text{ }^\circ\text{C}$  showed that for times up to 150 min, samples retained 94% of their mass [10]. PVA used here had lower molecular mass,  $78,000 \text{ g mol}^{-1}$ , and a degree of hydrolysis at the lower end of the range reported, at 98 mol%, and demonstrated greater sensitivity to thermal degradation. Thermogravimetric isothermal treatments were performed for  $T_s$  values between  $220 \text{ }^\circ\text{C}$  and  $240 \text{ }^\circ\text{C}$  in  $5 \text{ }^\circ\text{C}$  increments. For isothermal treatments within the melting endotherm (between  $220 \text{ }^\circ\text{C}$

and 230 °C) degradation mass loss was found to range between 2% and 6%. Thermogravimetric results can be seen in **Figure 4.2**.

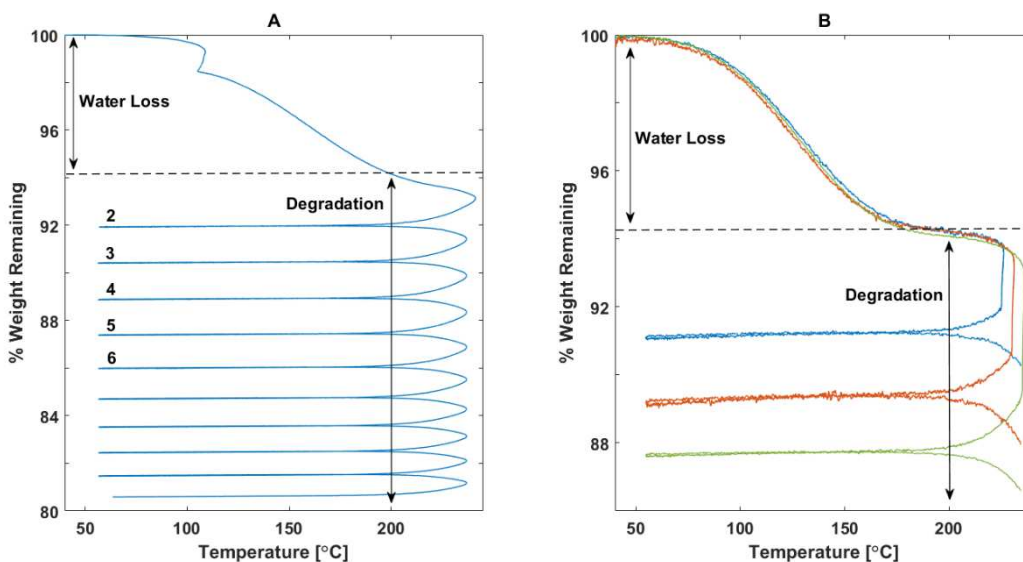


**Figure 4.2:** %Weight remaining vs Temperature for **(A)** TGA scans over subsequent cycles of heating and cooling to 240 °C at 10 °C/min. Cycles 2-6 are numbered for clarity. **(B)** TGA scans at different self nucleation temperatures:  $T_s = 225$  °C (blue), 230 °C (red), and 235 °C (green). Each sample is heated to  $T_s$ , held 5 min (vertical section of the curves), then cooled and reheated. The arrows signify the range of mass lost due to water removal and to degradation.

Thermogravimetric results indicate that all solution-cast PVA films contained an average of 5.5% bound water which is ejected during heating between 90 °C and 170 °C. After bound water is removed, samples do not show another large drop in % mass remaining until degradation sets in at temperatures in excess of 200 °C. All self nucleation temperatures are in excess of 170 °C, at which point all bound water has been removed. It was therefore not necessary to include a drying step prior to the isothermal hold at  $T_s$  since there is no bound water remaining in the sample. For self nucleation temperatures between 220 °C and 240 °C, the PVA film loses between 2 and 9% of its mass during the five minute isothermal hold at  $T_s$ . Mass loss per cycle and peak

crystallization temperature were tracked for the degradation ranging between 0 and 10%. The results are summarized below in **Table 4.1**. A linear relationship between the peak crystallization temperature and % mass lost (ML) of polymer is observed and serves as the baseline for any observations of the effect of self nucleation. At the lower bound,  $T_s = 220$  °C, samples lose about 2% of their mass during the isothermal self nucleation holding period. This increases to approximately 6% when the film is heated to a temperature near the endotherm foot, around  $T_s = 230$  °C. By the final self nucleation temperature,  $T_s = 240$  °C, samples lose about 9% of their mass. Mass loss during the isothermal hold at  $T_s$  was found to increase linearly with the value of  $T_s$  over the range of temperatures investigated. Mass losses for intermediate values were determined from the best fit to the data. Table 1 and Table 2 WL(Ts) Stats Here The TGA results were used to account for mass losses during the self nucleation experiments in order to obtain the correct endotherm and exotherm areas for calculation of sample crystallinity, as described below.

**Table 4.1:** % Sample mass loss per cycle and peak crystallization temperature

| <b>Cycle</b> | <b>ML %<br/>± 0.2%</b> | <b>Peak T<sub>c</sub> °C<br/>± 0.1 °C</b> |
|--------------|------------------------|---|
| 1            | 2.2                    | 197.2                                     |
| 2            | 3.8                    | 196.2                                     |
| 3            | 5.4                    | 194.8                                     |
| 4            | 6.9                    | 193.2                                     |
| 5            | 8.3                    | 192.0                                     |
| 6            | 9.5                    | 191.1                                     |

Samples were cast from an aqueous solution and as a result contain bound water; during the first heating this bound water is ejected and the initial crystallinity can be calculated after accounting for this loss. [10] The mass changing function,  $M_1$ , is used to correct the initial DSC mass,  $M_0$ , for water removal using the fraction of water lost ( $WL$ ) as measured in TGA:

$$M_l = M_0(1 - WL) \quad (2.1)$$

Sample masses after water removal correction,  $M_l$  (Eqn. 2.1), were adjusted once again to account for the mass loss due to degradation,  $M_{\text{deg}}$ , during the isothermal hold at  $T_s$  yielding the final sample mass,  $M_f$ . This was done by taking into account the fraction of mass loss ( $ML$ ) from TGA experiments in the following manner:

$$M_{\text{deg}} = ML(T_s) * M_0 \quad (2.2a)$$

$$M_f = M_l - M_{\text{deg}} \quad (2.2b)$$

Adjustments to the mass of the sample are summarized below in **Table 4.2**, to account both for bound water removal (allowing correction of the first melting endotherm area), and for degradation occurring during the hold at  $T_s$  (allowing correction of the subsequent crystallization exotherm and melting endotherm areas.) From the corrected endotherm area, crystallinity is calculated according to Eqn. 3.14.

#### **4.2 Self Nucleation of PVA by DSC**

Following the initial heating to  $T_s$ , the PVA film sample is isothermally held for 5 min then cooled, leaving the system in a semi-crystalline state (**Figure 4.3A**). Subsequent melting of this semi-crystalline state (**Figure 4.3B**) reveals thermal characteristics of the crystals subjected to, or formed by, the various treatments. Self nucleation temperatures,  $T_s$ , ranged from 220 °C to 230 °C in 1 °C increments revealing the transition from domain III into domain II and then from 230 °C to 240 °C in 2 °C increments revealing the transition from domain II to domain I.

The heat flow curves presented in **Figure 4.3** are a representative sampling of the self nucleation temperatures studied, as they present the general trends which allow for the characterization of self nucleation domains for PVA. In **Figure 4.3A** crystallization peaks upon

cooling from the selected self nucleation temperature can be grouped to show three distinct behaviors. First, at the bottom of **Figure 4.3A**, we see a group of curves (dark blue, red, and yellow) corresponding to lowest values of  $T_s$ . These curves display the smallest exotherm areas and highest peak crystallization temperatures. In the second group are the middle curves (purple and green) corresponding to intermediate values of  $T_s$ . These show much larger exotherm areas, and the second-highest peak crystallization temperatures which remain nearly constant within the group. Third, the last group corresponds to highest values of  $T_s$  (one example is shown in **Figure 4.3A** by the light blue curve). Within this group, the exotherm areas are similar to the second group but the exothermic peak temperatures are the lowest. These data display behaviors which are similar to that observed in isotactic polypropylene by Fillon *et al.* [2-4].

**Table 4.2:** Corrections to Initial Mass of PVA from Bound Water Removal and Degradation, at Various Self Nucleation Temperatures

| $T_s$ °C | $M_0$ <sup>a</sup> mg<br>± 0.01 mg | $M_{H_2O}$ <sup>b</sup> mg<br>± 0.01 mg | $M_{H_2O}/M_0$<br>x 100% | $M_1$ <sup>c</sup> mg<br>± 0.01 mg | $ML$ <sup>d</sup> %<br>± 0.5% | $M_f$ <sup>e</sup> mg<br>± 0.07 mg |
|----------|------------------------------------|---|--------------------------|------------------------------------|-------------------------------|------------------------------------|
| 220      | 6.63                               | 0.36                                    | 5.5                      | 6.27                               | 2.0                           | 6.14                               |
| 221      | 6.88                               | 0.38                                    | 5.5                      | 6.50                               | 2.3                           | 6.34                               |
| 222      | 6.90                               | 0.38                                    | 5.5                      | 6.52                               | 2.6                           | 6.34                               |
| 223      | 6.79                               | 0.37                                    | 5.5                      | 6.42                               | 3.0                           | 6.22                               |
| 224      | 4.46                               | 0.24                                    | 5.5                      | 4.22                               | 3.3                           | 4.07                               |
| 225      | 5.97                               | 0.33                                    | 5.5                      | 5.64                               | 3.6                           | 5.43                               |
| 226      | 5.03                               | 0.28                                    | 5.5                      | 4.75                               | 4.0                           | 4.55                               |
| 227      | 5.10                               | 0.28                                    | 5.5                      | 4.82                               | 4.3                           | 4.60                               |
| 228      | 6.31                               | 0.35                                    | 5.5                      | 5.96                               | 4.6                           | 5.67                               |
| 229      | 8.86                               | 0.49                                    | 5.5                      | 8.37                               | 5.0                           | 7.93                               |
| 230      | 7.64                               | 0.42                                    | 5.5                      | 7.22                               | 5.3                           | 6.82                               |
| 232      | 7.19                               | 0.39                                    | 5.5                      | 6.80                               | 6.0                           | 6.37                               |
| 234      | 7.27                               | 0.40                                    | 5.5                      | 6.87                               | 6.6                           | 6.39                               |
| 236      | 10.40                              | 0.57                                    | 5.5                      | 9.83                               | 7.3                           | 9.07                               |
| 238      | 6.56                               | 0.36                                    | 5.5                      | 6.20                               | 8.0                           | 5.68                               |
| 240      | 8.40                               | 0.46                                    | 5.5                      | 7.94                               | 8.7                           | 7.21                               |

<sup>a</sup> Initial sample mass

<sup>b</sup> Mass of water removed on first heating to  $T_s$

<sup>c</sup> Sample mass after correction for bound water removal (using Eqn. 2)

<sup>d</sup> Percent of mass lost by degradation during holding 5 min. at  $T_s$

<sup>e</sup> Final sample mass after correction for water removal and degradation (using Eqn. 3a,b)

Upon reheating the samples, the heat flow curves in **Figure 4.3B** exhibit two distinct types of behavior. When there is no annealing of pre-existing crystals (which occurs at the higher values of  $T_s$ ), there is only one endotherm present, as seen in the upper three curves in **Figure 4.3B** (light blue, green, purple). The second type of melting behavior can be seen in the lower three curves in **Figure 4.3B** (yellow, red, dark blue) where a melting doublet is observed. This is due to partial melting and annealing of crystals which were formed during the isothermal holding at relatively lower values of  $T_s$ .

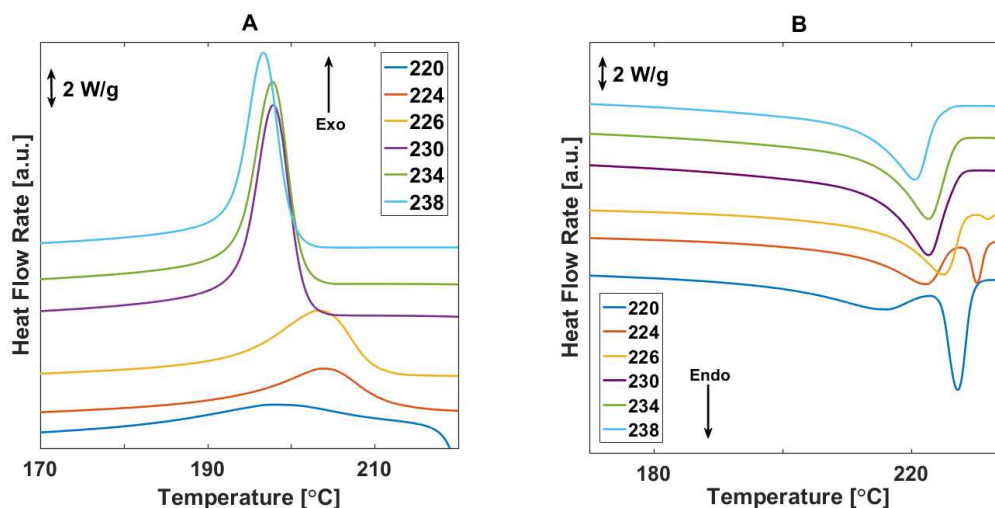


**Figure 4.3:** DSC heat flow rate vs. temperature, for (A) cooling and (B) reheating after thermal treatment at various self nucleation temperatures:  $T_s = 220$  °C (dark blue),  $224$  °C (red),  $226$  °C (yellow),  $230$  °C (purple),  $234$  °C (green),  $238$  °C (light blue). Curves have been vertically shifted for clarity.

As  $T_s$  is systematically increased from  $220$  °C the first region of interest comprises the lowest curves in **Figure 4.3A** which possess high crystallization temperatures and small peak area. Here there are very few crystals forming during the isothermal holding at  $T_s$ . For temperatures  $T_s < 227$  °C the system is in domain III (partial melting and annealing[2-4]) where semi-crystalline structure remains present because the existing crystals cannot fully melt. Some of these crystals

will anneal (thicken) requiring a higher temperature to melt than other less perfect crystals that were formed by non-isothermal crystallization during cooling from  $T_s$ . This annealing step results in two distinct populations of crystals contributing to the double melting peaks observed in the lowest three curves in **Figure 4.3B**. Here one population comprises some small crystals that either formed during cooling (or remained present in the initial film). These melt at lower temperatures than the second population of more stable, annealed crystals. Plotted in **Figure 4.4** are the observed melting onset temperatures as a function of self nucleation temperature,  $T_s$ . The domain boundary can be drawn following the last appearance of a melting doublet as  $T_s$  increases. We can identify the domain III boundary at 227 °C and further increases in self nucleation temperature will drive the system to exhibit crystallization behavior belonging to either domain I or II.

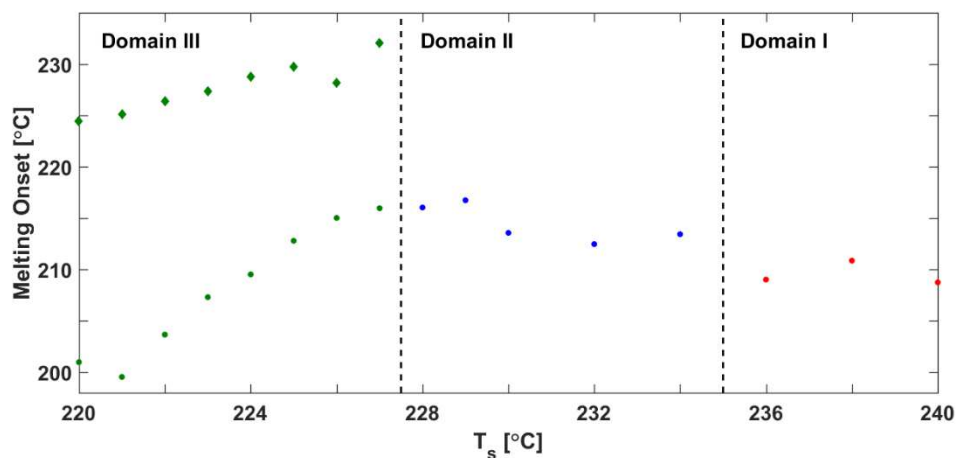


**Figure 4.4:** Melting onset temperatures as a function of  $T_s$  with low temperature onset plotted in circles and the second higher temperature onset (Domain III only) plotted in diamonds. Domain III - green symbols; Domain II - blue circles; Domain I - red circles. Domain boundaries are denoted by vertical dashed lines

A second shift can be observed in **Figure 4.4** as  $T_s$  is increased further. Between  $T_s = 228^\circ\text{C}$  and  $T_s = 234^\circ\text{C}$  the average peak melting temperature is observed to be  $214.5^\circ\text{C} \pm 1.2^\circ\text{C}$ . As self

nucleation temperatures exceed  $T_s = 235\text{ }^\circ\text{C}$  the peak melting temperature drops to an average of  $209.5\text{ }^\circ\text{C} \pm 0.7\text{ }^\circ\text{C}$ . This shift is indicative of a change in the non-isothermal crystallization occurring during cooling. Crystals formed within domain II, the exclusive self nucleation domain [4] form from either seed nuclei or regions within the melt where the polymer chains are sufficiently aligned to allow for rapid nucleation and crystallization. This results in formation of more thermally stable crystals as the system is able to crystallize at higher temperature where more perfect crystal structures are kinetically favored before the quenched and the system returns to the vitreous state.

The distinction between domains I and II can be made clearer based on evidence found in the cooling scans by plotting peak crystallization temperature,  $T_c$ , against self nucleation temperature,  $T_s$ , as presented below in **Figure 4.5**. With the domain III boundary identified in **Figure 4.4** as the last temperature where a melting doublet is observed, a corresponding downward (towards lower temperature) shift in the peak crystallization temperature can be used to identify the boundary between domains I and II. As  $T_s$  was increased from  $230\text{ }^\circ\text{C}$  to  $240\text{ }^\circ\text{C}$  in  $2\text{ }^\circ\text{C}$  increments a downward shift of approximately  $4\text{ }^\circ\text{C}$  in the peak crystallization temperature was observed for self nucleation values in excess of  $235\text{ }^\circ\text{C}$ . The self nucleation temperature range of  $227\text{ }^\circ\text{C} < T_s < 235\text{ }^\circ\text{C}$  shows an increase in both melting onset temperature and peak crystallization temperature, which remains nearly constant over the  $6\text{ }^\circ\text{C}$  range at  $198.1\text{ }^\circ\text{C} \pm 0.4\text{ }^\circ\text{C}$  before dropping to  $194.4\text{ }^\circ\text{C} \pm 0.7\text{ }^\circ\text{C}$ .

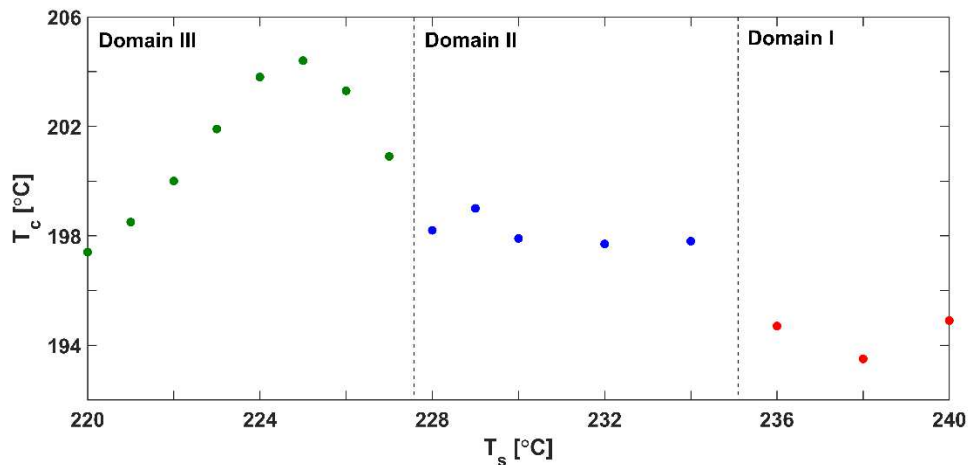


**Figure 4.5:** Crystallization peak temperatures as a function of  $T_s$ . Domain I (red), domain II (blue), domain III (green).

For self nucleation temperatures in excess of 235 °C the system will reside in domain I and the peak temperature of the crystallization exotherm will remain relatively invariant. As self nucleation temperatures are brought in excess of 240 °C any further depression of the peak crystallization temperatures will be due to thermal degradation which has been previously shown to reduce both exotherm area and peak exotherm temperature [9, 11]. Further evidence for this can be seen in **Figure 4.6**. Peak crystallization temperatures (red circles) were tracked for one sample over many cycles, as seen in the DSC data shown in **Figure 4.2A**, and correlated with TGA results reported in **Table 4.1** to obtain a relationship between peak crystallization temperature and % Mass Loss. For comparison, we also plot the peak crystallization temperature (blue squares) observed during self nucleation experiments (using a fresh sample for each test) where the observed % Mass Loss is due to the five minute hold at  $T_s$ .

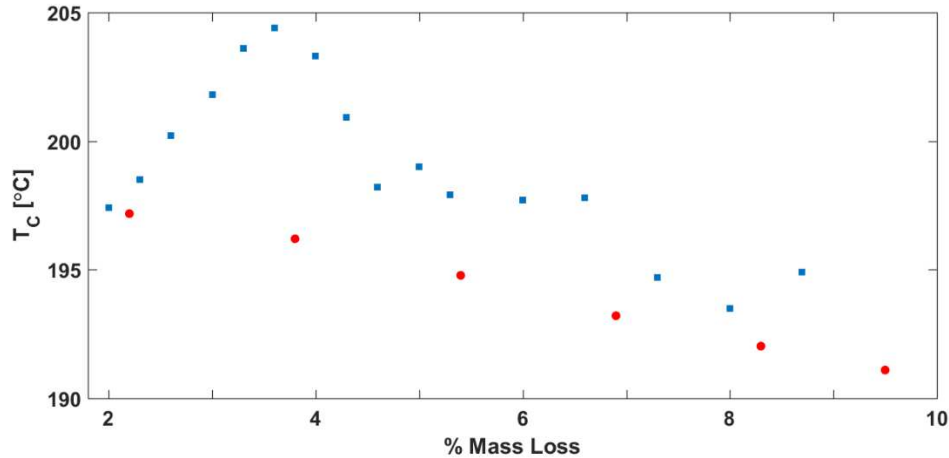


**Figure 4.6:** Peak crystallization temperature against % Mass Loss for self nucleation experiments with each point representing a fresh sample (blue squares) and for multicycle experiments performed on a single sample (red circles).

It can be seen in the multi-cycle data of **Figure 4.6** that the peak crystallization temperature decreases steadily with % Mass Loss (and increasing self nucleation temperature). Compared to this steady drop, the self-nucleation data show a nearly constant value of peak crystallization temperature, at  $198.1 \text{ °C} \pm 0.4 \text{ °C}$ , during domain II. This indicates that while degradation does occur, it does not mask or prevent self nucleation from taking place during the 5 min isothermal holds at  $T_s$ .

The driving mechanism for the nucleation and crystallization of PVA within domain I is heterogeneous nucleation relying on both impurities present in the sample during the creation of the parent film and those introduced as the sample degrades during the isothermal hold at  $T_s$ . The data presented in **Figures 4.4 and 4.5** show that for self nucleation temperatures belonging to domain II which is between  $228 \text{ °C}$  and  $234 \text{ °C}$  the crystallization relies on ‘melt memory’ effects which boosts nucleation density and allows crystallization to proceed at higher temperatures. This is a special case of heterogeneous nucleation, since the nucleating agents at work are oriented

regions of polymer in the melt and small crystal fragments which provide the best possible sites for crystal nucleation and growth.

Crystallinity was determined during the final step in the general self nucleation protocol from the endothermic peak temperature and peak area allowing for comparison between self nucleation temperatures. **Figure 4.7** shows the crystallinity as a function of  $T_s$  for samples which were treated to lie within domain I and II to assess if there was any difference in the final crystallinity as a result of the thermal treatments applied. The data show there is no observable trend between crystallinity and self nucleation temperature between domain II and domain I. The treatments within domain II allowed for the formation of slightly more stable crystals compared to domain I as indicated by the slight upward shift in melting onset shown in **Figure 4.4**.

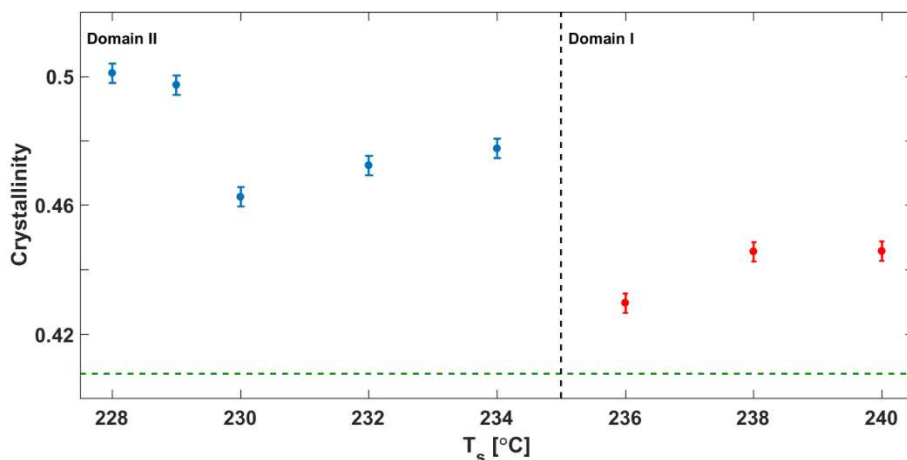


**Figure 4.7:** Domain II (blue circles) and Domain I (red circles) final crystallinity vs. self nucleation temperature with error bars  $\pm 0.004$ . The upper bound on the average initial crystallinity is indicated by the green dashed line.

The initial film samples had a crystallinity of  $39.2\% \pm 1.6\%$  and the crystallization proceeded by a solution crystallization process that occurred during the initial vacuum oven drying

of water-cast films. Following the self nucleation experiments the crystallinity of the samples increased. Within Domain II the average crystallinity increased to  $47.8\% \pm 1.0\%$ . Domain I also showed an increase in crystallinity as compared to the parent film with an average of  $43.7\% \pm 0.8\%$ . Self seeding increased density of nuclei throughout the melt within Domain II leading higher crystallinity following the non-isothermal crystallization upon cooling from  $T_s$  as compared to Domain I. The drop in the crystallinity for  $T_s > 234$  °C is further evidence for the Domain II-Domain I boundary. The crystallinity remains relatively constant within Domain I indicating that the thermal degradation of material has not progressed far enough to prevent the non-isothermal crystallization from running to completion for melt crystallization from temperatures between 240 °C and 235 °C.

### **4.3 Self Nucleation by FSC**

Insights gained from the conventional thermal analysis investigation into the self nucleation behavior of PVA were carried into fast scanning calorimetry (FSC) experiments. While it is true that the exact temperatures of the domain boundaries might not hold constant, due in part to the transition from a bulk material to a thin film (250  $\mu\text{m}$  down to 2-3  $\mu\text{m}$ ), the presence or absence of observed self nucleation effects will further the understanding of the nucleation and crystallization behavior of PVA. Unlike measurements made in standard DSC the thermal programs for self nucleation investigations by FSC take place on a single sample. A single sample is cut from the spin coated parent film as described in **Section 2.2.1** and loaded directly onto the UFSC1 sensor as shown in **Figure 2.2A**. Both ultra-fast heating and cooling rates of 2,000 K/s and the short hold times,  $t_s$ , of 0.05 s at  $T_s$  minimize sample degradation, (this is discussed in greater

detail in **Chapter 5**, see **Figure 5.2**) and the cycle to cycle recovery of glassy and melt baselines after each cooling and reheating from  $T_s$  are shown below in **Figure 4.8**.

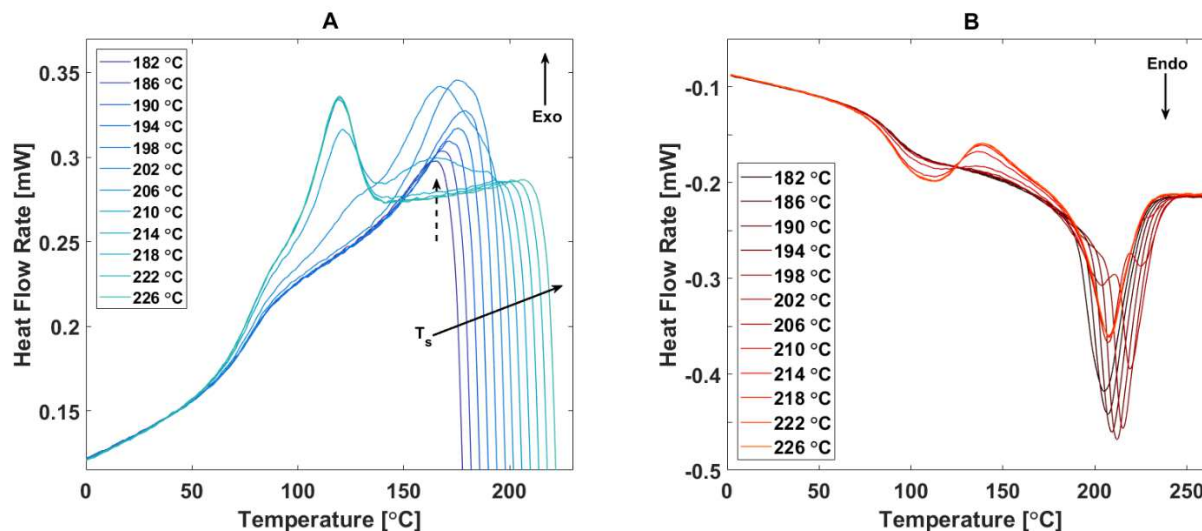


**Figure 4.8:** Sampling of FSC heat flow rates vs. Temperature for (a) cooling and (b) reheating for various self nucleation temperatures,  $T_s$ . In order to highlight the recovery of glassy and melt baselines, curves have not been separated.

Prior to the onset of each self nucleation run the sample is brought to the melt at 265 °C at 2,000 K/s, held for 0.01 seconds, and then cooled to -80 °C at -2,000 K/s. This results in a small amount of homogeneously nucleated crystals which grow further upon reheating by non-isothermal cold crystallization. It is this crystal population that will either anneal and thicken, partially melt, or return to a homogenous melt during the short isothermal hold at  $T_s$ . Self nucleation temperatures were sampled spanning a range from just below the initial melting endotherm onset at 180 °C up to above the endotherm foot at 226 °C. Cooling scans seen in **Figure 4.8a** present a transition from annealing and crystal growth, to a mixture of heterogeneous nucleation and crystallization from crystals surviving the partial melting at  $T_s$  and homogenous nucleation of amorphous material, and exclusively homogeneous nucleation of molten material at a large undercooling. For self

nucleation temperatures  $180\text{ }^{\circ}\text{C} < T_s < 198\text{ }^{\circ}\text{C}$  the onset of cooling at high temperature (marked by the dashed, vertical arrow in **Figure 4.8A**) masks much of the exothermic signal that would indicate heterogenous nucleation from pre-existing crystals or crystalline fragments. While exact peak temperatures cannot be obtained evidence for non-isothermal crystallization can still be found. Focusing on the purple to dark blue curves which intersect the x-axis between  $180\text{ }^{\circ}\text{C}$  and  $198\text{ }^{\circ}\text{C}$  in **Figure 4.8A** the tail end of a non-isothermal crystallization peak can be observed tracking back down to the semi-crystalline baseline around  $150\text{ }^{\circ}\text{C}$ . This observation combined with the constant yet reduced glass transition amplitude indicates that all crystals observed upon melting (**Figure 4.8B**) were annealed to a similar total mass fraction crystallinity during the hold at  $T_s$  for between  $180\text{ }^{\circ}\text{C}$  and  $198\text{ }^{\circ}\text{C}$ . As  $T_s$  increases the temperature of the observed glass transition temperature decreases, the amplitude increases, and distinct exothermic peak(s) become visible.

Just as was done for the conventional DSC data, the domain III boundary can be tracked by disappearance of the melting doublet, which in the case of fast scanning rates, corresponds with the emergence of a homogenous nucleation peak on cooling and a cold crystallization peak following the glass transition on heating. This is because at the scanning rate of  $2000\text{ K/s}$ , an undercooling sufficient to provide a driving force strong enough to trigger homogenous nucleation is achieved. The peak melting temperatures are plotted as function of  $T_s$  in **Figure 4.9**.

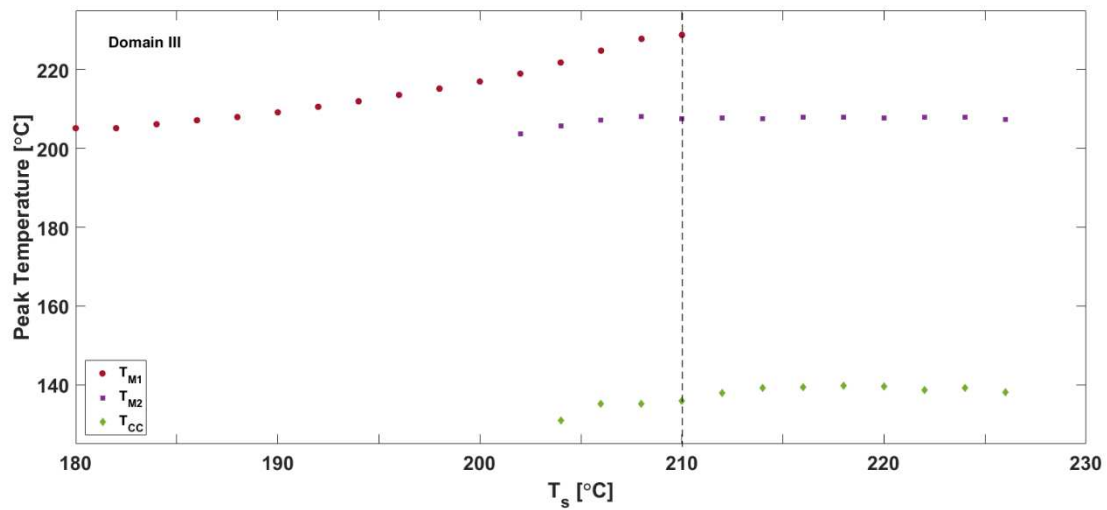


**Figure 4.9:** Melting peak temperatures as a function of  $T_s$  (red circles and purple squares) and cold crystallization peak temperatures (green diamonds) as a function of  $T_s$ . The domain III boundary is marked with a vertical, dashed line.

Keeping the appearance of the heating curves in mind it becomes clear that the highest temperature melting peak, seen in the bright, red curves in **Figure 4.8B**, is the result of annealing during the hold at  $T_s$ . The lower temperature peak reflects the melting of the combination of homogeneously nucleated and cold crystallized material. The disappearance of a high temperature melting peak, and the recovery of a single melting peak centered about an average of 207.7 °C for  $T_s > 210$  °C, defines the domain III boundary. The domain II and I boundary is more difficult to pin down. Peak crystallization temperature(s) is plotted as a function of  $T_s$  and shown below in **Figure 4.10**. With the domain III boundary marked (as determined in **Figure 4.9**) there is only one data point above  $T_s = 210$  °C indicating the presence of heterogeneous nucleation during cooling.

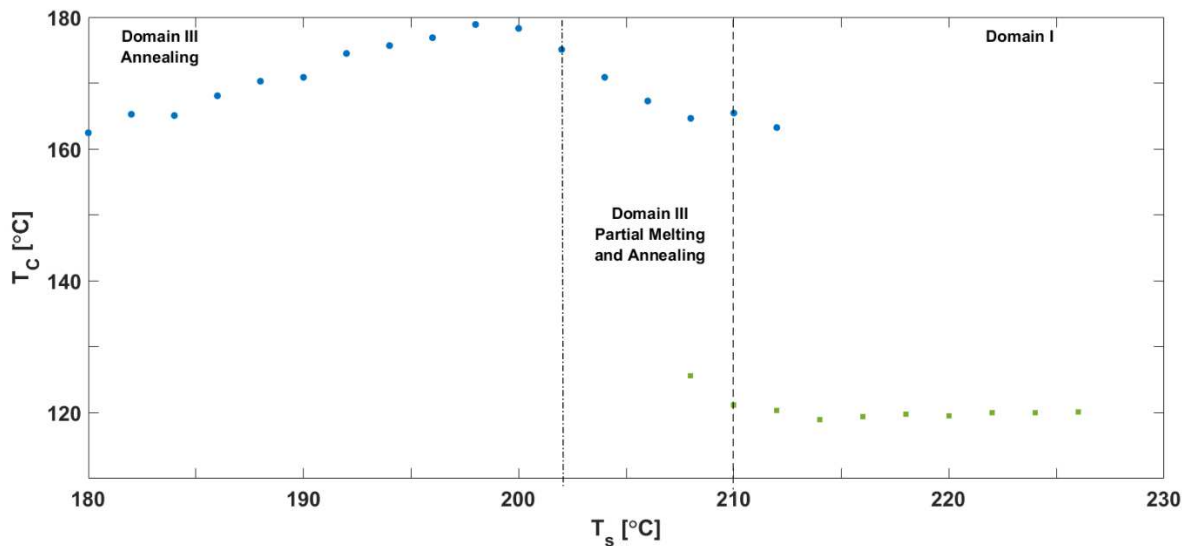


**Figure 4.10:** Crystallization peak temperatures as a function of  $T_s$ . Heterogeneously nucleated crystals (blue circles) and homogeneously nucleated crystals (green squares) formed non-isothermally during cooling. The vertical, dashed line marks the domain III boundary and the dashed and dotted line marks the shift from annealing to partial melting and annealing within domain III.

Self nucleation is a special case of heterogeneous nucleation where seed nuclei or aligned regions of the melt remain after heating, and allow nucleation and crystallization to proceed at a higher temperature (or lower supercooling) than typical, bulk heterogeneous nucleation. To best make sense of the final peak beyond the last observed doublet a plot of the heating and cooling curves at the boundary is shown below in **Figure 4.11**.

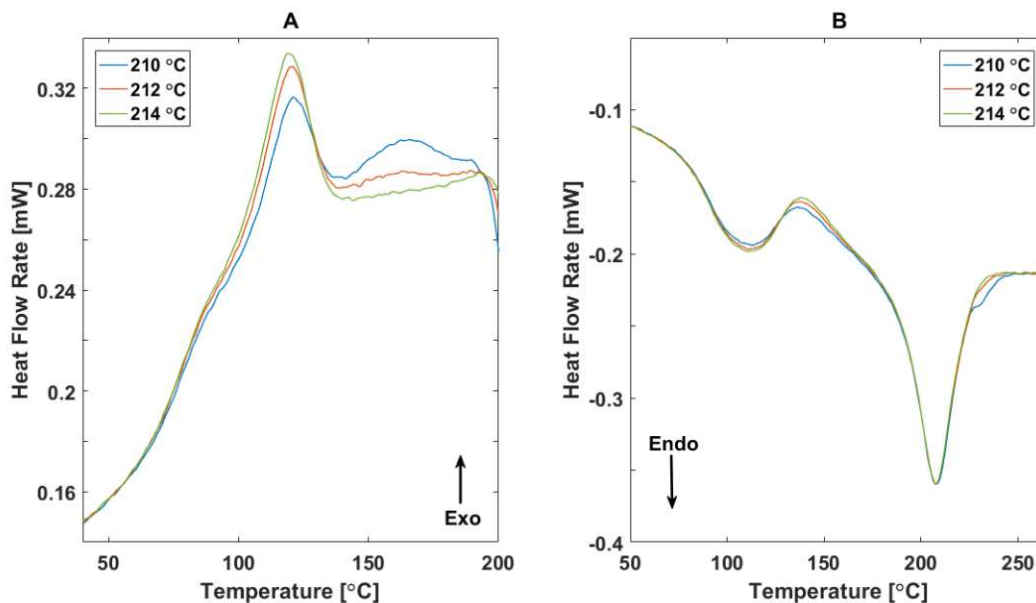


**Figure 4.11:** Fast scanning heat flow rates vs. temperature for (A) cooling from  $T_s$  and (B) reheating, for three values of  $T_s$  near the domain III boundary.

The heterogeneous nucleation point in question is shown above in **Figure 4.11** as the orange curve. A small, broad peak can be seen in the cooling scan (**Figure 4.11A**), preceding the onset of the larger homogeneous nucleation peak crystallizing a small amount of material which reduces both the peak area of the larger homogeneous nucleation peak as well as the subsequent cold crystallization peak observed in **Figure 4.11B**. Carefully looking at the endotherm foot of the orange curve in **Figure 4.11B** there is a small feature which could arguably be considered a shoulder resulting from residual, annealed crystals from the initial population brought to  $T_s$ . It is also possible that there were an abundance of seed nuclei and crystal fragments which underwent heterogeneous nucleation upon cooling from the melt and crystallized to the extent which was possible before the melt was sufficiently supercooled to drive homogenous nucleation.

Conventional DSC measurements on the self nucleation of PVA indicate that the effect of melt memory begins at temperatures in excess of the observed peak melting temperature of the

initial crystal population. The domain III – domain II boundary was found to be  $227.5 \pm 0.5$  °C, above the observed peak melting temperature of  $223.0 \pm 0.3$  °C, just before the melting endotherm foot. The domain II – domain I boundary was found to be at  $235 \pm 1.0$  °C which was past the endotherm foot within the melt region. While the complete melting domain I lies at temperatures  $T_s$  above the endotherm foot, it was possible to erase melt memory effects within a short time (5 min) and at 30 °C below the equilibrium melting point of PVA. The shift in peak crystallization temperature between domains I and II is small, about 4 °C, as compared to the approximate 20 °C shift seen in isotactic polypropylene [4]. The range within the melting endotherm where domain II behavior is observed for PVA spans 6 °C which is similar to the 4 °C range reported for isotactic polypropylene [4].

Comparing this with the FSC measurements, the peak melting temperature of the initial state, prior to any hold at  $T_s$ , was 207 °C and the domain III boundary was found to be  $212 \pm 2$  °C. Both experiments reveal that it is possible to nearly completely melt PVA crystals holding for short times roughly five degrees above the peak melting temperature of the initial crystalline state. The disappearance of the self nucleation domain in the FSC experiments is not likely due to the lack of aligned regions of melt or crystalline fragments, as evidenced by the ambiguous data point discussed above. It is more likely the case that the disappearance of self nucleated crystals is a result of the ultra high cooling rates used to mitigate sample degradation. Experiments on PCL doped with carbon nanotubes have demonstrated that heterogeneous nucleation sites only promote heterogeneous nucleation up until a sufficiently fast cooling rate, at which point heterogeneous nucleation and crystallization kinetics are frozen out and any crystallization observed is the result of mesophase or homogeneous nucleation. [14] These experiments show that, at a cooling rate of

2000 K/s, homogenous nucleation is the dominant mechanism for crystallization once bulk crystals have melted (the domain III boundary).

#### **4.4 References**

- [1] D. Thomas, P. Cebe, Self-nucleation and crystallization of polyvinyl alcohol, *Journal of Thermal Analysis and Calorimetry* 127(1) (2017) 885-894.
- [2] B. Fillon, B. Lotz, A. Thierry, J.C. Wittmann, Self-Nucleation and Enhanced Nucleation of Polymers – Definition of a Convenient Calorimetric Efficiency Scale and Evaluation of Nucleating Additives in Isotactic Polypropylene (Alpha-Phase) *Journal of Polymer Science Part B-Polymer Physics* 31(10) (1993) 1395-1405.
- [3] B. Fillon, A. Thierry, J.C. Wittmann, B. Lotz, Self-Nucleation and Recrystallization of Polymers – Isotactic Polypropylene, Beta-Phase – Beta-Alpha-Conversion and Beta-Alpha-Growth Transitions, *Journal of Polymer Science Part B-Polymer Physics* 31(10) (1993) 1407-1424.
- [4] B. Fillon, J.C. Wittmann, B. Lotz, A. Thierry, Self-Nucleation and Recrystallization of Isotactic Polypropylene (Alpha-Phase) Investigated by Differential Scanning Calorimetry *Journal of Polymer Science Part B-Polymer Physics* 31(10) (1993) 1383-1393.
- [5] E. Chiellini, A. Corti, S. D'Antone, R. Solaro, Biodegradation of poly (vinyl alcohol) based materials, *Progress in Polymer Science* 28(6) (2003) 963-1014.
- [6] R. Endo, S. Amiya, M. Hikosaka, Conditions for Melt Crystallization Without Thermal Degradation and Equilibrium Melting Temperature of Atactic Poly(Vinyl Alcohol), *Journal of Macromolecular Science, Part B* 42(3-4) (2003) 793-820.

- [7] B.J. Holland, J.N. Hay, The thermal degradation of poly(vinyl alcohol), *Polymer* 42(16) (2001) 6775-6783.
- [8] H. Huang, L. Gu, Y. Ozaki, Non-isothermal crystallization and thermal transitions of a biodegradable, partially hydrolyzed poly(vinyl alcohol), *Polymer* 47(11) (2006) 3935-3945.
- [9] C.P. Li, T.T. Hou, X.D. She, X.Y. Wei, F.H. She, W.M. Gao, L.X. Kong, Decomposition properties of PVA/graphene composites during melting-crystallization, *Polymer Degradation and Stability* 119 (2015) 178-189.
- [10] C.P. Li, T.T. Hou, J. Vongsvivut, Y.Z. Li, X.D. She, F.H. She, W.M. Gao, L.X. Kong, Simultaneous crystallization and decomposition of PVA/MMT composites during non-isothermal process, *Thermochimica Acta* 618 (2015) 26-35.
- [11] C.P. Li, J. Vongsvivut, X.D. She, Y.Z. Li, F.H. She, L.X. Kong, New insight into non-isothermal crystallization of PVA-graphene composites, *Physical Chemistry Chemical Physics* 16(40) (2014) 22145-22158.
- [12] O. Probst, E.M. Moore, D.E. Resasco, B.P. Grady, Nucleation of polyvinyl alcohol crystallization by single-walled carbon nanotubes, *Polymer* 45(13) (2004) 4437-4443.
- [13] C. Li, M. She, X. She, J. Dai, L. Kong, Functionalization of polyvinyl alcohol hydrogels with graphene oxide for potential dye removal, *Journal of Applied Polymer Science* 131(3) (2014) n/a-n/a.
- [14] E. Zhuravlev, A. Wurm, P. Pötschke, R. Androsch, J.W.P. Schmelzer, C. Schick, Kinetics of nucleation and crystallization of poly( $\epsilon$ -caprolactone) – Multiwalled carbon nanotube composites, *European Polymer Journal* 52 (2014) 1-11.

## ***Chapter 5 Fundamental Thermal Properties of PVA by FSC***

This chapter is organized as follows: **Section 5.1** presents results of thermal stability experiments on PVA; **Section 5.2** presents the determination of crystallinity of PVA; **Section 5.3** presents the liquid state heat capacity of PVA; **Section 5.4** presents the critical cooling rate needed to fully quench PVA; **Section 5.5** presents the glass transition behavior of PVA under conditions of fast scanning; **Section 5.6** discussion presents the fundamental thermal properties obtained by FSC, including  $c_p^{\text{Liquid}}(T)$ ,  $\Delta c_p^{\text{amor}}(T_g)$ , and the rigid amorphous fraction of PVA. Details of the sample preparation and mounting of polyvinyl alcohol (PVA) from spin coated films onto chip sensors is outlined in **Section 2.2.1** The specifics for each thermal experiment performed and schematics of the various temperature time profiles are found in **Section 3.4.3.1**. Methods of data analysis for fast scanning calorimetry (FSC) are outlined in **Section 3.5**.

## 5.1 Thermal Stability of PVA

Cyclic melting experiments were successfully utilized in the previous chapter to assess the impact that non-isothermal degradation had on the self nucleation and crystallization of PVA. A similar cyclic melting protocol serves as the starting point for experiments gain insights into the degradation of PVA under the conditions of fast scanning measurements. Prior work has shown that molecular weight [1-3], degree of hydrolysis [4], heating rate, and isothermal hold time at temperatures in excess of 200 °C [1-3] are all factors that determine the extent to which PVA will degrade. Length of time in the molten state is also a factor in degradation (see **Section 4.1** for comparison to conventional DSC conditions). Images collected after various numbers of meltings are shown in **Figure 5.1**. The experimental temperature range had a selected upper bound of 270 °C, which is 5 °C above the equilibrium melting temperature,  $T_m^0 = 265$  °C. [5, 6] Optical imaging after several cycles, combined with tracking the liquid phase heat flow baseline cycle to cycle, allows determination of the apparent onset of degradation.

Jagged edges which remained from the sample preparation (**Figure 5.1A**) are softened or disappear completely after 5 meltings (**Figure 5.1B**). The softening of edges in **Figure 5.1B**, overall smoother appearance, and slight reduction of sample area indicate effective melting of the sample. There are no visible signs of degradation such as charring, color change, or the formation of bubbles. Repeated exposure to high temperature causes the film to degrade, even at the fast heating and cooling rate of  $|\beta| = 2000$  K/s. A change in overall color between **Figure 5.1B** and **Figure 5.1C** indicates the sample is beginning to degrade, and this is most apparent after 45 meltings in **Figure 5.1D**. While the optical microscope images provide some insight in to the sample stability, use of the apparent heat flow rate baseline in the melt and the enthalpies of

crystallization and melting allows for more precise tracking of sample degradation. This approach has been previously utilized in standard DSC experiments on PVA to assess thermal stability. [2, 3] By comparing crystallization exotherms (**Figure 5.2A**) and melting endotherms (**Figure 5.2B**) an upper limit can be found on the number of heatings to the melting point which can be completed before degradation is initiated.

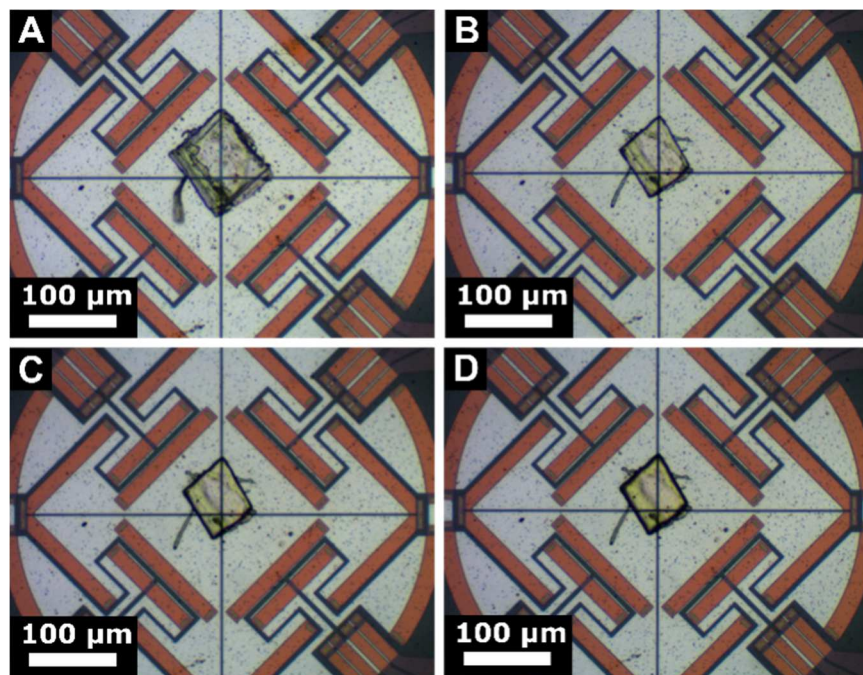


**Figure 5.1:** Optical microscope images of PVA films at magnification of 100x before and after heating and cooling at  $|\beta| = 2000$  K/s. (A) As prepared on sensor and before heating; (B) after 5 meltings; (C) after 20 meltings; (D) 45 meltings. Sample can be seen to shrink between (A) and (B) indicating melting and bulk reorganization. Color changes from (B) through (D) indicate increasing sample degradation.

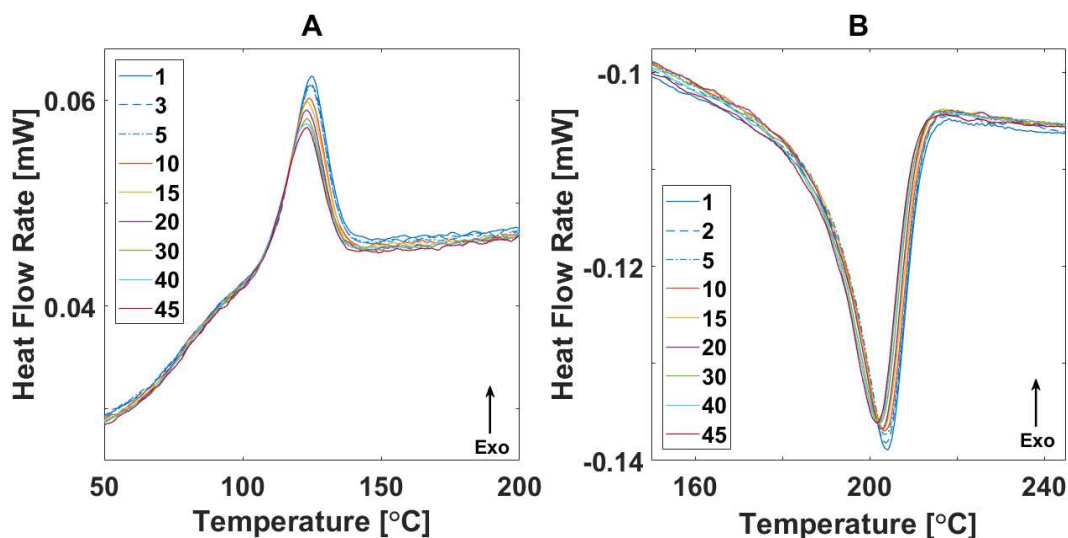


**Figure 5.2:** Heat flow rate from FSC as a function of temperature at  $|\beta| = 2000$  K/s after multiple meltings. Line styles are varied for clarity. (A) Cooling; (B) Heating.

For samples brought to the melt fewer than 5 times there is no evidence of degradation by either optical microscopy or from the FSC results. This stands in contrast to the conventional DSC case where, after a single melting, the sample is visually degraded. It is well known that as PVA degrades, exotherm and endotherm areas are reduced along with peak temperatures of crystallization and melting. [2, 3] The same phenomenon is seen in the fast scanning data after melting the sample 5 times. **Figure 5.2A** shows a steady drop in the crystallization peak area and temperature after the 10<sup>th</sup> melting and the same trend is shown in the reheating data in **Figure 5.2B**. Within each cycle the heat flow baselines in the melt and glass show good agreement, indicating that any changes in the heat capacity of the material due to degradation are small enough that they are within the noise level of the measurement. Following the onset of degradation after the 5<sup>th</sup> melting, the heat flow baseline remains relatively stable up until 30<sup>th</sup> melting where another drop in baseline is apparent. As degradation is apparently avoided in the samples for the first few (1-5) times the sample is brought to the melt, it is possible for the first time to make measurements

of the liquid phase heat capacity of PVA that are degradation free, provided exposure to high temperature is minimized by using fast scanning rates and limiting the number of meltings.

## 5.2 Degree of Crystallinity of PVA

Next, we use FSC to determine the degree of crystallinity of PVA whose crystals nucleated during cooling from the melt. Fourteen samples were prepared and the initial heat-cool-heat cycles were compiled for specific heat capacity analysis and their properties are listed in **Table 5.1**. For each sample the mass was determined using the method previously described. Then the area of each melting endotherm observed in the symmetry corrected heat flow rate is measured to obtain the mass-normalized enthalpy of melting,  $\Delta h_f$ .

It has been suggested that mass can be measured from optical microscope images of samples loaded onto sensors for samples with well controlled geometry and well known physical properties [7]. The density of PVA,  $\rho$ , is known to vary between  $1.26 \text{ g/cm}^3$  and  $1.35 \text{ g/cm}^3$  for the 100% amorphous and 100% crystalline cases, respectively [8]. Taking the assumptions that the spin coated parent film has both uniform thickness and crystallinity, estimates of the thickness can be made from the measured mass per unit area. Of the fourteen different samples prepared for experiments using the Mettler Flash DSC1, nine samples were cut from the thicker parent film. The thicker parent film had a well known mass per unit area which was measured to be  $3.80 \times 10^{-12} \text{ g}/\mu\text{m}^2$ . Using the amorphous density, the upper limit estimate of the thickness is found to be  $3.02 \mu\text{m}$ .

The mass as calculated per Eqn. 3.17 as a function of the surface area for samples cut from the thicker parent film are shown below in **Figure 5.3**. For samples cut from a parent film of uniform thickness and density, the measured mass should scale linearly with the surface area.

Samples with surface area less than 10,000  $\mu\text{m}^2$  the relationship between mass and surface area is observed to scale linearly.

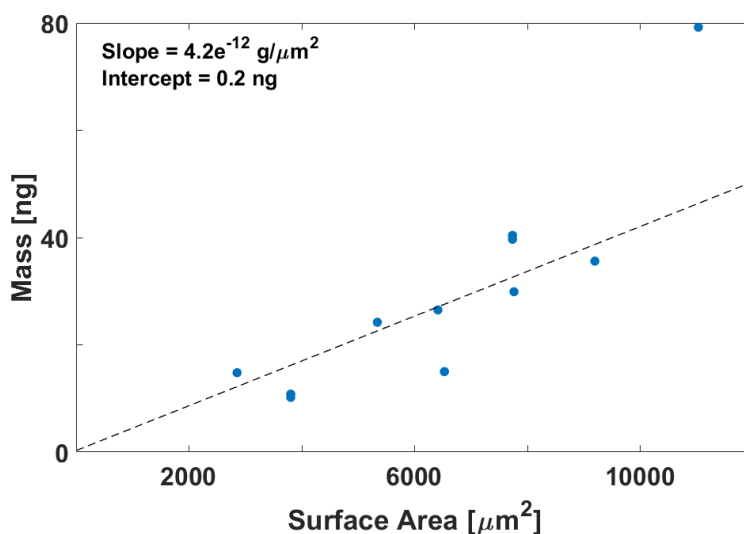


**Figure 5.3:** Mass calculated per Eqn. 3.17 vs. sample surface area measured as described in Section 2.6.

Again, operating with the assumption that the density (equivalently the crystallinity) and thickness of the samples are constant the slope of the line in **Figure 5.3** is the sample mass per unit area following the preconditioning treatment. Taking the amorphous density,  $\rho_a = 1.26 \text{ g/cm}^3$  [8], this results in an upper limit estimate of 3.33  $\mu\text{m}$ . The preconditioning treatment was found to result in a total crystallinity of  $\langle\phi_c^{\text{Tot}}\rangle = 0.30$ . This results in a sample thickness of 3.26  $\mu\text{m}$ . While it is possible to gain some insight into the sample geometry and physical properties by combining the optical measurements and the mass calculated by comparison to the literature values of the specific heat capacity, the overall correlation,  $r^2 = 0.79$ , between the sample mass and surface area is poor. The scatter in these data is consistent with what was observed in previous experiments on polypropylene samples prepared with an ultra-microtome [7]. This result suggests that optical

measurements do not provide enough information regarding sample to sensor contact or take into consideration any defects within the samples. It is suggested that optical measurements be used as a qualitative guide when designing and troubleshooting experiments performed on chip based calorimeter systems. Sample surface area, at best, can be a qualitative guide to varying the masses during experiments. Quantitative results require that masses be calculated by comparison to well-known thermal properties.

The enthalpy of melting is plotted as a function of calculated mass in **Figure 5.4**. If the use of identical thermal treatments results in the same crystallinity among similarly treated samples, then this relationship will be linear as all samples melt at nearly the same temperature,  $T_m$ . The slope of the line of best fit is equal to the crystallinity multiplied by the equilibrium heat of fusion. PVA samples brought through the same preconditioning protocol are expected to crystallize to the same extent. The enthalpy of melting as a function of mass is observed to increase linearly,  $r^2 = 0.9835$ , which suggests that the mass, as determined by the heat capacity of the glassy phase, is suitable for obtaining specific heat capacity and enthalpies from the symmetry-corrected data.

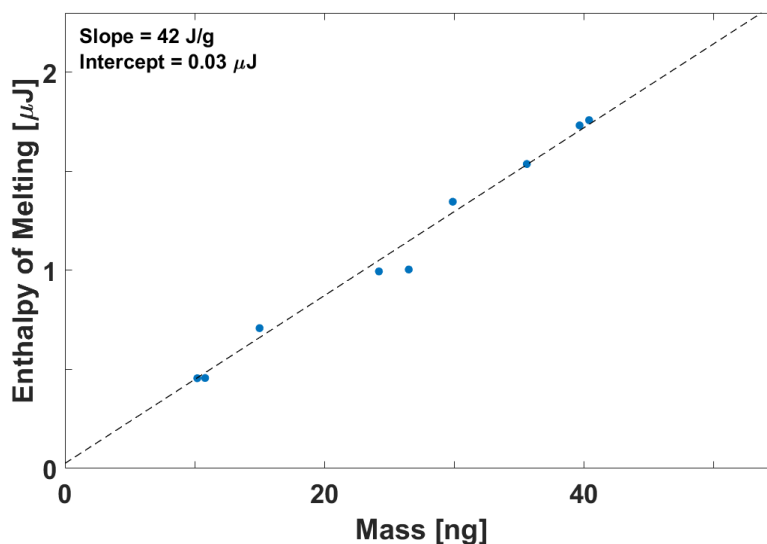


**Figure 5.4:** Enthalpy of melting,  $\Delta h_f$ , vs. mass calculated using Eqn. 1. Dashed, black line is the line of best fit. Intercept of 0.03  $\mu\text{J}$  indicates a systematic error and all reported enthalpies are adjusted accordingly.

PVA exhibits not only melt crystallization, but also cold crystallization upon reheating above  $T_g$  if the non-isothermal melt crystallization is incomplete. For the range of heating and cooling rates utilized in these experiments PVA immediately cold crystallized when reheated above  $T_g$ , and an example can be seen in the heating scan of **Figure 3.24B**. Melt crystallization exotherms, and melting endotherms, can be seen in **Figure 5.2A,B**, respectively. The total melting enthalpy in **Figure 5.2** includes the contribution from both crystal formation processes. To separate the contributions, the exotherm area from cooling was used to calculate the mass fraction of crystals melt crystallized on cooling,  $\phi_c^{\text{MC}}$ . Upon reheating, the melting endotherm area was used to calculate the total mass fraction crystallinity,  $\phi_c^{\text{Tot}}$ . Then,  $\phi_c^{\text{Tot}} = \phi_c^{\text{MC}} + \phi_c^{\text{CC}}$  where  $\phi_c^{\text{CC}}$  is the mass fraction of crystals form by cold crystallization. The results of the non-isothermal crystallization for each sample brought through the preconditioning cycle (see **Figure 3.21**) are summarized in **Table 5.1**.

The mass fraction crystallinity is calculated from measured specific enthalpy according to equation 3.14, reprinted below with specific notation relevant to this chapter: [9]

$$\phi_c^i = \Delta h_f^i / \Delta h_f^0 \quad (3.14)$$

where  $i = \text{Tot, MC or CC}$  (for total enthalpy, enthalpy of melt crystallization, or enthalpy of cold crystallization), and  $\Delta h_f^0$ , is 161.4 J/g [5, 6], the equilibrium heat of fusion for PVA at  $T_m^0 = 265$  °C. Due to the large undercooling achieved during fast scanning measurements equilibrium heat of fusion must be corrected. The temperature dependent heat of fusion is given by the following relationship:

$$\Delta h_f^{corr} = \frac{2T_m}{T_m + T_m^0} \Delta h_f^0 \quad (5.1a)$$

$$\phi_c^i = \Delta h_f^i / \Delta h_f^{corr} \quad (5.1b)$$

The slope of the line of best fit seen in **Figure 5.4** is equal to the average total crystallinity,  $\langle \phi_c^{\text{Tot}} \rangle$ , multiplied by the temperature corrected heat of fusion,  $\Delta h_f^{corr}$ . This results in a means of measuring the average total crystallinity,  $\langle \phi_c^{\text{Tot}} \rangle = 0.30$ , which is the combination of non-isothermal crystallization during cooling and subsequent cold crystallization.

**Table 5.1:** PVA sample properties: surface area, mass, enthalpy of crystallization, enthalpy of melting, and mass fraction crystallinity.

| Sample | Surface Area, $\mu\text{m}^2$ | Mass, ng<br>$\pm 0.2$ ng | Cooling Exotherm Area, $\mu\text{J}$<br>$\pm 0.02$ $\mu\text{J}$ | Melting Endotherm Area, $\mu\text{J}$<br>$\pm 0.02$ $\mu\text{J}$ | Crystal Fraction <sup>a</sup><br>$\phi_c^{\text{MC}}$<br>$\pm 0.01$ | Crystal Fraction <sup>b</sup><br>$\phi_c^{\text{Tot}}$<br>$\pm 0.01$ | Crystal Fraction <sup>c</sup><br>$\phi_c^{\text{CC}}$<br>$\pm 0.01$ |
|--------|-------------------------------|--------------------------|--|---|---|--|---|
| 1      | 2900                          | 14.8                     | -0.30  | 0.70  | 0.17  | 0.34   | 0.17  |
| 2      | 3800                          | 10.8                     | -0.11  | 0.43  | 0.10  | 0.28   | 0.18  |
| 3      | 5300                          | 24.2                     | -0.23  | 0.96  | 0.10  | 0.28   | 0.19  |
| 4      | 6400                          | 26.5                     | -0.35  | 0.97  | 0.13  | 0.26   | 0.13  |
| 5      | 6500                          | 15.0                     | -0.28  | 0.68  | 0.13  | 0.32   | 0.19  |
| 6      | 7700                          | 39.7                     | -0.65  | 1.70  | 0.15  | 0.30   | 0.15  |
| 7      | 7800                          | 29.9                     | -0.46  | 1.32  | 0.15  | 0.31   | 0.17  |
| 8      | 9200                          | 35.6                     | -0.52  | 1.51  | 0.13  | 0.30   | 0.17  |
| 9      | 11500                         | 79.2                     | -0.82  | 3.10  | 0.10  | 0.28   | 0.18  |
| 10*    | - <sup>d</sup>                | 8.6                      | -0.12  | 0.30  | 0.10  | 0.25   | 0.15  |
| 11*    | - <sup>d</sup>                | 19.1                     | -0.18  | 0.54  | 0.07  | 0.20   | 0.14  |
| 12*    | - <sup>d</sup>                | 24.0                     | -0.28  | 0.77  | 0.08  | 0.23   | 0.15  |
| 13*    | - <sup>d</sup>                | 31.0                     | -0.34  | 0.94  | 0.08  | 0.21   | 0.14  |
| 14*    | - <sup>d</sup>                | 35.2                     | -0.40  | 1.14  | 0.08  | 0.23   | 0.15  |

<sup>a</sup> Melt crystallized mass fraction crystallinity calculated from the cooling exotherm area

<sup>b</sup> Total mass fraction crystallinity calculated from the melting endotherm area

<sup>c</sup> Cold crystallized mass fraction crystallinity calculated by subtraction

<sup>d</sup> Data not available

\* From thinner samples ( $\sim 1$   $\mu\text{m}$  thick)

### 5.3 *Liquid Phase Heat Capacity of PVA*

Apparent specific heat capacity vs. temperature data for PVA using the Mettler flash DSC1 at  $\beta = 2000$  K/s are shown in **Figure 5.5**. In the solid state (from 200 K - 300 K), our calibration method aligns the measured data to the experimental literature values (solid black line) [6]. All 14 samples shown in Figure 6 are semicrystalline prior to heating (crystallinity ranges from 0.081 to 0.169). Samples crystallize non-isothermally as they are cooling from the melt at 2000 K/s. This implies that cooling rates greater than 2000 K/s are necessary to quench PVA from the melt to create an amorphous glass. The critical cooling rate needed to obtain fully amorphous PVA will be determined in Section 3.4. The degradation free, specific heat capacity of PVA,  $c_p^{\text{Liquid}}(T)$ , is determined at temperatures beyond the foot of the endotherm (*i.e.*, beyond the point of last departure from the heat capacity baseline following melting).  $c_p^{\text{Liquid}}(T)$  is obtained above the melt at temperatures from 490 K to 540 K, which is a greater temperature range than reported in previous investigations [2, 10]. Prior experiments used the slower scan rates of conventional DSC; degradation of PVA set in at about 480–500 K, and this degradation could have a negative effect on accurate determination of the specific heat capacity of the liquid. [1-3, 11]

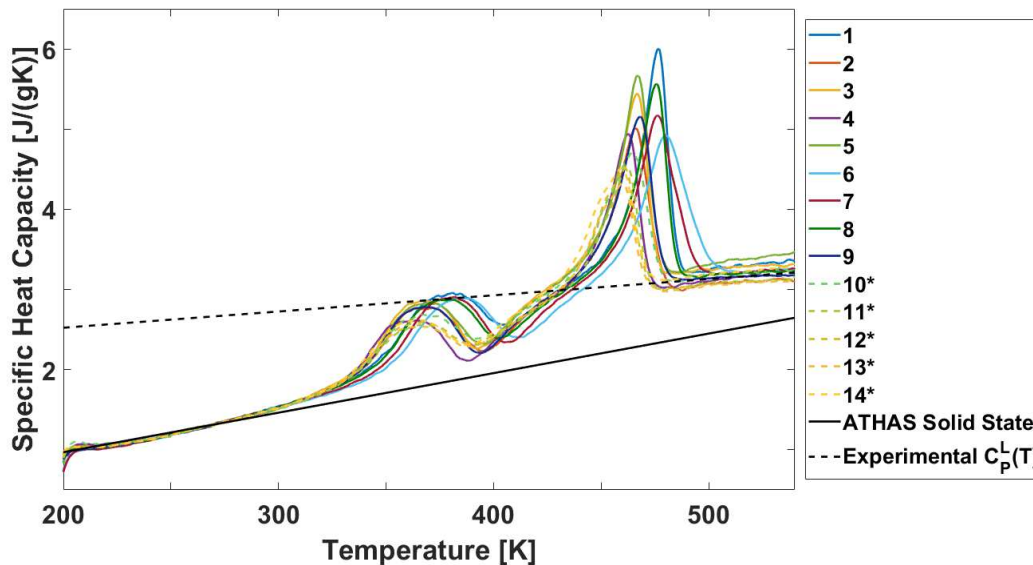


**Figure 5.5:** Apparent specific heat capacity of PVA as a function of temperature at  $\beta = 2000$  K/s for 14 samples measured using the Mettler Flash DSC1. The literature values for the solid state heat capacity of PVA [6] are shown by the solid black line. The average experimental liquid phase heat capacity is extrapolated beyond the range of measurement, as shown by the dashed black line.

#### 5.4 Critical Cooling Rate for PVA

To determine the critical cooling rate needed to form an amorphous PVA glass, we next used the custom-built chip based fast scanning calorimeter [12, 13]. With this equipment, a sample of PVA immersed in helium could be heated and cooled at rates up to 600,000 K/s. By increasing the cooling rates by more than two orders of magnitude above the cooling rates accessible with the Mettler Flash DSC1 we could quench PVA into an amorphous glass as shown in **Figure 5.6**. The apparent specific heat capacity as a function of temperature upon heating at 10,000 K/s following varied cooling rates is plotted in **Figure 5.6A**. PVA is observed to cold crystallize during heating at 10,000 K/s following all prior cooling rates, except for the sample cooled at the slowest rate, 1000 K/s. In that case, non-isothermal melt crystallization had proceeded far enough to inhibit

further crystallization on heating. Increasing the cooling rate results in an increase in the enthalpy of cold crystallization,  $\Delta h_f^{CC}$ , observed on heating while the enthalpy of melting,  $\Delta h_f^{Tot}$ , appears to remain constant. The difference between these two areas is the overall change in enthalpy,  $\Delta h_f^{Tot} - \Delta h_f^{CC}$ , and is also equal to the enthalpy of non-isothermal melt crystallization,  $\Delta h_f^{MC}$ .

After cooling at high rates,  $\beta \geq 10,000$  K/s, the cold crystallization exotherms converge suggesting that there is little, if any, crystallization now occurring during cooling. Any cooling rate which has successfully quenched the sample will result in equal enthalpies of cold crystallization and melting (equivalently,  $\Delta h_f^{MC} = 0$ ). The overall change in enthalpy is plotted as function of cooling rate in **Figure 5.6B**.

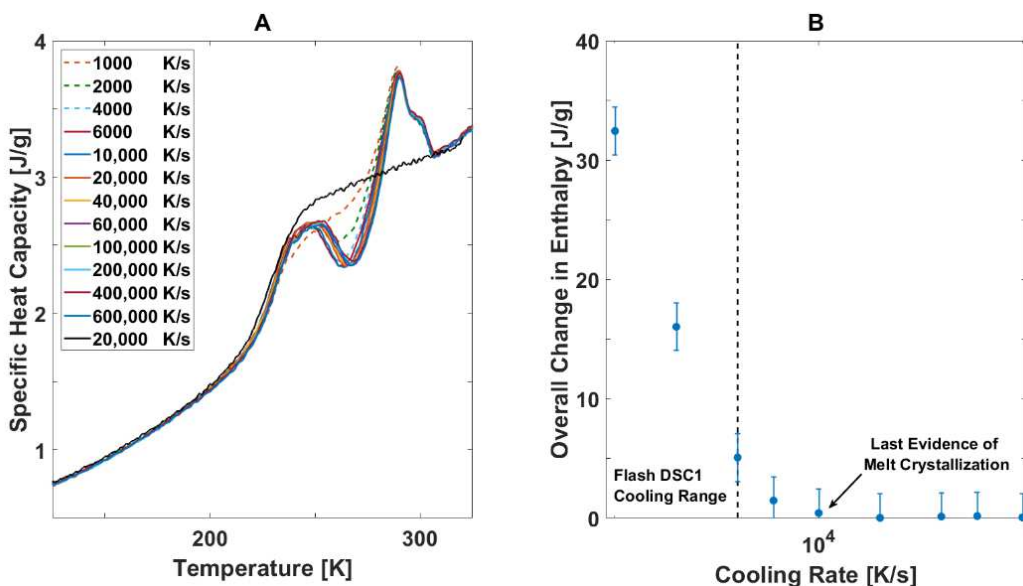


**Figure 5.6:** (A) Apparent specific heat capacity of PVA vs. temperature during heating at 10,000 K/s (colored curves), after cooling from the melt at the indicated rates using the custom calorimeter. Cooling at 20,000 K/s is overlaid (black line). (B) The overall change in enthalpy during heating at 10,000 K/s vs. prior cooling rate. Error bars are  $\pm 2.0$  J/g. The vertical dashed, black line indicates the upper limit of the cooling rate accessible for measurement in the Mettler Flash DSC1. Rates to the right of the dashed line are available only with the custom calorimeter.

The overall change in enthalpy observed for PVA cooled at 2000 K/s (green dashed curve in **Figure 5.6A**) corresponds to a crystallinity,  $\phi_c^{MC} = 0.13 \pm 0.01$ , in agreement with crystallinity of samples measured in the Mettler Flash DSC1. The last evidence for melt crystallization during cooling occurs at 10,000 K/s, annotated with an arrow in **Figure 5.6B**. Cooling rates  $|\beta| \geq 20,000$  K/s guarantee that PVA will form an amorphous glass, and the apparent specific heat capacity at the critical cooling rate,  $|\beta_c| = 20,000$  K/s is overlaid (black curve) for comparison to the heating curves in **Figure 5.6A**.

### 5.5 *Glass Transition of PVA*

The glass transition region was analyzed for PVA samples having crystallinities between 0.10 and 0.55 achieved by isothermally melt crystallizing in the Mettler Flash DSC1. A sampling of the nearly degradation free FSC isothermal melt crystallization of PVA can be seen in **Figures 5.7 and 5.8** for the short and long isothermal crystallization time experiments, respectively. **Figures 5.7A and 5.7B** show the heating scans of PVA isothermally melt crystallized for short times at 90 °C and 95 °C, respectively. Here a low temperature melting peak is observed immediately following the glass transition. Both the amplitude and the peak temperature of this initial endotherm increase with crystallization time. An increase in initial melting peak area corresponds with a reduction in the cold crystallization and reorganization before the final melting peak. Glass transition temperature, heat capacity increment, melting peak temperatures and crystallinities can be seen in **Tables 5.2 and 5.3**. Cold crystallization is not observed for samples crystallized beyond a mass fraction crystallinity of 0.34. The last observed cold crystallization is seen at 500 seconds (yellow curve) in **Figure 5.7B**.

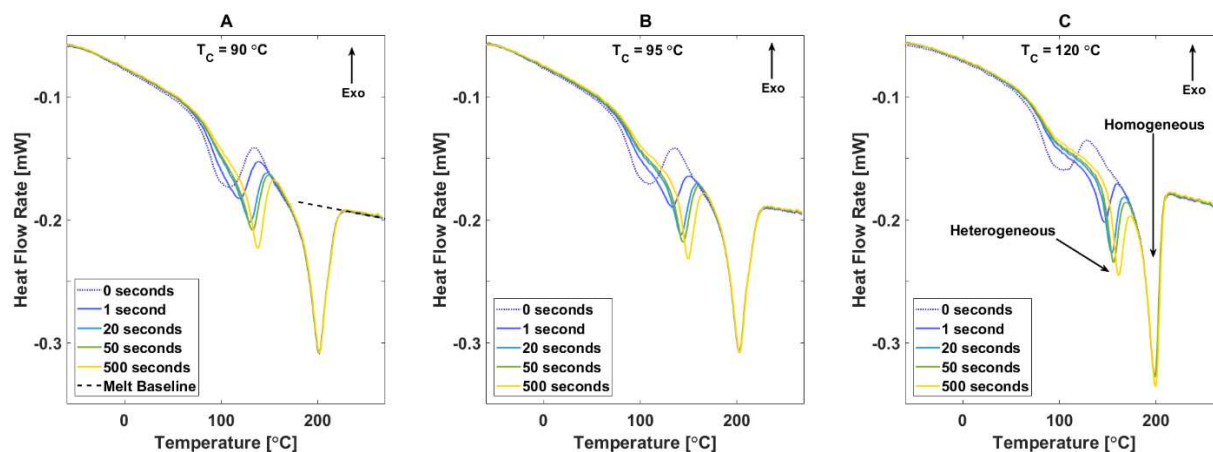


**Figure 5.7:** Heat flow rate vs. temperature for PVA heated at 2000 K/s after isothermal melt crystallization for various short times at a temperature of: **(A)** 90 °C; **(B)** 95 °C; **(C)** 120 °C. Crystallization time increases as the color changes from blue to yellow. The glass transition temperature increases with crystallization time.

The total mass fraction crystallinity,  $\phi_c^{\text{Tot}}$ , is calculated for each heating curve from the specific enthalpy of melting calculated between the glass transition and the endotherm foot compared against the liquid phase heat flow baseline. A typical liquid phase heat flow baseline is plotted in **Figure 5.7A**. This means of measurement takes into consideration the portion of the melting which results from cold crystallization following the low temperature melting observed in **Figures 5.7A and 5.7B** resulting in an enthalpy of melting which only represents the population of crystals which formed non-isothermally upon cooling from the melt to the crystallization temperature,  $T_c$ , in addition to those formed during the isothermal hold at  $T_c$ . At the lowest crystallization temperatures of 90 °C and 95 °C the onset of melting immediately following  $T_g$  can obscure the measurement of the heat capacity increment as it is difficult to identify end point of the transition and the onset of the first melting peak.

Increasing the isothermal melt crystallization temperature to 120 °C, which is near the onset temperature of the non-isothermal crystallization, results in sufficient crystallization for all

times, that there is no cold crystallization or reorganization upon reheating. For all crystallization times at 120 °C, a sampling of which are shown in **Figure 5.7C**, the semi crystalline heat flow baseline is observed following the glass transition and the onset of the first melting peak.

As seen in **Figure 5.8A**, increasing the isothermal crystallization temperature to 140 °C or to 150 °C (**Figure 5.8B**) gives a glass transition region free of any signature of cold crystallization. For these temperatures,  $\phi_c^{\text{Tot}} > 0.43$  is obtained for all crystallization times greater than 1 s. Now, the onset of melting is at temperatures far enough above  $T_g$  that the semi-crystalline glass transition is fully expressed.

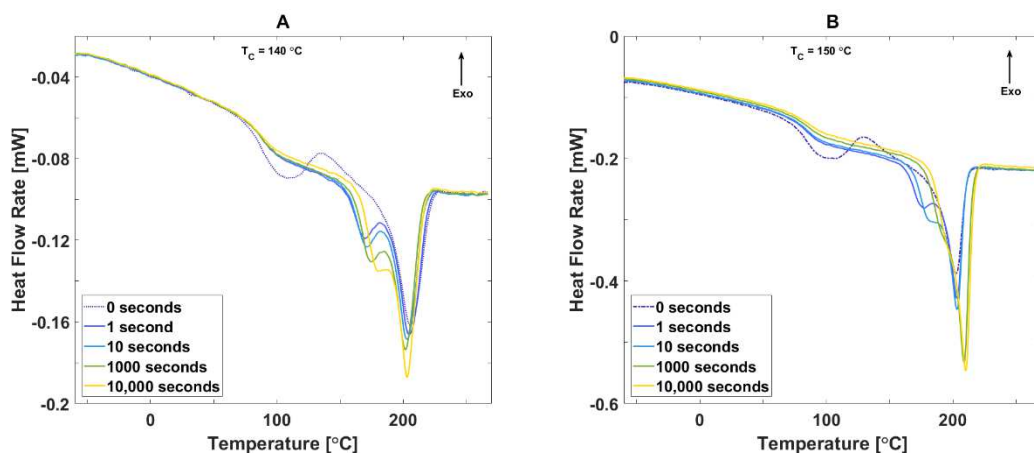


**Figure 5.8:** Heat flow rate vs. temperature for PVA heated at 2000 K/s after isothermal melt crystallization for various long times at a temperature of: (A) 140 °C; (B) 150 °C. Crystallization time increases as the color changes from blue to yellow. The glass transition temperature increases with crystallization time.

In all isothermally melt crystallized samples a melting doublet is observed with the first, lower temperature melting peak temperature varying with the crystallization temperature. The peak observed around 200 °C in all samples is independent of thermal treatment. Melting peak temperatures are reported in the supporting information **Tables 5.2 and Table 5.3**. Observation of double melting indicates a mixture of crystal populations exist in the samples, arising from crystals

grown during the isothermal melt crystallization from nuclei formed either heterogeneously or homogeneously.

The heat capacity increment at the glass transition is measured for each heating curve and reported in **Tables 5.2 through 5.4**. At melt crystallization temperatures of 90 °C and 95 °C, where the onset of melting obscures the glass transition, the heat capacity increment was measured by identifying the semi-crystalline heat capacity at the inflection point between the glass transition and the low temperature melting peak and subtracting from this the glassy phase heat capacity at  $T_g$ . When there is a semi crystalline heat capacity baseline between the glass transition and the onset of melting, the standard technique for measuring the heat capacity increment is used. The heat capacity increment is reported as the difference between the glassy and semi crystalline baselines extrapolated to glass transition temperature, which is the inflection point in the heat capacity between the two phases. An example of this type of measurement is shown in **Figure 5.9** for the heating scan of PVA isothermally crystallized at 150 °C for 1 second.

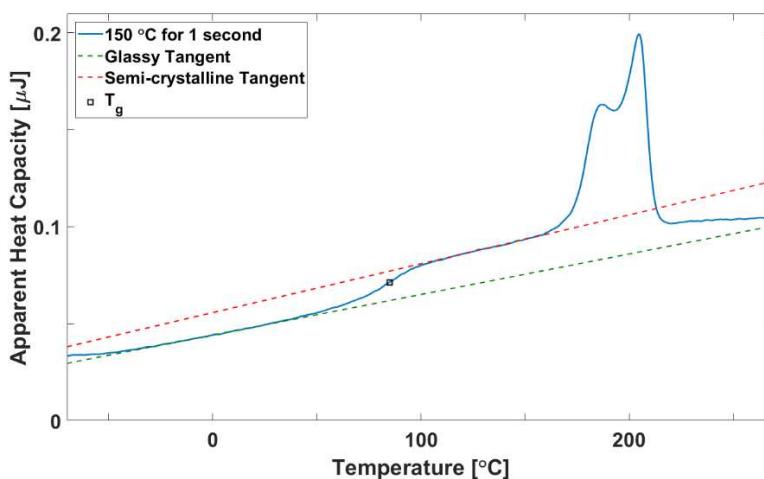


**Figure 5.9:** Apparent heat capacity vs. temperature and an example of the measurement of the heat capacity increment at the glass transition for PVA isothermally crystallized at 150 °C for 1 second. The dashed, green line is the tangent line of the glassy phase heat capacity taken below the glass transition (hollow, black square) and the dashed, red line is the tangent line of the semi-crystalline heat capacity taken above the glass transition.

**Table 5.2:** Short time isothermal melt crystallization

| $T_C$<br>°C | $t_c$<br>s | Crystal<br>Fraction <sup>a</sup><br>$\phi_C$ | $T_g$<br>°C | $T_g$<br>Error<br>°C | $\Delta C_p(T_g)$<br>J/(gK) | $\Delta C_p(T_g)$<br>error J/(gK) | $T_{M1}^b$<br>°C | $T_{M2}^b$<br>°C |
|-------------|------------|--|-------------|----------------------|-----------------------------|-----------------------------------|------------------|------------------|
| 90          | 2          | 0.21   | 93          | 4                    | 0.69                        | 0.05                              | 203              | 115              |
| 90          | 10         | 0.24   | 103         | 4                    | 0.74                        | 0.05                              | 203              | 120              |
| 90          | 20         | 0.25   | 108         | 4                    | 0.84                        | 0.05                              | 202              | 123              |
| 90          | 50         | 0.28   | 108         | 4                    | 0.80                        | 0.05                              | 202              | 126              |
| 90          | 100        | 0.28   | 109         | 4                    | 0.78                        | 0.05                              | 202              | 127              |
| 90          | 200        | 0.29   | 107         | 4                    | 0.66                        | 0.05                              | 202              | 130              |
| 90          | 500        | 0.32   | 108         | 4                    | 0.65                        | 0.05                              | 202              | 131              |
| 95          | 1          | 0.23   | 92          | 4                    | 0.72                        | 0.05                              | 202              | 119              |
| 95          | 20         | 0.28   | 108         | 4                    | 0.71                        | 0.05                              | 202              | 130              |
| 95          | 50         | 0.31   | 109         | 4                    | 0.69                        | 0.05                              | 202              | 133              |
| 95          | 500        | 0.35   | 110         | 4                    | 0.61                        | 0.05                              | 202              | 138              |
| 120         | 2          | 0.43   | 82          | 2                    | 0.60                        | 0.03                              | 199              | 148              |
| 120         | 5          | 0.45   | 84          | 2                    | 0.61                        | 0.02                              | 199              | 151              |
| 120         | 20         | 0.46   | 80          | 2                    | 0.60                        | 0.02                              | 199              | 154              |
| 120         | 50         | 0.48   | 84          | 2                    | 0.56                        | 0.02                              | 199              | 156              |
| 120         | 100        | 0.49   | 84          | 2                    | 0.55                        | 0.02                              | 199              | 158              |
| 120         | 200        | 0.50   | 80          | 2                    | 0.55                        | 0.02                              | 199              | 160              |
| 120         | 1000       | 0.52   | 85          | 2                    | 0.52                        | 0.03                              | 200              | 163              |

<sup>a</sup> Mass fraction crystallinity,  $\phi$ , calculated from melting endotherm using Eqn. 5.1b

<sup>b</sup> First and second melting peak temperatures

**Table 5.3:** Long time isothermal melt crystallization

| T <sub>c</sub><br>°C | t <sub>c</sub><br>s | Crystal<br>Fraction <sup>a</sup><br>φ <sub>c</sub> | T <sub>g</sub><br>± 2 °C | ΔC <sub>p</sub> (T <sub>g</sub> )<br>J/(gK) | ΔC <sub>p</sub> (T <sub>g</sub> )<br>error<br>J/(gK) | T <sub>M1</sub> <sup>b</sup> °C | T <sub>M2</sub> <sup>b</sup> °C |
|----------------------|---------------------|--|--------------------------|---|--|---------------------------------|---------------------------------|
| 140 <sup>c</sup>     | 1                   | 0.45   | 89                       | 0.54  | 0.03   | 205                             | 170                             |
| 140 <sup>c</sup>     | 10                  | 0.46   | 88                       | 0.53  | 0.03   | 203                             | 171                             |
| 140 <sup>c</sup>     | 100                 | 0.49   | 89                       | 0.54  | 0.03   | 202                             | 174                             |
| 140 <sup>c</sup>     | 1000                | 0.50   | 88                       | 0.50  | 0.02   | 202                             | 175                             |
| 140 <sup>c</sup>     | 2000                | 0.50   | 89                       | 0.49  | 0.02   | 202                             | 177                             |
| 140 <sup>c</sup>     | 5000                | 0.53   | 88                       | 0.49  | 0.02   | 203                             | 180                             |
| 140 <sup>c</sup>     | 10000               | 0.55   | 85                       | 0.49  | 0.02   | 203                             | 181                             |
| 140 <sup>c</sup>     | 1                   | 0.45   | 89                       | 0.51  | 0.03   | 202                             | 170                             |
| 150 <sup>d</sup>     | 10                  | 0.45   | 86                       | 0.52  | 0.02   | 204                             | 186                             |
| 150 <sup>d</sup>     | 100                 | 0.50   | 87                       | 0.51  | 0.02   | 206                             | 155                             |
| 150 <sup>d</sup>     | 1000                | 0.53   | 87                       | 0.49  | 0.01   | 209                             | 159                             |
| 150 <sup>d</sup>     | 2000                | 0.37   | 87                       | 0.58  | 0.01   | 203                             | 173                             |
| 150 <sup>d</sup>     | 5000                | 0.54   | 84                       | 0.47  | 0.01   | 210                             | 165                             |
| 150 <sup>d</sup>     | 10000               | 0.55   | 87                       | 0.43  | 0.01   | 210                             | 164                             |

<sup>a</sup> Mass fraction crystallinity, φ<sub>c</sub>, calculated from melting endotherm

<sup>b</sup> First and second melting peak temperatures

<sup>c</sup> Single sample used for isothermal melt crystallization at 140°C

<sup>d</sup> Single sample used for isothermal melt crystallization at 150 °C

**Table 5.4:** DSC isothermally crystallized samples

| Sample | Mass<br>g | T<br>°C          | t<br>s | Crystal<br>Fraction <sup>a</sup><br>$\phi_c$ | T <sub>g</sub><br>°C | $\Delta C_p(T_g)$<br>$\pm 0.02$<br>J/(gK) |
|--------|-----------|------------------|--------|--|----------------------|---|
| 1      | 2.09      | 170 <sup>a</sup> | 30     | 0.63   | 74.9                 | 0.38                                      |
| 2      | 2.37      | 170 <sup>a</sup> | 120    | 0.66   | 76.3                 | 0.34                                      |
| 3      | 2.31      | 170 <sup>a</sup> | 300    | 0.65   | 78.6                 | 0.34                                      |
| 4      | 2.05      | 150 <sup>b</sup> | 15     | 0.60   | 74.5                 | 0.42                                      |
| 5      | 2.09      | 140 <sup>b</sup> | 5      | 0.60   | 73.7                 | 0.44                                      |
| 6      | 2.22      | 160 <sup>b</sup> | 5      | 0.59   | 71.3                 | 0.43                                      |
| 7      | 1.97      | 150 <sup>b</sup> | 600    | 0.64   | 79.9                 | 0.37                                      |
| 8      | 2.13      | 130 <sup>b</sup> | 60     | 0.62   | 75.4                 | 0.41                                      |

<sup>a</sup> Samples partially melted and then isothermally crystallized at 170 °C

<sup>b</sup> Cold crystallized samples

Finally, **Figure 5.10** shows the heat capacity increment at T<sub>g</sub>,  $\Delta C_p(T_g)$  vs. mass fraction crystallinity,  $\phi_c$ , for a wide range of preparations and techniques. FSC results are shown for non-isothermally crystallized samples (blue x), and isothermally crystallized samples with different crystallization temperatures, T<sub>c</sub>. Samples were treated for short times for T<sub>c</sub> = 90 °C (orange □), 95 °C (yellow □), and 120 °C (red □) or for long times at T<sub>c</sub> = 140 °C (green o), and 150 °C (light blue o). Conventional DSC results are also shown, and complement the FSC results since larger degrees of crystallinity were obtained from DSC. The heat capacity increment is observed to decrease linearly as the crystallinity increases.

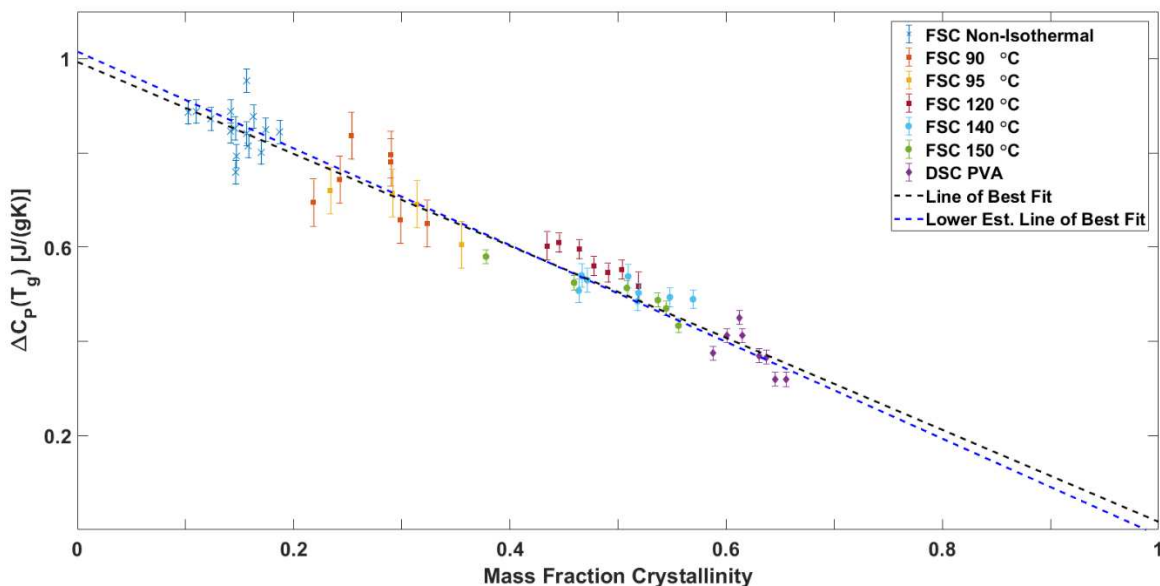


**Figure 5.10:** Specific heat capacity increment at  $T_g$  vs. mass fraction crystallinity. Non-isothermally crystallized samples (blue x); Samples isothermally crystallized for short times at different temperatures: 90 °C (orange □), 95 °C (yellow □), 120 °C (red □). Samples isothermally crystallized for long times at different temperatures: 140 °C (green o), 150 °C (light blue o). Conventional DSC results are shown for comparison: PVA isothermally cold crystallized from 130-160 °C for various times or partially melted and annealed at 170 °C for various times (purple diamonds).

## 5.6 Discussion of Fundamental Thermal Properties

The combination of chip calorimetry techniques has allowed for the measurement of the degradation free liquid phase specific heat capacity of PVA over a range of temperatures extending from the last observed melting temperature up to the equilibrium melting point ( $T_m^0 = 538$  K [6]), a range of temperatures obscured by degradation in conventional thermal analysis techniques. We calculate the average value of the liquid state heat capacity using Mettler Flash DSC1 data from **Figure 5.5**, and confirm the result with more limited data from the custom calorimeter (**Figure 5.6A**), which allows full quenching of the PVA to the glassy amorphous state.

Using data in **Figure 5.5** from the Mettler Flash DSC1 at  $\beta = 2000$  K/s, the average liquid state heat capacity,  $\langle c_p^{\text{Liquid}}(T) \rangle$ , was obtained by averaging the individual liquid phase data from many experiments. The best fit to a linear relationship ( $p = 3.6 \times 10^{-09}$ ) is:

$$c_p^{\text{Liquid}}(T) = (0.0024 \pm 0.0007) * T + (1.9 \pm 0.3), \text{ in J/(gK)} \quad (5.2)$$

This linear relationship was shown in **Figure 5.6** by the dashed line.

With the custom calorimeter, we use the cooling scan at 20,000 K/s (black curve in **Figure 5.6A**) to provide a second estimate of the specific heat capacity of the liquid phase of PVA. Fitting the amorphous cooling scan over all temperatures above  $T_g$  we find:  $c_p^{\text{Liquid}}(T) = (0.0029 \pm 0.001) * T + (1.68 \pm 0.01)$ , in J/(gK). This result is in good agreement with that presented in Eqn. (5.2).

Another important thermal parameter is the specific heat capacity increment for 100% amorphous material,  $\Delta c_p^{\text{amor}}(T_g)$ . This value has been unavailable to date, because of the inability to obtain an amorphous glassy sample of PVA owing to its very fast crystallization kinetics. We use several approaches to determine this parameter. First, we are able to obtain a fully amorphous sample by cooling at 20,000 K/s in the custom calorimeter. The heat capacity increment at  $T_g$ , determined from the reheating scan of **Figure 5.6A** yields:  $\Delta c_p^{\text{amor}}(T_g) = (0.96 \pm 0.01)$  J/(gK).

Second, using the average liquid phase heat capacity from Eqn. 5.2, a value for  $\Delta c_p^{\text{amor}}(T_g)$  is found by extrapolation of  $\Delta c_p^{\text{Liquid}}(T)$  to  $T = T_g$  and then subtracting the solid state heat capacity at the same temperature,  $\Delta c_p^{\text{Solid}}(T_g)$ :

$$\Delta c_p^{\text{amor}}(T_g) = \Delta c_p^{\text{Liquid}}(T_g) - \Delta c_p^{\text{Solid}}(T_g) \quad (5.3)$$

Eqn. 5.1 is solved using the literature value for the amorphous phase glass transition temperature of  $T_g = 358 \text{ K}$  ( $85 \text{ }^\circ\text{C}$ )[6]. This results in an average value of:

$$\Delta c_p^{\text{amor}}(T_g) = (1.01 \pm 0.08) \text{ J}/(\text{gK}) \quad (5.4)$$

The two values of  $\Delta c_p^{\text{amor}}(T_g)$ , one obtained by measurement of the heat capacity increment at the glass transition during the critical cooling rate scan, and the other by extrapolation of the liquid line, are in close agreement.

The third set of experiments, shown in **Figure 5.10**, smoothly merges FSC results with conventional DSC measurements. Using the approach developed earlier from studies of silk biopolymer we extract another measure of  $\Delta c_p^{\text{amor}}(T_g)$  [14]. The data plotted in **Figure 5.10** are fit by the following linear relationship ( $r^2 = 0.9735$ ):

$$\Delta C_p^{\text{Meas}}(T_g) = (-0.9763 \pm 0.051) * \phi_c + (0.99 \pm 0.02) \quad (5.5)$$

Extrapolating the linear relationship between  $\Delta c_p(T_g)$  vs.  $\phi_c$ , back to the intersection at  $\phi_c = 0$  we obtain a measurement of  $\Delta c_p^{\text{amor}}(T_g)$  which does not rely solely upon any one thermal analysis technique. A value of  $\Delta c_p^{\text{amor}}(T_g) = 0.99 \pm 0.02 \text{ J}/(\text{gK})$  is obtained.

In the case of a two-phase polymer model a linear fit of the heat capacity increment vs. mass fraction crystallinity should intersect the x-axis as  $\phi_c = 1.0$ . [14] However, most polymers cannot be modeled as two-phase systems because of the existence of rigid amorphous phase (RAF). The RAF does not contribute to the glass transition increment as it is kinetically arrested by the presence of crystals, nor is it incorporated into the polymer crystals. [14-17] This will cause the line of best fit to intercept the x-axis at a mass fraction crystallinity less than unity.

The line of best fit through the data in **Figure 5.10** passes through the point  $\phi = 1$ , with a value of  $\phi = 1.02 \pm 0.7$  at the x-intercept (based on the extremes of the error bars of the fit). The dashed blue line in **Figure 5.10** shows another line of fit within the 95% confidence interval of the best fit to the data with the following linear relationship:

$$\Delta C_p^{\text{Meas}}(T_g) = -1.03 * \phi_c + 1.02 \quad (5.6)$$

Here the relationship intersects the x-axis at a mass fraction crystallinity of  $\phi = 0.99$ . Any x-intercept less than 1 indicates that PVA contains RAF. In the three-phase polymer model the sum of the mobile amorphous fraction (MAF), which contributes to the glass transition, the RAF, and the crystalline fraction must be unity. [14-17]

$$\phi_{\text{MAF}} + \phi_{\text{RAF}} + \phi = 1 \quad (5.7a)$$

where

$$\phi_{\text{MAF}} = \Delta C_p^{\text{meas}}(T_g) / \Delta C_p^{\text{amor}}(T_g) \quad (5.7b)$$

Solving for the x-intercept of the line in Eqn. 5.6 and using the relationship in Eqn. 5.7, the rigid amorphous fraction of PVA is estimated around 0.01. Taking the most extreme values within the range of error for the line of best fit in Eqn. 5 the RAF of PVA is determined to be < 5%.

The method of measuring  $\Delta C_p^{\text{amor}}(T_g)$  as seen in **Figure 5.10** provides a measurement that is in good agreement with the value obtained by extrapolation of Eqn. 5.2. The method presented here relies on extrapolation of the heat capacity increment as a function of crystallinity. In cases where it is possible to combine experiments on samples using different thermal analysis instrumentation, a much wider range of crystallinities may be achieved. As seen in **Figure 5.10** results from PVA crystallized in a conventional DSC show excellent agreement with the line of

best fit for the FSC samples isothermally melt crystallized. This indicates that the method of calibrating the data by the symmetry correction and mass determination outlined in previous sections is effective and allows for precise, quantitative measurements of fundamental thermal properties.

When degradation becomes significant, as was the case for samples which were melted more than 30 times under fast scanning conditions or brought into the melt under conventional DSC conditions, a second trend is observed. The fast scanning data presented in **Figure 5.10** was obtained from samples which were less than 3% degraded. The remaining FSC isothermal crystallization scans were performed once the sample had lost between 3% and 10% of its initial mass. This extent of degradation overlaps with that present in the conventional DSC self nucleation experiments presented in the previous chapter. Flash isothermal crystallization scans for  $T = 100$ - $115$  °C and  $125$ - $130$  °C are combined with self nucleation scans to form the “less than gently degraded” data set. The “nearly degradation free”  $\Delta C(T_g)$  vs.  $\phi_c$  **Figure 5.10** is reproduced with the “more than gently degraded data” for both the FSC isothermal crystallization experiments and self nucleation data in **Figure 5.11**.

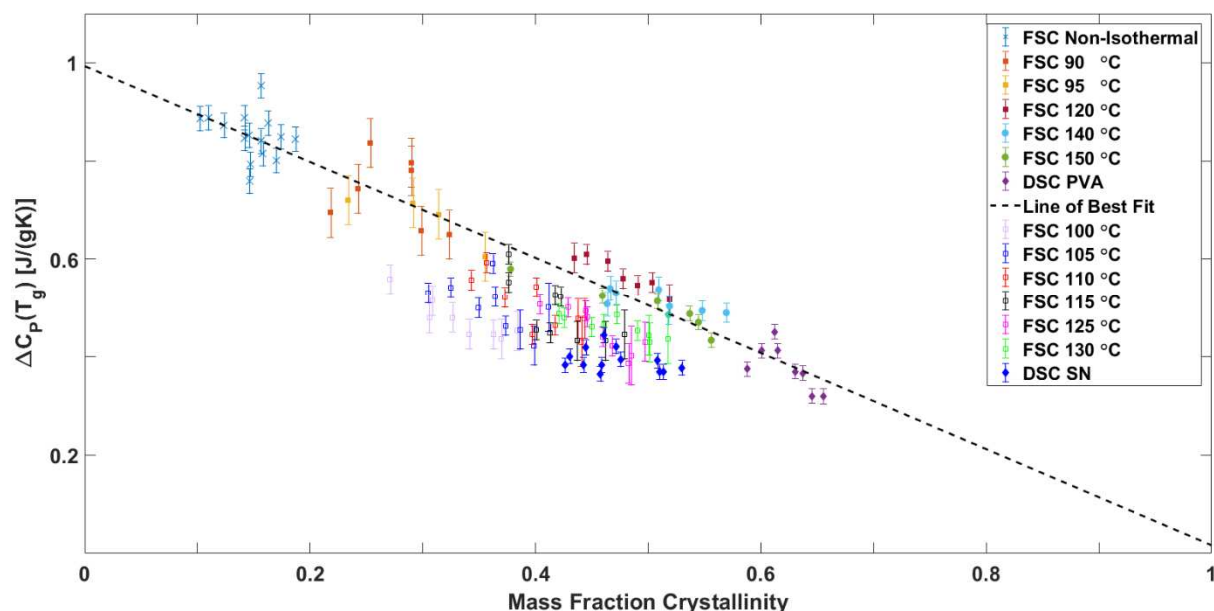


**Figure 5.11:** Recreation of **Figure 5.10** with the addition of “less than gently degraded” data. Samples isothermally crystallized for short times at different temperatures: 100 °C (hollow pink □), 105 °C (hollow blue □), 110 °C (hollow red □), 115 °C (hollow black □), 125 °C (hollow fuchsia □), 130 °C (hollow green □). Conventional DSC Self Nucleation results are shown in dark blue diamonds for comparison, the meaning of other symbols can be found in the caption to **Figure 5.10**. The black dotted line is the best fit not including the newly added data.

All the data for samples which have lost 3% or more of their mass to thermal degradation appear below the line of best fit for the nearly degradation free case. The depression of the glass transition and the enthalpy of melting (from which the crystallinity is calculated) are well reported for PVA. However, the difference in the relationship between the heat capacity increment at the glass transition and mass fraction crystallinity for the case of degraded samples provides new insights. The impact of thermal degradation on PVA is observed to have a substantial impact on the formation of the rigid amorphous fraction. With the primary mechanism of PVA degradation being random chain scission [18], it appears that these chain fragments are unable to be fully incorporated into the crystalline phase and restrict overall chain amorphous chain mobility.

The overall agreement in both the nearly degradation free and the “less than gently degraded” case across both instruments demonstrates the success of the application of fast scanning calorimeters to measuring the fundamental thermal properties of polyvinyl alcohol.

### 5.7 *References*

- [1] C.P. Li, J. Vongsivut, X.D. She, Y.Z. Li, F.H. She, L.X. Kong, New insight into non-isothermal crystallization of PVA-graphene composites, *Physical Chemistry Chemical Physics* 16(40) (2014) 22145-22158.
- [2] C.P. Li, T.T. Hou, X.D. She, X.Y. Wei, F.H. She, W.M. Gao, L.X. Kong, Decomposition properties of PVA/graphene composites during melting-crystallization, *Polymer Degradation and Stability* 119 (2015) 178-189.
- [3] D. Thomas, P. Cebe, Self-nucleation and crystallization of polyvinyl alcohol, *Journal of Thermal Analysis and Calorimetry* 127(1) (2017) 885-894.
- [4] N.A. Peppas, P.J. Hansen, Crystallization kinetics of poly(vinyl alcohol), *Journal of Applied Polymer Science* 27(12) (1982) 4787-4797.
- [5] H.S. Bu, W. Aycock, S.Z.D. Cheng, B. Wunderlich, Heat capacities of various solid linear macromolecules, *Polymer* 29(8) (1988) 1485-1494.
- [6] M. Pyda, Polyvinyl Alcohol (PVA) Heat Capacity, Enthalpy, Entropy, Gibbs Energy, 2014. [http://materials.springer.com/polymerthermodynamics/docs/athas\\_0147](http://materials.springer.com/polymerthermodynamics/docs/athas_0147). (Accessed 27-10-2015 2015).

- [7] G.V. Poel, D. Istrate, A. Magon, V. Mathot, Performance and calibration of the Flash DSC 1, a new, MEMS-based fast scanning calorimeter, *Journal of Thermal Analysis and Calorimetry* 110(3) (2012) 1533-1546.
- [8] T. Hiroyuki, S. Syûzô, N. Isamu, The Crystallinity of Solid High Polymers. I. The Crystallinity of Polyvinyl Alcohol Film, *Bulletin of the Chemical Society of Japan* 28(8) (1955) 559-564.
- [9] A.P. Gray, Polymer crystallinity determinations by DSC, *Thermochimica Acta* 1(6) (1970) 563-579.
- [10] D. Thomas, P. Cebe, Self Nucleation and Crystallization of Polyvinyl Alcohol, *Journal of Thermal Analysis and Calorimetry* (2015).
- [11] C.P. Li, T.T. Hou, J. Vongsvivut, Y.Z. Li, X.D. She, F.H. She, W.M. Gao, L.X. Kong, Simultaneous crystallization and decomposition of PVA/MMT composites during non-isothermal process, *Thermochimica Acta* 618 (2015) 26-35.
- [12] E. Zhuravlev, C. Schick, Fast scanning power compensated differential scanning nanocalorimeter: 1. The device, *Thermochimica Acta* 505(1-2) (2010) 1-13.
- [13] E. Zhuravlev, C. Schick, Fast scanning power compensated differential scanning nanocalorimeter: 2. Heat capacity analysis, *Thermochimica Acta* 505(1-2) (2010) 14-21.
- [14] X. Hu, D. Kaplan, P. Cebe, Determining Beta-Sheet Crystallinity in Fibrous Proteins by Thermal Analysis and Infrared Spectroscopy, *Macromolecules* 39(18) (2006) 6161-6170.
- [15] H. Suzuki, J. Grebowicz, B. Wunderlich, Heat capacity of semicrystalline, linear poly(oxymethylene) and poly(oxyethylene), *Die Makromolekulare Chemie* 186(5) (1985) 1109-1119.

- [16] S.Z.D. Cheng, M.Y. Cao, B. Wunderlich, Glass transition and melting behavior of poly(oxy-1,4-phenyleneoxy-1,4-phenylenecarbonyl-1,4-phenylene) (PEEK), *Macromolecules* 19(7) (1986) 1868-1876.
- [17] P. Huo, P. Cebe, Effects of thermal history on the rigid amorphous phase in poly(phenylene sulfide), *Colloid and Polymer Science* 270(9) (1992) 840-852.
- [18] B.J. Holland, J.N. Hay, The thermal degradation of poly(vinyl alcohol), *Polymer* 42(16) (2001) 6775-6783.

## ***Chapter 6 Novel Method for Fast Scanning Calorimetry of Electrospun Fibers: Polyethylene Terephthalate (PET) Nanofibers***

### ***6.0 Introduction and Proof of Concept***

Prior to the development of the technique outlined in this chapter, we found that pieces cut from empty TEM grids of sizes ranging from typical sample size to much larger than the active sensor area, did not rupture the sensor membrane. The UFSC1 membrane was tolerant of any size TEM grid segment and it was possible to proceed to the development and testing of the electrospinning fiber deposition technique. Details of the electrospinning conditions are outlined in **Section 2.3.0** and the direct spinning onto TEM grids is outlined in **Section 2.4**. Details of the fast scanning calorimetry (FSC) methods are outlined in **Section 3.4.3.2**.

This chapter is organized as follows: **Section 6.1** presents results of the electrospinning and determination of appropriate electrospinning time,  $t_{spin}$  and XRD measurements on “as spun” samples; **Section 6.2** presents the successful preparation of TEM grid segments and sample loading onto UFSC1 sensors; **Section 6.3** presents results of cold crystallization and melting of fibers; **Section 6.4** presents conventional DSC work on PET with a similar temperature – time profile to that used in FSC experiments; **Section 6.5** presents results of melt crystallized droplets formed by melting the PET fibers; **Section 6.6** presents results of tests on empty TEM grids and TEM grids loaded with indium.

## **6.1 Analysis of Electrospun PET Fibers**

Polyethylene terephthalate is readily electrospun and can be spun into well aligned, bead free fibers. [1-7] To the naked eye the fibers appeared to be successfully deposited across the TEM grids mounted along the center of the rotating drum counter electrode as seen in **Figure 2.8d**. The aluminum foil was unwrapped from the rotating drum and the conductive copper tape was cut away from the edges of the grids. Grids were easily lifted off the foil and transferred to glass slides for imaging and FSC sample preparation. Sections of aluminum foil between the TEM grids served as witness samples. These were cut away, mounted onto stubs, and sputter coated in gold-palladium for scanning electron microscopy (SEM) imaging using the Phenom G2 Pure. SEM imaging at 5300X indicates that the fibers formed were bead free, had fiber diameters most frequently in the range from 300-400 nm, and were aligned along the spin direction as seen in **Figure 6.1A**.

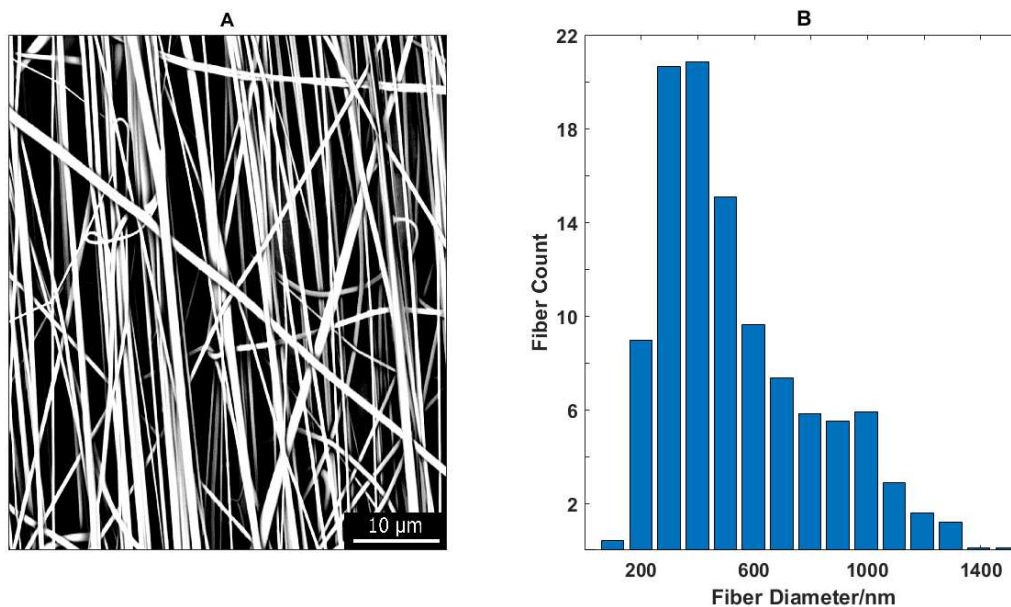


**Figure 6.1:** (A) SEM image of PET nanofibers taken from the aluminum foil between TEM grids. The spin direction is vertical. Images were collected at 5300X magnification where it was possible to resolve the fiber diameter and assess fiber quality. (B) Fiber diameter distribution obtained using ImageJ [8] with the DiamterJ plugin [8]. The cluster of diameters between 800 nm and 1200 nm is the result of fiber mergers and fiber bundles which are not separated in ImageJ.

The spin conditions used were found to result in nanofibers with an average fiber diameter of 350 nm, in agreement with literature on electrospinning of PET [1-7]. An example fiber diameter distribution is shown in **Figure 6.1B**. The average fiber diameter allows for calculation of the average mass per unit length of the fibers. In addition to measuring the fiber diameter the average fiber number density,  $n$ , is measured perpendicular to the spin direction (i.e., measured horizontally in **Figure 6.1A**). This parameter allows for an estimation of the fiber mass per unit area,  $m$ , on the TEM grids using the following relation:

$$m \approx (2\pi l(\bar{d}/2)^2)\rho n w \quad (6.1)$$

where  $l$  is the length of the TEM grid in the fiber direction,  $w$  is the width perpendicular to the fiber direction,  $\bar{d}$ , is the average fiber diameter, and  $\rho$  is the density of the fibers. A second fiber mat, spun for  $t_{spin} = 1$  hour was made under the conditions detailed in **Section 2.3.0** to produce a mat suitable for X-ray Diffraction (XRD) measurements. XRD was performed on the “as spun” PET fiber mat for scattering angles between 5-45  $^{\circ}2\theta$  as outlined in **Section 3.2.2**. The XRD pattern for the “as spun” PET fiber mat is shown in **Figure 6.2**.

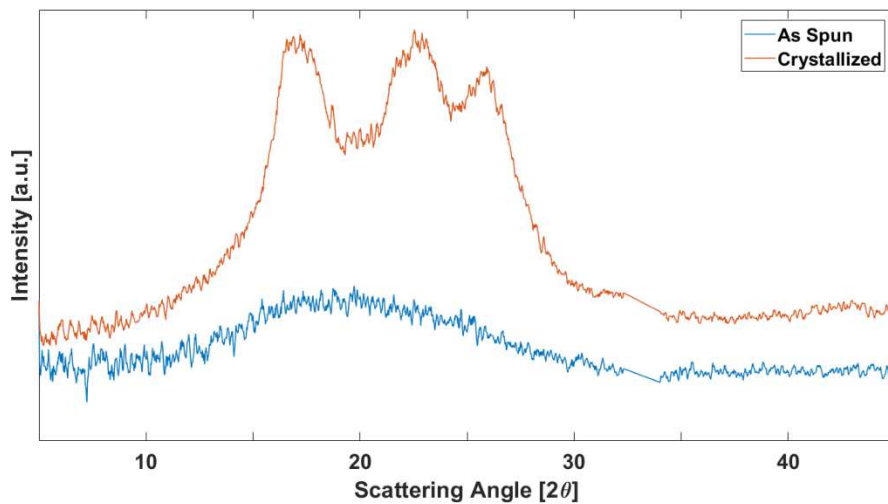


**Figure 6.2:** X-ray diffraction patterns for “as spun” (blue) and crystallized (orange) PET fibers. Fibers “as spun” are amorphous. The line segment at about 33  $^{\circ}2\theta$  replaces the silicon peak (100) peak from the sample holder.

X-ray measurements indicate that PET nanofibers are amorphous “as spun” as evidenced by scattering coming only from the amorphous halo. A diffraction pattern for semi-crystalline PET nanofibers is included for comparison. This result allows for the use of the amorphous density,  $\rho_a = 1.36$  [9], in Eqn. 6.1 to estimate the mass of fibers in a given area. While it is possible to obtain fiber mats of any mass by spinning for longer times, sample thickness needs to be no greater than 10  $\mu\text{m}$  for high quality FSC measurements. [10, 11] A unique challenge to FSC measurements on

electrospun fibers is that the fibers are dispersed and collected fibers contain many voids which will impair effective heating of any fiber which is not in direct contact with the sensor. Samples were electrospun such that TEM grids were coated with the minimum number of fibers to obtain masses greater than 5 ng per 1000  $\mu\text{m}^2$ , as it was difficult to reliably produce clean cut samples less than 100  $\mu\text{m}$  on a given edge. A short spin time,  $t_{spin}$ , of 45 s was found to result in samples which had an average mass of 10 ng per 1000  $\mu\text{m}^2$  and were suitable for FSC experiments.

## 6.2 *Fiber Integrity During Handling*

Optical images of each TEM grid were collected prior to sample preparation to ensure that the fibers were not damaged or disturbed by handling. The fiber bundles appear to be well aligned along the spin direction and undisturbed by handling during removal from the aluminum foil on the counter electrode. The fiber loaded TEM grid following removal is shown in **Figure 6.3A**. Each grid was cut into smaller parent sections roughly between 300  $\mu\text{m}$  and 500  $\mu\text{m}$  on edge. From these, those with the smoothest edges and least evidence of disturbed fibers were further subdivided for FSC sample preparation. An example of a typical parent section is seen in **Figure 6.3B**. Images shown in **Figure 6.3A and 6.3B** were collected using Nikon POL E600 microscope in room 421B and the image in **Figure 6.3C** was collected using the Olympus BX41 reflection microscope in Rostock, Germany. The backgrounds appear black due to the incident polarized light being blocked by the analyzer. Additional illumination was provided from above the sample by an external light source. Fibers appear white due to the diffuse scattering of white light.

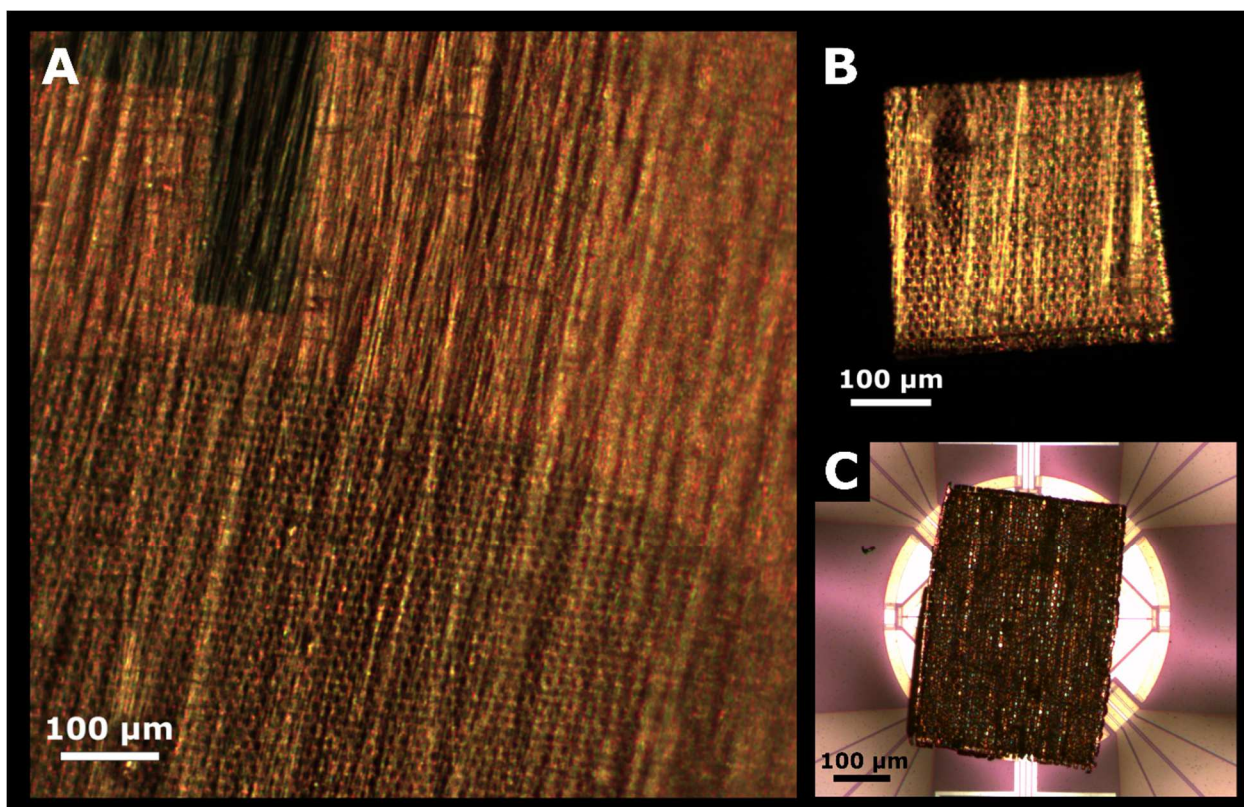


**Figure 6.3:** (A) Optical image of ESPET loaded TEM grid through a 10X objective with 100x total magnification. Fiber bundles are observed to be running parallel to the spin direction. The alignment notch can be seen in the top left of the image. (B) Example of parent sample cut from the center of the ESPET loaded TEM grid. Fibers show no signs of being disturbed by the cutting process. (C) Oversized ESPET loaded TEM grid sample loaded onto Mettler UFSC1 sensor with fiber side up. Dark streaks running top to bottom are fiber bundles.

The upper limit of sample size is set by the Mettler UFSC1 chip sensor which has a diameter of 500 μm. An example of an oversized TEM grid sample is seen in **Figure 6.3C**, imaged fiber side up, to demonstrate that, when placed gently, the membrane will not rupture under the load of the samples. Fiber bundles can still be seen running along the vertical direction in **Figure 6.3C** indicating that the entire sample preparation process can be performed without damaging the fibers. Several exploratory scans were taken with the TEM grid segments loaded face up as seen in **Figure 6.3C**. However all FSC experiments performed on PET nanofibers are performed with the TEM grids loaded face down; an example is seen in **Figure 6.4**.

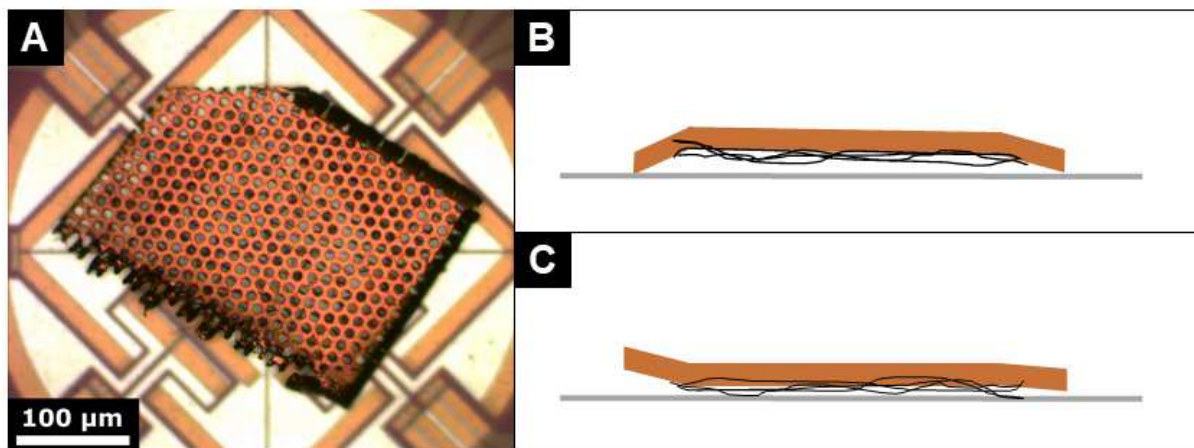


**Figure 6.4:** (A) A typical example of a fiber loaded TEM grid loaded face down for FSC measurements. Here the jagged edges seen in the bottom left of the image show the last tolerable cut before a scalpel blade needs to be changed. (B) and (C) Cartoon schematics of fiber loaded sensor. The sensor is the gray oval, seen from an angled view. The orange polygon represents the TEM grid, the circular gray region represents the active sensor area on the UFSC1 chip, and the black lines represent the electrospun fibers. (B) Fibers loaded face down with minimal TEM grid impact. This sample has optimal contact with the sensor. (C) Grid cutting with a dull blade can result in crimping along the cut edges which prevents optimum sample to sensor contact.

It is important to use a fresh stainless steel scalpel when cutting the grids as the preparation of one parent, which is then further subdivided into multiple pieces by a series of perpendicular cuts, will sufficiently dull the blade preventing clean cuts. The bottom left side of the sample shown in **Figure 6.4A** is an example of the last tolerable cut before a blade is changed. Smooth edges and cuts are essential to ensure clean contact. **Figure 6.4B and 6.4C** diagram the two possible conditions a cut sample can be in contact with the sensor where the grid and fibers lay either flat on the membrane or the cut edges obstruct complete contact, respectively.

The fiber side down approach leads to an interaction between the liquid phase polymer and the thermal expansion of the TEM grids under heating which causes an apparent exothermic

upward trend in the data and prevents symmetry correction by the method previously described. When loaded fiber side up symmetry correction is possible in the standard way. The drawback to the fiber side up approach is evidenced by the apparent double glass transition which indicates that the upper layers of fibers not effectively being heated, likely due to the insulating effect of the voids between the fibers. The curvature prevents quantitative measurements of the heat capacity of the sample but does not prevent measuring the step change at the glass transition or the enthalpy of crystallization or melting. It is possible to measure the heat capacity increment at the glass transition as the curvature does not set in until the polymer is in the liquid phase.

### **6.3 Cold Crystallization and Melting of PET Fibers**

The residual solvents in the electrospun PET fibers require them to be heated to near or just above the glass transition temperature,  $T_g$ , or, depending upon the boiling point of the solvent, much higher than the glass transition. The boiling point of trifluoroacetic acid,  $T_{\text{boil}} = 74\text{ }^\circ\text{C}$ , [12] is above the equilibrium glass transition temperature of PET,  $T_g = 69\text{ }^\circ\text{C}$  [13]. Because of the high heating rate,  $\beta = 2000\text{ K/s}$ , the glass transition can be pushed to temperatures as high as  $90\text{ }^\circ\text{C}$  where the coincident solvent evaporation can obscure the glass transition (as was the case with bound water in PVA films discussed in **Chapters 4 and 5**). An incremental drying protocol was implemented where the sample was heated to temperatures,  $T_{\text{dry}}$ , between  $50\text{ }^\circ\text{C}$  and  $110\text{ }^\circ\text{C}$  and held isothermally for 1 minute. By tracking the glassy heat flow baseline, it was determined that complete drying was not achieved until the sample had been heated to  $80\text{ }^\circ\text{C}$ . Grids loaded fiber side down were brought through the dry, cold crystallization, and melting temperature – time profile, shown as the purple and blue curves in **Figure 3.23**. Cold crystallization experiments

following this profile were performed at various temperatures,  $T_{CC}$ , between 120 °C and 160 °C in 10 °C increments, isothermally holding for 15 minutes. An example of one of these experiments is shown below in **Figure 6.5** for  $T_{CC} = 150$  °C. The figure shows the raw data exported from Mettler STARE [14] software plotted using MATLAB [15].

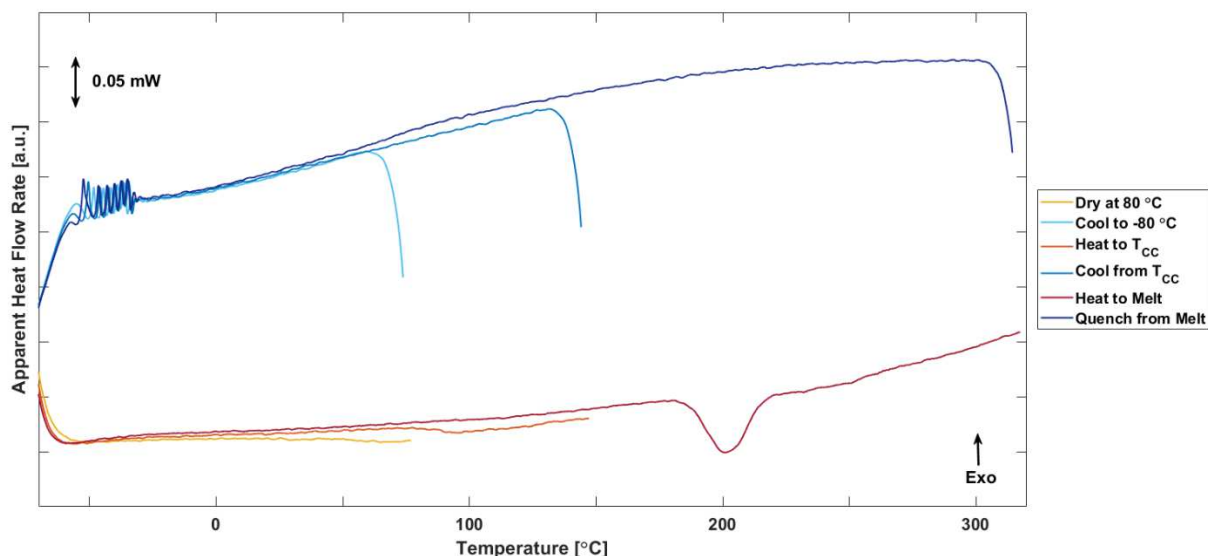


**Figure 6.5:** Heat flow rate vs. temperature for a typical dry, isothermally cold crystallize, and melt experiment performed on electrospun fibers. The cold crystallization temperature,  $T_{CC}$ , is 150 °C and the heating and cooling rate,  $\beta$ , is  $\pm 2000$  K/s.

The yellow curve in **Figure 6.5** shows the initial heating to 80 °C. The endothermic drop in the curve between 50 °C and 80 °C corresponds to both a plasticized glass transition and the onset of solvent ejection. After the sample is held at 80° C for 1 minute it is then cooled and reheated to the cold crystallization temperature,  $T_{CC}$ . The drying step is confirmed to be successful as the heat flow baselines in the glassy regions overlap well on heating and cooling suggesting that the sample mass in contact with the sensor is not changing. Due to the interaction between the

tacky, liquid phase polymer and the thermal expansion of the TEM grids, there are asymmetries between the heating and cooling scans which prevent the use of the previously developed and tested symmetry corrections to the electrospun fiber data when samples are loaded face down. While this curvature makes measurements of the liquid phase heat capacity difficult it is still possible to measure the enthalpy of melting following cold crystallization.

Unlike the PVA thin films discussed in the previous chapter the heat capacity increment at the glass transition for PET is well known,  $\Delta c_p^{\text{amor}}(T_g) = [13]$ , and allows for the determination of the mass of each sample. Because PET is tolerant of temperatures above its equilibrium melting point and because the critical cooling rate for PET is much below 2000 K/s (reported between 2-3 K/s [16-18]) it is easy to obtain an amorphous rescan of PET free of any nuclei which would contribute the rigid amorphous phase [2, 19, 20]. An example of an amorphous rescan is shown in

**Figure 6.6.**

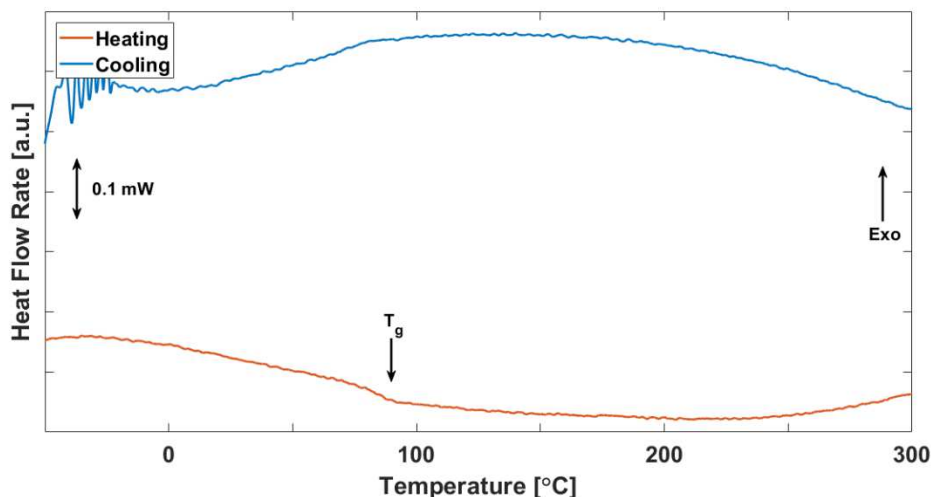


**Figure 6.6:** Example of a PET amorphous rescan following fiber melting. The curvature at high temperature seen here is due to the interaction between the tacky, liquid phase polymer and the thermal expansion and contraction of the TEM grid. The glass transition is fully expressed at 84 °C, which is about 15 °C above the equilibrium glass transition temperature,  $T_g = 69$  °C [13].

By measuring the heat capacity increment at the glass transition,  $\Delta C_p^{\text{amor}}(T_g)$ , observed during the amorphous rescan it is possible to obtain a measurement of the sample mass using the following relation:

$$m = \Delta C_p^{\text{amor}}(T_g) / \Delta c_p(T_g) \quad (6.2)$$

where  $\Delta c_p(T_g)$  is the specific heat capacity increment at the glass transition of PET which is well known in the literature ( $\Delta c_p(T_g) = 0.405 \text{ J/gK}$  [13]). This mass is then used to convert the heat capacity at the glass transition and the enthalpy of melting to the specific heat capacity increment and the specific enthalpy which are used to determine the mobile amorphous and crystalline fractions, respectively.

Using this procedure, the mass of fibers on each TEM grid is measured. This allows for the conversion of enthalpy to the specific enthalpy which, when combined with the temperature corrected heat of fusion, allows for the measurement of the crystallinity. The mass fraction crystallinity,  $\phi_c$ , is calculated using Eqn. 3.14 and correcting for the heat of fusion of the finite crystal using the following relationship [21]:

$$\Delta H_{f0}^{\text{corr}} = \Delta H_{f0} (2 * T_m / (T_m + T_m^0)) \quad (6.3a)$$

$$\phi_c = \Delta H_{f0}^{\text{meas}} / \Delta H_{f0}^{\text{corr}} \quad (6.3b)$$

where the equilibrium melting point and heat of fusion of PET are:  $T_m^0 = 280 \text{ }^\circ\text{C}$  and  $\Delta H_{f0} = 139.96 \text{ J/g}$  [13, 22, 23].

As discussed in **Section 5.6**, rigid amorphous phase material does not contribute to observed heat capacity increment at the glass transition. It is possible to measure the rigid

amorphous phase content directly from the observed semicrystalline heat capacity increment using the following relationships [ref]:

$$\phi_{MAF} = \Delta c_p^{\text{semicryst}}(T_g) / \Delta c_p^{\text{amor}}(T_g) \quad (6.4a)$$

$$\phi_{MAF} + \phi_{RAF} + \phi_C = 1 \quad (6.4b)$$

For fibers with mass greater than 5 ng it is possible to fully attain amorphous glass transitions and melting transitions. As the sample mass approaches this limit, the semicrystalline glass transition is no longer apparent as there is insufficient material contributing to a change in the heat capacity at  $T_g$  for a signal to be observed above the baseline signal to noise level. Results of the cold crystallization experiments on fibers are summarized in **Table 6.1**. Crystallinity is calculated using Eqn. 3.14 with the equilibrium heat of fusion for PET,  $\Delta H_{f0} = 139.96$  [13], adjusted for the melting point observed at the fast scanning rate of 2000 K/s. Recall that with the mass fraction crystallinity,  $\phi_C$ , and the mobile amorphous fraction,  $\phi_{MAF}$ , known the rigid amorphous fraction,  $\phi_{RAF}$ , can be determined using Eqn. 6.4b.

**Table 6.1:** Glass transition temperature, sample mass, mobile amorphous fraction, crystalline fraction, and rigid amorphous fraction for each cold crystallized fiber sample, as a function of crystallization conditions.

| $T_{CC}^a$<br>°C | $t_{CC}^a$<br>min | Mass <sup>b</sup><br>±0.5 ng | $T_g^b$ °C<br>±1 °C | $\Delta c_p^{semicrystc}$<br>±0.005<br>J/gK | $T_m^c$<br>±0.2°C | $\phi_{MAF}^c$<br>±0.02 | $\phi_C^c$<br>±0.02 | $\phi_{RAF}^c$<br>±0.03 |
|------------------|-------------------|------------------------------|---------------------|---|-------------------|-------------------------|---------------------|-------------------------|
| 120              | 15                | 7.1                          | 83                  | 0.155                                       | 169.8             | 0.38                    | 0.24                | 0.38                    |
| 130              | 15                | 19.0                         | 83                  | 0.161                                       | 178.6             | 0.40                    | 0.25                | 0.35                    |
| 140              | 15                | 6.2                          | 83                  | 0.094                                       | 189.4             | 0.23                    | 0.25                | 0.52                    |
| 150              | 15                | 9.4                          | 90                  | 0.061                                       | 201.1             | 0.15                    | 0.36                | 0.49                    |
| 160              | 15                | 5.3                          | 84                  | - <sup>d</sup>                              | 206.6             | - <sup>d</sup>          | 0.39                | - <sup>d</sup>          |

<sup>a</sup> Sample treatment conditions

<sup>b</sup> values measured from the amorphous rescan

<sup>c</sup> values measured from the semicrystalline fiber melting scan

<sup>d</sup> data not available

The relationship between cold crystallized PET and the rigid amorphous fraction has been previously studied [19, 24-29] and these results are within what is expected for a rigid amorphous fraction for PET. Additionally, the masses as measured by the heat capacity increment of the rescan are within the range of values predicted from the fiber distributions per Eqn. 6.1. This agreement with literature and the physical measurements made on the fiber loaded grids prior to fast scanning measurements suggests that this is an effective approach to obtain quantitative data from electrospun fibers loaded into chip based calorimeters on TEM grids.

It was observed that the heat capacity increment at the glass transition following the drying step is less than that of the amorphous rescan suggesting the presence of crystals, or minimally, nuclei and rigid amorphous phase material in the PET fibers. To better understand what is happening during the drying step and the initial heat to the crystallization temperature conventional DSC is used.

#### 6.4 Conventional DSC on PET fibers

The same bulk PET tapes that were spun for X-ray diffraction measurements and imaging provide ample material for conventional DSC experiments to be performed. These experiments utilize the Q100 DSC and the same temperature – time scheme (see **Figure 3.23**) can be run at a scanning rate of 0.5 K/s. This will be referred to as “the rate adjusted temperature-time profile” and is shown below in **Figure 6.7**.

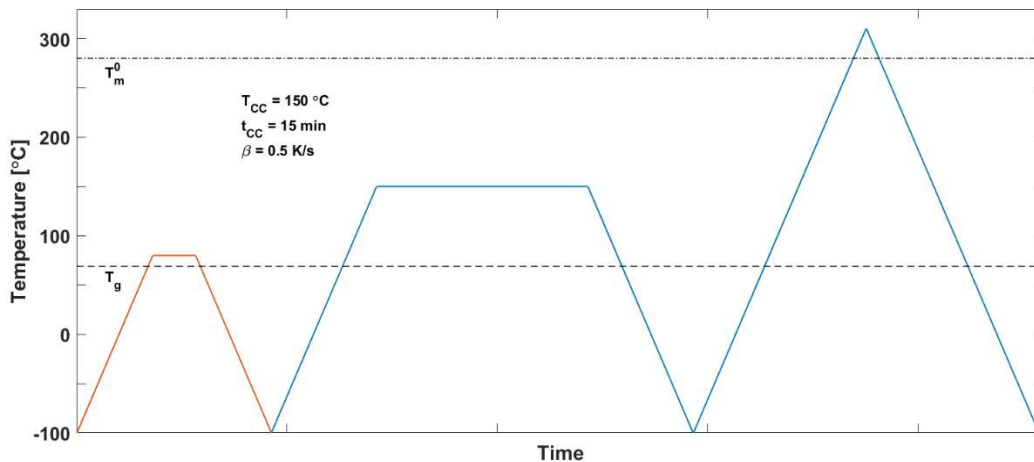


**Figure 6.7:** The rate adjusted temperature-time profile for replicating the FSC fiber drying and cold crystallization method (see **Figure 3.23**) in the Q100 DSC. Heating and cooling rates,  $\beta = \pm 0.5\text{ K/s}$ . The orange segments correspond to the drying step and the blue segments correspond to the cold crystallization and fiber melting steps.

Ideally scanning rates closer to the critical cooling rate should be used to prevent any non-isothermal crystallization of PET but rates of 2-3 K/s are beyond the range of scanning rates accessible to the instrument. An example of an electrospun PET fiber sample, prepared as

described in **Section 2.6**, is shown in **Figure 6.8** for a cold crystallization temperature,  $T_{CC} = 150$  °C.

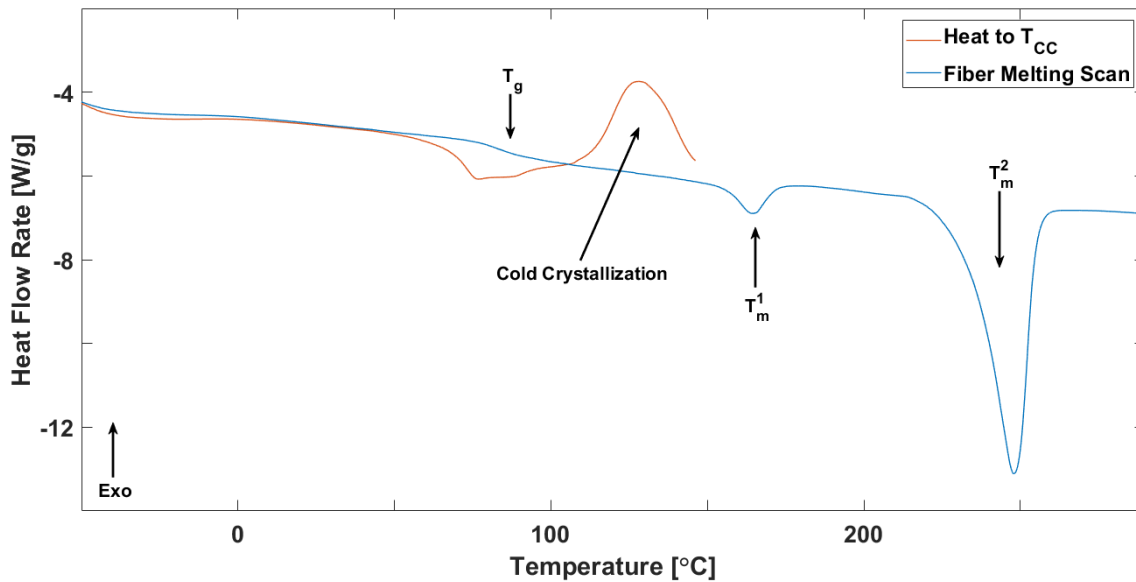


**Figure 6.8:** Standard DSC heat flow rate vs. temperature for PET brought through the rate adjusted temperature-time profile. Non-isothermal cold crystallization is observed on the heating ramp to the crystallization temperature,  $T_{CC} = 150$  °C.

With conventional DSC the fiber mass can be measured directly before and after the sample is run. Because PET does not degrade at its melting point the heat flow data can be corrected for solvent loss by massing the sample after it has been brought through the temperature-time profile. The heat flow rate data can be corrected for changes in the sample mass between the drying step and the rest of the scan. With the corrected heat flow, the mass fraction crystallinity,  $\phi_C$ , the mobile amorphous fraction,  $\phi_{MAF}$ , and the rigid amorphous fraction,  $\phi_{RAF}$ , can be calculated in the manner described previously. The results of these experiments are summarized in **Table 6.2**.

**Table 6.2:** Standard DSC results of glass transition temperature and heat capacity increment, melting peak temperatures and endotherm area, mobile amorphous, crystal, and rigid amorphous mass fractions for electrospun PET brought through the rate adjusted temperature-time profile.

| $T_{CC}^a$  | $T_g$              | $\Delta c_p(T_g)$  | $T_{m1}$           | $\Delta H_{f1}$   | $T_{m2}$           | $\Delta H_{f2}$   | $\phi_{MAF}$ | $\phi_C$   | $\phi_{RAF}$ |
|-------------|--------------------|--------------------|--------------------|-------------------|--------------------|-------------------|--------------|------------|--------------|
| $^{\circ}C$ | $\pm 0.1^{\circ}C$ | $\pm 0.01$<br>J/gK | $\pm 0.1^{\circ}C$ | $\pm 0.02$<br>J/g | $\pm 0.1^{\circ}C$ | $\pm 0.02$<br>J/g | $\pm 0.01$   | $\pm 0.01$ | $\pm 0.02$   |
| 120         | 84.8               | 0.14               | 137.4              | 1.17              | 247.8              | 43.88             | 0.35         | 0.35       | 0.30         |
| 130         | 83.1               | 0.17               | 145.9              | 2.97              | 247.4              | 40.07             | 0.41         | 0.34       | 0.25         |
| 140         | 84.4               | 0.13               | 155.8              | 2.73              | 247.6              | 42.13             | 0.32         | 0.35       | 0.33         |
| 150         | 82.0               | 0.14               | 164.4              | 3.39              | 247.9              | 45.69             | 0.35         | 0.38       | 0.27         |
| 160         | 86.8               | 0.14               | 173.3              | 3.81              | 246.7              | 45.08             | 0.35         | 0.38       | 0.27         |

<sup>a</sup> Isothermal cold crystallization temperature

These results show a similar trend in the generally increasing crystallinity with the cold crystallization temperature but a rigid amorphous fraction that is decreasing with higher crystallinity. Unlike the FSC data, the fibers crystallized at the slower scanning rate exhibit melting doublets as indicated by the arrows in **Figure 6.8**. This is due to the degree to which PET can non-isothermally cold crystallize while being heated to the preset cold crystallization temperature. Here a fraction of the polymer is already crystalline before the isothermal hold. During the isothermal hold these crystals will continue to grow. Additionally, new crystals are nucleating off of the preexisting crystals. The melting points of these crystals (the smaller, low temperature melting peak identified in **Figure 6.8**) scales with the crystallization temperature as those that formed at higher temperature are more stable.

The contrast between the conventional DSC measurements and the FSC measurements of PET fibers is due to a combination of the non-isothermal cold crystallization present at conventional scanning rates and the solvent ejection step. Conventional DSC results revealed that

PET begins to cold crystallize just above the observed glass transition at 73 °C. This is in the range of the boiling point of TFA and it is likely that, during the 1 minute drying step at 80 °C, PET will nucleate and crystallize to a small extent. However, in FSC any further non-isothermal crystallization during the reheat to the crystallization temperature is prevented by the scanning rate of 2000 K/s. Once the fibers reach the cold crystallization temperature, the nuclei which formed during the drying step proceed to crystallize and anneal to the extent that is possible during the 15 min isothermal hold. The trends observed in the FSC measurements suggest that once the nuclei are formed, isothermal crystallization kinetics dominate and the crystals which grow from the nuclei introduced at the drying step will form crystals whose stability increases with crystallization temperature.

### **6.5 *Melt Crystallization of PET confined to Droplets***

A unique advantage to the method of depositing electrospun fibers on the chip based sensors is that it enables the study of crystallization confined to micro and possibly nano droplets. As electrospun fibers melt they break up into droplets with dimensions that are smaller than typical spherulites in the bulk. Polymer crystallization experiments confined to droplets require carefully selected, immiscible polymers where the polymer of interest is confined by some liquid phase matrix [30-35]. Utilizing the rarefied electrospun fibers on TEM grids, crystallization of a single homopolymer can be achieved without confinement in a matrix. This not possible in a standard DSC pan as the droplets will coalesce and the crystallization observed is bulk, melt crystallization.

One of the samples with the fibers facing up, as mentioned in **Section 6.2**, can be seen in **Figure 6.9**. After the fibers break up they form droplets that scale with the fiber diameter. Because

the fibers are rarefied and will interact with the TEM grids via surface tension, the degree to which droplets coalesce is minimized.

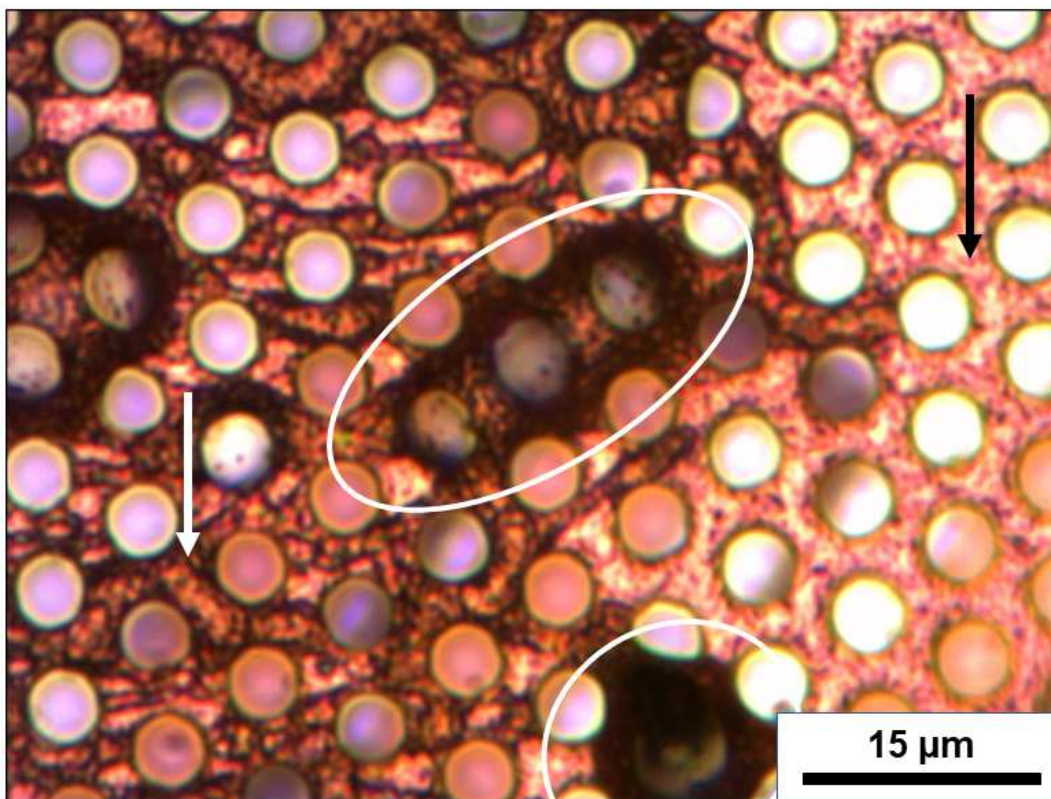


**Figure 6.9:** Following a single heating fibers are observed to breakup into droplets (dark regions outlined with white ovals) or streams of continuous material (white arrow). As the fibers melt and coalesce into droplets regions of the TEM grid are left dry (black arrow).

Following any given cold crystallization scan, a melt crystallization of a confined droplet sequence can be run on the fibers corresponding to the green segments in **Figure 3.23**. This allows for two distinct experiments to be performed on a single sample on a single chip, something that is advantageous when designing fast scanning experiments. Following the cold crystallization scan a melt crystallization sweep for melt temperatures between 240 °C and 100 °C in 20 °C was

performed. The heat flow rate vs. temperature for each heating scan in this sweep is shown in **Figure 6.10**.

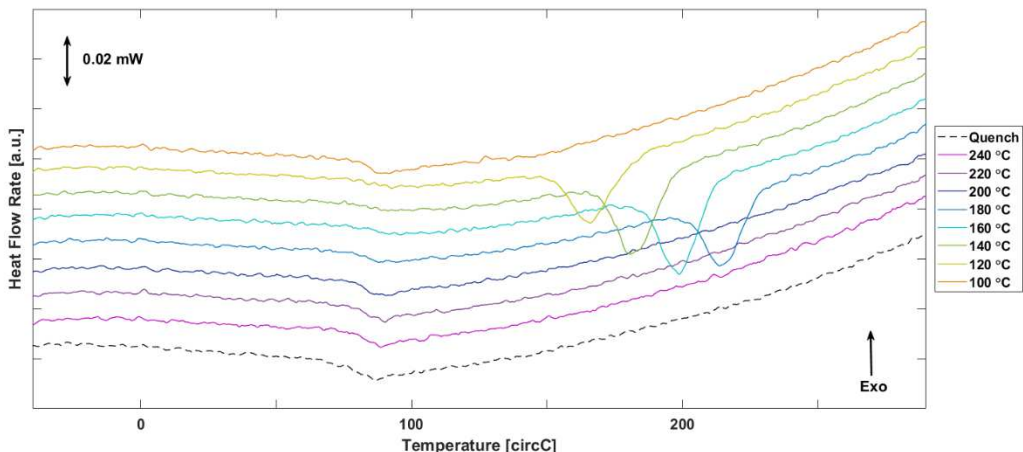


**Figure 6.10:** Melt crystallization of PET confined to droplets following the complete melting of electrospun fibers. Moving from the bottom up the dashed, black curve is the first scan where the sample is quenched and reheated. Then the samples are melt crystallized between 240 °C and 100 °C in 20 °C increments. Samples are isothermally melt crystallized at each temperature for 5 minutes and thermal history is completely erased by holding at 30 °C above the equilibrium melting temperature,  $T_m^0 = 280$  °C, for 1 minute between each scan.

The first heating scan, shown as the black, dotted line in **Figure 6.10** is from quenching of PET from the melt. This allows for the measurement of the sample mass in contact with the sensor following five minutes in the melt after the fiber scans. After each melting scan the sample is cooled to the melt crystallization temperature,  $T_{MC}$ , where it is held isothermally for 5 minutes. On each subsequent heating scan the heat capacity increment at the glass transition, peak melting temperature, and the enthalpy of melting are measured. The crystallinity and mobile and rigid amorphous fractions are calculated. Results are presented in **Table 6.3**.

**Table 6.3:** Temperature series isothermal melt crystallization data on PET: heat capacity increment, peak melting temperature, temperature corrected heat of fusion, and crystalline, mobile amorphous, and rigid amorphous mass fractions.

|        | $\Delta c_p(T_g)$<br>$\pm 0.005 \text{ J/gK}$ | $T_m$<br>$\pm 1 \text{ }^\circ\text{C}$ | $\Delta H_f^{\text{meas}}$<br>$\pm 0.2 \text{ J/g}$ | $\phi_C$<br>$\pm 0.02$ | $\phi_{\text{MAF}}$<br>$\pm 0.02$ | $\phi_{\text{RAF}}$<br>$\pm 0.03$ |
|--------|---|---|---|------------------------|-----------------------------------|-----------------------------------|
| Quench | 0.409   | -                                       | -   | -                      | 1.00                              | 0.00                              |
| 240 °C | 0.401   | -                                       | -   | -                      | 0.98                              | 0.02                              |
| 220 °C | 0.400   | -                                       | -   | -                      | 0.98                              | 0.02                              |
| 200 °C | 0.398   | -                                       | -   | -                      | 0.97                              | 0.03                              |
| 180 °C | 0.260   | 214                                     | 27.1  | 0.22                   | 0.63                              | 0.14                              |
| 160 °C | 0.219   | 198                                     | 34.5  | 0.30                   | 0.54                              | 0.17                              |
| 140 °C | 0.193   | 182                                     | 35.3  | 0.32                   | 0.47                              | 0.21                              |
| 120 °C | 0.236   | 166                                     | 28.0  | 0.27                   | 0.58                              | 0.15                              |
| 100 °C | 0.409   | -                                       | -   | -                      | 1.00                              | 0.00                              |

It was observed that, prior to any evidence of melting there was a depression in the heat capacity increment at the glass transition indicating the presence of rigid amorphous phase material. This is due to the presence of nuclei forming throughout the melt, or in this case in many droplets. It is known that even a small number of nuclei throughout the melt can give rise to rigid amorphous phase material. Interestingly, the confined crystallization at high temperatures gave rise to smaller rigid amorphous fraction (i.e. larger mobile amorphous phase) at crystallinities which normally result in more than 20% rigid amorphous phase [24].

Two additional melt crystallization experiments were performed at variable holding times. Two melt crystallization temperatures,  $T_{MC} = 150 \text{ }^\circ\text{C}$  and  $T_{MC} = 180 \text{ }^\circ\text{C}$  were selected and the isothermal crystallization time was varied between 0.1 and 1000 seconds. Each crystallization experiment begins by heating the sample after it has been quenched from the melt to assess the mass of PET droplets in contact with the sensor. The results of the time series isothermal melt crystallization are summarized in **Table 6.4**. Each time series was performed a different sample.

**Table 6.4:** Time series melt crystallization data on PET: glass transition temperatures, peak melting temperatures, and crystalline, mobile amorphous, and rigid amorphous mass fractions.

| $T_{MC}^a$<br>°C | $t_{MC}^a$<br>s | $T_g^b$<br>±1 °C | $T_m^b$<br>±1 °C | $\phi_{MAF}^b$<br>±0.02 | $\phi_C^b$<br>±0.02 | $\phi_{RAF}^b$<br>±0.03 |
|------------------|-----------------|------------------|------------------|-------------------------|---------------------|-------------------------|
| 150              | 0               | 82               | -                | 1.0                     | 0.00                | 0.00                    |
| 150              | 0.1             | 89               | -                | 0.96                    | 0.00                | 0.04                    |
| 150              | 1               | 88               | -                | 0.95                    | 0.00                | 0.05                    |
| 150              | 10              | 88               | -                | 0.78                    | 0.00                | 0.22                    |
| 150              | 100             | 89               | 189              | 0.58                    | 0.20                | 0.22                    |
| 150              | 1000            | 86               | 192              | 0.53                    | 0.31                | 0.17                    |
| 150              | 0.1             | 87               | -                | 0.96                    | 0.00                | 0.04                    |
| 180              | 0               | 81               | -                | 1.00                    | 0.00                | 0.0                     |
| 180              | 0.1             | 83               | -                | 0.95                    | 0.00                | 0.05                    |
| 180              | 1               | 83               | -                | 0.92                    | 0.00                | 0.08                    |
| 180              | 10              | 84               | -                | 0.91                    | 0.00                | 0.09                    |
| 180              | 100             | 83               | -                | 0.86                    | 0.00                | 0.14                    |
| 180              | 1000            | 86               | 216              | 0.59                    | 0.30                | 0.11                    |
| 180              | 1500            | 85               | 217              | 0.54                    | 0.31                | 0.15                    |

<sup>a</sup> confined melt crystallization parameters

<sup>b</sup> values measured from the semicrystalline confined droplet melting scan

The results from the time series isothermal melt crystallization experiments show a similar trend to the temperature sweep. Confinement to droplets results in both a decrease in crystallinity when compared to the cold crystallization in the fibers. Moreover, for comparable mass fraction crystallinity, confined droplets show a reduction in the rigid amorphous fraction when compared to the fibers or the bulk [2, 19, 24, 36, 37]. This unexpected result is worth further investigation to determine why confinement at scanning rates fast enough to prevent any non-isothermal crystallization results in a disproportionate depression of the rigid amorphous fraction in PET.

## 6.6 *Empty TEM grids and Indium Loaded Grids*

The final portion of this set of experiments was to verify that the presence of the heavy (compared to the PET nanofibers) copper TEM grids did not negatively impact the accuracy of the temperature and heat flow measured. This was done in two steps, the first was to place increasingly large, empty TEM grids on the sensor and cool them between -100 °C and 400 °C at 2000 K/s. These temperatures span the operating range of the UFSC1 chip sensor. In total five empty grids were brought across this range.

In the absence of tacky, liquid phase polymer it is possible to follow the standard empty sensor subtraction and symmetry correction protocol outline in **Section 3.5**. Because copper does not undergo a phase change over the range of the range of temperatures accessible to the Mettler Flash DSC the symmetry correction can be simplified and taken as the average between the heating and cooling scan at every temperature. Once the corrections are applied and the data are converted to heat capacity there is near perfect agreement at every point for each grid. The apparent heat capacity vs. temperature scans for a series of sensor and symmetry corrected empty TEM grid scans are shown in **Figure 6.11**.

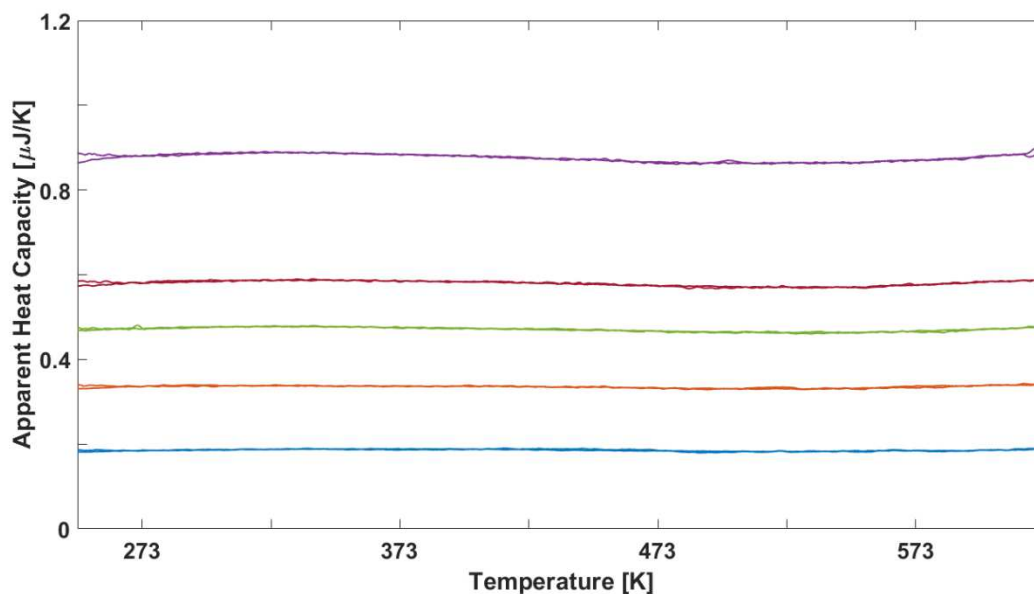


**Figure 6.11:** Apparent heat capacity vs. temperature for a series of TEM grids of increasing area. Mass decreases from top to bottom in this image. Each curve comprises both the heating and cooling scans and shows nearly perfect overlap between heating and cooling following empty sensor subtraction and symmetry correction.

From the corrected apparent heat capacity data, the mass of each grid can be determined by comparing to literature values for the specific heat capacity of copper at various temperatures [38]. There was no trend observed in the mass as a function of temperature. The specific heat capacity for all five curves are averaged. **Figure 6.12** shows the average specific heat capacity of the TEM grids as a function of temperature compared to literature values for the specific heat capacity of copper.

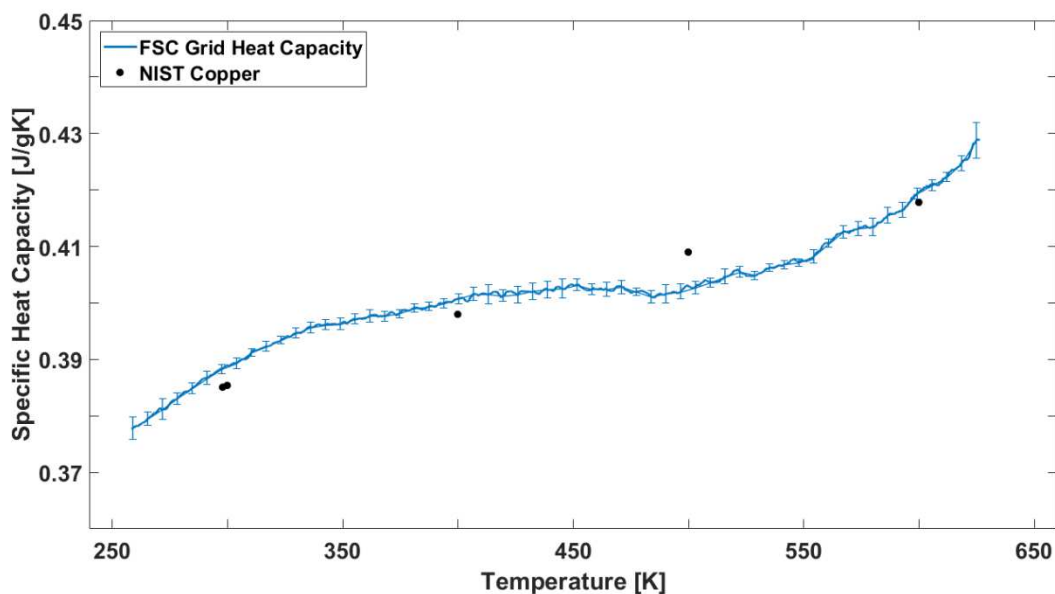


**Figure 6.12:** Average specific heat capacity of the copper TEM grids as measured from the five grids of increasing size. Black points are the NIST values [39] for the specific heat capacity of copper at various temperatures.

Having determined that the presence of the copper grids, independent of their size/ mass does not prevent repeatable and accurate measurement of heat capacity, attention is turned to the question of temperature accuracy. After the last TEM grid in **Figure 6.11** was brought through the heating and cooling cycle a flake of pure indium was placed on top of the grid. The indium flake was first heated to 300 °C and held isothermally for several minutes to flatten it out and prevent any thermal gradients from impacting the measurements. Once flattened the indium loaded TEM grid was heated over the same temperature range as the empty grids at the scanning rate of 2000 K/s to track the temperature accuracy in the presence of the grids. The melting scans of indium loaded on the TEM grid are shown in **Figure 6.13** and the indium flake on the grid is bottom left inset.

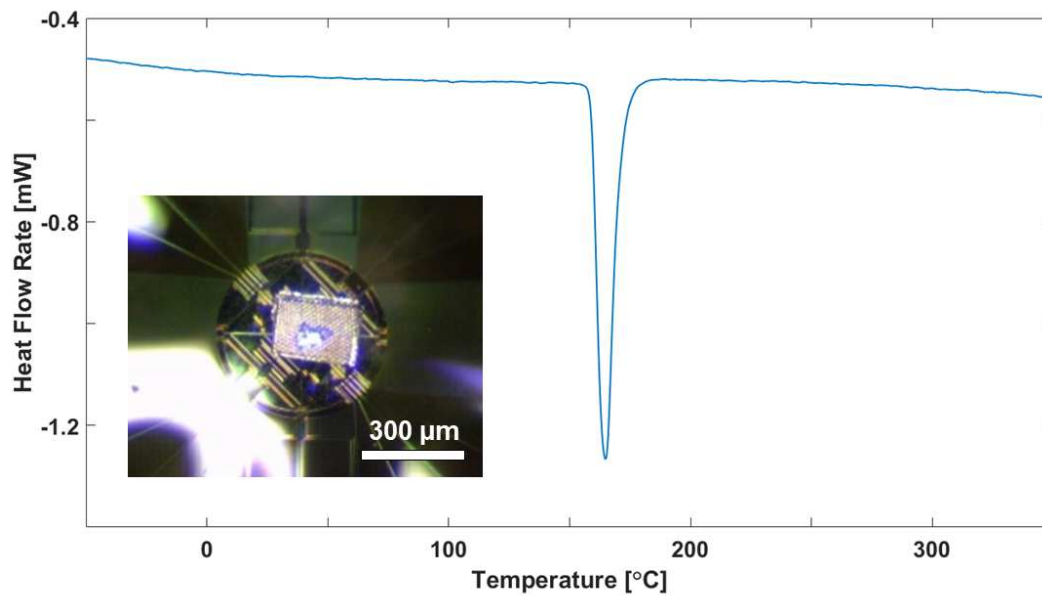


**Figure 6.13:** Heat flow rate vs. temperature for indium loaded TEM grid. Inset shows the initial flake of indium loaded onto the rectangular section of TEM grid.

The melting of indium observed here is consistent with that of indium on the empty UFSC1 chip sensor or when a polymeric sample is present [40]. At the scanning rate of 2000 K/s the melting point of indium was observed to be 156.9 °C, which is very near the equilibrium value of 156.6 °C [38]. The broadening of the peak is due to the high scanning rate. In typical DSC calibrations, the onset of the melting of pure metal, such as indium is used for temperature accuracy calibration and the width of the melting peak is used for correcting any thermal lag in the system. Both the melting of pure indium and the heat capacity analysis of the empty copper grids indicate the presence of the grids will not obscure measurements of fiber samples.

## 6.7 References

- [1] K.W. Kim, K.H. Lee, M.S. Khil, Y.S. Ho, H.Y. Kim, The effect of molecular weight and the linear velocity of drum surface on the properties of electrospun poly(ethylene terephthalate) nonwovens, *Fibers and Polymers* 5(2) (2004) 122-127.
- [2] H. Chen, Z. Liu, P. Cebe, Chain confinement in electrospun nanofibers of PET with carbon nanotubes, *Polymer* 50(3) (2009) 872-880.
- [3] K. Li, B. Mao, P. Cebe, Electrospun fibers of poly(ethylene terephthalate) blended with poly(lactic acid), *Journal of Thermal Analysis and Calorimetry* 116(3) (2014) 1351-1359.
- [4] S. Mazinani, A. Ajji, C. Dubois, Fundamental study of crystallization, orientation, and electrical conductivity of electrospun PET/carbon nanotube nanofibers, *Journal of Polymer Science Part B: Polymer Physics* 48(19) (2010) 2052-2064.
- [5] T. Subbiah, G.S. Bhat, R.W. Tock, S. Parameswaran, S.S. Ramkumar, Electrospinning of nanofibers, *Journal of Applied Polymer Science* 96(2) (2005) 557-569.
- [6] W.E. Teo, S. Ramakrishna, A review on electrospinning design and nanofibre assemblies, *Nanotechnology* 17(14) (2006) R89.
- [7] B. Veleirinho, J.A. Lopes-da-Silva, Application of electrospun poly(ethylene terephthalate) nanofiber mat to apple juice clarification, *Process Biochemistry* 44(3) (2009) 353-356.
- [8] J. Schindelin, I. Arganda-Carreras, E. Frise, V. Kaynig, M. Longair, T. Pietzsch, S. Preibisch, C. Rueden, S. Saalfeld, B. Schmid, J.-Y. Tinevez, D.J. White, V. Hartenstein, K. Eliceiri, P. Tomancak, A. Cardona, Fiji: an open-source platform for biological-image analysis, *Nat Meth* 9(7) (2012) 676-682.
- [9] W.L. Lindner, Characterization of the crystalline, intermediate and amorphous phase in poly(ethylene terephthalate) fibres by X-ray diffraction, *Polymer* 14(1) (1973) 9-15.

- [10] A. Toda, M. Konishi, An evaluation of thermal lags of fast-scan microchip DSC with polymer film samples, *Thermochimica Acta* 589 (2014) 262-269.
- [11] J.E.K. Schawe, Analysis of non-isothermal crystallization during cooling and reorganization during heating of isotactic polypropylene by fast scanning DSC, *Thermochimica Acta* 603 (2015) 85-93.
- [12] Trifluoroacetic acid, 2016. [http://webbook.nist.gov/cgi/inchi/InChI%3D1S/C2HF3O2/c3-2\(4%2C5\)1\(6\)7/h\(H%2C6%2C7\)](http://webbook.nist.gov/cgi/inchi/InChI%3D1S/C2HF3O2/c3-2(4%2C5)1(6)7/h(H%2C6%2C7)).
- [13] M. Pyda, Poly(ethylene terephthalate) (PET) Heat Capacity, Enthalpy, Entropy, Gibbs Energy: Datasheet from "The Advanced Thermal Analysis System (ATHAS) Databank – Polymer Thermodynamics" Release 2014 in SpringerMaterials ([http://materials.springer.com/polymerthermodynamics/docs/athas\\_0110](http://materials.springer.com/polymerthermodynamics/docs/athas_0110)), 2014. [http://materials.springer.com/polymerthermodynamics/docs/athas\\_0110](http://materials.springer.com/polymerthermodynamics/docs/athas_0110). (Accessed 10/16/2016 2016).
- [14] STARe Evaluation, Mettler Toledo GmbH, Analytical, Schwerzenbach, Switzerland, 2016.
- [15] MATLAB R2017a, The Mathworks, Inc, Natick, MA, 2017.
- [16] A. Toda, R. Androsch, C. Schick, Insights into polymer crystallization and melting from fast scanning chip calorimetry, *Polymer* 91 (2016) 239-263.
- [17] R. Androsch, C. Schick, A.M. Rhoades, Application of Tammann's Two-Stage Crystal Nuclei Development Method for Analysis of the Thermal Stability of Homogeneous Crystal Nuclei of Poly(ethylene terephthalate), *Macromolecules* 48(22) (2015) 8082-8089.
- [18] V. Mathot, M. Pyda, T. Pijpers, G. Vanden Poel, E. van de Kerkhof, S. van Herwaarden, F. van Herwaarden, A. Leenaers, The Flash DSC 1, a power compensation twin-type, chip-based fast

scanning calorimeter (FSC): First findings on polymers, *Thermochimica Acta* 522(1) (2011) 36-45.

[19] H. Chen, P. Cebe, Vitrification and Devitrification of Rigid Amorphous Fraction of PET during Quasi-Isothermal Cooling and Heating, *Macromolecules* 42(1) (2009) 288-292.

[20] M.C. Righetti, M. Laus, M.L. Di Lorenzo, Temperature dependence of the rigid amorphous fraction in poly(ethylene terephthalate), *European Polymer Journal* 58 (2014) 60-68.

[21] J.D. Hoffman, J.I. Lauritzen Jr, Crystallization of Bulk Polymers with Chain Folding: Theory of Growth of Lamellar Spherulites *Journal of Research of the National Bureau of Standards - A. Physics and Chemistry* 65A(4) (1961) 297-336.

[22] A. Mehta, U. Gaur, B. Wunderlich, Equilibrium melting parameters of poly(ethylene terephthalate), *Journal of Polymer Science: Polymer Physics Edition* 16(2) (1978) 289-296.

[23] B. Wunderlich, CHAPTER VIII - Equilibrium Melting, *Macromolecular Physics*, Academic Press, San Diego, 1980, pp. 1-127.

[24] R. Androsch, B. Wunderlich, The link between rigid amorphous fraction and crystal perfection in cold-crystallized poly(ethylene terephthalate), *Polymer* 46(26) (2005) 12556-12566.

[25] J. Lin, S. Shenogin, S. Nazarenko, Oxygen solubility and specific volume of rigid amorphous fraction in semicrystalline poly(ethylene terephthalate), *Polymer* 43(17) (2002) 4733-4743.

[26] Q. Ma, B. Mao, P. Cebe, Chain confinement in electrospun nanocomposites: using thermal analysis to investigate polymer–filler interactions, *Polymer* 52(14) (2011) 3190-3200.

[27] M.C. Righetti, M.L. Di Lorenzo, E. Tombari, M. Angiuli, The Low-Temperature Endotherm in Poly(ethylene terephthalate): Partial Melting and Rigid Amorphous Fraction Mobilization, *The Journal of Physical Chemistry B* 112(14) (2008) 4233-4241.

- [28] M.C. Righetti, E. Tombari, M. Angiuli, M.L.D. Lorenzo, Enthalpy-based determination of crystalline, mobile amorphous and rigid amorphous fractions in semicrystalline polymers, *Thermochimica Acta* 462(1) (2007) 15-24.
- [29] I. Okazaki, B. Wunderlich, Modulated differential scanning calorimetry in the glass transition region. V. Activation energies and relaxation times of poly(ethylene terephthalate)s, *Journal of Polymer Science Part B: Polymer Physics* 34(17) (1996) 2941-2952.
- [30] M.V. Massa, K. Dalnoki-Veress, Homogeneous Crystallization of Poly(Ethylene Oxide) Confined to Droplets: The Dependence of the Crystal Nucleation Rate on Length Scale and Temperature, *Physical Review Letters* 92(25) (2004) 255509.
- [31] M.V. Massa, J.L. Carvalho, K. Dalnoki-Veress, Direct visualisation of homogeneous and heterogeneous crystallisation in an ensemble of confined domains of poly(ethylene oxide), *The European Physical Journal E* 12(1) (2003) 111-117.
- [32] M.V. Massa, J.L. Carvalho, K. Dalnoki-Veress, Confinement Effects in Polymer Crystal Nucleation from the Bulk to Few-Chain Systems, *Physical Review Letters* 97(24) (2006) 247802.
- [33] J.L. Carvalho, K. Dalnoki-Veress, Homogeneous Bulk, Surface, and Edge Nucleation in Crystalline Nanodroplets, *Physical Review Letters* 105(23) (2010) 237801.
- [34] H. Wang, J.K. Keum, A. Hiltner, E. Baer, Crystallization Kinetics of Poly(ethylene oxide) in Confined Nanolayers, *Macromolecules* 43(7) (2010) 3359-3364.
- [35] G. Zhong, K. Wang, L. Zhang, Z.-M. Li, H. Fong, L. Zhu, Nanodroplet formation and exclusive homogeneously nucleated crystallization in confined electrospun immiscible polymer blend fibers of polystyrene and poly(ethylene oxide), *Polymer* 52(24) (2011) 5397-5402.

- [36] J.D. Badia, E. Strömberg, S. Karlsson, A. Ribes-Greus, The role of crystalline, mobile amorphous and rigid amorphous fractions in the performance of recycled poly (ethylene terephthalate) (PET), *Polymer Degradation and Stability* 97(1) (2012) 98-107.
- [37] B. Wunderlich, Reversible crystallization and the rigid–amorphous phase in semicrystalline macromolecules, *Progress in Polymer Science* 28(3) (2003) 383-450.
- [38] M. Chase Jr, JANAF thermochemical tables third edition, *J. Phys. Chem. Ref. Data* 14(1) (1985).
- [39] Copper, 2017.
- [40] E. Zhuravlev, C. Schick, Fast scanning power compensated differential scanning nano-calorimeter: 2. Heat capacity analysis, *Thermochimica Acta* 505(1-2) (2010) 14-21.

## ***Chapter 7 Electrospun Polyvinyl Alcohol Nanofibers: Potential as Neural Tissue Scaffolds (PAT 2016 Internship) and Investigation into Fundamental Thermal Properties***

This chapter discusses the work done on electrospun polyvinyl alcohol (PVA) during the Polymers for Advanced Technologies (PAT) Summer Internship for Deaf and Hard of Hearing Students during the summer of 2016 and subsequent fast scanning calorimetry experiments performed on PVA nanofibers in Rostock, Germany in the fall of 2016. This chapter is organized as follows: **Section 7.1** presents the results of electrospinning PVA from various solvents and the characterization of the fibers produced and subsequent stabilization of the fibers to resist dissolution in water. **Section 7.2** presents the application of these fibers as neural tissue scaffolds as work done in collaboration with the Staii group. **Section 7.3** presents the structural analysis of these fibers; **Section 7.4** presents the results of the thermal analysis of these fibers using conventional thermal analysis techniques and fast scanning calorimetry (FSC). Details of the solution preparation and electrospinning can be found in **Section 2.2.2** and **Section 2.3.1**, respectively. Details of the imaging, structural, and thermal analysis techniques can be found in **Chapter 3**.

## 7.1 Characterization of Electrospun PVA Fibers

### 7.1.1 Assessment of “as spun” Fibers

Electrospun fibers, regardless of spin conditions, were sputter coated with gold-palladium and imaged with the Phenom tabletop or Zeiss scanning electron microscope (SEM) as outlined in **Section 3.1.2**. Beyond the specific biocompatibility of a polymer, the two most important parameters for creating viable neural tissue scaffolds are the average fiber orientation and fiber diameter [1-12]. The first stage in SEM analysis is to qualitatively assess the fiber quality. Fibers should be free of beads or splashes as these features indicate that spin conditions are poor. The spin conditions outlined in **Section 2.3.1** for polyvinyl alcohol were tuned for the needle diameters used and resulted in high quality electrospun fibers. A selection of images can be seen in **Figure 7.1**.

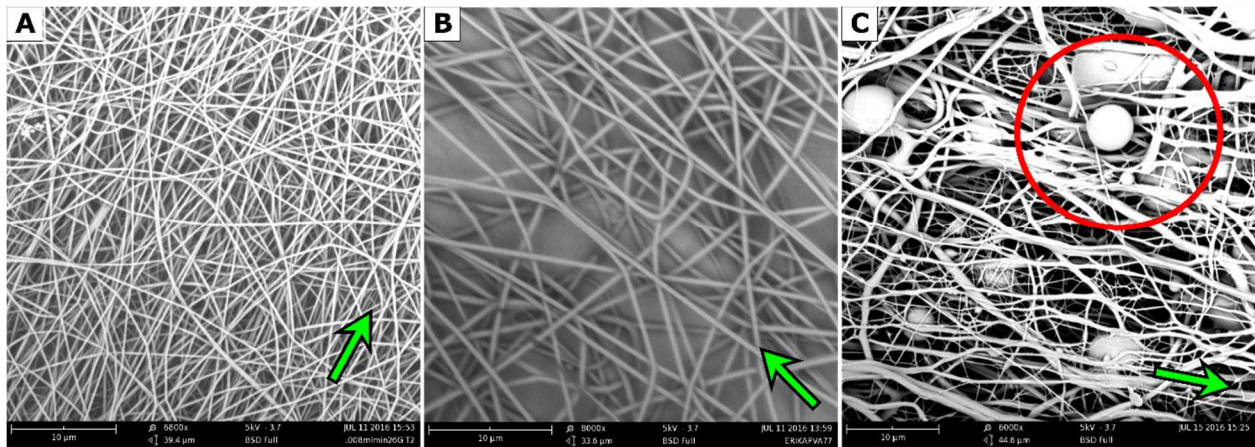


**Figure 7.1:** Images PVA fibers spun with various conditions obtained with the Phenom G2 SEM. (A) 8 wt.% PVA spun through a 26 gauge needle (B) and (C) 10 wt.% PVA spun through a 20 gauge needle. Green arrows indicate the prevailing fiber direction. Red circle highlights bead defects in the fiber mat. Electrospinning parameters can be found **Section 2.3.1**.

The spin or fiber direction is indicated by the green arrow in all images. Electrospinning PVA can be an inconsistent process where conditions such as time in solution or humidity can impact the quality of fibers. Fibers seen in **Figure 7.1A** were spun from 8 wt.% PVA in DI water through a 26 gauge ( $\text{\O} 0.260$  mm) needle and resulted in moderately well aligned nanofibers free of beads or defects. But the spins were difficult to perform for long times due to repeated jamming of the needle. Increasing the concentration to 10 wt.% PVA and the needle diameter up to 20 gauge ( $\text{\O} 0.603$  mm) resulted in reliable spins where jamming rarely occurred. These fibers were moderately well aligned as well, as seen in **Figure 7.1B**. In both images, there is a bulk alignment in the direction indicated by the green arrow, however, the whipping motion of the fibers during spinning resulted in the curling of fibers which run at various angles to the spin direction.

It was often the case that electrospinning under the same conditions from fresh solutions resulted in vastly different fiber quality as seen in **Figure 7.1C**. If solutions were left to sit for too long at room temperature, or the initial filling of the syringe was not done quickly and resulted in long times to degas the solution, beads (as indicated by the red circle in **Figure 7.1C**) or splashes were observed throughout the fiber mat. When preparing samples which will ultimately serve as neural tissue scaffolds, tapes with the best fiber quality were selected. Fiber runs which resulted in poorer fiber quality were utilized for testing various chemical and thermal stabilization treatments or destructive testing such as thermogravimetric analysis.

The high-quality fibers will serve as tissue scaffolds for neurons which can grow along, or perpendicular to the fiber direction. Neurons have large bodies, or somas, which will sit on top of many fibers. Long protrusions from the soma, known as axons are equipped with a growth cone that effectively “feels” the substrate and dictates the directional growth as group of neurons form a network. The spacing of fibers, their alignment, and fiber diameters will all impact the how the

neurons can grow on the surface. [3, 13-23] Atomic force microscopy (AFM) provides a topographical map of the surface on which neurons can grow. An example can be seen in **Figure 7.2**.

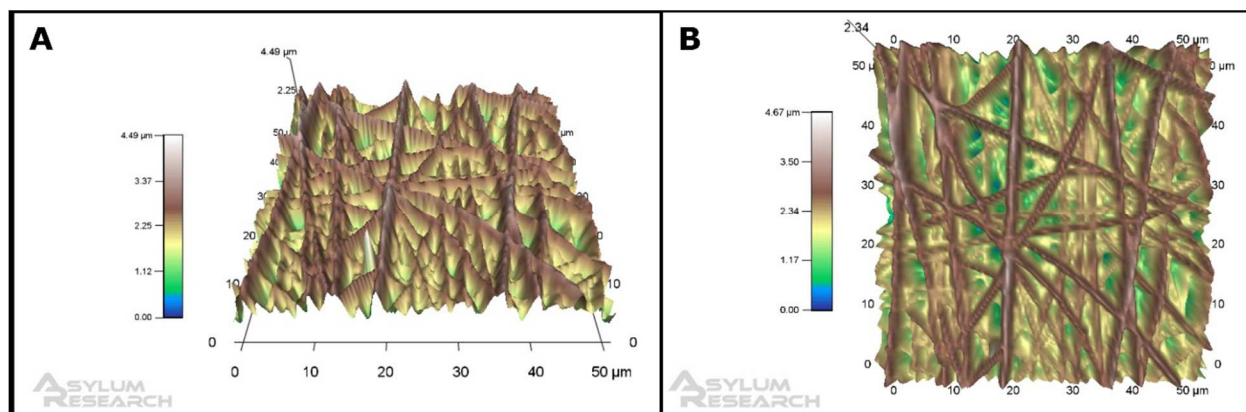


**Figure 7.2:** AFM topography scans of Electrospun PVA fiber mats over 50  $\mu\text{m}$  x 50  $\mu\text{m}$  area from **(A)** 30° tilt side view and **(B)** top down view. The fiber diameters are in agreement with the those observed in the SEM images. Data were taken by Derek Walkama and Peter Riley.

### 7.1.2 7.1.2 Stabilization of Nanofibers

The two approaches to stabilize the fibers, outlined in **Section 2.5**, involved isothermally crystallizing the fibers [24, 25] or chemically crosslinking the PVA by exposing fibers to glutaraldehyde [24, 26-28]. Two 24 – well plates were prepared, one from fiber tapes exposed to glutaraldehyde and one from fiber tapes which were isothermally crystallized at 150 °C for 15 minutes. Within these well plates the fiber mats were exposed to water for times between 15 min and 96 hours. Soak times between 24 hours and 96 hours are typical of tissue culture times used by our collaborators and any viable substrate must remain stable for these times.

As mentioned in **Section 2.5** glutaraldehyde did not prove to be an effective means of stabilizing the fibers, despite some groups seeing success crosslinking PVA by exposure to

glutaraldehyde vapor [26-28]. Following glutaraldehyde exposure there was no appreciable change between the “as spun” fiber, shown in **Figure 7.3A**, and the fibers following glutaraldehyde exposure, shown in **Figure 7.3B**. Glutaraldehyde exposed fibers were soaked in water for an hour, as seen in **Figure 7.3C**, and soaked in water for 16 hours, as seen in **Figure 7.3D**.

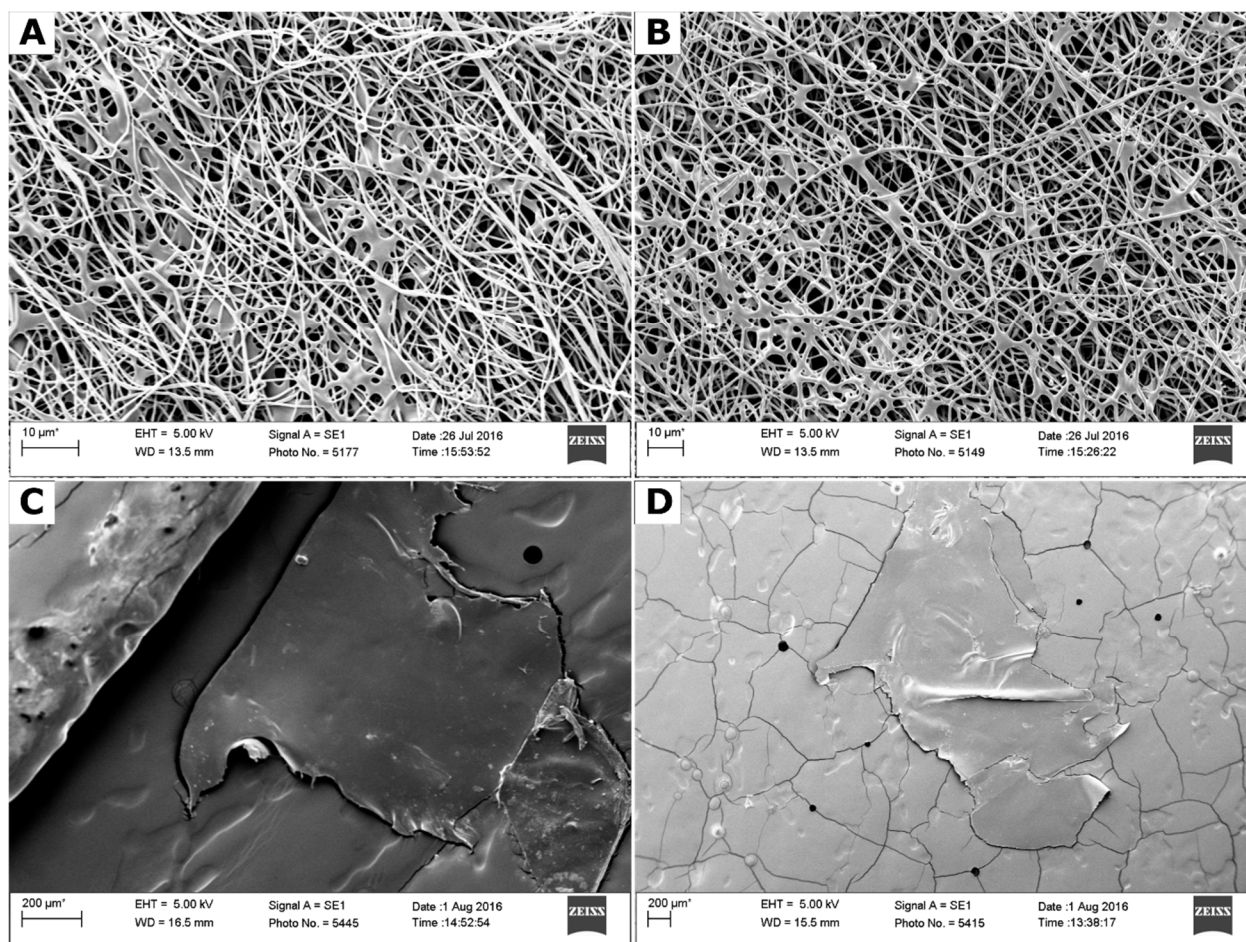


**Figure 7.3:** Electron microscope images collected with the Zeiss SEM for (A) PVA “as spun” from mixed solvents and (B) following exposure to glutaraldehyde. Optical microscope images (obtained with the Zeiss internal microscope) of glutaraldehyde exposed dry fiber mats (C) after 1 hour in water and (D) after 16 hours in water.

Once soaked in water the glutaraldehyde exposed fibers swelled and appeared to partially dissolve. After soaking for either one or sixteen hours the wells were drained of water leaving behind a semi-transparent film of PVA. In the dish these films were tacky but returned to a solid film that could be easily handled and mounted on SEM stubs after drying. Unlike “as spun” PVA which will completely dissolve in water at room temperature in less than 30 minutes, the glutaraldehyde exposure appeared to stabilize the system to a small degree. The similarity in the SEM images seen in **Figure 7.3C** and **Figure 7.3D** indicate that soak time has less impact than the specific chemical treatment with respect to the fiber stability, at least on timescales relevant to tissue scaffolds. While we could prevent complete dissolution of the PVA fibers, none of our attempts to preserve fiber structure by chemically crosslinking PVA could reproduce literature [26-28]. The images in **Figure 7.3C** and **Figure 7.3D** are shown at low magnification, utilizing the optical microscope inside the SEM. This is due to the complete lack of fiber structure or any discernable features on which the SEM could be focused once magnification was increased.

Cold crystallizing PVA by isothermally holding at 150 °C for 15 minutes proved to be an effective means of stabilizing the fibers. SEM images were collected on the “as spun” fiber mat, following the isothermal crystallization, and after each exposure time. A sampling of these can be seen in **Figure 7.4**.

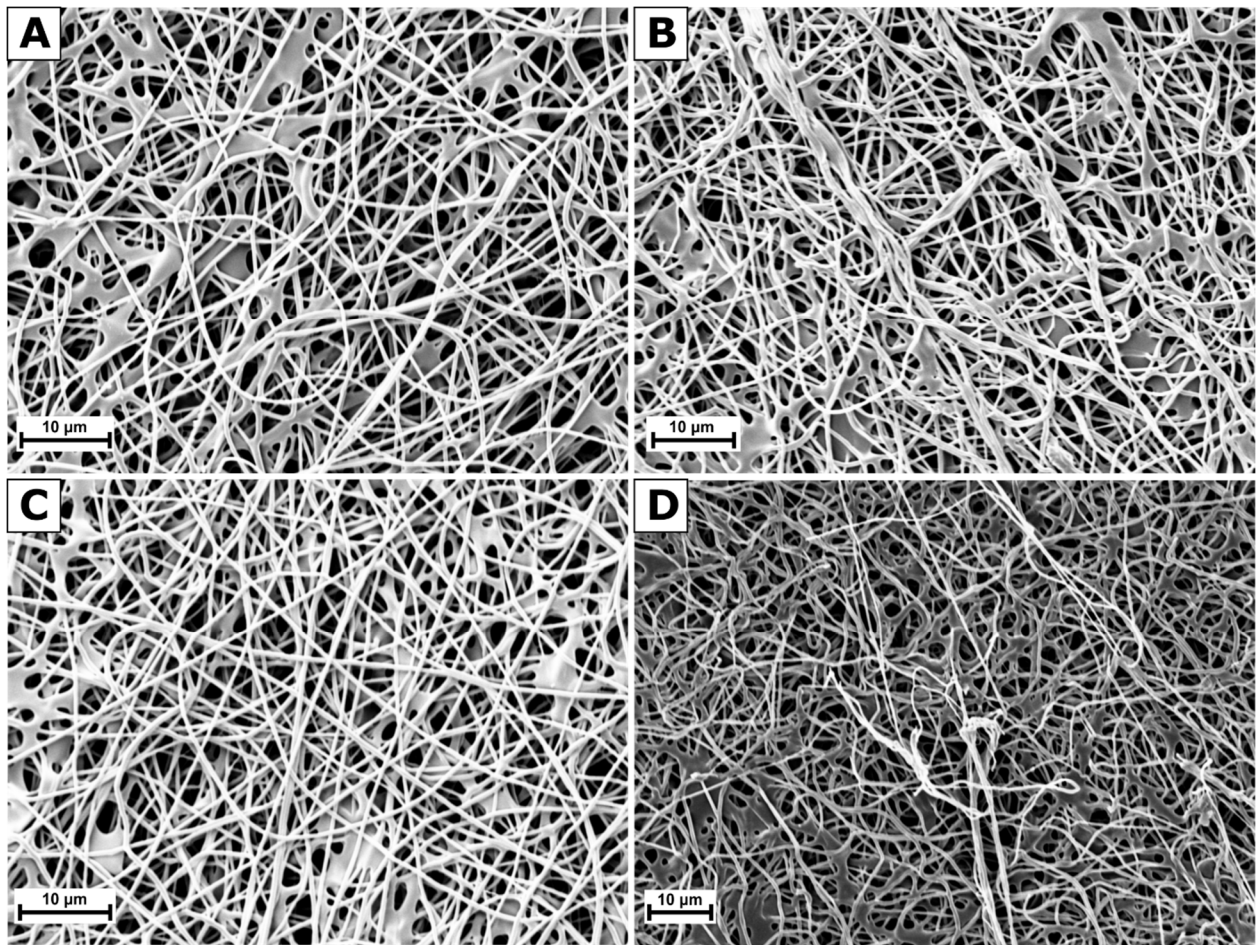


**Figure 7.4:** Images of PVA fiber mats at magnifications ranging between 4500-6000X collected with the Zeiss SEM for: (A) “as spun”, (B) following thermal stabilization treatment, (C) stabilized and soaked in water for 1 hour, (D) stabilized and soaked in water for 96 hours.

The overall fiber alignment and fiber quality remains unchanged following thermal stabilization treatment as seen in **Figure 7.4A** (“as spun”) and in **Figure 7.4B** (150 °C for 15 min). Following soaking in water the fibers appear to slightly swell but there is no evidence for dissolving or fiber merging following partial dissolution. There was no visual evidence for a loss of fiber structure following soaking for 1 hour (**Figure 7.4C**) or 96 hours (**Figure 7.4D**). The apparent discoloration seen in the sample soaked for 96 hours is a result of contrast settings on Zeiss which were tuned to deal with the warping of the fibers as they dried before being sputter

coated. Fiber diameters were quantitatively measured using the DiameterJ [29] plugin as outlined in **Section 3.1.2**. Fiber diameter distributions were measured for the “as spun” tape, after isothermal crystallization, and following each soak. An example of the fiber diameter distribution for the “as spun” fiber tape can be seen in **Figure 7.5A** and the average fiber diameter for each case is plotted in **Figure 7.5B**.

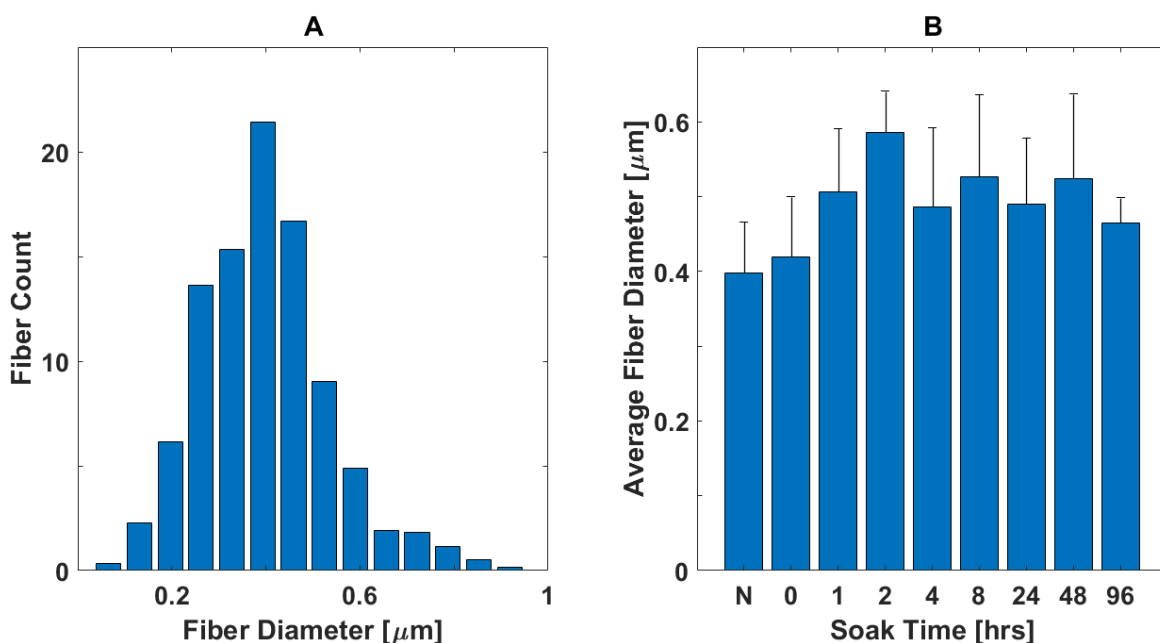


**Figure 7.5:** (A) Example fiber diameter distribution for the “as spun” fiber mat, pictured in **Figure 7.4A**, and (B) average fiber diameters following each treatment where N is the “as spun” fiber, 0 received only thermal stabilization treatment with no water exposure, and each number corresponds to the number of hours fiber mats were soaked in water.

All fiber diameter distributions obtained using the DiameterJ plugin for ImageJ showed an asymmetric distribution with a shoulder at higher diameters between 700 nm and up to 1200 nm. These high diameter shoulders are the result of fiber mergers or tightly bundled fibers where images had insufficient contrast between fibers preventing the software from correctly segmenting

the fibers and measuring diameters. Average fiber diameter and the standard deviation of the fiber diameter were calculated from the frequency data used to generate the histograms for individual SEM images, as shown in **Figure 7.5A**. The diameter frequencies which resulted from poor contrast preventing fiber differentiation were excluded from the statistics. Data is summarized in **Table 7.1**.

**Table 7.1:** Average fiber diameters in nm corresponding to the data presented in **Figure 7.5B**

| Soak Time<br>hours | Diameter<br>nm | Diameter<br>Error<br>± nm |
|--------------------|----------------|---------------------------|
| 0 <sup>a</sup>     | 400            | 70                        |
| 0 <sup>b</sup>     | 420            | 80                        |
| 1                  | 510            | 80                        |
| 2 <sup>c</sup>     | 590            | 60                        |
| 4                  | 490            | 110                       |
| 8                  | 530            | 110                       |
| 24                 | 490            | 90                        |
| 48                 | 520            | 110                       |
| 96 <sup>c</sup>    | 460            | 30                        |

<sup>a</sup> “as spun” fibers, never exposed to water

<sup>b</sup> These fibers were thermally stabilized but never exposed to water

<sup>c</sup> Fiber diameters measured by hand due to fiber bundling and contrast issues

The “as spun” fibers have an average fiber diameter of 400 nm ± 70 nm. Following isothermal crystallization at 150 °C for 15 min this increases to an average diameter of 420 nm ± 80 nm. As the polymer crystallizes elongated, amorphous, polymer chain segments pack into lamellar structures. This results in both a contraction of the fibers along the fiber direction and an increase in the fiber diameter. After soaking there is only a small increase in the average fiber diameter, to an average of 510 nm. Excluding the cases where fiber diameters were measured by hand from the SEM images where the statistics are much lower than the large images compiled

using DiameterJ, the distribution of fiber diameters is observed to increase. This suggests that the fibers are swelling due to the uptake of water by the amorphous regions within the fibers. The swelling is expected to vary with crystallinity and the least crystalline fibers will swell more than those with higher crystallinity. As mentioned in **Section 2.5** PVA crystals act like “staples” which prevent the amorphous PVA from being completely solvated by the water. PVA crystals are nearly insoluble in water and complete dissolution requires long times (not in this lifetime) [30]. Semi-crystalline PVA is only water soluble above the glass transition,  $T_g = 85\text{ }^\circ\text{C}$  [31], where the amorphous phase material is mobile enough to allow effective solvent penetration [30]. These results are in agreement with literature where fibers were thermally stabilized to prevent dissolution [24].

## ***7.2 Protein Coating and Creation of Neural Tissue Scaffold***

The effective preservation of fiber structure, alignment, and fiber diameter to within 100 nm of their original, “as spun” diameter makes isothermal crystallization the ideal means of stabilizing fibers. One major drawback to thermally stabilizing PVA by crystallization at temperatures in excess of 100 °C is that it prevents the addition of biopolymers or proteins to the electrospinning solution as many proteins will denature at these temperatures. Conditions where PVA can be vapor crosslinked with glutaraldehyde [27, 28] or stabilized by other solvents [25] will similarly denature most proteins. Because of this limitation, PVA fibers are first stabilized and then coated with proteins prior to being plated with neurons. However, it is worth noting that small molecule drugs can still be added to the electrospinning solution [12, 32, 33] if the dissolution of PVA is not a factor.

While PVA is biocompatible and widely used in biomedical applications [1, 34-37] it is coated in poly-D-lysine to promote neuron attachment to the fibers and improves their viability as a tissue scaffold [6, 38]. Fibers coated in PDL, PDL and fibronectin, PDL and laminin, and PDL with both fibronectin and laminin proved to be viable substrates for neurons as evidenced by the presence of living neurons seen in **Figure 7.6**.

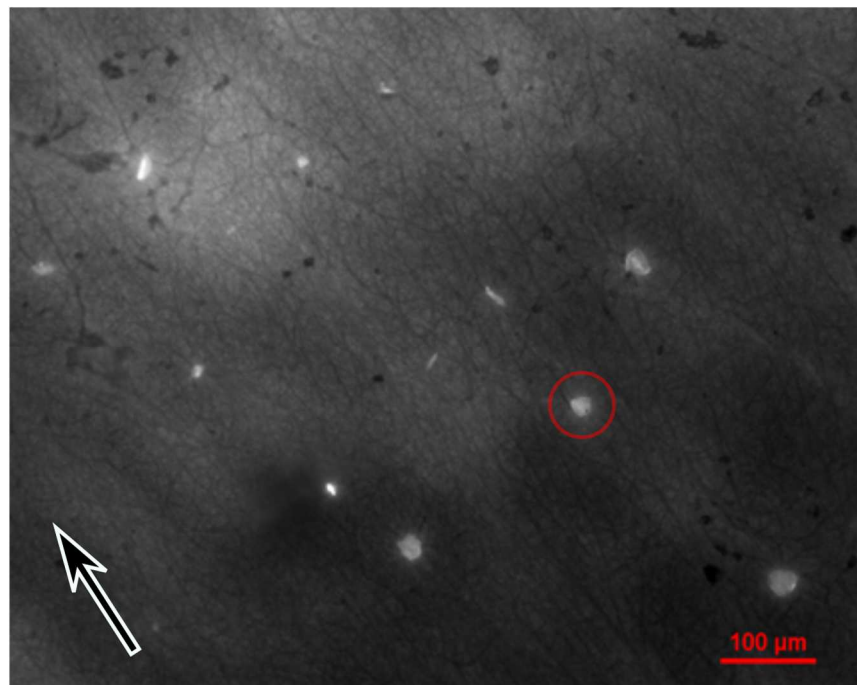


**Figure 7.6:** Neurons successfully plated and observed to be alive on the thermally stabilized, PDL, laminin, and fibronectin coated PVA tissue scaffold. The black and white arrow in the bottom left corner indicates the average fiber direction and one neuron is highlighted by the red circle. Image taken by Derek Walkama and Peter Riley.

Our findings on PVA based tissue scaffolds are in line with other investigations [2, 13-20, 22, 23]. Due to limitations on experimental time, the impact of the addition of laminin and fibronectin, both of which are known to promote neuron growth on substrates [39], could not be further investigated. The challenges that PVA presented in terms of reliably producing highly aligned nanofibers made it difficult to complete a study on the controlled growth of neurons.

However our results suggest that that PVA loaded with fibronectin and laminin serves as a highly viable neural tissue scaffold. It is possible to improve fiber alignment by altering the counter electrode geometry [40-42] and future studies can build from the thermal stabilization and protein coating process to create highly aligned nanofiber tissue scaffolds. The unique non-toxicity, biocompatibility, and biodegradation properties of PVA combined with the possibility of processing the polymer with water (as opposed to highly toxic organic solvents) reinforce the conclusion that this work serves as a solid foundation for further study [34, 35].

### **7.3 *Structural Analysis of PVA Nanofibers:***

Motivated by the successful growth of neurons on PVA, structural and thermal properties of the fibers are investigated, particularly the relationship between the crystallinity and solubility of the fibers. Following electrospinning and thermal stabilization of the fibers samples were cut and prepared for X-ray diffraction (XRD) and Fourier Transform Infrared Spectroscopy (FTIR). XRD and FTIR scans of PVA fibers both “as spun” from each solvent and following thermal stabilization treatments are shown in **Figure 7.7** and **Figure 7.8**, respectively.

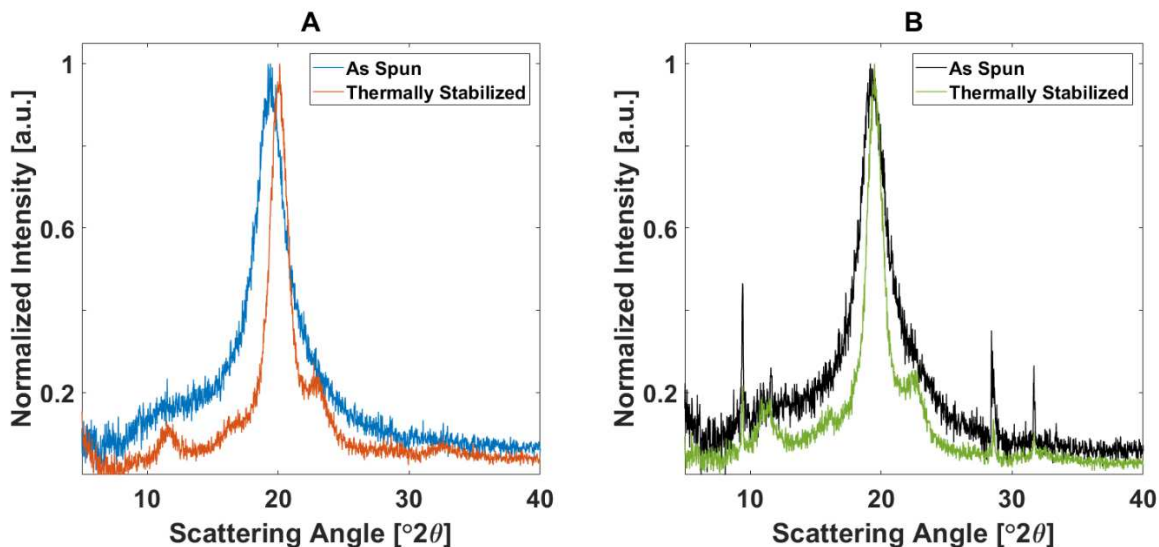


**Figure 7.7:** X-ray diffraction patterns for **(A)** “as spun” (blue) and thermally stabilized (orange) PVA spun from DI water and **(B)** “as spun” (black) and thermally stabilized (green) PVA spun from 98/2 DI water/ acetic acid mixed solvent.

The diffraction patterns for PVA electrospun from the deionized water solution can be seen in **Figure 7.7A**. The “as spun” case is plotted in blue and following isothermal crystallization at 150 °C for 15 min is plotted in orange. PVA electrospun from the deionized water/ acetic acid mixed solvent solution can be seen in **Figure 7.7B**. The “as spun” case is plotted in black and following isothermal crystallization at 150 °C for 15 min is plotted in green. Regardless of the solvent, both solutions resulted in fibers which appear to be amorphous following electrospinning which explains how the fibers readily dissolve in water at room temperature. Between the “as spun” and thermally stabilized scans the full width at half maximum (FWHM) of the main diffraction peak around 20 °2 $\theta$  is observed to decrease from 2.89 °2 $\theta$  to 1.51 °2 $\theta$  for the fibers spun from water, and decreased from 2.59 °2 $\theta$  to 1.36 °2 $\theta$  for the fibers spun from the mixed solvent. This indicates that the amorphous material reorganized during the isothermal hold at 150 °C. The appearance of diffraction peaks at 16, 19, 20, and 22.7 °2 $\theta$  following the thermal

stabilization treatment indicate that the samples are semi-crystalline [43-47] and the peaks correspond to the (100), (10 $\bar{1}$ ), (101), and (200) reflections, respectively. This supports the explanation of fiber stability in water following heat treatments. The peaks around 12, 29, and 33  $^{\circ}2\theta$  correspond to diffraction peaks of the mechanical grade silicon substrate under the PVA nanofiber mats. The prominence of these peaks varies with the thickness of the fiber mat on top of the silicon substrate.

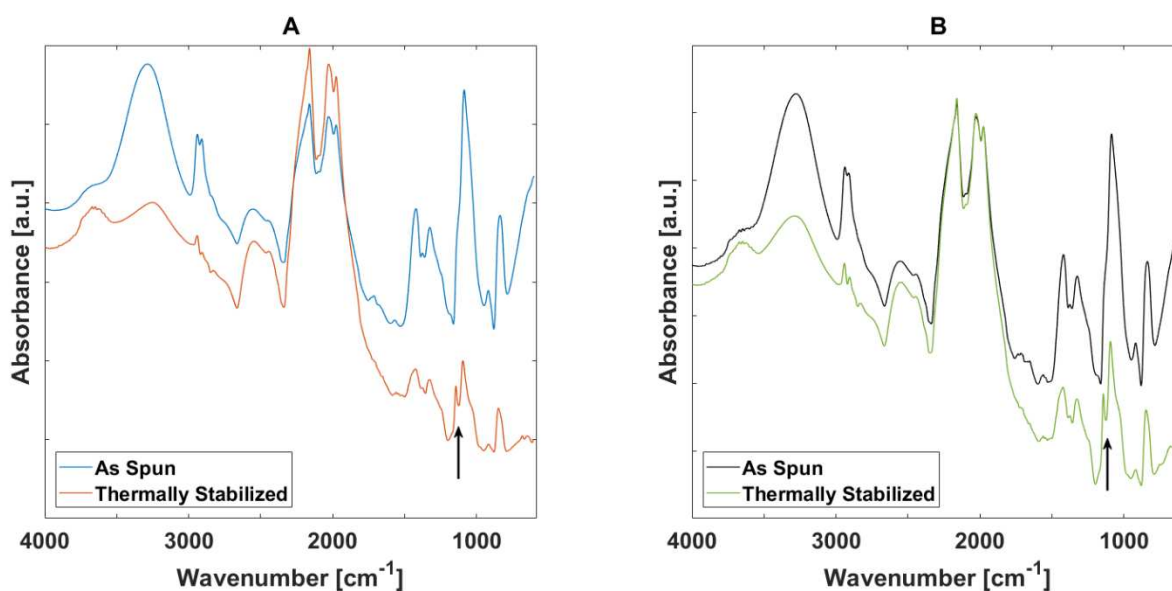


**Figure 7.8:** Fourier Transform Infrared Spectroscopy absorbance spectra for (A) “as spun” (blue) and thermally stabilized (orange) PVA spun from DI water and (B) “as spun” (black) and thermally stabilized (green) PVA spun from 98/2 DI water/ acetic acid mixed solvent. The black arrow refers to the crystalline vibration at 1140  $\text{cm}^{-1}$ .

In order to compare the spectra between “as spun” and thermally stabilized samples the raw data are normalized by the total area. Both absorbance spectra for “as spun” fibers (blue and black curves in **Figure 7.8**) show a broad peak between 3550  $\text{cm}^{-1}$  and 3200  $\text{cm}^{-1}$  which corresponds to the inter and intra molecular hydrogen bonds [28]. The presence of bound water (recall that the mixed solvent is 98% water) strongly interacts with the hydroxyl groups along the

PVA backbone by hydrogen bonding. This peak is observed to decrease following thermal stabilization (orange and green curves in **Figure 7.8**) indicating that water has been ejected during the heating. But it does not completely disappear as there is still inter and intra molecular hydrogen bonding between hydroxyl groups which are present both in amorphous and semicrystalline PVA.

The main evidence for the increase in crystallinity is the splitting of the peak spanning  $1080\text{ cm}^{-1}$  to  $1150\text{ cm}^{-1}$  in the blue and black curves into two peaks, with the smaller peak at  $1140\text{ cm}^{-1}$  in the orange and green curves. The peak at  $1140\text{ cm}^{-1}$  is due to the C-O crystalline vibration [30], which is distinct from the general spectrum of C-O-C vibrations. PVA is known to crystallize, independent of the tacticity of the molecule, by inter chain hydrogen bonding of the hydroxyl groups. It is worth noting that the “as spun” spectra show an asymmetric peak with a shoulder near  $1140\text{ cm}^{-1}$ , this could indicate the presence of a small amount of crystallinity in the fibers as spun. Calculations based on these spectra are in agreement with the XRD data.

## **7.4 Thermal Analysis of Electrospun Nanofibers**

### **7.4.1 Conventional Thermal Analysis**

Thermogravimetric analysis (TGA) was performed at  $5\text{ }^{\circ}\text{C}/\text{min}$  on fibers which were spun from both deionized water and the deionized water/ acetic acid mixed solvent. This is the same baseline heating rate used during temperature modulated DSC (TMDSC) scans. Rates are matched between TGA and DSC since thermal degradation is a kinetic process. Because PVA is a hydrophilic polymer [30] samples are kept in the vacuum oven for several hours prior to thermogravimetric analysis to prevent water picked up from the atmosphere from binding to the surface of the fibers and obscuring results. Percent mass remaining as a function of temperature is

plotted in **Figure 7.9** The onset of thermal degradation, at temperatures just in excess of 200 °C is consistent with what has been observed in solution cast films (see **section 4.1**).

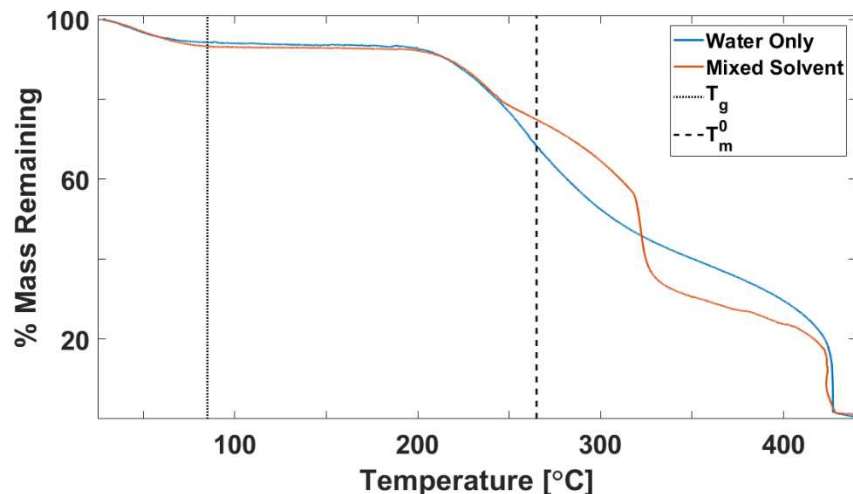


**Figure 7.9:** Thermogravimetric %mass remaining vs. temperature for “as spun” PVA spun from DI water (blue) and the 98/2 DI water/ acetic acid mixed solvent (orange). The glass transition is marked by the vertical, dotted line at  $T_g = 85$  °C [31] and the equilibrium melting point is marked by the vertical, dashed line at  $T_m^0 = 265$  °C [31]. Both fibers show similar (6-7%) solvent retention and lose between 20-30% of their mass by  $T_m^0$ .

As samples are heated above room temperature, there is a constant loss of mass until the signal stabilizes around 80 °C. This initial mass loss is the ejection of electrospinning solvent. PVA electrospun from deionized water (blue curve) shows a mass loss of 6.3% and a mass loss of 7.1% when electrospun from the mixed solvent (orange curve). The last traces of solvent are removed at 80 °C, which is around 5 °C above the typical onset of the glass transition for PVA ( $T_g$  reported at the inflection point is 85 °C [31]). Any thermal stabilization treatments involving isothermal crystallization will result in all solvent being ejected. The choice of solvent does not appear to substantially affect the onset of thermal degradation. PVA spun from DI water begins to degrade at  $191$  °C  $\pm$  1 °C and PVA spun from the mixed solvent begins to degrade at  $187$  °C  $\pm$  1

°C. The addition of acetic acid shifts thermal degradation profile of PVA where a pronounced, multi-step degradation process is observed. The presence of the acid in the electrospinning solvent impacts the protonation states of the hydroxyl groups along the PVA backbone is likely causing changes in the thermal degradation profile of PVA.

TMDSC was performed as described in **Section 3.3.2.3**. Experiments were performed both for PVA spun from DI water and PVA spun from the mixed solvent. Scans were taken for each fiber “as spun” and following thermal stabilization. Because each scan brings the fibers to high temperature, fresh samples are prepared for each measurement. Thermal stabilization can be performed on fibers inside the DSC as the small amount of bound solvent, when ejected, is not likely to cause damage to the cell. It is worth commenting that if the fibers contained more than 10% bound solvent, performing many experiments inside the Q100 DSC will cause solvent vapors to condense in the cell resulting in damage to the instrument. TMDSC scans were performed following either the drying treatment (isothermal hold at 80 °C for 30 min) or thermal stabilization (150 °C for 15 min).

The total heat flow rate as a function of temperature for PVA spun from DI water during heating following the drying treatment and heating following thermal stabilization are shown in **Figure 7.10A**. The total heat flow rate as a function of temperature for PVA spun from mixed solvent during heating following drying and thermal stabilization are shown in **Figure 7.10B**. The heating rates accessible by TMDSC are low enough that the complete melting endotherm of PVA is not always measurable before the signal is overtaken by endothermic thermal degradation of the sample at high temperature.

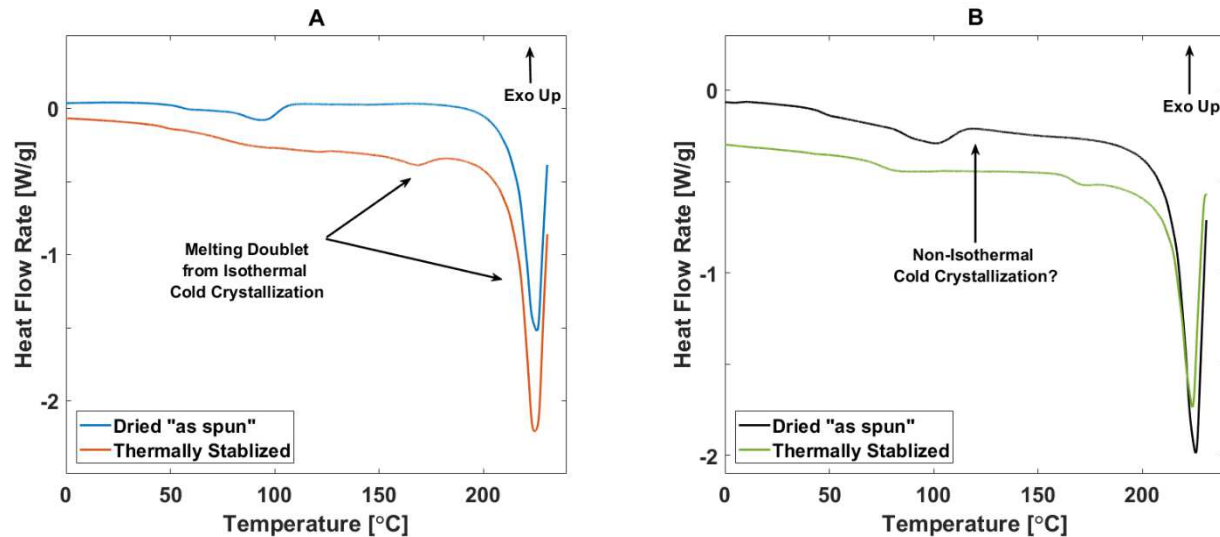


**Figure 7.10:** Heat flow rate vs. temperature for (A) dried “as spun” (blue) and thermally stabilized (orange) PVA spun from DI water and (B) dried “as spun” (black) and thermally stabilized (green) PVA spun from 98/2 DI water/ acetic acid mixed solvent. Heating was performed at a rate of 5 °C/min.

The drying treatment was designed such that the fibers would remain as close to the “as spun” condition as possible but without solvent ejection occurring during the melting scan. Total heat flow rate vs. temperature scans are used to measure the total enthalpy of melting allowing for measurements of crystallinity. All scans exhibit a melting endotherm, indicating the presence of crystals in all fibers by the time the fibers are brought to high temperature. The thermally stabilized fibers, shown as the orange and green curves in **Figure 7.10A** and **figure 7.10B**, respectively, have a melting doublet with the first, smaller peak melting around 160 °C, and then the larger melting peak around 225 °C. This small peak is due to crystals which nucleated and grew during the isothermal hold at 150 °C. The melting behavior observed during scans on the dried, “as spun” fibers contrasts with the expected results from the structural analysis which indicated that fibers should be nearly amorphous. Both dried, “as spun” curves, the blue and black curves in **Figure 7.10A** and **Figure 7.10B**, respectively, exhibit an exothermic upturn or possibly a broad, low

amplitude peak suggesting that there is some non-isothermal cold crystallization occurring. To unpack this, the first step is quantifying the total enthalpy of melting observed, which would be the melting of 1. any pre-existing crystals, 2. material which was formed by non-isothermal crystallization during heating above  $T_g$  (cold crystallization), and 3. crystals formed during the thermal stabilization treatment.

Due to the truncation of the endotherm an approximation must be made for the complete endotherm area. By approximating the melting endotherm as symmetric about the peak temperature,  $T_m$ , the total enthalpy of melting can be calculated from the half melting area.

$$\Delta H_{1/2} = \int_{T_{onset}}^{T_m} \Phi dT \quad (7.1a)$$

where  $\Phi$  is the heat flow rate (detailed in **Section 3.3.2.2**). This allows for the determination of the mass fraction crystallinity,  $\phi$

$$\phi = (2\Delta H_{1/2} + \Delta H_{low}) / \Delta H_{f0} \quad (7.2b)$$

where  $\Delta H_{low}$  is the enthalpy of the low temperature melting peak observed in the thermally stabilized samples. This is not included in the assumption of the symmetric melting peak which has a peak around 225 °C. The equilibrium melting point ( $\Delta H_{f0} = 161.4$  [31]) has been corrected for the melting point of the finite crystal using the following relationship [48, 49]:

$$\Delta H_{f0}^{corr} = \Delta H_{f0} (2 * T_m / (T_m + T_m^0)) \quad (7.2)$$

Applying Eqn. 7.1 to the total heat flow data collected during the TMDSC scans it is possible to estimate the enthalpy of melting after various sample treatments. This allows for the calculation of the crystallinity using Eqn. 3.14 (shown in the modified form in Eqn. 7.1b) and the heat of fusion of PVA [31]. Independent of solvent choice during electrospinning, fibers contained

6-7 mass% bound solvent. This required the fibers to be dried by heating to temperatures just above the glass transition as the ejection of solvent can mask transitions in the sample as discussed previously (**Section 4.2**). While TMDSC allows the fully reversible glass transition to be separated from irreversible events, the endothermic signal produced when the bound solvent is ejected will mask any low temperature cold crystallization or enthalpic signal from fiber shrinkage.

**Table 7.2:** Thermal properties of electrospun PVA fibers as measured by DSC

| Solvent  | Treatment               | $T_g^a$ °C<br>± 0.2 °C | $T_m^a$ °C<br>± 0.2 °C | $\phi$<br>±0.2 |
|----------|-------------------------|------------------------|------------------------|----------------|
| DI Water | Dried <sup>b</sup>      | 81.8                   | 225.7                  | 0.20           |
| DI Water | Stabilized <sup>c</sup> | 74.4                   | 225.3                  | 0.29           |
| Mixed    | Dried <sup>b</sup>      | 85.2                   | 225.6                  | 0.25           |
| Mixed    | Stabilized <sup>c</sup> | 74.7                   | 224.1                  | 0.32           |

<sup>a</sup> Values obtained from total heat flow rate vs. temperature (standard DSC mode)

<sup>b</sup> Samples are dried by heating to 80 °C and holding isothermally for 30 minutes

<sup>c</sup> Samples are thermally stabilized by isothermal cold crystallization at 150 °C for 15 minutes

Independent of the electrospinning solvent, the total crystallinity appears to change less than 7% between the dried, “as spun” fiber and the thermally stabilized fibers. This means that either, the fibers are not completely amorphous as spun, or the exothermic increase between  $T_g$  and the onset of melting is non-isothermal cold crystallization occurring during heating. As discussed in **Section 3.3.2.3**, TMDSC allows for the total heat flow signal to be separated into two components, the heat capacity and the kinetic components (reversing and non-reversing, respectively). The results of TMDSC heating scans following the drying or thermal stabilization treatment are shown in **Figure 7.11**.

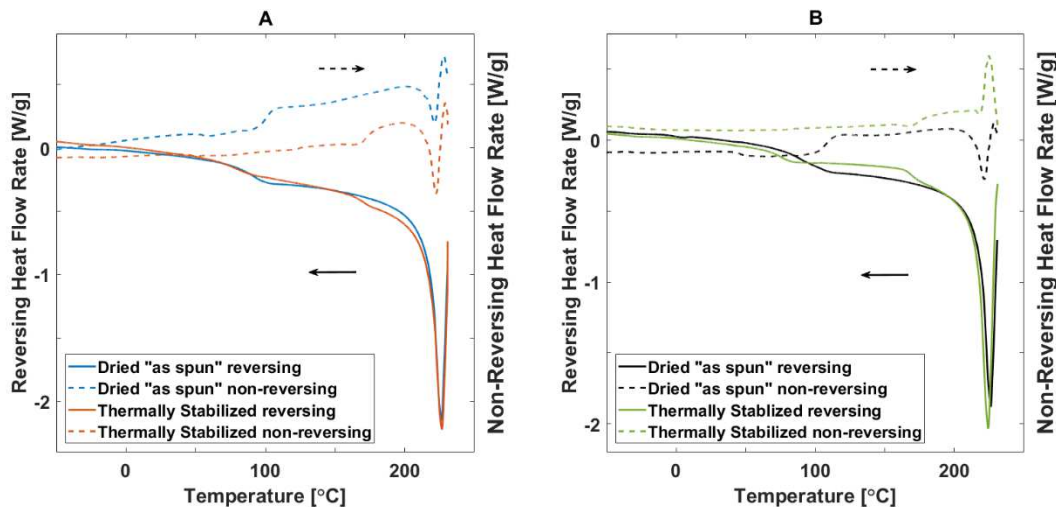


**Figure 7.11:** Reversing and non-reversing heat flow rate vs. temperature. **(A)** PVA spun from DI water. Dried “as spun” is shown in blue and thermally stabilized shown in orange. The solid and dashed curves corresponding to the reversing and non-reversing heat rates, respectively. **(B)** PVA spun from mixed solvent. Dried “as spun” is shown in black and thermally stabilized shown in green. The solid and dashed curves corresponding to the reversing and non-reversing heat rates, respectively.

The reversing heat flow rate vs. temperature provides information regarding the heat capacity contribution to the total heat flow rate. The curves above, regardless of the sample, show a smooth glassy heat flow baseline, a clearly expressed glass transition, and then a rubbery baseline prior to the onset of melting. In the case of the thermally stabilized fibers, the solid orange curve in **Figure 7.11A** and the solid green curve in **Figure 7.11B** (where the fibers were isothermally cold crystallized at 150 °C for 15 min) both show a decrease in the amplitude of the glass transition when compared to the dried, “as spun” curves (solid blue and black in **Figure 7.11**). This decrease in the heat capacity increment at the glass transition is indicative of increased crystallinity, consistent with the overall increase in enthalpy of melting reported in **Table 7.2** and the structural analysis results presented in the previous section.

Non-reversing heat flow data allows for deeper insights into the presence of cold crystallization, which is a kinetic process which occurs non-isothermally during heating. As expected, and consistent with the total heat flow rate data in **Figure 7.10**, the thermally stabilized fibers do not show any cold crystallization. The first signal in the non-reversing heat flow for the thermally stabilized fibers spun does not occur until the samples are heated to onset of the melting, around 160 °C where some of the crystals which formed during the isothermal crystallization step begin to melt. Polymer melting is generally an irreversible process [50-52] however some of the reversing heat flow signal may come from chains detaching reversibly and reattaching to the parent crystal during the melting process. The erratic heat flow seen in all four dashed curves in **Figure 7.11** which begins around 215 °C is due to the thermal degradation of PVA which is coincident with the crystal melting [53-55].

The non-reversing heat flow rate vs. temperature data for the dried, “as spun” fibers spun from DI water (dotted, blue curve in **Figure 7.11A**) and from the mixed solvent (dotted, black curve in **Figure 7.11B**) both exhibit an exothermic increase following the glass transition. This increase around 105 °C accounts for the upshifted heat flow baseline following  $T_g$  in the total heat flow data presented in **Figure 7.10**. This confirms that the dried, “as spun” PVA is cold crystallizing during heating, giving an additional contribution of which are observed to melt. Because the thermal stabilization is performed at 150 °C and the onset of this cold crystallization occurs around 105 °C, the melting common to all four samples observed in the peak around 225 °C is due to crystal which formed by the same mechanism.

Integrating the total heat flow rate for the dried, “as spun” fibers (blue in **Figure 7.10A** and black in **Figure 7.10B**) between the end of the glass transition and the onset of melting provides the enthalpy of cold crystallization. This will allow for the total crystallinity,  $\phi$ , value reported in

**Table 7.2** to be separated into the crystals which formed from cold crystallization,  $\phi_{CC}$ , and those which might be native to the fibers,  $\phi_{Initial}$ , from the electrospinning process. The results of this are summarized in **Table 7.3**.

**Table 7.3:** Assessment of the thermal properties during heating of dried, “as spun” fibers and stabilized fibers:

| Solvent | Treatment               | $T_{CC}^a$<br>$\pm 1\text{ }^\circ\text{C}$ | $\Delta H_{CC}^a$<br>$\pm 0.02$<br>J/g | $\phi_{CC}^a$<br>$\pm 0.02$ | $T_{m1}^b$<br>$\pm 1\text{ }^\circ\text{C}$ | $T_{m2}^b$<br>$\pm 0.2$<br>$^\circ\text{C}$ | $\Delta H_f^b$<br>$\pm 0.02$<br>J/g | $\phi^b$<br>$\pm 0.02$ | $\phi_{Initial}^c$<br>$\pm 0.02$ |
|---------|-------------------------|---|--|-----------------------------|---|---|-------------------------------------|------------------------|----------------------------------|
| DI      | Dried <sup>d</sup>      | 109   | 20.3                                   | 0.21                        | -   | 225.7                                       | 41.2                                | 0.28                   | 0.06                             |
| DI      | Stabilized <sup>e</sup> | -   | -                                      | -                           | 168   | 225.27                                      | 46.4                                | 0.31                   | -                                |
| Mixed   | Dried <sup>d</sup>      | 116   | 17.5                                   | 0.18                        | -   | 225.6                                       | 37.4                                | 0.25                   | 0.07                             |
| Mixed   | Stabilized <sup>e</sup> | -   | -                                      | -                           | 171   | 224.1                                       | 47.4                                | 0.32                   | -                                |

<sup>a</sup> Cold crystallization temperature, exotherm area, and crystallinity

<sup>b</sup> Melting temperature, endotherm area, and crystallinity

<sup>c</sup> Initial crystallinity from difference between endo and exotherm areas

<sup>d</sup> Samples are dried by heating to 80 °C and holding isothermally for 30 minutes

<sup>e</sup> Samples are thermally stabilized by isothermal cold crystallization at 150 °C for 15 minutes

Combining TMDSC and standard mode DSC it was possible to measure the impact of the thermal stabilization treatment on the crystallinity of PVA nanofibers. These modified DSC results no longer stand in contrast with the structural analysis data from **Section 7.3**. The difference between the crystallinity as measured from the total melting endotherm and the crystallinity measured from the broad cold crystallization exotherm indicates that the fibers, as spun are less than 10% crystalline. Generally, differential scanning calorimetry provides a more accurate measurement of polymer crystallinity than X-ray or spectroscopy methods. This is because small or dispersed crystals within the sample will not provide strong scattering nor will they absorb

enough radiation that the difference in the signal at the detector is beyond the signal to noise ratio. In the DSC, the total heat flow signal will reflect all the heat absorbed by the melting of these small crystals. Given the sharpness of the amorphous halo seen in the “as spun” scans in **Figure 7.7**, and the shoulder on the C-O-C vibration at C-O PVA crystalline vibration peak in **Figure 7.8**, a crystallinity < 10% is reasonable, but unfortunately is not sufficient to stabilize fibers from dissolving in water at room temperature [30].

It was shown during experiments discussed in **Chapter 5**, that when PVA is amorphous or has low mass fraction crystallinity, it will rapidly cold crystallize at temperatures above the glass transition. The slow scanning DSC results agree with what was observed in the fast scanning DSC measurements presented in **Section 5.5** where samples with less than 10% mass fraction crystallinity cold crystallize once heated above  $T_g$ , however there is no cold crystallization observed once the mass fraction crystallinity approaches 40%. Utilizing the methods discussed in **Chapter 6** it is possible to study similar PVA nanofibers by fast scanning calorimetry (FSC) to gain additional insights into the crystallinity of the “as spun” fiber.

#### **7.4.2 FSC based Thermal Analysis of PVA Fibers**

Fibers suitable for fast scanning calorimetry (FSC) experiments were electrospun as detailed in **Section 2.4**. The thermal treatments performed on the fibers in the Mettler Flash DSC1 are outlined in **Section 3.4.3.2**. An electrospun PVA loaded grid (ESPVA) was placed face down on the UFSC1 sensors as detailed in **Section 6.2**. Unlike the bulk fibers studied in the conventional DSC, fibers were dried at 80 °C for 10 minutes as it was found that time was sufficient for the rarefied fibers loaded into the Flash DSC1. Once dried fibers were heated to 270 °C at 2000 K/s,

cooled from the melt at 2000 K/s and reheated at the same rate to 270 °C. This fiber scan is the FSC analog to the drying and melting protocol ran on the bulk fibers in **Section 7.4.1**. The heat flow rate as a function of temperature following the drying step is shown in **Figure 7.13**.

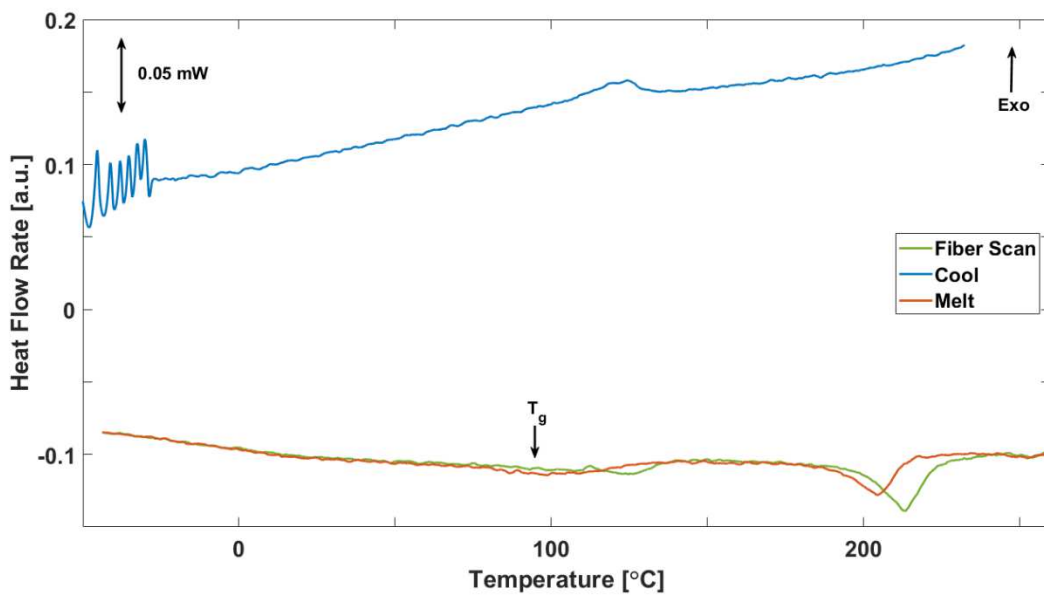


**Figure 7.13:** Heat flow rate vs. temperature for the melting of dried fibers (green curve), cooling from the melt (blue curve), and final reheating (orange curve). The heating and cooling rate is 2000 K/s.

The orange and blue curves in **Figure 7.13** correspond to the same cooling and heating profile applied to the PVA thin films discussed in **Chapter 5**. Here, fibers have been melted and non-isothermal crystallization is observed during cooling. The peak crystallization temperature is 125 °C which is consistent with the peak non-isothermal crystallization temperature observed when cooling PVA thin films from the melt. Upon reheating, cold crystallization is observed following the glass transition. Melting of the non-isothermally crystallized and cold crystallized material is observed with a peak melting temperature of 205 °C, consistent with what was observed in the thin films.

The green curve in **Figure 7.13** shows the heating scan of the fibers following the drying step. Here a higher melting point and larger endotherm area is observed than in the final melting scan following non-isothermal melt crystallization and subsequent cold crystallization. This indicates the presence of initial crystallinity in addition to the cold crystallization observed once the fibers are heated above  $T_g$ . Similar to what was observed during heating of fibers at conventional DSC scanning rates, there is continuous cold crystallization until the crystals begin to melt with peak melting at  $T_m = 214$  °C.

Unlike the PET nanofibers discussed in **Chapter 6**, the expression of the glass transition is very near the signal to noise threshold for the electrospun PVA fibers. This makes obtaining an accurate measurement of the heat capacity increment difficult, preventing it from being used to determine the sample mass. Using the melting endotherm area of the final melting scan, shown as the orange curve in **Figure 7.13** an endotherm area of  $0.24 \mu\text{J}$  is obtained. Comparing this to the PVA thin film fast scanning results from **Chapter 5** the average total crystallinity,  $\langle\phi\rangle = 0.30 \pm 0.01$ , it is possible to determine the mass of the fibers. This results in a fiber mass of  $4.3 \pm 0.2$  ng. To determine the initial fiber crystallinity,  $\phi^{\text{Initial}}$ , the total enthalpy between the glass transition and completion of melting (where the liquid phase heat flow baseline is recovered) is measured. The total initial fiber crystallinity is measured to be  $\phi^{\text{Initial}} = 0.09 \pm 0.02$ . This value is within the range of crystallinities measured by the conventional DSC. A particular advantage of this method is the complete melting of the fibers is observed as the scanning rate of 2000 K/s mitigates sample degradation.

## 7.5 References

- [1] S.N. Alhosseini, F. Moztarzadeh, M. Mozafari, S. Asgari, M. Dodel, A. Samadikuchaksaraei, S. Kargozar, N. Jalali, Synthesis and characterization of electrospun polyvinyl alcohol nanofibrous scaffolds modified by blending with chitosan for neural tissue engineering, *Int. J. Nanomed.* 7 (2012) 25-34.
- [2] L. Binan, A. Ajji, G. De Crescenzo, M. Jolicoeur, Approaches for Neural Tissue Regeneration, *Stem Cell Rev. Rep.* 10(1) (2014) 44-59.
- [3] L. Binan, C. Tendey, G. De Crescenzo, R. El Ayoubi, A. Ajji, M. Jolicoeur, Differentiation of neuronal stem cells into motor neurons using electrospun poly-L-lactic acid/gelatin scaffold, *Biomaterials* 35(2) (2014) 664-674.
- [4] X. Dai, Y.-C. Huang, Electrospun fibrous scaffolds of Poly(glycerol-dodecanedioate) for engineering neural tissues from mouse embryonic stem cells, *Journal of visualized experiments : JoVE* (88) (2014).
- [5] C. Huang, R. Chen, Q.F. Ke, Y. Morsi, K.H. Zhang, X.M. Mo, Electrospun collagen-chitosan-TPU nanofibrous scaffolds for tissue engineered tubular grafts, *Colloid Surf. B-Biointerfaces* 82(2) (2011) 307-315.
- [6] Y.-S. Lee, T. Livingston Arinzeh, Electrospun Nanofibrous Materials for Neural Tissue Engineering, *Polymers* 3(1) (2011) 413.
- [7] M.P. Prabhakaran, E. Vatankhah, S. Ramakrishna, Electrospun Aligned PHBV/Collagen Nanofibers as Substrates for Nerve Tissue Engineering, *Biotechnol. Bioeng.* 110(10) (2013) 2775-2784.

- [8] S. Sahoo, L.T. Ang, J.C.H. Goh, S.L. Toh, Growth factor delivery through electrospun nanofibers in scaffolds for tissue engineering applications, *J. Biomed. Mater. Res. Part A* 93A(4) (2010) 1539-1550.
- [9] T.J. Sill, H.A. von Recum, Electro spinning: Applications in drug delivery and tissue engineering, *Biomaterials* 29(13) (2008) 1989-2006.
- [10] G.L. Wang, X.D. Hu, W. Lin, C.C. Dong, H. Wu, Electrospun PLGA-silk fibroin-collagen nanofibrous scaffolds for nerve tissue engineering, *In Vitro Cell. Dev. Biol.-Anim.* 47(3) (2011) 234-240.
- [11] F. Yang, R. Murugan, S. Wang, S. Ramakrishna, Electrospinning of nano/micro scale poly(L-lactic acid) aligned fibers and their potential in neural tissue engineering, *Biomaterials* 26(15) (2005) 2603-2610.
- [12] E.-R. Kenawy, F.I. Abdel-Hay, M.H. El-Newehy, G.E. Wnek, Controlled release of ketoprofen from electrospun poly(vinyl alcohol) nanofibers, *Materials Science and Engineering: A* 459(1-2) (2007) 390-396.
- [13] J.L. Bourke, H.A. Coleman, V. Pham, J.S. Forsythe, H.C. Parkington, Neuronal Electrophysiological Function and Control of Neurite Outgrowth on Electrospun Polymer Nanofibers Are Cell Type Dependent, *Tissue Eng. Part A* 20(5-6) (2014) 1089-1095.
- [14] B. Carlberg, M.Z. Axell, U. Nannmark, J. Liu, H.G. Kuhn, Electrospun polyurethane scaffolds for proliferation and neuronal differentiation of human embryonic stem cells, *Biomed. Mater.* 4(4) (2009) 7.
- [15] G.T. Christopherson, H. Song, H.Q. Mao, The influence of fiber diameter of electrospun substrates on neural stem cell differentiation and proliferation, *Biomaterials* 30(4) (2009) 556-564.

- [16] J.M. Corey, D.Y. Lin, K.B. Mycek, Q. Chen, S. Samuel, E.L. Feldman, D.C. Martin, Aligned electrospun nanofibers specify the direction of dorsal root ganglia neurite growth, *J. Biomed. Mater. Res. Part A* 83A(3) (2007) 636-645.
- [17] G.G. Genchi, G. Ciofani, A. Polini, I. Liakos, D. Iandolo, A. Athanassiou, D. Pisignano, V. Mattoli, A. Menciassi, PC12 neuron-like cell response to electrospun poly (3-hydroxybutyrate) substrates, *J. Tissue Eng. Regen. Med.* 9(2) (2015) 151-161.
- [18] J. Gerardo-Nava, T. Fuhrmann, K. Klinkhammer, N. Seiler, J. Mey, D. Klee, M. Moller, P.D. Dalton, G.A. Brook, Human neural cell interactions with orientated electrospun nanofibers in vitro, *Nanomedicine* 4(1) (2009) 11-30.
- [19] A.N. Koppes, N.W. Zaccor, C.J. Rivet, L.A. Williams, J.M. Piselli, R.J. Gilbert, D.M. Thompson, Neurite outgrowth on electrospun PLLA fibers is enhanced by exogenous electrical stimulation, *J. Neural Eng.* 11(4) (2014) 11.
- [20] X.R. Li, H. Liang, J. Sun, Y. Zhuang, B. Xu, J.W. Dai, Electrospun Collagen Fibers with Spatial Patterning of SDF1 alpha for the Guidance of Neural Stem Cells, *Adv. Healthc. Mater.* 4(12) (2015) 1869-1876.
- [21] Y. Liu, Y. Sun, H. Yan, X. Liu, W. Zhang, Z. Wang, X. Jiang, Electrospun Fiber Template for Replica Molding of Microtopographical Neural Growth Guidance, *Small* 8(5) (2012) 676-681.
- [22] H. Xia, Q. Chen, X. Bo, X. Sun, D. Zhong, Y. Xia, Morphology of rat dorsal root ganglion neurons and Schwann cells cocultured on polymethylmethacrylate electrospun nanofibers with different topographic features, *Journal of Jilin Univeristy. Medicine edition* 42(1) (2016) 1-6.
- [23] H.J. Xia, Q. Chen, Y.X. Fang, D. Liu, D. Zhong, H.T. Wu, Y.Z. Xia, Y. Yan, W.Y. Tang, X.C. Sun, Directed neurite growth of rat dorsal root ganglion neurons and increased colocalization

with Schwann cells on aligned poly(methyl methacrylate) electrospun nanofibers, *Brain Res.* 1565 (2014) 18-27.

[24] R.A. Franco, Y.-K. Min, H.-M. Yang, B.-T. Lee, On Stabilization of PVPA/PVA Electrospun Nanofiber Membrane and Its Effect on Material Properties and Biocompatibility, *Journal of Nanomaterials* 2012 (2012) 9.

[25] M. Mirafteb, A.N. Saifullah, A. Çay, Physical stabilisation of electrospun poly(vinyl alcohol) nanofibres: comparative study on methanol and heat-based crosslinking, *J. Mater. Sci.* 50(4) (2015) 1943-1957.

[26] A.G. Destaye, C.-K. Lin, C.-K. Lee, Glutaraldehyde Vapor Cross-linked Nanofibrous PVA Mat with in Situ Formed Silver Nanoparticles, *ACS Applied Materials & Interfaces* 5(11) (2013) 4745-4752.

[27] Y. Wang, Y.-L. Hsieh, Crosslinking of polyvinyl alcohol (PVA) fibrous membranes with glutaraldehyde and PEG diacylchloride, *Journal of Applied Polymer Science* 116(6) (2010) 3249-3255.

[28] H.S. Mansur, C.M. Sadahira, A.N. Souza, A.A.P. Mansur, FTIR spectroscopy characterization of poly (vinyl alcohol) hydrogel with different hydrolysis degree and chemically crosslinked with glutaraldehyde, *Materials Science and Engineering: C* 28(4) (2008) 539-548.

[29] J. Schindelin, I. Arganda-Carreras, E. Frise, V. Kaynig, M. Longair, T. Pietzsch, S. Preibisch, C. Rueden, S. Saalfeld, B. Schmid, J.-Y. Tinevez, D.J. White, V. Hartenstein, K. Eliceiri, P. Tomancak, A. Cardona, Fiji: an open-source platform for biological-image analysis, *Nat Meth* 9(7) (2012) 676-682.

[30] S.K. Mallapragada, N.A. Peppas, Dissolution mechanism of semicrystalline poly(vinyl alcohol) in water, *Journal of Polymer Science Part B: Polymer Physics* 34(7) (1996) 1339-1346.

- [31] M. Pyda, Polyvinyl Alcohol (PVA) Heat Capacity, Enthalpy, Entropy, Gibbs Energy, 2014. [http://materials.springer.com/polymerthermodynamics/docs/athas\\_0147](http://materials.springer.com/polymerthermodynamics/docs/athas_0147). (Accessed 27-10-2015 2015).
- [32] S. Tungprapa, I. Jangchud, P. Supaphol, Release characteristics of four model drugs from drug-loaded electrospun cellulose acetate fiber mats, *Polymer* 48(17) (2007) 5030-5041.
- [33] P. Taepaiboon, U. Rungsardthong, P. Supaphol, Drug-loaded electrospun mats of poly(vinyl alcohol) fibres and their release characteristics of four model drugs, *Nanotechnology* 17(9) (2006) 2317-2329.
- [34] N. Alexandre, J. Ribeiro, A. Gärtner, T. Pereira, I. Amorim, J. Fragoso, A. Lopes, J. Fernandes, E. Costa, A. Santos-Silva, M. Rodrigues, J.D. Santos, A.C. Maurício, A.L. Luís, Biocompatibility and hemocompatibility of polyvinyl alcohol hydrogel used for vascular grafting—In vitro and in vivo studies, *J. Biomed. Mater. Res. Part A* 102(12) (2014) 4262-4275.
- [35] E. Chiellini, A. Corti, S. D'Antone, R. Solaro, Biodegradation of poly (vinyl alcohol) based materials, *Progress in Polymer Science* 28(6) (2003) 963-1014.
- [36] S.-H. Hyon, W.-I. Cha, Y. Ikada, M. Kita, Y. Ogura, Y. Honda, Poly(vinyl alcohol) hydrogels as soft contact lens material, *Journal of Biomaterials Science, Polymer Edition* 5(5) (1994) 397-406.
- [37] M.I. Baker, S.P. Walsh, Z. Schwartz, B.D. Boyan, A review of polyvinyl alcohol and its uses in cartilage and orthopedic applications, *Journal of Biomedical Materials Research Part B: Applied Biomaterials* 100B(5) (2012) 1451-1457.
- [38] J.W. Xie, X.R. Li, Y.N. Xia, Putting Electrospun Nanofibers to Work for Biomedical Research, *Macromol. Rapid Commun.* 29(22) (2008) 1775-1792.

- [39] S.E. Stabenfeldt, A.J. García, M.C. LaPlaca, Thermoreversible laminin-functionalized hydrogel for neural tissue engineering, *J. Biomed. Mater. Res. Part A* 77A(4) (2006) 718-725.
- [40] T. Subbiah, G.S. Bhat, R.W. Tock, S. Parameswaran, S.S. Ramkumar, Electrospinning of nanofibers, *Journal of Applied Polymer Science* 96(2) (2005) 557-569.
- [41] W.E. Teo, S. Ramakrishna, A review on electrospinning design and nanofibre assemblies, *Nanotechnology* 17(14) (2006) R89.
- [42] Z.-M. Huang, Y.Z. Zhang, M. Kotaki, S. Ramakrishna, A review on polymer nanofibers by electrospinning and their applications in nanocomposites, *Composites Science and Technology* 63(15) (2003) 2223-2253.
- [43] K.E. Strawhecker, E. Manias, Structure and Properties of Poly(vinyl alcohol)/Na<sup>+</sup> Montmorillonite Nanocomposites, *Chemistry of Materials* 12(10) (2000) 2943-2949.
- [44] H.E. Assender, A.H. Windle, Crystallinity in poly(vinyl alcohol). 1. An X-ray diffraction study of atactic PVOH, *Polymer* 39(18) (1998) 4295-4302.
- [45] R. Ricciardi, F. Auriemma, C. De Rosa, F. Lauprêtre, X-ray Diffraction Analysis of Poly(vinyl alcohol) Hydrogels, Obtained by Freezing and Thawing Techniques, *Macromolecules* 37(5) (2004) 1921-1927.
- [46] R.C. Mooney, An X-ray study of the structure of polyvinyl alcohol, *Journal of the American Chemical Society* 63(10) (1941) 2828-2832.
- [47] C. Bunn, Crystal structure of polyvinyl alcohol, *Nature* 161(4102) (1948) 929-930.
- [48] J.D. Hoffman, Thermodynamic driving force in nucleation and growth processes, *The Journal of Chemical Physics* 29(5) (1958) 1192-1193.
- [49] J.D. Hoffman, G.T. Davis, J.I. Lauritzen Jr, The rate of crystallization of linear polymers with chain folding, *Treatise on solid state chemistry*, Springer 1976, pp. 497-614.

- [50] B. Wunderlich, Thermal Analysis Tools, Thermal Analysis of Polymeric Materials, Springer Berlin Heidelberg, Berlin, Heidelberg, 2005, pp. 279-454.
- [51] B. Wunderlich, CHAPTER VIII - Equilibrium Melting, Macromolecular Physics, Academic Press, San Diego, 1980, pp. 1-127.
- [52] B. Wunderlich, CHAPTER IX - Irreversible Melting, Macromolecular Physics, Academic Press, San Diego, 1980, pp. 128-253.
- [53] C.P. Li, T.T. Hou, X.D. She, X.Y. Wei, F.H. She, W.M. Gao, L.X. Kong, Decomposition properties of PVA/graphene composites during melting-crystallization, Polymer Degradation and Stability 119 (2015) 178-189.
- [54] C.P. Li, T.T. Hou, J. Vongsvivut, Y.Z. Li, X.D. She, F.H. She, W.M. Gao, L.X. Kong, Simultaneous crystallization and decomposition of PVA/MMT composites during non-isothermal process, Thermochimica Acta 618 (2015) 26-35.
- [55] D. Thomas, P. Cebe, Self-nucleation and crystallization of polyvinyl alcohol, Journal of Thermal Analysis and Calorimetry 127(1) (2017) 885-894.

## ***Chapter 8 Conclusions and Future Work***

### ***8.1 Conclusions***

The body of research presented in this thesis relies on a combination of conventional thermal and structural analysis techniques and cutting edge fast scanning calorimeters to study the crystallization kinetics and fundamental thermal properties of semicrystalline polymers. With careful sample preparation and experiment design it was possible to probe the crystallization kinetics and fundamental thermal properties of polyvinyl alcohol despite the thermal degradation that sets in at temperatures within its melting range [1-4]. At conventional scanning rates,  $\beta < 0.5$  K/s, the self nucleation behavior of polyvinyl alcohol was studied [4]. This resulted in a measurement of the Domain II – I boundary at 235 °C. This temperature is beyond the melting endotherm foot, where the liquid phase heat capacity baseline is recovered, and is 30 °C below the equilibrium melting point ( $T_m^0 = 265$  °C). Heating PVA to 235 °C at 10 °C/min and holding isothermally for 5 mins erases any melt memory effects. It was interesting to note that the temperature range over which Domain II behavior is observed (exclusive self nucleation) spans 6 °C which is similar to the range reported for other polymers [5], but the shift in the peak crystallization temperature is much smaller. In the case of isotactic polypropylene, self nucleation increased the onset temperature of crystallization by approximately 20 °C [5] compared to the approximate 4 °C increase seen in PVA [4].

In the case of fast scanning rates,  $\beta = 2000$  K/s it was found that melt memory had little to no impact on the crystallization of PVA. Heterogenous nucleation was only observed when crystals remained from incomplete melting (Domain III). This suggests that self nucleation kinetics, which are a special case of heterogenous nucleation, are frozen out at high rates. To the

best knowledge of the author, these experiments are the first measurements of homogenous nucleation in PVA cooled from the melt.

Fast scanning calorimetry experiments utilizing both the Mettler Flash DSC1 and the custom built calorimeter [6] allowed for further investigations into the crystallization kinetics of PVA and fundamental thermal properties which were previously elusive due to the thermal degradation of the material at high temperatures. Sample mass was successfully measured following subtraction of the empty sensor and symmetry correction using the literature values for the glassy phase specific heat capacity of PVA [7]. The thermal stability testing demonstrated that, at scanning rates of 2000 K/s, PVA remains thermally stable when brought into the melt fewer than 5 times. This is an important result as it allows for multiple crystallization conditions to be tested on a single sample, something that is not possible at conventional scanning rates. By demonstrating that the sample does not show any measurable signs of degradation during the first scans it was possible to collect quantitative liquid phase heat capacity measurements.

These experiments resulted in the first degradation free measurements of the following thermal properties of PVA:

1. Temperature dependent liquid phase heat capacity:

$$c_p^{\text{Liquid}}(T) = (0.0024 \pm 0.0007) * T + 1.92 \pm 0.3 \text{ J/(gK)}$$

2. Heat capacity increment of PVA at  $T_g$ :  $\Delta c_p^{\text{amor}}(T_g) = (0.99 \pm 0.02) \text{ J/(gK)}$
3. Critical cooling rate to achieve fully amorphous PVA:  $|\beta_c| = 20,000 \text{ K/s}$
4. Rigid amorphous phase fraction:  $\phi < 5\%$

Because there is no general model for the liquid phase heat capacity of polymers, the measurement of the liquid phase heat capacity using the methods outlined in this thesis will be

useful for any polymer or biopolymer which degrades upon melting, or for those which crystallize rapidly while cooled. Furthermore, these results are relevant to current simulations aimed at modelling polymer crystallization. PVA is used to generate the force fields used in the coarse-graining procedures from fully atomistic simulations [8, 9]. These simulations predict critical cooling rates orders of magnitude greater than the critical cooling rate measured by our experiment. Additionally, it was shown that PVA has little, if any rigid amorphous fraction and can reasonably be treated as a two-phase polymer system. It is interesting to note that PVA has an unusually high heat capacity increment at the glass transition as compared to other poly(vinyl)s [10] which is most likely due to the interactions between hydroxyl groups.

The combination of conventional and fast scanning calorimetry also provided new insights into the crystallinity of PVA nanofibers prepared by electrospinning. It is well known that PVA nanofibers need to be stabilized either by chemical crosslinking [11, 12] or physically stabilizing by crystallization [13]. “As spun” fibers were measured to have an initial mass fraction crystallinity around 10% and readily dissolve in water. Increasing the crystallinity to around 30% was sufficient to prevent dissolution in water at room temperature. Upon heating of the “as spun” PVA fibers, cold crystallization was observed to proceed continuously between the glass transition and onset of melting.

A novel technique was developed for preparing electrospun fibers for chip based fast scanning calorimeters and successfully tested on polyethylene terephthalate nanofibers. Previous attempts to directly electrospin fibers onto chip sensors resulted in inconsistent fiber deposition across the active sensor area, and depending upon the particular polymer being electrospun, fibers often collided with the sensor leads preventing sample to sensor contact. TEM grids provided a

substrate that was both thermally conductive and mechanically durable enough to transfer fibers to the sensors.

Measurements of empty TEM grids at a scanning rate of  $\pm 2000$  K/s showed excellent agreement with literature values for the specific heat capacity of copper. The melting of an indium flake on top of the empty TEM grid was consistent with that of indium placed directly on the sensor indicating that the presence of the relatively heavy grid does not affect the temperature or heat flow accuracy of the sensor. When fiber loaded grids are placed fiber side up it is possible for thermal gradients to develop in the upper layer of fibers. Because of this grids should be loaded fiber side down. Placing the fiber loaded TEM grids face down on the sensor provided excellent sample to sensor contact but had an unexpected result. The interaction between the thermal expansion of the TEM grids and the “tacky” high viscosity liquid polymer resulted in curvature of the heat flow rate signal.

This curvature did not prevent the measurement of the heat capacity increment at the glass transition which was used to determine the fiber mass nor did it prevent the measurement of the melting endotherm area. The crystalline, mobile amorphous, and rigid amorphous fractions for cold crystallized PET nanofibers were measured. Crystalline fractions ranged between 0.24 and 0.39 and rigid amorphous fractions ranged between 0.35 and 0.52 depending upon the cold crystallization temperature. It was found that, for samples with mass less than 5 ng, the semicrystalline glass transition was very near the signal to noise threshold in the signal, preventing an effective measurement of the mobile amorphous fraction.

The melt crystallization experiments performed on the droplets formed by fiber breakup showed that the rigid amorphous fraction appeared before a measurable melting endotherm indicating the presence of nuclei or small crystals throughout the droplets. Contrary to what was

observed in the fibers, the rigid amorphous fraction appeared to be depressed in the droplets. In the droplets crystallinities around 0.30 corresponded to rigid amorphous fractions between 0.10 and 0.20. This is an unexpected result as compared to the bulk where crystallinities of 0.30 will result in more  $RAF > 0.30$ .

## **8.2 Future Work**

The successful development of new methods for obtaining quantitative fast scanning calorimetry [14, 15] data and for the delivery of polymer confined to nanofibers onto chip sensors open new avenues for future studies. Utilizing the empty sensor subtraction and symmetry correction procedures outlined here and in previous works [14, 15] coupled with high accuracy, high precision thermal properties measured by conventional DSC it is possible to measure the liquid phase heat capacity, the enthalpy of fusion, and the crystallization kinetics of polymers which undergo thermal degradation in the melt or have phase change kinetics which cannot be quenched at conventional scanning rates.

Polymer thin films studied by FSC have masses which range between 10 and 50 ng. Assuming an average molecular weight of 100,000 g/mol these samples will contain on the order of 1 to 10 billion molecules. Because typical lamellar thickness is on the order of tens of nanometers, the confinement of polymer to thin films on the order of 1  $\mu\text{m}$  to 10  $\mu\text{m}$ , the nucleation behavior and crystallization kinetics observed during FSC experiments can still shed light on bulk systems. Ongoing experiments on polymers which are widely used throughout industry, particularly polyethylene, nylons, polyvinylidene fluoride, polyesters (polyethylene terephthalate, polybutylene terephthalate, and polytrimethylene terephthalate), and even natural rubbers can improve the material properties of these polymers in the bulk following industrial processing.

Future investigations into biopolymers and composites of synthetic and biopolymers can now include complete measurements of their fundamental thermal properties. This is of particular interest to biomedical applications where materials are designed to have optimal compatibility with living tissues while possessing the excellent mechanical properties of synthetic polymers. Over the past ten years there have been many investigations which rely on synthetic polymers as the carrier for biopolymers which cannot (by themselves) be electrospun to create highly aligned nanofiber mats suitable for tissue scaffolds and meshes for drug delivery [16-19].

The experiments performed on polyvinyl alcohol were limited to one variety of PVA which was 98 mol% hydrolyzed. It is known that the degree of hydrolysis impacts the degradation profile of PVA [1-4]. There is currently no consensus on the impact the degree of hydrolysis of PVA has on the crystallization kinetics or the liquid phase heat capacity. Furthermore, the tacticity of PVA is not well reported for commercially available materials and this could impact both the equilibrium melting point and heat of fusion of the crystals formed [20]. Utilizing the methods outlined in this thesis for FSC on PVA thin films it would be possible to expand the parameter space to various degrees of hydrolysis, molecular weights, and tacticities of PVA to address these open questions.

Investigations into droplet confined crystallization have previously relied on the spinodal formation of droplets on top of substrates [21-23] or by careful encapsulation of crystallizable domains of one polymer inside a matrix [24] of another, immiscible polymer. While these approaches have been successful they are limited in that only a small number of polymeric materials can be investigated. Any polymer which can be electrospun and brought into the melt can be broken into droplets and the crystallization kinetics can be studied under heating and cooling rates spanning several orders of magnitude allowing for the study of polymer which

possess many crystal polymorphs, for example polyvinylidene fluoride for example which has five well known crystal forms.

While it is recommended that fiber loaded grids are placed fiber side down to optimize sample to sensor contact, there are still challenges with this approach that need to be addressed. The main challenge to overcome is the curvature of the heat flow rate signal caused by the interaction between the thermal expansion of the grids during heating. In future experiments, it would be worth investigating the creation of an encapsulation method not unlike the aluminum pans used in conventional DSC. This could be accomplished by direct electrospinning onto gold TEM grids and then placing a layer of gold leaf over the electrospun fibers effectively sandwiching the fibers between two layers of gold. The TEM grids will provide a substrate which is mechanically durable enough to handle, cut, and move the fibers onto the sensor and the gold leaf would prevent the fibers from sticking to the silicon nitride sensor without impeding the sample to sensor contact during experiments. Additionally, gold TEM grids will be easier to cut than copper and could result in a higher success rate in the manual preparation of samples.

Finally, the recent development of *in-situ* X-ray diffraction combined with chip based calorimeters allows for real time structural information to be collected during thermal experiments at scanning rates spanning orders of magnitude [25-27]. This allows for the identification of specific crystal polymorphs within samples, formation of mesophases, and can identify any oriented liquid phase behavior. This technique would be particularly useful when applied to electrospun fibers which can possess aligned crystals that reorganize during heating. As applied to polymer thin films, this would allow experiments to probe any spinodal precursors to homogeneous nucleation and crystallization.

### 8.3 References

- [1] C.P. Li, T.T. Hou, X.D. She, X.Y. Wei, F.H. She, W.M. Gao, L.X. Kong, Decomposition properties of PVA/graphene composites during melting-crystallization, *Polymer Degradation and Stability* 119 (2015) 178-189.
- [2] C.P. Li, J. Vongsvivut, X.D. She, Y.Z. Li, F.H. She, L.X. Kong, New insight into non-isothermal crystallization of PVA-graphene composites, *Physical Chemistry Chemical Physics* 16(40) (2014) 22145-22158.
- [3] C.P. Li, T.T. Hou, J. Vongsvivut, Y.Z. Li, X.D. She, F.H. She, W.M. Gao, L.X. Kong, Simultaneous crystallization and decomposition of PVA/MMT composites during non-isothermal process, *Thermochimica Acta* 618 (2015) 26-35.
- [4] D. Thomas, P. Cebe, Self-nucleation and crystallization of polyvinyl alcohol, *Journal of Thermal Analysis and Calorimetry* 127(1) (2017) 885-894.
- [5] B. Fillon, J.C. Wittmann, B. Lotz, A. Thierry, Self-Nucleation and Recrystallization of Isotactic Polypropylene (Alpha-Phase) Investigated by Differential Scanning Calorimetry *Journal of Polymer Science Part B-Polymer Physics* 31(10) (1993) 1383-1393.
- [6] E. Zhuravlev, C. Schick, Fast scanning power compensated differential scanning nano-calorimeter: 1. The device, *Thermochimica Acta* 505(1-2) (2010) 1-13.
- [7] M. Pyda, Polyvinyl Alcohol (PVA) Heat Capacity, Enthalpy, Entropy, Gibbs Energy, 2014. [http://materials.springer.com/polymerthermodynamics/docs/athas\\_0147](http://materials.springer.com/polymerthermodynamics/docs/athas_0147). (Accessed 27-10-2015 2015).

- [8] C. Luo, M. Kröger, J.-U. Sommer, Molecular dynamics simulations of polymer crystallization under confinement: Entanglement effect, *Polymer* 109 (2017) 71-84.
- [9] H. Meyer, F. Müller-Plathe, Formation of chain-folded structures in supercooled polymer melts, *The Journal of Chemical Physics* 115(17) (2001) 7807-7810.
- [10] B. Wunderlich, Study of the Change in Specific Heat of Monomeric and Polymeric Glasses During the Glass Transition, *J. Phys. Chem.* 64(8) (1960) 1052-1056.
- [11] Y. Wang, Y.-L. Hsieh, Crosslinking of polyvinyl alcohol (PVA) fibrous membranes with glutaraldehyde and PEG diacylchloride, *Journal of Applied Polymer Science* 116(6) (2010) 3249-3255.
- [12] A.G. Destaye, C.-K. Lin, C.-K. Lee, Glutaraldehyde Vapor Cross-linked Nanofibrous PVA Mat with in Situ Formed Silver Nanoparticles, *ACS Applied Materials & Interfaces* 5(11) (2013) 4745-4752.
- [13] R.A. Franco, Y.-K. Min, H.-M. Yang, B.-T. Lee, On Stabilization of PVPA/PVA Electrospun Nanofiber Membrane and Its Effect on Material Properties and Biocompatibility, *Journal of Nanomaterials* 2012 (2012) 9.
- [14] P. Cebe, B.P. Partlow, D.L. Kaplan, A. Wurm, E. Zhuravlev, C. Schick, Using flash DSC for determining the liquid state heat capacity of silk fibroin, *Thermochimica Acta* 615 (2015) 8-14.
- [15] P. Cebe, B.P. Partlow, D.L. Kaplan, A. Wurm, E. Zhuravlev, C. Schick, Fast Scanning Calorimetry of Silk Fibroin Protein: Sample Mass and Specific Heat Capacity Determination, in: C. Schick, V. Mathot (Eds.), *Fast Scanning Calorimetry*, Springer International Publishing, Cham, 2016, pp. 187-203.

- [16] Y. Zhou, D. Yang, X. Chen, Q. Xu, F. Lu, J. Nie, Electrospun Water-Soluble Carboxyethyl Chitosan/Poly(vinyl alcohol) Nanofibrous Membrane as Potential Wound Dressing for Skin Regeneration, *Biomacromolecules* 9(1) (2008) 349-354.
- [17] C. Huang, R. Chen, Q.F. Ke, Y. Morsi, K.H. Zhang, X.M. Mo, Electrospun collagen-chitosan-TPU nanofibrous scaffolds for tissue engineered tubular grafts, *Colloid Surf. B-Biointerfaces* 82(2) (2011) 307-315.
- [18] S.N. Alhosseini, F. Moztaarzadeh, M. Mozafari, S. Asgari, M. Dodel, A. Samadikuchaksaraei, S. Kargozar, N. Jalali, Synthesis and characterization of electrospun polyvinyl alcohol nanofibrous scaffolds modified by blending with chitosan for neural tissue engineering, *Int. J. Nanomed.* 7 (2012) 25-34.
- [19] L. Binan, C. Tendey, G. De Crescenzo, R. El Ayoubi, A. Ajji, M. Jolicoeur, Differentiation of neuronal stem cells into motor neurons using electrospun poly-L-lactic acid/gelatin scaffold, *Biomaterials* 35(2) (2014) 664-674.
- [20] R. Endo, S. Amiya, M. Hikosaka, Conditions for Melt Crystallization Without Thermal Degradation and Equilibrium Melting Temperature of Atactic Poly(Vinyl Alcohol), *Journal of Macromolecular Science, Part B* 42(3-4) (2003) 793-820.
- [21] M.V. Massa, J.L. Carvalho, K. Dalnoki-Veress, Confinement Effects in Polymer Crystal Nucleation from the Bulk to Few-Chain Systems, *Physical Review Letters* 97(24) (2006) 247802.
- [22] M.V. Massa, J.L. Carvalho, K. Dalnoki-Veress, Direct visualisation of homogeneous and heterogeneous crystallisation in an ensemble of confined domains of poly(ethylene oxide), *The European Physical Journal E* 12(1) (2003) 111-117.

- [23] M.V. Massa, K. Dalnoki-Veress, Homogeneous Crystallization of Poly(Ethylene Oxide) Confined to Droplets: The Dependence of the Crystal Nucleation Rate on Length Scale and Temperature, *Physical Review Letters* 92(25) (2004) 255509.
- [24] G. Zhong, K. Wang, L. Zhang, Z.-M. Li, H. Fong, L. Zhu, Nanodroplet formation and exclusive homogeneously nucleated crystallization in confined electrospun immiscible polymer blend fibers of polystyrene and poly(ethylene oxide), *Polymer* 52(24) (2011) 5397-5402.
- [25] M. Rosenthal, D. Doblas, J.J. Hernandez, Y.I. Odarchenko, M. Burghammer, E. Di Cola, D. Spitzer, A. Antipov, L. Aldoshin, D.A. Ivanov, High-resolution thermal imaging with a combination of nano-focus X-ray diffraction and ultra-fast chip calorimetry, *Journal of synchrotron radiation* 21(1) (2014) 223-228.
- [26] M. van Drongelen, T. Meijer-Vissers, D. Cavallo, G. Portale, G.V. Poel, R. Androsch, Microfocus wide-angle X-ray scattering of polymers crystallized in a fast scanning chip calorimeter, *Thermochimica acta* 563 (2013) 33-37.
- [27] K. Xiao, J.M. Gregoire, P.J. McCluskey, D. Dale, J.J. Vlassak, Scanning AC nanocalorimetry combined with in-situ x-ray diffraction, *Journal of Applied Physics* 113(24) (2013) 243501.

## ***Appendix A      Thermal Characterization of Thermotropic Nematic Liquid-Crystalline Elastomers***

This appendix is based on the following publication of the same name:

D. Thomas, M. Cardarelli, A. Sánchez-Ferrer, B.L. Mbanga, T.J. Atherton, P. Cebe, Thermal characterisation of thermotropic nematic liquid-crystalline elastomers, *Liquid Crystals* 43(1) (2016) 112-123.

### **Abstract**

Nematic Liquid-Crystalline Elastomers (LCEs) are weakly crosslinked polymeric networks that exhibit rubber elasticity and liquid-crystalline orientational order due to the presence of mesogenic groups. Three end-on side-chain nematic LCEs were investigated using real-time synchrotron wide-angle X-ray scattering (WAXS), differential scanning calorimetry (DSC), and thermogravimetry (TG) to correlate thermal behavior with structural and chemical differences among them. The elastomers differed in crosslinking density and mesogen composition. Thermally reversible glass transition temperature,  $T_g$ , and nematic-to-isotropic transition temperature,  $T_{ni}$ , were observed upon heating and cooling for all samples. By varying the heating rate,  $T_g^0$  and  $T_{ni}^0$  were determined at zero heating rate. The temperature dependence of the orientational order parameter was determined from the anisotropic azimuthal angular distribution of the equatorial reflection seen during real-time WAXS experiments. Our results show that the choice of crosslinking unit, its shape, density, as well as the structure of co-monomers, all influence the temperature range over which the thermal transitions take place. Including multi-ring aromatic groups as crosslinkers increased the effective stiffness of the crosslinking resulting in a higher glass transition temperature. The nematic-to-isotropic transition temperature increased with the presence of multi-ring aromatic structures, as either crosslinkers or mesogens, particularly when

the multi-ring structures were larger than the low molar-mass mesogen common to all three samples.

## **INTRODUCTION**

Liquid-crystalline elastomers (LCEs) are highly versatile materials with unique properties arising from the coupling of the rubber-like elasticity and the liquid-crystalline phase. As a result of this coupling, mechanical deformations result in changes to the local orientational order of the mesogens. The reverse transitions also occur: the response of the mesogens to stimuli such as heat, electric fields, or light, can result in a mechanical response [1-3]. These materials are formed with mesogenic units embedded in a weakly crosslinked polymer network either as part of the polymer backbone (main chain) or as side groups branching off the polymer backbone (side chain) [2,3]. This combined effect allows these materials to withstand very large strains and shear deformations [3,4].

The particular samples discussed in this paper belong to the subset of LCEs known as thermotropic nematic side-chain liquid-crystalline elastomers (SCLCEs). SCLCEs contain mesogens as pendant side groups off the main polymer backbones which form a weakly crosslinked network [1]. When the density of cross-links is low, as is the case here, the mesogens will arrange into liquid-crystalline mesophases. Because the system is thermotropic, the mesogens undergo temperature dependent phase transition from the nematic to isotropic phase at a temperature that depends not only on the particular mesogen but also on the cross-linking density [5].

By selecting appropriate functional groups for the mesogens and the crosslinkers, it is possible to create different materials that mechanically respond to heat, light, magnetic or electric

fields. This has led to the creation of SCLCEs for applications including mechanically tunable optical systems, forming small actuators or generators, and creating new types of displays [6-22]. In recent years many SCLCEs have been synthesized with azobenzene structures as crosslinkers and/or mesogens which has led to materials with coupled opto-mechanical properties [6-13,22]. These azobenzene compounds respond to light by undergoing a reversible *trans*→*cis* photoisomerization where they become bent-shape, lowering the nematic order and changing the mechanical response of the material [7]. In their relaxed *trans*-state, the azobenzene molecules act as rigid rod-like molecules that contribute to the overall nematic order in the same manner as any other mesogen. Azobenzene-dyed materials have been shown to act as optically controlled actuators [6-22] which have been used to make micropumps and valves [20], show great potential in creating artificial muscles [13-16], and are candidates for creating haptic displays [9,17].

The thermal properties of various azobenzene-dyed thermotropic SCLCEs have been studied by wide angle X-ray scattering (WAXS), differential scanning calorimetry (DSC), and polarizing optical microscopy (POM) [8,11,17-20]. In this paper we investigated a series of three SCLCEs with azobenzene groups present in various concentrations, as both mesogens and crosslinkers, which had been synthesized to investigate their opto-mechanical responses [9-11,22]. The nematic-to-isotropic transition is partially first order in these systems and the specific temperature and temperature range over which the transition occurs depends upon the chemical composition of the elastomer, the concentration and chemical structures of the crosslinkers and mesogens present. The response observed in DSC is known to be broader and more diffuse for elastomeric systems. This arises due to the quenching of sites of random disorder induced by the crosslinks which serve to broaden the thermal transitions [17,18].

In addition to a basic mesogen and crosslinker, the three SCLCEs discussed in this paper contained varied azobenzene crosslinkers and azobenzene mesogens. For two of the three samples, the total concentration of crosslinks and mesogenic units was fixed; in the third sample, the overall crosslinking density was reduced. We used real-time synchrotron X-ray scattering experiments during heating, and temperature modulated DSC, to characterize how these structural variations led to the differences in both thermal properties and mesogenic ordering.

## EXPERIMENTAL SECTION

### *Materials*

The three samples selected for this study are nematic end-on side-chain LCEs, called SCE03, SCE14, and SCE17, which were synthesized at the Institute for Macromolecular Chemistry, Albert Ludwigs University, Freiburg, Germany. Details of the synthesis are available in the literature [9-12]. **Figure A1** shows the chemical structures of these materials. Samples were prepared with varying mesogenic pendant groups and crosslinkers. The materials comprise the mesogen, 4-methoxyphenyl 4-(but-3-en-1-yloxy)benzoate (M4OMe [17,19], MPBB) [11]; the isotropic crosslinker, 1,4-bis(undec-10-en-1-yloxy)benzene (SCC) [11]; and the flexible polymer backbone, poly(methylhydrogensiloxane) (PMHS) [11]. The samples also include azobenzene molecules which are the crosslinker in SCE03 and SCE14, and the co-monomer in SCE17. The SCE03 elastomer contained 5.6 mol-% of two-aromatic ring azobenzene crosslinker, Azo2-c [11]; 5.6 mol-% of the isotropic crosslinker SCC; and 88.9 mol-% of MPBB, exclusive of the polymer backbone. The second sample, SCE14 contained 5.3 mol-% of four-aromatic ring azobenzene crosslinker, Azo4-c [11]; no isotropic crosslinker SCC; and 94.7 mol-% of MPBB. The third sample, SCE17, contained 11.1 mol-% isotropic crosslinker SCC; 5.6 mol-% of four-aromatic

rings azobenzene mesogen Azo4-p [11]; and 83.3 mol-% of MPBB, exclusive of the polymer backbone. Both SCE03 and SCE17 had the same total mol-% of crosslinker and the same total mol-% of mesogenic units, however the specific chemistry of these two components varied [9-11].

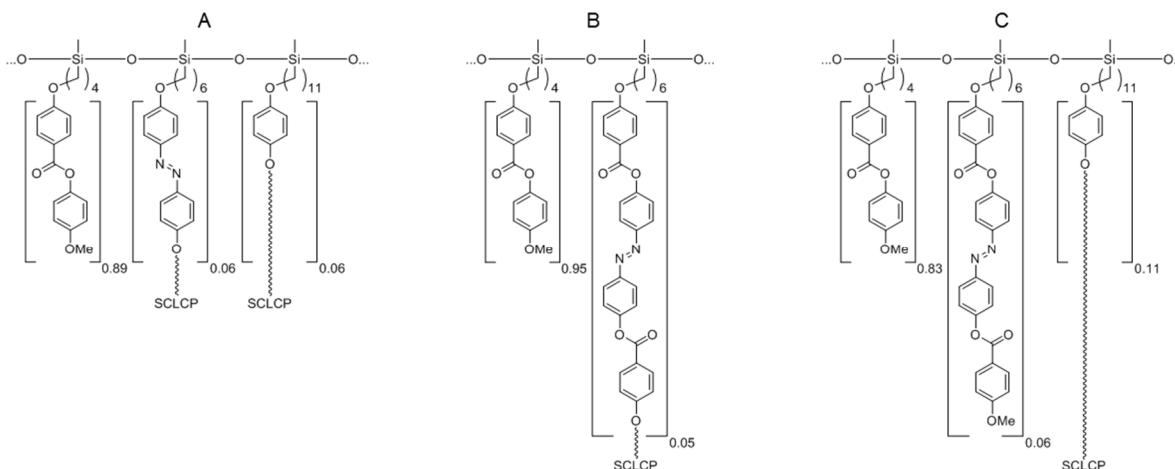


**Figure A1** Chemical composition for SCLCE samples; a) SCE03, b) SCE14, and c) SCE17. Values in brackets next to each pendant group refer to the concentration in mol-%.

### Thermal Analysis

To determine the thermal stability of the LCEs, thermogravimetry (TG) experiments were performed on a TA Instruments Q500 series thermogravimetric analyzer from 30 °C to 800 °C at a heating rate of 20 °C·min<sup>-1</sup>, under nitrogen gas flow at a rate of 50 mL·min<sup>-1</sup>.

Both differential scanning calorimetry (DSC) and its temperature modulated variant (TMDSC) were performed on a TA Instruments Q100 series DSC equipped with a TA Instruments Refrigerated Cooling System. Small amounts (approximately 2-5 mg) of each sample were sealed in standard aluminum DSC pan. The pans were first rinsed in methanol to remove any oils that could have been deposited due to manufacturing and handling. Standard DSC runs were performed on each sample: six heating and cooling cycles were performed at different rates over the temperature range from -50 to 130 °C, with the exception of SCE14 which spanned the range from

-50 to 150 °C. All three samples were brought through the temperature range at 2, 5, 10, 15, 20, and 25 °C·min<sup>-1</sup>. The sample masses for the standard DSC experiments were about 5 mg. One TMDSC cycle was performed for each sample with lighter masses of approximately 2 mg at a heating and cooling rate of 5 °C·min<sup>-1</sup> with temperature modulation amplitude of +/- 0.796 °C and a period of 60 s. The DSC cell was purged with nitrogen at a flow rate of 50 mL·min<sup>-1</sup>. The cell was calibrated for temperature and heat flow accuracy using indium standard, and for heat capacity using sapphire standard. Analysis of the TG and DSC data was performed using TA Instruments Universal Analysis 2000 and MATLAB<sup>TM</sup> (from Mathworks).

### *Synchrotron Wide-Angle X-ray Scattering*

Real-time synchrotron wide-angle X-ray scattering (WAXS) experiments were performed on beam line X27C at the Brookhaven National Laboratory's National Synchrotron Light Source NSLS-I. A Mettler Toledo FP82HT hot stage paired with a Mettler Toledo FP90 Central Processor was used to control the heating and cooling of the samples. The LCE samples were mounted in the hot stage under 1 layer of Kapton<sup>TM</sup> high temperature tape and aligned such that the nematic director was approximately horizontal. Aligned samples were heated to 130 °C and held isothermally for 15 min, then cooled at a rate of 3 °C·min<sup>-1</sup> to 50 °C. The samples equilibrated at 50 °C for approximately 2 min, and subsequently were heated from 50 °C to 130 °C at a rate of 3 °C·min<sup>-1</sup>, held at 130 °C for approximately 2 min, and then cooled to 50 °C at a rate of 3 °C·min<sup>-1</sup>. Finally, the samples were heated once again to 130 °C at a rate of 3 °C·min<sup>-1</sup>. Real-time data were collected at approximately 2 frames per minute with 23.5 seconds of exposure time per frame. Temperature and upstream (incident) intensity were recorded periodically on MAR CCD 165 detector while frames were collected continuously for each heating and cooling event. The

isothermal hold and first controlled cooling and reheating were performed to rejuvenate the samples and remove any biases from the handling of the samples while being mounted in the hot stage.

The X-ray wavelength was  $\lambda = 0.1371$  nm and the sample to detector distance was 15.94 cm. The scattering vector,  $q$  (where  $q = 4\pi\sin\theta/\lambda$  for  $\theta$  the half-scattering angle) was calibrated using Al<sub>2</sub>O<sub>3</sub> standard reference powder. Intensity was corrected for Kapton<sup>TM</sup> background.

## RESULTS AND DISCUSSION

### *Thermal Analysis*

TG was performed to determine the upper limit stability temperature of SCE03, SCE14, and SCE17. As shown in **Figure A2a**, both samples were thermally stable up to moderately high temperatures, around 175 °C. SCE03 proved to be slightly more tolerant of high temperatures retaining at least 97% of its weight until 400 °C. Between 185 and 225 °C a small amount of mass is lost (about 2%). SCE14 and SCE17 showed a similar initial drop in mass above 188 and 175 °C, respectively, and then remained stable before rapidly losing mass at temperatures in excess of 400 °C. The degradation temperatures,  $T_{d1}$  and  $T_{d2}$ , are listed in **Table A1** below and correspond to the point where the % mass remaining first begins to decrease. The upper limit temperatures for DSC studies on SCE03, SCE14, and SCE17 were set at 200 °C, 150 °C, and 130 °C, respectively.

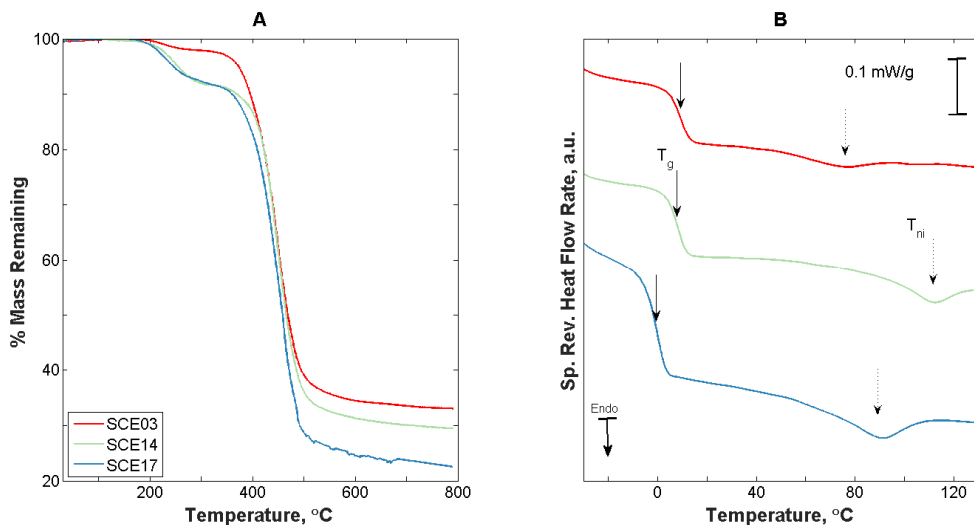


**Figure A2** Thermal data for SCE03 (red), SCE14 (green) SCE17 (blue) during heating. A) TG curve showing mass remaining vs. temperature, at a heating rate of  $20\text{ }^{\circ}\text{C}\cdot\text{min}^{-1}$ . B) Specific reversing heat flow rate at a heating rate of  $5\text{ }^{\circ}\text{C}\cdot\text{min}^{-1}$ . Arrows mark the approximate locations of  $T_g$  (solid arrow) and  $T_{ni}$  (dashed arrow). The curves have been displaced vertically for clarity.

We performed TMDSC experiments to determine the glass transition temperature,  $T_g$ ; the heat capacity increment,  $\Delta C_p$ , evaluated at the glass transition; and  $T_{ni}$ , the nematic-to-isotropic transition temperature (often referred to as the clearing temperature,  $T_c$ ). Results are shown in **Figure A2b** and **Table A1**.

**Table A1** Thermal properties of SCLCEs: degradation temperatures  $T_d$ , glass transition  $T_g$ , heat capacity increment  $\Delta C_p$ , nematic-to-isotropic transition temperature  $T_{ni}$ , and latent heat  $L^0$ .

|       | $T_{d1}$ (°C) <sup>a</sup> | $T_{d2}$ (°C) <sup>a</sup> | $T_g^0$ (°C) <sup>b</sup> | $\Delta C_p$ (J·g <sup>-1</sup> °C <sup>-1</sup> ) <sup>c</sup> | $T_{ni}^0$ (°C) <sup>d</sup> | $L^0$ (J·g <sup>-1</sup> ) <sup>e</sup> |
|-------|----------------------------|----------------------------|---------------------------|---|------------------------------|---|
|       | ± 1 °C                     | ± 1 °C                     | ± 0.7 °C                  | ± 0.06 (Jg <sup>-1</sup> °C <sup>-1</sup> )                     |                              | ± 0.1 (Jg <sup>-1</sup> )               |
| SCE03 | 185                        | 310                        | 8.6                       | 0.35  | 85 ± 1                       | 1.3                                     |
| SCE14 | 188                        | 320                        | 7.7                       | 0.41  | 121 ± 2                      | 1.4                                     |
| SCE17 | 175                        | 360                        | -0.3                      | 0.46  | 103 ± 1                      | 1.9                                     |

<sup>a</sup> Determined from the peak of the derivative of TGA curve at 20 °C·min<sup>-1</sup>.

<sup>b</sup> Determined from the inflection point of the DSC curve extrapolated to a heating rate of 0 °C·min<sup>-1</sup>.

<sup>c</sup> Determined from the difference between the extrapolated tangents to the glass and liquid-crystalline states, evaluated at  $T_g$  from the reversing heat flow curve at 5 °C·min<sup>-1</sup>.

<sup>d</sup> Determined from last departure point of the endothermic peak in the DSC curve from the liquid state baseline, extrapolated to a heating rate of 0 °C·min<sup>-1</sup>.

<sup>e</sup> Determined from the area of the endothermic peak in the DSC curve extrapolated to a heating rate of 0 °C·min<sup>-1</sup>.

To allow scanning at rates faster than those available with temperature modulated DSC, a series of standard (non-modulated) DSC scans were performed between -50 and 130 °C (-50 and 150 °C for SCE14) at heating rates from 2 to 25 °C·min<sup>-1</sup> (**Figure A3**).

Transition temperatures,  $T_g$  and  $T_{ni}$ , are shown as functions of heating rate in **Figures A4a** and **A4b**, respectively.  $T_g$  was determined from the inflection point, and  $T_{ni}$  from the local minima which for a first order phase transition appears as a small endothermic peak at higher temperature than  $T_g$ . At the slowest heating rate,  $T_{ni}$  was not distinguishable from the noise level.  $T_{ni}$  was determined from the endpoint temperature, *i.e.*, from the first departure point of the endothermic peak from the heat flow baseline following the nematic-to-isotropic transition. The latent heat was determined by integration of the endotherm.

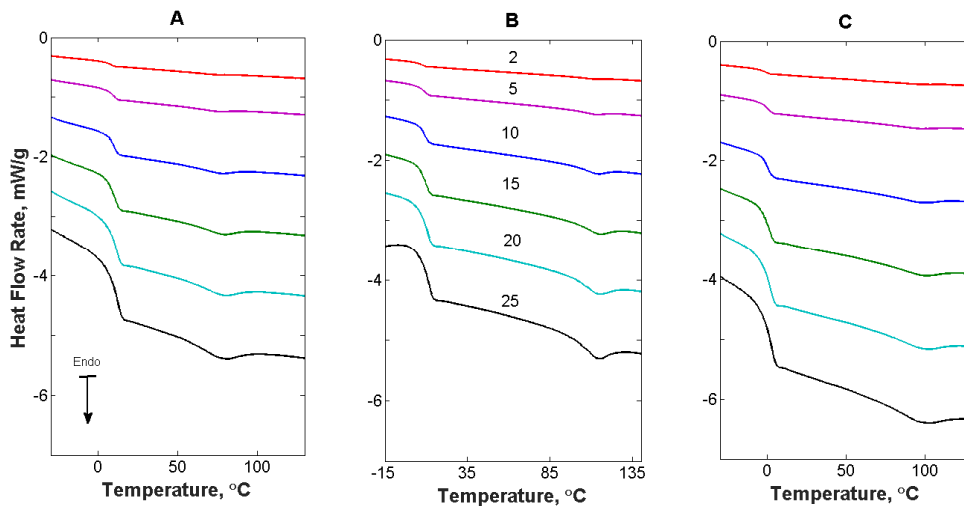


**Figure A3** DSC curves at various heating rates for: A) SCE03; B) SCE14; and, C) SCE17. From top to bottom the heating rates are: 2 (red), 5 (purple), 10 (blue), 15 (green), 20 (cyan), and 25 (black)  $^{\circ}\text{C}\cdot\text{min}^{-1}$ .

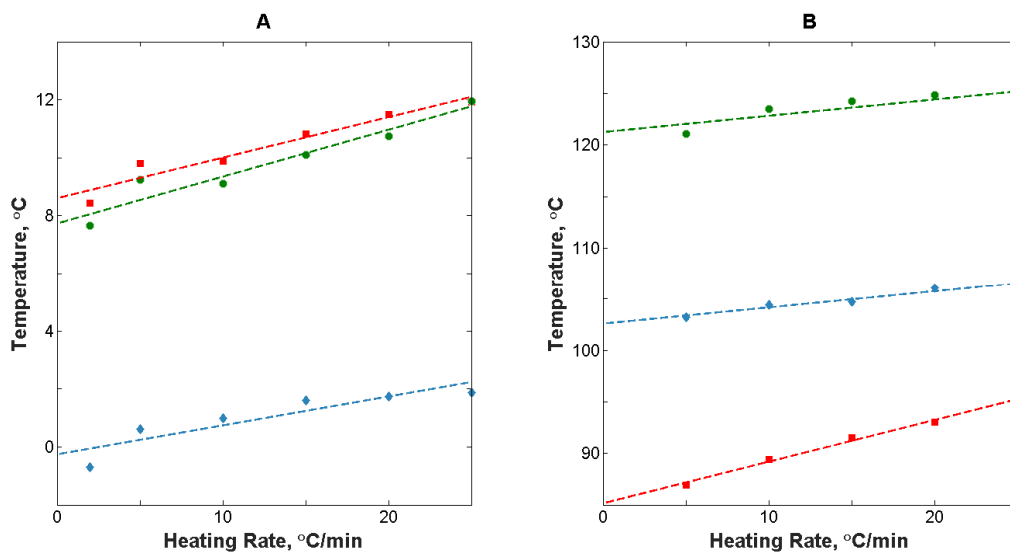


**Figure A4** Thermal properties vs. heating rate for SCE03 (red squares), SCE14 (green circles), and SCE17 (blue diamonds). A) Glass transition temperature,  $T_g$ ; B) Nematic-to-isotropic transition temperature,  $T_{ni}$ . Dashed lines represent best linear fits to the data.

Extrapolation of the data in **Figure A4** (shown by the dashed lines), allows us to determine  $T_g^0$  and  $T_{ni}^0$ , the values of these parameters at zero heating rate. We found  $T_g^0 = 8.6$   $^{\circ}\text{C}$  (SCE03),

$T_g^0 = 7.7\text{ }^\circ\text{C}$  (SCE14), and  $T_g^0 = -0.3\text{ }^\circ\text{C}$  (SCE17). The values of the nematic-to-isotropic transition were determined to be  $T_{ni}^0 = 85\text{ }^\circ\text{C}$  (SCE03),  $T_{ni}^0 = 121\text{ }^\circ\text{C}$  (SCE14), and  $T_{ni}^0 = 103\text{ }^\circ\text{C}$  (SCE17).

The glass transition temperature measured for SCE03 and SCE17 differ from the value of  $-2.0\text{ }^\circ\text{C}$  reported in the literature. The nematic-to-isotropic transitions were reported to occur at  $85\text{ }^\circ\text{C}$  and  $97\text{ }^\circ\text{C}$  for SCE03 and SCE17, respectively [11]. SCE14 was reported to have a glass transition temperature of  $6.0\text{ }^\circ\text{C}$  and a nematic-to-isotropic transition of  $113\text{ }^\circ\text{C}$  [12]. Following long storage periods all samples showed signs of aging that only disappeared after heating and annealing above the nematic-to-isotropic transition temperature. The differences between the previously reported values for both the glass and nematic-to-isotropic transitions can be attributed to both differences in thermal analysis methods, as well as the differences in chemical structure differences (*e.g.*, possible transesterification above  $120\text{ }^\circ\text{C}$ ) at the time of measurement.

There were two main differences between these SCLCEs: the type of crosslinker and the type of mesogen. SCE14 and SCE17 each only had one type of crosslinker, the rigid azo4-c and the isotropic and flexible crosslinker SCC, respectively, as described in the literature [9-12]. SCE03 possessed not only the isotropic crosslinker SCC but also a less rigid azo2-c crosslinker [9-12]. The azobenzene crosslinkers can be regarded as molecularly ‘stiffer’ than the isotropic crosslinker SCC. The azo2-c crosslinker is a smaller and less rigid molecule than the big and rigid azo4-c. Regarding the mesogen type, SCE03 and SCE14 only possessed one mesogen, MPBB, whereas SCE17 has a blend of both MPBB and the azo4-p mesogen as described in the literature [9-12]. These differences in molecular composition are reflected in the thermograms and transition temperatures.

A divergence of our polymeric materials from the expected behavior of a low molar-mass thermotropic liquid crystal can be seen in **Figure A2**. In low molar-mass thermotropic liquid

crystals, the phase change from an ordered, *i.e.*, nematic, to a disordered isotropic state happens over a few degrees with a distinct endothermic peak at the transition temperature [28]. Embedding the mesogens in a weakly crosslinked polymer network significantly broadens the transition, due in part to polydispersity and chain conformation, causing the endothermic peaks to span a temperature interval of about ten degrees at low rates and up to forty at higher rates in the polymeric systems.

### *Synchrotron Wide-Angle X-ray Scattering*

X-ray scattering provides complementary insight as to how the mesogen and crosslinker composition of these elastomers give rise to the specific thermal properties observed in DSC. The real-time WAXS data allow for the characterization of the molecular ordering present in the material as a function of temperature. The observed scattering pattern of all LCEs appears as two distinct meridional lobes (a typical intensity pattern is shown in **Figure A5a** for SCE17) when the elastomer is in the nematic phase.

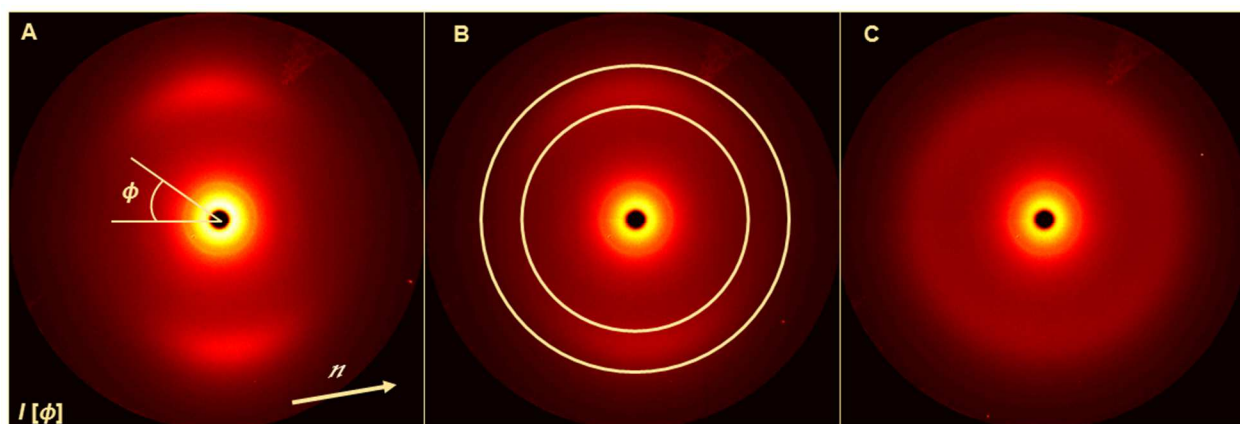


**Figure A5** 2D WAXS intensity profile of SCE17 at different temperatures: A) 53.6 °C, in the nematic phase; B) 84.3 °C, at the inflection point of the nematic-to-isotropic transition; C) 129.6 °C, in the isotropic phase. The yellow arrow in (A) indicates the nematic director. The yellow circles in (B) define the annulus used in radial integration of the azimuthal intensity distribution. (The irregular intensity seen in the upper right quadrant at about the one-o'clock position arises from a flaw in the detector.)

The intensity in these lobes spreads into diffuse arcs as the elastomer begins its transition into the isotropic phase (**Figure A5b**). Following the phase change, as the amount of orientational order is reduced (**Figure A5c**), the intensity distribution appears as a ring, which is typical for an isotropic sample. We note that the azimuthal intensity distribution, measured at a fixed radius from the center of reciprocal space, is always largest on the meridian. Taking intensity **Figure A6** presents normalized WAXS intensity distributions obtained along the radial direction through the centers of the meridional lobes for the three samples. While intensity is observed over a greater range of azimuthal angles as the samples are heated, the locations of the intensity maxima remain between  $2\theta = 15^\circ$ - $18^\circ$ .

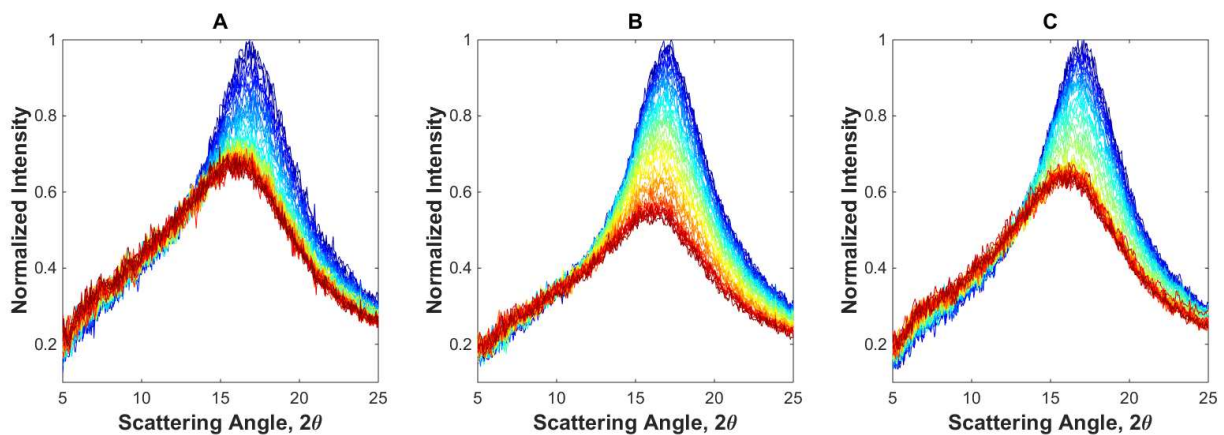


**Figure A6** Normalized 1D WAXS radial intensity distributions for: A) SCE03, B) SCE14, and C) SCE17. Color scale indicates the relative temperature of the samples, with the blue curves representing the low temperature limit at 50 °C, and the red curves representing the high temperature limit at 130 °C.

Common to all three samples is the decrease in overall intensity and shift of the  $2\theta$  peak position as the samples are heated. This is indicative of thermal expansion effects, polymer backbone chain conformational changes, and disordering of the mesogens upon heating. Both the

mesogen-to-mesogen spacing and the backbone spacing were obtained from the scattering angle profiles for each sample in the nematic phase at 50 °C, at the inflection point in the nematic-to-isotropic transition curves shown in **Figure A9**, and in the isotropic phase at 130 °C (**Table A2**). As the samples are heated, the polymer backbone conformation changes toward a more random coil chain conformation as depicted in **Figure A7**. The conformational change of the backbone results in a disordering of the mesogens which drives the system from the nematic to the isotropic phase.

**Table A2** WAXS  $d$ -spacing ( $\pm 0.01$  nm) for polymer backbone ( $d_{pb}$ ) and mesogens ( $d_m$ ) at different temperatures.

|       | $T$ ( $^{\circ}\text{C}$ ) <sup>a</sup> | $d_m$ (nm) | $d_{pb}$ (nm) | $T$ ( $^{\circ}\text{C}$ ) <sup>b</sup> | $d_m$ (nm) | $d_{pb}$ (nm) | $T$ ( $^{\circ}\text{C}$ ) <sup>c</sup> | $d_m$ (nm) | $d_{pb}$ (nm) |
|-------|---|------------|---------------|---|------------|---------------|---|------------|---------------|
| SCE03 | 50                                      | 0.44       | 0.8           | 72.0                                    | 0.45       | 0.8           | 130                                     | 0.45       | 0.8           |
| SCE14 | 50                                      | 0.44       | 0.8           | 109.5                                   | 0.45       | 0.8           | 130                                     | 0.45       | 0.8           |
| SCE17 | 50                                      | 0.44       | 0.8           | 91.6                                    | 0.45       | 0.8           | 130                                     | 0.46       | 0.8           |

<sup>a</sup> – nematic state; <sup>b</sup> - at the inflection point of nematic-to-isotropic transition; <sup>c</sup> – isotropic state

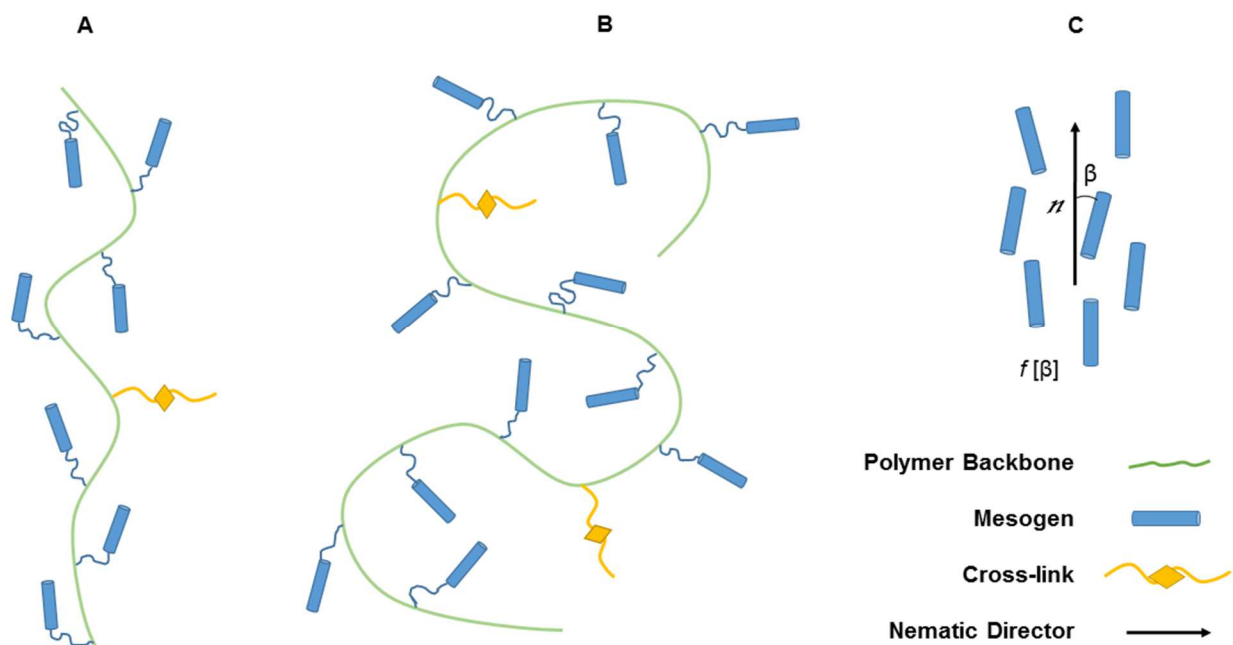


**Figure A7** Schematic of the polymer backbone and pendant mesogens. A) At low temperatures in the nematic phase, the mesogens are aligned parallel to the polymer backbone; B) At high temperatures in the isotropic phase, mesogens are randomly oriented and the polymer backbone adopts a more random coil conformation; C) The distribution of mesogen orientations, represented by angle  $\beta$ , with respect to the nematic director,  $n$ , shown by an arrow.

**Figure A5** shows the WAXS scattering patterns of SCE17 as it is brought from the nematic to the isotropic phase. The nematic scattering pattern (**Figure A5a**) results from mesogens being well ordered parallel to the polymer backbone as shown in **Figure A7a**. As the mesogens become disordered by heating, the X-rays are no longer scattered into two distinct meridional lobes; rather, they are scattered along diffuse arcs (**Figure A5b**) until the material is in the isotropic state (**Figure**

**A5c)** in which the mesogens have random alignment and no longer remain predominantly parallel to the polymer backbone in the conformation shown in **Figure A7b**.

The scattering patterns in **Figure A5** are dependent upon the average orientations of the mesogens (and the mesogen-like crosslinkers which contribute to the molecular ordering). As the temperature increases, the mesogens become disordered, causing X-rays to be scattered through a greater range of azimuthal angles. The radii at which scattered intensity is observed were fixed for each sample to lie between 11 and 22.5 degrees in  $2\theta$ . Radial integration over a circular annulus (Figure 5b) was performed using Matlab<sup>TM</sup>, to generate the intensity profile as a function of azimuthal angle, **Figure A8**. In order to quantify the degree to which these samples are ordered as a function of temperature it is necessary to convert the intensity profile to a description of the molecular orientations of the mesogens. Mitchell and Lovell [30,31], and Leadbetter and Norris [32] have considered the problem of describing the mesogen orientation. They demonstrated a relationship between the intensity profile and the orientational distribution function (ODF),  $f[\beta]$ . The ODF describes how the distribution of the alignment of mesogens with respect to the director  $n$  gives rise to the scattering patterns seen in **Figure A5**.

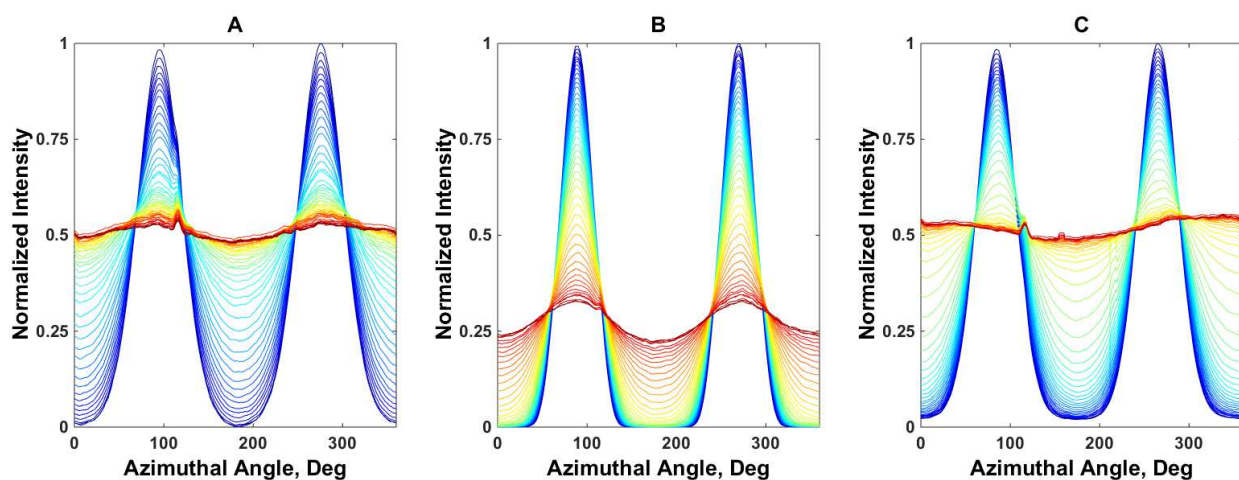


**Figure A8** WAXS azimuthal intensity profiles during heating for: A) SCE03, B) SCE14, and C) SCE17. Color scale represents the temperature of the samples, with the blue curves representing

the low temperature, nematic phase at 50 °C, and the red curves representing high temperature up to 130 °C. The tiny spike at around  $\phi = 120^\circ$  is an artifact from a defect on the CCD detector.

Based on the work done by Leadbetter and Norris [32], Davidson *et al.* [34] demonstrated that the ODF can be expressed as a series of  $\cos^{2n}(\phi)$  functions:

$$f[\beta] = \sum_{n=0}^{\infty} f_{2n} \text{Cos}^{2n}[\beta] \quad (1)$$

where  $n$  is an integer. The coefficients for the  $\cos^{2n}(\phi)$  functions,  $f_{2n}$ , can be calculated directly by fitting the intensity profiles in Figure 6 to the following equation [34]:

$$I[\phi] = \sum_{n=0}^{\infty} f_{2n} \frac{2^{2n} n!}{(2n+1)!!} \text{Cos}^{2n}[\phi] \quad (2)$$

The ODF allows for direct calculation of the scalar order parameter,  $S$ , as shown below in equations 3 and 4. The scalar order parameter is given by the average of the ODF over the second Legendre polynomial. This quantity can vary from -0.5 to 1 with a value of -0.5 corresponding to a perfectly ordered oblate crystalline phase (oblate or perpendicular order), a value of zero corresponding to randomly oriented mesogens in the isotropic phase, and a value of unity corresponding to a perfectly prolate crystalline phase (prolate or parallel order).

$$\langle \text{Cos}^2[\beta] \rangle = \frac{\int_0^{\pi} f[\beta] \text{Cos}^2[\beta] \text{Sin}[\beta] d\beta}{\int_0^{\pi} f[\beta] \text{Sin}[\beta] d\beta} \quad (3)$$

$$S = \frac{1}{2} (3 \langle \text{Cos}^2[\beta] \rangle - 1) \quad (4)$$

The order parameters in the nematic phase were obtained by averaging over the values from two data sets at the lower bound temperature of 50 °C. The order parameters at the lower bound temperature for SCE03, SCE14, and SCE17 were 0.47, 0.77, and 0.62, respectively. The variation of the order parameter with temperature is shown in **Figure 9**.

SCE14 has a high order parameter in the nematic phase at room temperature. Such large values are typically indicative of a smectic mesophase, as has been observed, for example, in siloxane based liquid crystalline elastomers [41-43]. Evidence for a smectic mesophases in these elastomers was obtained using small angle X-ray scattering (SAXS) and typical smectic layer spacings were reported to be between 4.5 and 4.9 nm [41-43]. In addition to our WAXS experiments, we also performed synchrotron SAXS studies on the three LCEs reported herein using a sample-to-detector distance of 1836.8 mm. We observed no scattering in the small angle intensity patterns in the q-vector range corresponding to spacings from 1.595 nm to 7.974 nm. In the WAXS scattering patterns for SCE14, we observed only the meridional lobes shown in Figure 5, which correspond to orientational order and mesogen-mesogen periodicity. The SAXS and WAXS results taken together confirm that our LCE samples are all in the nematic phase at room temperature.

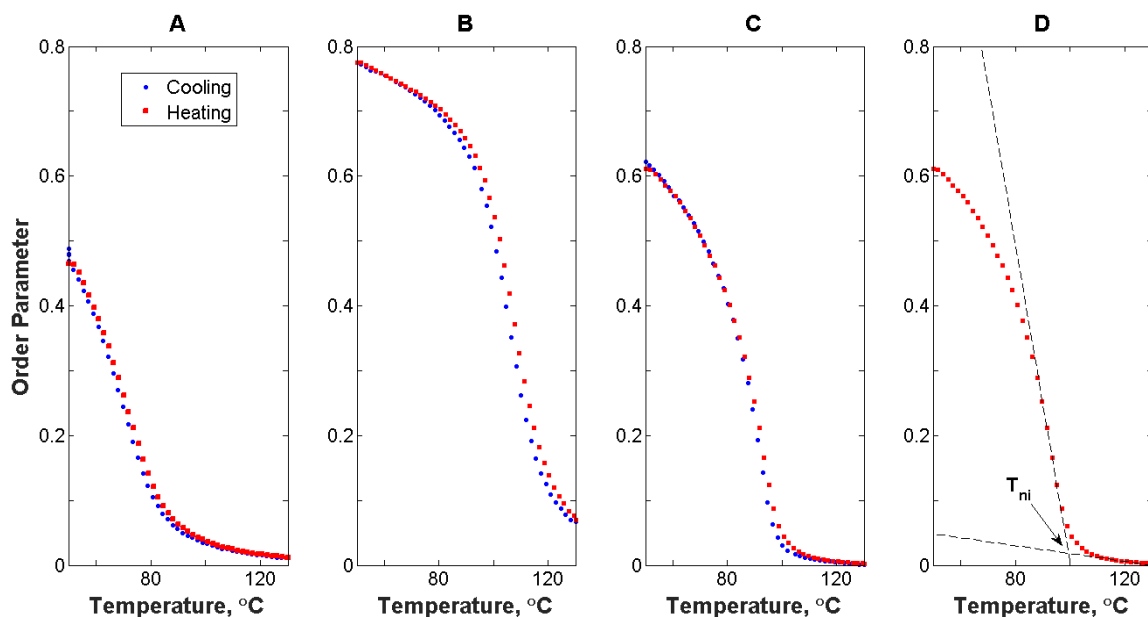


**Figure A9** Order parameter,  $S$ , as a function of temperature for SCLCEs upon cooling (blue) and heating (red) between 50 °C and 130 °C: A) SCE03; B) SCE14; C) SCE17; D) SCE17 at 50 °C and an example of the extrapolation method used to determine the nematic-to-isotropic transition temperature.

Comparing the DSC data of **Figure A2b** and **Figure A3**, with the order parameter data of **Figure A9**, there is a broadening of the nematic-to-isotropic transition resulting from the mesogens embedded in the lightly crosslinked polymer network. For a low molecular weight nematic liquid crystal, the nematic-to-isotropic transition would be sharper [1, 37-39, 42]. Transition breadth reflects the local variation in bonding environment. If most of the mesogens are embedded in a similar local environment, the transition will be sharper. If the local bonding environment varies, as would likely be the case with mesogens embedded in the polymer network, then the transition will be broadened. The order parameter vs. temperature curves in **Figure A9** also lack the characteristic discontinuity or sharp change in slope as the sample enters the isotropic phase [1, 37-39]. The lack of a sharp discontinuity at the nematic-to-isotropic transition as observed in conventional liquid crystals has received attention in recent work relying on NMR measurements [44-48]. This work, on thermotropic liquid crystal elastomers, used NMR [44-48] to study residual orientational ordering that was present following departure from the nematic mesophase upon heating [44-48]. Orientational order parameters obtained from NMR measurements show the same continuous behavior as observed in WAXS measurements.

During the two-step crosslinking procedure [4], these elastomers reported here are crosslinked in the nematic, aligned phase. As the mesogens are disordered and the backbone reorganizes into a more random coil conformation an internal stress field drives the nematic-to-isotropic transition into a supercritical regime, or a paranematic phase where the values of the order parameter are small but non zero [44,45]. As a result, the order parameter vs. temperature curve is continuous as the system transitions from the nematic phase to its final isotropic phase. The effect

of this supercritical regime is minimal and the overall transition manifests as a first order phase transition as there is a latent heat associated with the departure from the nematic phase.

In the order parameter vs. temperature plots, the nematic-to-isotropic transition was identified using the intersection between two tangents to the curve shown in **Figure A9d**. The first tangent line runs through the inflection point in the order parameter vs. temperature curve and the second tangent tracks the isotropic baseline following the supercritical range as the order parameter values decrease toward zero. These data points can be compared to the thermally determined transition temperatures identified at the endpoint of the endothermic peak by interpolating the data in **Figure A4b** to a heat rate of  $3\text{ }^{\circ}\text{C}\cdot\text{min}^{-1}$ . The values obtained by this interpolation are in good agreement with those obtained at the intersection of tangents in the order parameter data. The transition temperatures determined by WAXS for cooling and heating and the interpolated values are recorded in **Table A3**.

**Table A3** Nematic-to-isotropic transition temperature  $T_{\text{ni}}$  and average order parameter  $S$  in the nematic phase at  $50\text{ }^{\circ}\text{C}$ .

|       | $T_{\text{ni}}\text{ (}^{\circ}\text{C)} \pm 1\text{ }^{\circ}\text{C}$<br>Cooling <sup>a</sup> | $T_{\text{ni}}\text{ (}^{\circ}\text{C)} \pm 1\text{ }^{\circ}\text{C}$<br>Heating <sup>a</sup> | $S$<br>$\pm 0.1$ | $T_{\text{ni}}\text{ (}^{\circ}\text{C)} \pm 2\text{ }^{\circ}\text{C}$<br>Heating <sup>b</sup> |
|-------|---|---|------------------|---|
| SCE03 | 85  | 86  | 0.5              | 86  |
| SCE14 | 120   | 123   | 0.8              | 122   |
| SCE17 | 98  | 99  | 0.6              | 103   |

<sup>a</sup> Determined from the order parameter vs. temperature curves for heating and cooling rates of  $3\text{ }^{\circ}\text{C}\cdot\text{min}^{-1}$  obtained by WAXS experiment.

<sup>b</sup> Interpolated nematic-to-isotropic transition temperatures for a heating rate of  $3\text{ }^{\circ}\text{C}\cdot\text{min}^{-1}$  obtained by DSC experiments.

SCE03 contained one mesogen, MPBB, and a mixture of two crosslinkers, the isotropic crosslinker SCC and a mesogenic crosslinker. The mesogenic crosslinker in this sample was a two ring azobenzene molecule, azo2-c, similar in size to the MPBB mesogen. The addition of this

azobenzene crosslinker created a polymer network ‘stiffer’ than a network with the same crosslinking concentration made of purely isotropic linkages. This resulted in the highest glass transition temperature observed in the three samples. While the azobenzene crosslinker contributes to the nematic ordering of the mesogens, it does not have as high a nematic-to-isotropic transition, and does not bring the transition temperature to the range of SCE14 or SCE17 as the mesogens and azobenzene groups are of similar size. As seen in **Figure A3b** the nematic-to-isotropic transition endotherm begins just after 50 °C and this can be seen in **Figure A9a** as the order is sharply decreasing between 50 and 70 °C.

SCE17 has the same total mesogen and crosslinking concentration as SCE03. This sample only possesses the isotropic crosslinker SCC resulting in a less ‘rigid’ polymer network with the lowest glass transition temperature of the three samples. From **Figure A9c**, it can be seen that this sample is more ordered than SCE03 while exhibiting a behavior similar to that of a low molar-mass liquid crystal. This is due to the presence of the four-ring azobenzene mesogens azo4-p intermixed with the MPBB throughout the sample along with minimal constraint from the isotropic crosslinker. The larger mesogen stabilizes the nematic phase requiring both a higher temperature to induce the phase transition to an isotropic liquid but also requires more energy per unit mass than either of the other samples (see **Table A1**). Further evidence of the effect of larger mesogenic structures being added to the network can be seen in the change in heat capacity at the glass transition. The heat capacity increment is the largest for this sample as it has the greatest concentration of four aromatic rings of all three samples which become free to rotate and move once out of the vitreous state.

SCE14 differed from the other two samples in that it had less than half the total crosslinking concentration. Despite having the lowest concentration of crosslinker, the four ring azobenzene

structure was the most 'rigid' crosslinker azo4-c present among the samples. **Figure A4a** illustrates this, as SCE14 has a glass transition temperature similar to SCE03. Similar to SCE17, the heat capacity increment at the glass transition is higher than that of SCE03 due to the presence of the four aromatic rings core. These 'rigid' crosslinker serve to stabilize the nematic phase to high temperatures. This results in the most ordered nematic phase as seen in **Figure A9b**.

## Conclusions

The SCLCEs studied here varied in three constituent parameters: mesogen type, crosslinker type, and component concentration. Chemical structure differences affected the temperature ranges over which each sample underwent the glass-to-rubber and nematic-to-isotropic transitions. In order to observe the glass transition process, the polymer molecular chain must undergo changes in conformation brought about by free rotation about chemical bonds in the molecular chain, either in the backbone or in the side groups. The glass transition of the SCLCE materials studied here showed dependence on the density and rigidity of the crosslinker molecules present. Both SCE03 and SCE17 had more than double the concentration of crosslinkers compared to SCE14. However, SCE14 exhibited a higher glass transition temperature than SCE17. This can be attributed to the four aromatic ring azobenzene structure, which comprised the crosslinker in SCE14, and which was substantially more rigid than the isotropic crosslinker in SCE17. SCE03 possessed both the isotropic crosslinker and a two aromatic ring azobenzene crosslinker which resulted in the highest glass transition temperature.

The nematic-to-isotropic liquid crystal phase transition is a first order phase transition, which requires a latent heat.  $T_{ni}$  showed dependence on both the mesogen and crosslinker selection. The crosslinkers present in SCE03 and SCE14 (two and four ring azobenzene structures,

respectively) contributed to the liquid-crystalline order of the material in the nematic liquid state. However, the two ring azobenzene present in SCE03 did not impact the ordering to the same degree as the four ring azobenzene structures present in SCE14 and SCE17. The four ring azobenzene structures are effectively twice the length of the mesogen, MPBB, present in all three SCLCEs. The addition of these larger molecules results in a higher nematic-to-isotropic transition. In the case of SCE14 the four ring azobenzene is present as the crosslinker but behaves also as a mesogen insofar as it contributes to the nematic ordering of the system. It is observed that while SCE14 had the highest nematic-to-isotropic transition, due to the ordering contribution of the mesogenic crosslinker, the latent heat of this phase change was very close to that of SCE03. SCE17 possesses a mixture of two mesogens and required the greatest amount of energy per unit mass to undergo the nematic-to-isotropic phase change. These results suggest that the latent heat will vary with the mesogen concentration and type, while the transition temperature will be affected by the ordering contributions of mesogenic crosslinkers.

These novel SCLC elastomers synthesized with the addition of various azobenzene molecules acting as either mesogenic units or crosslinkers afford the system the ability to undergo conformational changes in response to polarized light [9-12, 33]. Understanding how their bulk thermal properties and structural transitions are affected by the selection of azobenzene groups, it becomes possible to create responsive materials that have favorable thermal characteristics for industrial applications.

## **Acknowledgements**

Support for this research was provided in part, by the National Science Foundation, Polymers Program of the Division of Materials Research, under DMR-1206010, and through the

MRI Program under DMR-0520655 which provided thermal analysis instrumentation. A portion of this research was conducted at the Brookhaven National Synchrotron Light Source, beam line X27C, supported by the Department of Energy. The authors thank Dr. Lixia Rong and Dr. Maya K. Endoh (Koga) for assistance with X-ray experiments.

## References

1. Warner M, Terentjev E M. Liquid Crystal Elastomers. Clarendon: Oxford; 2007
2. Davis F. Liquid-crystalline elastomers. *J. Mater. Chem.* 1993;3:551-562
3. Terentjev E M. Liquid-crystalline elastomers. *J. Phys; Condens. Matter.* 1999; 11:R239-257
4. K pfer J, Finkelmann H. Nematic liquid single crystal elastomers. *Macromol. Chem., Rapid Commun.* 1991; 12:717-726
5. Dubois J C, Le Barny P, M. Mauzac, Noel C. Behavior and properties of side chain thermotropic liquid crystal polymers. *Acta Polymer*, 1997; 48:47-87
6. Finkelmann H, Nishikawa E, Pereira G G, Warner M. A New Opto-Mechanical Effect in Solids. *Phys. Rev. Lett.* 2001; 87:015501
7. Yu Y, Nakano M, Ikeda T. Directed bending of a polymer film by light. *Nature.* 2003; 425:145
8. Domenici V, Ambrozi  G,  opi  M, Lebar A, Dreven ek-Olenik I, Umek P, Zalar B, Zupan i  B,  igon M. Interplay between nematic ordering and theromechanical response in a side-chain liquid single crystal elastomer containing pendant azomesogen units. *Polymer*, 2009; 50:4837-4844

9. Sánchez-Ferrer A. Light-induced disorder in liquid-crystalline elastomers for actuation, Proc. SPIE 8107, Nano-Opto-Mechanical Systems (NOMS), 810702
10. Sánchez-Ferrer A, Fischl T, Stubenrauch M, Wurmus H, Hoffman M, Finkelmann H. Photo-Crosslinked Side-Chain Liquid Crystalline Elastomers for Microsystems. Macromol. Chem. Phys. 2009; 210:1671-1677
11. Sánchez-Ferrer A, Merkalov A, Finkelmann H. Opto-Mechanical Effect in Photoactive Nematic Side-Chain Liquid-Crystalline Elastomers. Macromol. Rapid Commun. 2011; 32:671-678
12. Sánchez-Ferrer A. Photoactive Liquid-Crystalline Elastomers [dissertation]. Barcelona (ES): University of Barcelona; Freiburg (DE): University of Freiburg; 2007
13. Camacho-Lopez M, Finkelmann H, Palfy-muhoray P, Shelley M. Fast liquid-crystal elastomer swims into the dark. Nature Mater. 2004; 3:307-310
14. Thomsen D L III, Keller P, Naciri J, Pink T, Jeon H, Shenoy D, Ratna B R. Liquid Crystal Elastomers with Mechanical Properties of a Muscle. Macromol. 2001; 34:5868-5875
15. Madden J, Vandesteeg N, Anquetil P A, Madden P G A, Takshi A, Pytel R Z, Lafontaine S R, Wieringa P A, Hunter I W. Artificial Muscle Technology: Physical Principles and Naval Prospects. IEEE J. Oceanic Eng. 2004; 29:706-728
16. Buguim A, Li M, Silberzan P, Ladoux B, Keller P. Micro-Actuators: When Artificial Muscles Made of Nematic Liquid Crystal Elastomers Meet Soft Lithography. J. Am. Chem. Soc. 2006; 128:1088-1089
17. Torras N, Zinoviev K, Esteve J, Sánchez-Ferrer A. Liquid-crystalline elastomer micropillar array for haptic actuation. J. Mater. Chem. C. 2013; 1:5183-5190

18. Selinger J V, Ratna B R. Isotropic-nematic transition in liquid-crystalline elastomers: Lattice model with quenched disorder. *Phys. Rev. E.* 2004; 70: 041707
19. Garcia-Amoros J, Finkelmann H, Velasco D. Influence of the photo-active azo cross-linker spacer on the opto-mechanics of polysiloxane elastomer actuators. *J. Mater. Chem.* 2011; 21:1094-1101
20. Garcia-Amoros J, Velasco D. Understanding the fast thermal isomerization of azophenols in glass and liquid crystalline polymers. *Phys. Chem. Chem. Phys.* 2014; 16:39-52
21. Tajbakhsh A R, Terentjev E M. Spontaneous thermal expansion of nematic elastomers, *Eur. Phys. J. E.* 2001; 6:181-188
22. Sánchez-Ferrer A, Fischl T, Stubenrauch M, Albrecht A, Wurmus H, Hoffmann M, Finkelmann H. Liquid-Crystalline Elastomer Microvalve for Microfluidics. *Adv. Mater.* 2011; 23:4526–4530
23. Sánchez-Ferrer A, Finkelmann H. Opto-mechanical effect in photoactive nematic main-chain liquid-crystalline elastomers. *Soft Matter.* 2013; 9:4621–4627
24. Jeong H M, Kim B K, Choi Y J. Synthesis and properties of thermotropic liquid crystalline polyurethane elastomers. *Polymer.* 2000; 41:1849-1855
25. Li X, Fang L, Hou L, Zhu L, Zhang Y, Zhang B, Zhang H. Photoresponsive side-chain liquid crystalline polymers with amide group-substituted azobenzene mesogens: effects of hydrogen bonding, flexible spacers, and terminal tails. *Soft Matter.* 2012; 8:5532-5542
26. *Properties and Behavior of Polymers.* Wiley: Hoboken, 2011
27. Neuenfeld S, Schick C. Verifying the symmetry of differential scanning calorimeters concerning heating and cooling using liquid crystal secondary temperature standards. *Thermochemica Acta.* 2006; 446:55-65

28. Oweimreen G A, Morsy M A. DSC studies on p-(n-alkyl)-p'-cyanobiphenyl (RCB's) and p-(n-alkoxy)-p'-cyanobiphenyl (ROCB's) liquid crystals. *Thermo. Acta.* 2000; 346:37-47
29. Deutsch M. Orientational order determination in liquid crystals by X-ray diffraction, *Phys. Rev. A.* 1991; 4:8264-8270
30. Lovell R, Mitchell G R. Molecular orientation distribution derived from an arbitrary reflection. *Acta Cryst.* 1981; 37:135-137
31. Mitchell G R, Lovell R. Application of Cylindrical Distribution Functions to Wide-Angle X-ray Scattering from Oriented Polymers. *Acta Cryst.* 1981; 37:189-196
32. Leadbetter A J, Norris E K. Distribution functions in three liquid crystals from X-ray diffraction measurements. *Mol. Phys.* 1979; 38:669-686
33. Leadbetter A J, Wrighton P G. Order Parameters in  $S_A$ ,  $S_C$  and N phases by X-Ray Diffraction, *Journal de Physique.* 1979; 40:234-242
34. Davidson P, Petermann D, Levelut A M. The Measurement of the Nematic Order Parameter by X-ray Scattering Reconsidered. *J. Phys. II France.* 1995; 5:113-131
35. Giesselmann F, Germer R, Saipa A. Orientational order in smectic liquid-crystalline phases of amphiphilic diols. *J. Chem. Phys.* 2005; 123:034906
36. Sanchez-Castillo A, Osipov M A, Giesselmann F. Orientational order parameters in liquid crystals: A comparative study of X-ray diffraction and polarized Raman spectroscopy results. *Phys. Rev. E.* 2010; 81:021707
37. Sengupta A. Topological Microfluidics: Nematic Liquid Crystals and Nematic Colloids in Microfluidic Environment. Springer; 2013

38. Kurochkin O, Atkuri H, Buchnev O, Glushchenko A, Grabar O, Karapinar R, Reshetnyak V, West J, Reznikov Y. Nano-colloids of Sn<sub>2</sub>P<sub>2</sub>S<sub>6</sub> in Nematic Liquid Crystal Pentyl-cyanobiphenile, *Condensed Matter Physics*. 2010; 13:33701
39. Quan L. *Liquid Crystals Beyond Displays*. John Wiley & Sons: Hoboken; 2012
40. Tašič B, Li W, Sánchez-Ferrer A, Čopič M, Drevenšek-Olenik I. Light-Induced Refractive Index Modulation in Photoactive Liquid-Crystalline Elastomers. *Macromol. Chem. Phys.* 2013; 214:2744–2751
41. Aksenov V, Bläsing J, Stannarius R, Rössle M, Zentel R. Strain-induced compression of smectic layers in free-standing liquid crystalline elastomer films. *Liq. Cryst.* 2005; 32:805-813
42. Rössle M, Braun L, Schollmeyer D, Zentel R. Differences between smectic homo- and co-polysiloxanes as a consequence of microphase separation. *Liq. Cryst.* 2005; 35:533-538
43. Ahn S, Deshmukh P, Gopinadhan M, Osuji C O, Kasi R M. Side-Chain Liquid Crystalline Polymer Networks: Exploiting Nanoscale Smectic Polymorphism To Design Shape-Memory Polymers. *ACS Nano*. 2011; 5:3085-3095
44. Selinger J V, Jeon H G, Ratna B R. Isotropic-Nematic Transition in Liquid-Crystalline Elastomers. *Phys. Rev. Lett.* 2002; 89:225701
45. Lebar A, Kutnjak Z, Zumer S, Finkelmann H, Sánchez-Ferrer A, Zalar B. Evidence of Supercritical Behavior in Liquid Single Crystal Elastomers. *PRL*. 2005; 94:197801

46. Domenici V.  $^2\text{H}$  NMR studies of liquid crystal elastomers: Macroscopic vs. molecular properties. *Prog. Nucl. Magn. Reson. Spectrosc.* 2012; 63:1-32
47. Cifelli M, Domenici V, Veracini C A. Recent advancements in understanding thermotropic liquid crystal structure and dynamics by means of NMR spectroscopy. *Curr. Opin. Colloid Interface Sci.* 2013; 18: 190-200
48. Domenici V, Milavec J, Zupančič B, Bubnov A, Hamplova V, Zalar B. Brief overview on  $^2\text{H}$  NMR studies of polysiloxane-based side-chain nematic elastomers. *Magn. Reson. Chem.* 2014; 52:649-655

## ***Appendix B          MATLAB Code***

All MATLAB code will be copied to directories on the main (C:/) drives of the shared lab computers in addition to backups stored with the hard copy of this thesis work in the lab file cabinets.

### ***B.1    FSC Unpack***

```
function varnameout = FSCunpack_2016(data)

% FSC Unpack handles the separation of curves as exported from the Mettler
% Toledo STARE software. Data exported in arrays(Index,Abcissa,Ts,Value)
%
% Note from Peggy (see notebook 4) - the code works well to a point but the
% curve data gets flipped in the process.
%
% ----- CHECK PRIOR TO DATA IMPORT -----
%
% 1)    It is important that curves are prepared for
%       export by selecting the 'open apart' and the isothermal segments
%       are deselected prior to export from STARE to a .txt file.
%
% 2)    Make sure the following boxes are selected under 'Settings' ->
%       'Print/Export Settings' in the STARE software:
%            Curve Name, Curve Values, Curve Sample Temp., Curve Time/
%            Abcissa, Results, Sample
%
% 3)    Ensure that the data is exported to within the working path within
%       your MATLAB file directory.

Index = data(:,1);
Abcissa = data(:,2);
Ts = data(:,3);
Value = data(:,4);

segments = find(Index==0); % Find the indices where each new curve begins

% Index runs from zero to some finite value, each time it hits zero a new
% temperature ramp has begun. Data will be segmented from a given index to
% the next index in 'segments'-1.

l = length(segments); % This will ultimately be the number of heating and
cooling curves stored in the struct

% The struct will contain nx4 {index,abcissa,Ts,Value} for each of the
% curves created

varname = cell(1,1); % Creates an empty cell array with indices for each
individual curve
```

```

for i = 1:l-1
    varname{i,1}={Index(segments(i):segments(i+1)-
1),Abscissa(segments(i):segments(i+1)-1),Ts(segments(i):segments(i+1)-
1),Value(segments(i):segments(i+1)-1)};
end
varname{1,1} =
{Index(segments(1):end),Abscissa(segments(1):end),Ts(segments(1):end),Value(s
egments(1):end)};

for i = 1:l
    varname{i,1}= cell2mat(varname{i,1});
end
% The first command inside the loop will create three cells inside the cell
% at index i. The second command contracts the three cells at index i into
% an Nx3 matrix containing the Temperature, Heatflow Value, and the
% Abscissa. The end result is a cell array containing individually callable
% matrices for each segment of the FSC experiment.

% Data contained in the vectors Ts, Value, and Abscissa can contain NaN or
% regions where the data is not monotonic. This loop will pull any row
% which contains a NaN element in any of the three columns contained within
% the matrix.

for i = 1:length(varname) % Looping over the length of the cell array
    vi = varname{i};
    nans = isnan(vi);
    for j = 1:length(vi(:,1)) % Looping over the length of Nx3 array to check
for NaN entries in either Ts, Value, or Abscissa
        if any(isnan(vi(j,:)))
            nans(j,:)=true;
        end
    end
    vi(nans)=[];
    vi = reshape(vi,[numel(vi)/4,4]); % The logical operations above flatten
the Nx3 array into a 1xN*3 vector, this fixes that
    varname{i}=vi;

% Data returned is an array of cells containing Nx3 matrices with Ts,
% Value, and Abscissa as the first, second, and third columns respectively.

varnamesub = flip(varname);
varnameout = varnamesub;

% Mettler STARe software exports the data with the curves running from the
% last collected curved down to the first collected curve, this last
% commands flips the data set so that the data appears in chronological
% order.

End

```

## ***B.2 Single Cool – Heat FSC Pair Analysis***

```

function [s,final] = PVAmeltpair_new(firstpairin,sensor)
% Created: 2017-01-10
% Author: Dave

```

```

%
% ** Backwards Euler Method w(T) determination modified from the program
% written by Qian Ma "QianMa_Crystvs.T.m"
%
% ----- Stuff to Keep Working On -----
%   Date: 2017-01-13
% *a*   Add in a user prompt with the option to extrapolate apparent heat
%       flow prior to sensor subtraction and symmetry correction for the
%       case of curves obscured by noise at the isotherm to heat rate
%       onset.
%
% *b*   This code works only on pair data and all outputs are as such, if
%       time allows (or necessary) overhaul the code to handle stacks of
%       data. (1/19 - this can be done using 'size' in stead of 'length')
%
% *c*   Finish the Temperature Dependent Crystallinity portion
%
% *d*   Finish the peak integration segments of the code
%
% *e*   Add in more general functionality, prompt to input specific thermal
%       properties and filepath/ filename of ATHAS data (application to
%       other polymers)
%
% ----- Input Structure -----
%
% First iteration of this code designed for the 4 step melt loop program
% run in November 2016 - mpin needs to be a 4x1 cell array. Row 1 is the
% initial melt of the sample as prepared, Row 2 is the first cooling from
% the melt (controlled at 2000 K/s), Row 3 is the melting of the controlled
% cooling, and Row 4 is the final controlled cooling. Rows 2 and 3 are the
% cool - melt pair used to determine all relevant parameters. When
% importing 2015 data toss in dummy rows for 1 and 4. Sensor needs to be
% cool - heat on the empty sensor.
%
% ----- Output summary -----
% final: 1 = heat flow, 2 = specific heat flow, 3 = heat capacity, 4 =
% specific heat capacity s: a struct containing the symmetry line as a fit
% object, the rotation matrix (if user elects to rotate the data), mass(T)
% for rotated and unroated, the average mass
%

figure(1);clf
figure(2);clf
figure(3);clf

mpsub = cell(4,1);

if length(firstpairin) == 2
    mpsub{1,1} = [];
    mpsub{2,1} = firstpairin{1,1};
    mpsub{3,1} = firstpairin{2,1};
    mpsub{4,1} = [];
    mpin = mpsub;
else
    mpin = firstpairin;

```

```
end
```

```
lit = importdata('athas_PVA.txt'); % Experimental PVA specific heat capacity
from the ATHAS database
molwt = 44.0526; % Ethanol monomer unit, NIST value g/mol
hf0w = 7.11; % kJ/mol
hf = 161.4; % Heat of Fusion in J/g
Tm0 = 265; % Equilibrium Melting Point in Celsius from ATHAS
%labdata = importdata('lab_PVA.txt');
```

```
% Find regions where sensor and melt pair of interest are monotonic and
% interpolate all data to share the common x-axis of the melt heating
```

```
temp = [];
for i = 1:length(mpin{2})-1
    temp(i,1) = mpin{2}(i,3)-mpin{2}(i+1,3);
end
for i = 1:length(mpin[1])-1
    temp(i,2) = mpin[1](i,3)-mpin[1](i+1,3);
end
for i = 1:length(sensor[1])-1
    temp(i,3) = sensor[1](i,3)-sensor[1](i+1,3);
end
for i = 1:length(sensor{2})-1
    temp(i,4) = sensor{2}(i,3)-sensor{2}(i+1,3);
end
```

```
% Limits on find set by the heating or cooling rate
```

```
datarangec = find(temp(:,1) > .15);
datarangeh = find(temp(:,2) < -.19); % increments good only for 2000 K/s
sensorc = find(temp(:,3) > .15);
sensorh = find(temp(:,4) < -.19);
temp = [];
```

```
% Setting the common x-axis to be the temperature values of the sample
% melting scan
```

```
crunch{1,1}(:,1:3) = mpin[1](datarangeh,1:3);
crunch{2,1} = mpin[1](datarangeh,:);
x = mpin[1](datarangeh,3);
s.col123 = crunch{1,1}(:,1:3);
s.x = x;
s.sensorc = sensorc;
s.sensorh = sensorh;
```

```
% Interpolation over common axis and sensor subtraction
```

```
crunch{1,1}(:,4) =
interpl(mpin{2}(datarangec,3),mpin{2}(datarangec,4),x,'spline');
crunch{1,2}(:,1:3) = crunch{1,1}(:,1:3);
sensorcint = interpl(sensor[1](sensorc,3),sensor[1](sensorc,4),x,'spline');
crunch{1,2}(:,4) = crunch{1,1}(:,4) - sensorcint;
crunch{2,2}(:,1:3) = crunch{2,1}(:,1:3);
sensorhint = interpl(sensor{2}(sensorh,3),sensor{2}(sensorh,4),x,'spline');
crunch{2,2}(:,4) = crunch{2,1}(:,4) - sensorhint;
```

```
s.sensorcool = sensorcint;
s.sensorheat = sensorhint;
```

```

% ***** Patched in on 01/30 - check that this will run later *****
% Extrapolation and treatment of cooling data at cooling onset
%%% NOTE: 2017-02-08 ADD OPTION TO SKIP THIS STEP
figure(1); hold on
plot(crunch{1,2}(:,3),crunch{1,2}(:,4))
xlim([100 270]); %%%%%%%%%% Manipulate if you have to
title('Plese select the extrapolation sampling region')
extrapbounds = ginput(2);
hffitrange = find(crunch{1,2}(:,3) > extrapbounds(1) & crunch{1,2}(:,3) <
extrapbounds(2));
hffit = fit(crunch{1,2}(hffitrange,3),crunch{1,2}(hffitrange,4),'poly1');
patchrange = find(crunch{1,2}(:,3) > extrapbounds(2));
crunch{1,2}(patchrange,4) = hffit(crunch{1,2}(patchrange,3));
%for i = 1:length(semi)
%   if mod(i,2) == 1
%       hffitrange = find(semi{i,1}(:,3) > extrapbounds(1) & semi{i,1}(:,3)
< extrapbounds(2));
%       hffit =
fit(semi{i,1}(hffitrange,3),semi{i,1}(hffitrange,4),'poly1');
%       patchrange = find(semi{i,1}(:,3) > extrapbounds(2));
%       semi{i,1}(patchrange,4) = hffit(semi{i,1}(patchrange,3));
%   end
%end
clf

% Symmetry correction step, user prompted to select bounds for the glassy
% and melt symmetry region. (If needed modify with melt extrapolation code)
figure(1); hold on
plot(crunch{1,2}(:,3),crunch{1,2}(:,4),crunch{2,2}(:,3),crunch{2,2}(:,4))
legend('cooling','heating','location','northwest')
xlim([-60 280]) %%%%%%%%%% Manipulate if you have to
title('Select the upper and lower bounds for glass and melt symmetry')

symmpts = ginput(4);
glassrange = find(x > symmpts(1) & x < symmpts(2));
meltrange = find(x > symmpts(3) & x < symmpts(4));

glassavg = (crunch{1,2}(glassrange,4)+crunch{2,2}(glassrange,4))/2;
meltavg = (crunch{1,2}(meltrange,4)+crunch{2,2}(meltrange,4))/2;
avgx = [x(glassrange);x(meltrange)];
avgy = [glassavg;meltavg];
symmfit = fit(avgx,avgy,'poly3');

plot(x(glassrange),glassavg,'.g',x(meltrange),meltavg,'.g')
plot(x,symmfit(x))
hold off

% Apply the symmetry line from the first pair correct data in the semi
% processed array (isotherm scans stitched together and stacked cool-heat)
% and convert data to apparent heat capacity

crunch{1,3}(:,1:3) = crunch{1,2}(:,1:3);

```

```

crunch{1,3}(:,4) = (crunch{1,2}(:,4) - symmfit(x))*10^(-3); % Convert data
from mW to W
crunch{2,3}(:,1:3) = crunch{2,2}(:,1:3);
crunch{2,3}(:,4) = (crunch{2,2}(:,4) - symmfit(x))*10^(-3); % Convert data
from mW to W
crunch{1,4}(:,1:3) = crunch{1,2}(:,1:3);
crunch{1,4}(:,4) = crunch{1,3}(:,4)/2000; % data in J/k
crunch{2,4}(:,1:3) = crunch{2,2}(:,1:3);
crunch{2,4}(:,4) = crunch{2,3}(:,4)/(-2000); % data in J/k
s.symmpts = symmpts;
s.symmline = symmfit;
s.semiprocessed = crunch;
figure(2);
plot(crunch{1,4}(:,3),crunch{1,4}(:,4),crunch{2,4}(:,3),crunch{2,4}(:,4))

% Mass determination by fitting the data within the glassy symmetry range
% overlapping the ATHAS experimental data. Athas data needs to be converted
% from J/(mol K) to J/(g C) - this is done here by dividing by the
% molecular weight of the polymer repeat (monomer) unit. From NIST ethanol
% homopolymer molecular weight = 44.0526 g/mol

litvalsexp(:,1) = lit(:,1) - 273.15; % Convert ATHAS data to deg. C
litvalsexp(:,2) = lit(:,2)/molwt; % Convert to J/gK
litvalsthry(:,1) = lit(:,1) - 273.15; % Convert ATHAS data to deg. C
litvalsthry(:,2) = lit(:,3)/molwt; % Convert to J/gK
% Trim litvals to contain only the region where experimental data exists
litvalsexp = litvalsexp(~any(isnan(litvalsexp),2),:);
litvalsthry = litvalsthry(~any(isnan(litvalsthry),2),:);
% Mass determination by fitting the solid state (glassy) heat capacity on
% heating, using the temperature bounds (hg) obtained above

prompt = questdlg('Do you want to use ATHAS Experimental Cp Values or
Theoretical Cp?', 'Mass Determination Method', 'Experiment', 'Theory', 'Lab
Measured', 'Experiment');
switch prompt
    case 'Experiment'
        a = litvalsexp;
    case 'Theory'
        a = litvalsthry;
    case 'Lab Measured'
        a = labdata;
end
% Find the region where bounded by the overlap of the glassy symmetry
% correction range and the ATHAS experiment data
if symmpts(2) > a(end,1)
    overlap = find(a(:,1) > -45);
else
    overlap = find(a(:,1) > -45 & a(:,1) < symmpts(2));
end

massrange = find(x > a(overlap(1),1) & x < a(overlap(end),1));
litoverlap = a(overlap,1:2);
litinterp = interp1(litoverlap(:,1),litoverlap(:,2),x(massrange), 'spline');

temp(:,1) = x(massrange);
temp(:,2) = crunch{2,4}(massrange,4)./litinterp;

```

```

s.raw_mass = temp;
figure(3); plot(temp(:,1),temp(:,2))

% *b* See note above

prompt = questdlg('Does the data need to be rotated?');
switch prompt
    case 'Yes' % Data requires rotation, find and apply the rotation angle
        % Rotation steps: find the slope of the temperature dependence of
        % the mass and rotate the data set about T = 0 degC so that the
        % mass is constant
        line = polyfit(temp(:,1),temp(:,2),1);
        semic = crunch{1,4}(:,3:4);
        semih = crunch{2,4}(:,3:4);
        semic_t = transpose(semic);
        semih_t = transpose(semih);
        angle = -1*atan(line(1));
        rot = [cos(angle) -1*sin(angle);sin(angle) cos(angle)];
        s.rot = rot;
        semic_r = rot*semic_t;
        semih_r = rot*semih_t;
        figure(2); hold on
    % % % %%%%%%%%% SOMETHING IS BEING DONE TWICE FIX THIS 2017-02-03
    % crunch{i,1} = interp
    % crunch{i,2} = crunch{i,1} - sensor
    % crunch{i,3} = crunch{i,2} - symmetry
    % crunch{i,4} = heat capacity

    semichf_t = transpose(crunch{1,3}(:,3:4));
    semichf_r = rot*semichf_t;
    semihhf_t = transpose(crunch{2,3}(:,3:4));
    semihhf_r = rot*semihhf_t;

    % rotated apparent heat flow and rotated specific heat capacity
    final{1,1}(:,1:2) = crunch{1,3}(:,1:2);
    final{1,1}(:,3:4) = transpose(semichf_r);
    final{2,1}(:,1:2) = crunch{2,3}(:,1:2);
    final{2,1}(:,3:4) = transpose(semihhf_r);
    final{1,3}(:,1:2) = crunch{1,4}(:,1:2);
    final{1,3}(:,3:4) = transpose(semic_r);
    final{2,3}(:,1:2) = crunch{2,4}(:,1:2);
    final{2,3}(:,3:4) = transpose(semih_r);
    temp = [];
    temp(:,1) = x(massrange);
    temp(:,2) = final{2,3}(massrange,4)./litinterp;
    s.corr_mass = temp;
    s.m = mean(s.corr_mass(:,2));
    % rotated specific heat
    final{1,2}(:,1:3) = final{1,1}(:,1:3);
    final{1,2}(:,4) = final{1,1}(:,4)/s.m;
    final{2,2}(:,1:3) = final{2,1}(:,1:3);
    final{2,2}(:,4) = final{2,1}(:,4)/s.m;
    final{1,4}(:,1:3) = final{1,3}(:,1:3);
    final{1,4}(:,4) = final{1,3}(:,4)/s.m;
    final{2,4}(:,1:3) = final{2,3}(:,1:3);
    final{2,4}(:,4) = final{2,3}(:,4)/s.m;

```

```

plot(semic_r(1,:),semic_r(2,:),semih_r(1,:),semih_r(2,:))

case 'No' % No rotation to the data, create the final output cell array
% Apparent Heat Flow Rate {:,3} and Apparent Heat Capacity {:,4}
final{1,1} = crunch{1,3};
final{1,3} = crunch{1,4};
final{2,1} = crunch{2,3};
final{2,3} = crunch{2,4};
% Specific Heat Flow Rate {:,3} and Specific Heat Capacity {:,4}
s.m = mean(s.raw_mass(:,2));
final{1,2}(:,1:3) = final{1,1}(:,1:3);
final{1,4}(:,1:3) = final{1,3}(:,1:3);
final{2,2}(:,1:3) = final{2,1}(:,1:3);
final{2,4}(:,1:3) = final{2,3}(:,1:3);
final{1,2}(:,4) = final{1,1}(:,4)/s.m;
final{1,4}(:,4) = final{1,3}(:,4)/s.m;
final{2,2}(:,4) = final{2,1}(:,4)/s.m;
final{2,4}(:,4) = final{2,3}(:,4)/s.m;

s.rot = [1 0;0 1];
end

end

```

### ***B.3 Isothermal Melt Crystallization Stack Analysis***

This program runs following the first pair analysis, see **Appendix B.2**, the output struct “s” contains all necessary initial sample mass and applies the same rotation corrections to the isothermal stack data. Remember when programming temperature time profiles to include an initial melt – cool – melt cycle.

```

function out = FSC_PVAisotherms_new(s,isostack)
% Created: 2017-02-01
% Author: Dave
%
% Takes as input the output struct of PVAmeltpair.m, in particular the
% rotation matrix applied to the curves for agreement with ATHAS glassy
% data, interpolated heating and cooling scans of the empty sensor, the
% common X-axis used for interpolation, and the average mass deterimed from
% the glassy symmetry region.

% output listed by column: symmetry corrected and rotated heat flow data,
% specific heat flow, apparent heat capacity, specific heat capacity

```

```

figure(1); clf
figure(2); clf

% Stitch together the isothermal cooling segments
l = length(isostack);
semi = cell((2/3)*l,1);
n = length(semi);
i=1; j=1;
while i <= l-2
    semi{j,1} = [isostack{i,1}(5:end-5,:);isostack{i+1,1}(5:end-5,:)];
    semi{j+1,1} = isostack{i+2,1};
    j = j+2;
    i = i+3;
end

figure(1); clf
% Apply the X-axis from the first pair and subtract the empty sensor from
% the data

for i = 1:n
    for j = 1:length(semi{i,1}(:,3))-1
        temp(j,1) = semi{i,1}(j,3)-semi{i,1}(j+1,3);
    end
    if mod(i,2) == 1
        intrange = find(temp > 0.17); % for cooling rate of 2000 K/s
        crunch{i,1}(:,1:3) = s.coll23;
        crunch{i,1}(:,4) =
        interp1(semi{i,1}(intrange,3),semi{i,1}(intrange,4),s.x,'linear') -
        s.sensorcool;

        else
            intrange = find(temp < -0.19); % for cooling rate of 2000 K/s
            crunch{i,1}(:,1:3) = s.coll23;
            crunch{i,1}(:,4) =
            interp1(semi{i,1}(intrange,3),semi{i,1}(intrange,4),s.x,'linear') -
            s.sensorheat;
        end
        temp = [];

        figure(1); hold on
        plot(crunch{i,1}(:,3),crunch{i,1}(:,4))
        xlim([-65 280])
        title('Select the upper and lower bounds for glass and melt symmetry')
    end

symmpts = ginput(4);

% Perform a simple interpolation on the onset of the cooling scan to remove
% the small junk region at high temp (cooling onset)

for i = 1:n
    if mod(i,2) == 1
        figure(2); hold on
        plot(crunch{i,1}(:,3),crunch{i,1}(:,4))
        xlim([0 270])
    end
end

```

```

        title('Plese select the extrapolation sampling region')
    end
end
extrapbounds = ginput(2);
for i = 1:n
    if mod(i,2) == 1
        hffitrange = find(crunch{i,1}(:,3) > extrapbounds(1) &
crunch{i,1}(:,3) < extrapbounds(2));
        hffit =
fit(crunch{i,1}(hffitrange,3),crunch{i,1}(hffitrange,4),'poly1');
        patchrange = find(crunch{i,1}(:,3) > extrapbounds(2));
        crunch{i,1}(patchrange,4) = hffit(crunch{i,1}(patchrange,3));
    end
end

% Calculate the symmetry line for each pair with common symmetry bounds
% that apply to the entire stack
i = 1; j = 2;
while i <= n-1
    grange = find(crunch{i,1}(:,3) > symmpts(1) & crunch{i,1}(:,3) <
symmpts(2));
    mrange = find(crunch{i,1}(:,3) > symmpts(3) & crunch{i,1}(:,3) <
symmpts(4));

    glassavg(:,1) = crunch{i,1}(grange,3);
    glassavg(:,2) = (crunch{i,1}(grange,4)+crunch{j,1}(grange,4))/2;
    meltavg(:,1) = crunch{i,1}(mrange,3);
    meltavg(:,2) = (crunch{i,1}(mrange,4)+crunch{j,1}(mrange,4))/2;
    symmavg = [glassavg;meltavg];
    symmfit = fit(symmavg(:,1),symmavg(:,2),'poly3');

    crunch{i,2}(:,1:3) = s.col123;
    crunch{i,2}(:,4) = (crunch{i,1}(:,4) - symmfit(s.x))*(10^(-3)); %
conversion from mW to W
    crunch{j,2}(:,1:3) = s.col123;
    crunch{j,2}(:,4) = (crunch{j,1}(:,4) - symmfit(s.x))*(10^(-3)); %
conversion from mW to W
    i = i + 2;
    j = j + 2;
end

% Apply rotation used on first pair in PVAmeltpair.m and generate output
% matrix
for i = 1:n
    crunch{i,3}(:,1:2) = crunch{i,2}(:,1:2);

    tempmat = transpose(crunch{i,2}(:,3:4));
    rotmat = s.rot*(tempmat);
    crunch{i,3}(:,3:4) = transpose(rotmat);

    out{i,1} = crunch{i,3};
    out{i,2}(:,1:3) = s.col123;
    out{i,2}(:,4) = crunch{i,3}(:,4)/s.m;
    out{i,3}(:,1:3) = s.col123;
    out{i,4}(:,1:3) = s.col123;
    if mod(i,2) == 1

```

```

        out{i,3}(:,4) = crunch{i,3}(:,4)/(2000); % conversion to J/K
    else
        out{i,3}(:,4) = crunch{i,3}(:,4)/(-2000); % conversion to J/K
    end
    out{i,4}(:,4) = out{i,3}(:,4)/s.m;
end

end

```

## ***B.4 FSC Glass Transition, $\Delta C_p(T_g)$ , and Enthalpy Measurement***

### ***B.4.1 Single Cool – Heat FSC Pair***

```

unction [enth,tgstuff] = FSC_enthalpy(s,in)
% Written 2017-02-06

% Takes input from either the output of PVAmeltpair or FSC_PVAisotherms and
% loops over the data pairwise to assess melt heatflow baseline and return
% peak areas determined from the integrals of the apparent heat flow on
% heating and cooling.

figure(1); clf
figure(2); clf
figure(3); clf
l = length(in);
j = 1;
figure(1);

% Loop over the data and average the heat flow in the melt to create
% integration baseline to determine enthalpy of crystallization and melting
while j < l-1
    figure(1); plot(in{j,1}(:,3),in{j,1}(:,4),in{j+1,1}(:,3),-
1*in{j+1,1}(:,4))
    bds = ginput(2);
    range = find(in{j,1}(:,3) > bds(1) & in{j,1}(:,3) < bds(2));
    meltavg = (in{j,1}(range,4)+(-1)*in{j+1,1}(range,4))/2;
    bline = fit(in{j,1}(range,3),meltavg,'poly1');
    curve{j,1}(:,1:3) = in{j,1}(:,1:3);
    curve{j,1}(:,4) = in{j,1}(:,4) - bline(in{j,1}(:,3));
    curve{j+1,1}(:,1:3) = in{j+1,1}(:,1:3);
    curve{j+1,1}(:,4) = in{j+1,1}(:,4) + bline(in{j+1,1}(:,3));

    j = j + 2;
end

% It is likely that many of the curves will have regions outside of the
% main peaks which will be above/ below the baseline determined above so
% the user is prompted to select shorter bounds if necessary.
n = length(curve);
for i = 1:n
    if mod(i,2) == 1
        region = find(curve{i,1}(:,4) > 0);

```

```

        figure(1);
plot(curve{i,1}(:,3),curve{i,1}(:,4), 'b',curve{i,1}(region,3),curve{i,1}(region,4), '.k')
    xlim = ([-60 280]);
    prompt = questdlg('Does the integration range need to be adjusted?');
    switch prompt
        case 'Yes'
            adjbds = ginput(2);
            adjregion = find(curve{i,1}(:,3) > adjbds(1) &
curve{i,1}(:,3) < adjbds(2));
            enth(i,1) =
trapz(curve{i,1}(adjregion,3),curve{i,1}(adjregion,4));
            tmpt = find(curve{i,1}(adjregion,4) ==
max(curve{i,1}(adjregion,4)));
            tm = curve{i,1}(tmpt+adjregion(1),3);
            enth(i,3) = tm;
        case 'No'
            enth(i,1) = trapz(curve{i,1}(region,3),curve{i,1}(region,4));
    end
else
    region = find(curve{i,1}(:,4) < 0);
    figure(1);
plot(curve{i,1}(:,3),curve{i,1}(:,4), 'b',curve{i,1}(region,3),curve{i,1}(region,4), '.k')
    xlim = ([-60 280]);
    prompt = questdlg('Does the integration range need to be adjusted?');
    switch prompt
        case 'Yes'
            adjbds = ginput(2);
            adjregion = find(curve{i,1}(:,3) > adjbds(1) &
curve{i,1}(:,3) < adjbds(2));
            enth(i,1) =
trapz(curve{i,1}(adjregion,3),curve{i,1}(adjregion,4));
            tmpt = find(curve{i,1}(adjregion,4) ==
min(curve{i,1}(adjregion,4)));
            tm = curve{i,1}(tmpt+adjregion(1),3);
            enth(i,3) = tm;
        case 'No'
            enth(i,1) = trapz(curve{i,1}(region,3),curve{i,1}(region,4));
    end

end

figure(2); plot(in{i,3}(:,4))
[x y] = ginput(3);
x = round(x);

SGFilter = sgolayfilt(diff(in{i,3}(x(1):x(2),4)),5,99);
SGFilterMax = max(SGFilter);

Indx1 = find(SGFilter == SGFilterMax);
tg = in{i,3}(Indx1 + x(1),3);

gextrange = find(in{i,3}(:,3) > s.symmpts(1,1) - 10 & in{i,3}(:,3) <
s.symmpts(2,1));
glassfit = fit(in{i,3}(gextrange,3),in{i,3}(gextrange,4), 'poly1');

```

```

    tgstuff.tg = tg;
    tgstuff.glassfit = glassfit;

    semicry = fit(in{i,3}(x(2):x(3),3),in{i,3}(x(2):x(3),4), 'poly1');
    tgstuff.semicry = semicry;
    tgstuff.cptg = semicry(tg) - glassfit(tg);

    hfdadj = 161.4*(2*enth(i,3))/(enth(i,3)+265);
    enth(i,2) = enth(i,1)/(2000*s.m); % Enthalpy in J/g
    enth(i,4) = abs(enth(i,2)/161.4); % Crystallinity with hf0
    enth(i,5) = abs(enth(i,2)/hfdadj); % Crystallinity with temperature adj.
hf
    enth(i,6) = tgstuff.cptg/s.m;
    enth(i,7) = tg;

    figure(3); plot(in{i,3}(:,3),in{i,3}(:,4), '-
b',in{i,3}(Indx1+x(1),3),in{i,3}(Indx1+x(1),4), '.k')
    hold on
    plot(glassfit)
    plot(semicry)

end

end

```

### ***B.4.2 Isothermal Melt Crystallization Stack***

```

function [enth,curve] = FSC_enthalpy_iso(s,in)
% Written 2017-02-06

% Takes input from either the output of PVAmeltpair or FSC_PVAisotherms and
% loops over the data pairwise to assess melt heatflow baseline and return
% peak areas determined from the integrals of the apparent heat flow on
% heating and cooling.

% Initial while loop chops off final pair in cell array "in"

figure(1); clf
l = length(in);
j = 1;
figure(1);

% Loop over the data and average the heat flow in the melt to create
% integration baseline to determine enthalpy of crystallization and melting
while j <= l-1
    figure(1); plot(in{j,1}(:,3),in{j,1}(:,4),in{j+1,1}(:,3),-
1*in{j+1,1}(:,4))
    bds = ginput(2);
    range = find(in{j,1}(:,3) > bds(1) & in{j,1}(:,3) < bds(2));
    meltavg = (in{j,1}(range,4)+(-1)*in{j+1,1}(range,4))/2;
    bline = fit(in{j,1}(range,3),meltavg, 'poly1');
    curve{j,1}(:,1:3) = in{j,1}(:,1:3);

```

```

curve{j,1}(:,4) = in{j,1}(:,4) - bline(in{j,1}(:,3));
curve{j+1,1}(:,1:3) = in{j+1,1}(:,1:3);
curve{j+1,1}(:,4) = in{j+1,1}(:,4) + bline(in{j+1,1}(:,3));

j = j + 2;
end

% It is likely that many of the curves will have regions outside of the
% main peaks which will be above/ below the baseline determined above so
% the user is prompted to select shorter bounds if necessary.
n = length(curve);
for i = 1:n
    figure(4); clf
    if mod(i,2) == 1
        enth(i,1) = NaN;
        region = find(curve{i,1}(:,4) > 0);
        %
        plot(curve{i,1}(:,3),curve{i,1}(:,4),'b',curve{i,1}(region,3),curve{i,1}(region,4),'.k')
        % prompt = questdlg('Does the integration range need to be
adjusted?')
        % switch prompt
        % case 'Yes'
        %     adjbds = ginput(2);
        %     adjregion = find(curve{i,1}(:,3) > adjbds(1) &
curve{i,1}(:,3) < adjbds(2));
        %     enth(i,1) =
trapz(curve{i,1}(adjregion,3),curve{i,1}(adjregion,4));
        % case 'No'
        %     enth(i,1) =
trapz(curve{i,1}(region,3),curve{i,1}(region,4));
        % end
    else
        region = find(curve{i,1}(:,4) < 0);
        figure(1);
        plot(curve{i,1}(:,3),curve{i,1}(:,4),'b',curve{i,1}(region,3),curve{i,1}(region,4),'.k')
        prompt = questdlg('Does the integration range need to be adjusted?');
        switch prompt
            case 'Yes'
                adjbds = ginput(2);
                adjregion = find(curve{i,1}(:,3) > adjbds(1) &
curve{i,1}(:,3) < adjbds(2));
                enth(i,1) =
trapz(curve{i,1}(adjregion,3),curve{i,1}(adjregion,4));
            case 'No'
                enth(i,1) = trapz(curve{i,1}(region,3),curve{i,1}(region,4));
        end
    end
    enth(i,2) = enth(i,1)/(2000*s.m); % Enthalpy in J/g
    %enth(i,3) = 100*abs(enth(i,2)/140); % Percent Crystallinity for PET
    enth(i,3) = 100*abs(enth(i,2)/161.4); % Percent Crystallinity for PVA

    figure(2); plot(in{i,3}(:,4))
    [x y] = ginput(3);
    x = round(x);

```

```

    SGFilter = sgolayfilt(diff(in{i,3}(x(1):x(2),4)),5,99);
    SGFilterMax = max(SGFilter);

    Indx1 = find(SGFilter == SGFilterMax);
    tg = in{i,3}(Indx1 + x(1),3);

    gextrange = find(in{i,3}(:,3) > s.symmpts(1,1) - 10 & in{i,3}(:,3) <
s.symmpts(2,1));
    glassfit = fit(in{i,3}(gextrange,3),in{i,3}(gextrange,4),'poly1');

    tgstuff.tg = tg;
    tgstuff.glassfit = glassfit;
    tgstuff.tgupper =
[max(in{i,3}(x(2):x(3),3),max(in{i,3}(x(2):x(3),4)))]);
    semicry = fit(in{i,3}(x(2):x(3),3),in{i,3}(x(2):x(3),4),'poly1');
    tgstuff.semicry = semicry;
    tgstuff.cptg = semicry(tg) - glassfit(tg);
    enth(i,4) = tgstuff.tg;
    enth(i,5) = tgstuff.cptg;
    enth(i,6) = enth(i,5)/s.m;
    figure(4); hold on
    figure(4); plot(in{i,3}(:,3),in{i,3}(:,4))
    figure(4); plot(glassfit)
    figure(4); plot(semicry)
    figure(4); plot(in{i,3}(Indx1+x(1),3),in{i,3}(Indx1+x(1),4),'.b')
end

% Integration against temperature not time, have to divide by the heat
% rate and the mass to get the observed enthalpy in J/g

end

end

```

### ***B.5 FSC Unpack to Cebe FSC GUI Compatibility Program***

This program takes output from the FSC unpack program, **Appendix B.1**, ensures the data is monotonically increasing and converts the format to a struct compatible with the input requirements of Peggy's custom FSC GUI analysis program.

```

function [out,logic] = ccmonotonic(in,sensor)
temp = [];
for i = 1:length(in{3,1})-1
    temp(i,1) = in{3,1}(i,3) - in{3,1}(i+1,3);
end

```

```

for i = 1:length(in{4,1})-1
    temp(i,2) = in{4,1}(i,3) - in{4,1}(i+1,3);
end
for i = 1:length(in{5,1})-1
    temp(i,3) = in{5,1}(i,3) - in{5,1}(i+1,3);
end
for i = 1:length(in{6,1})-1
    temp(i,4) = in{6,1}(i,3) - in{6,1}(i+1,3);
end
logic = cell(4,1);
logic{1} = find(temp(:,1) < -0.19);
logic{2} = find(temp(:,2) > 0.1);
logic{1} = find(temp(:,3) < -0.19);
logic{4} = find(temp(:,4) > 0.1);

out.heat1 = in[1](logic[1],:);
out.cool1 = in{4}(logic{2},:);
out.heat2 = in{5}(logic[1],:);
out.cool2 = in{6}(logic{4},:);
out.emptyh = sensor[1];
out.emptyc = sensor{2};

end

```

## ***B.6 Wide Angle X-Ray Orientational Order Parameter***

This set of programs utilizes the output data from synchrotron data analysis programs written by Peggy. There are variants of all of these programs for real time and single frame data sets. Because all work presented in **Appendix A1** and in the interest of minimizing extra pages in this document only the real time data set variants of the programs are included here.

### ***B.6.1 Phi Shift 90 (orients data for samples aligned 90° off center)***

```

function pc = Phi_shift90(dataset)

% Function Phi_shift90.m takes WAXS azimuthal intensity data vs. phi angle,
% and shifts it so that the peaks are centered at 90 and 270 degrees.
%
% Strategy: Divide the entire x-range (angle, phi) in half. Evaluate
% the peak maximum in each half. Select the larger peak max value between
% the two halves, and return its index. Find the difference between the
% index of the peak max, and the row-size of matrix. Shift all data below
% the peak max upward by adding the peak max index to the row; shift all
% data above the peak max downward by subtracting peak max index -1.

```

```

[mm,n]=size(dataset); % Find the size of the data set.
mover2=round(mm/2); % Find the half way point.

max1 = max(dataset(1:mover2,2)); % Find maximum intensity in first half...
max2 = max(dataset(mover2+1:mm,2)); % ... and in the second half.

maxI = max([max1 max2]); % Compare the two intensities and pick the larger.
% Find the index of the largest peak. If the two are equal, chose the
% larger.
indx_maxI = max(find( dataset(:,2) == maxI ));

delta = round(3*mm/4) - indx_maxI; % Delta determines the amount of shift.

shift = zeros(mm,n); % Reserve space in shifted matrix.

% Shift low angle data upward so peak is at 270 deg (index shifts to 3*mm/4).
shift(1:delta+1,1) = dataset(1:delta+1,1);
shift(1:delta+1,2) = dataset(mm-delta:mm,2);

% Fold high angle data back to start of the scan.
shift(delta+1:mm,1) = dataset(delta+1:mm,1);
shift(delta+1:mm,2) = dataset(1:mm-delta,2);

plot(dataset(:,1),dataset(:,2),'b.')
hold on
plot(shift(:,1),shift(:,2), 'r. ');shg
hold off

%keyboard

pc = shift;

```

### ***B.6.2 Shift (orients data which is off center by an arbitrary angle)***

```

%%%%%%%%%%%%%%%%%%%%%%%%%%%%%%%%%%%%%%%%%%%%%%%%%%%%%%%%%%%%%%%%%%%%%%%%
% This program shifts multiframe data such that the main peaks are centered
% about 90 and 270 so that the data set can be passed into the order
% parameter analysis program Order_Parameter_Apr14.m.
%
% Author: Dave Thomas
% Created: 19 June 2014
%
%%%%%%%%%%%%%%%%%%%%%%%%%%%%%%%%%%%%%%%%%%%%%%%%%%%%%%%%%%%%%%%%%%%%%%%%
function shiftedset = shift(RTdataset,n)
%%%%%%%%%%%%%%%%%%%%%%%%%%%%%%%%%%%%%%%%%%%%%%%%%%%%%%%%%%%%%%%%%%%%%%%%
% Step 1: Read in the real time data set and select a frame to determine
% the shift of the main peaks from 90. The parameter n specifies the frame
% number used to determine this shift - for a cooling run n would be
% towards the end of the data set, for heating n should be set to 1. This
% program assumes that the sample is not rotating in the stage.
%%%%%%%%%%%%%%%%%%%%%%%%%%%%%%%%%%%%%%%%%%%%%%%%%%%%%%%%%%%%%%%%%%%%%%%%
[pk1, loc1] = findpeaks(RTdataset(:,2,n));

```

```

firstsmooth = fit(loc1,pks1, 'smoothingspline');
x361 = linspace(0,360,361);
x361 = transpose(x361);
for i = 1:361
    firstsmoothsub(i) = firstsmooth(x361(i));
end
[pks,loc] = findpeaks(firstsmoothsub);
delta = abs(loc(1)-90);
%%%%%%%%%%%%%%%%%%%%%%%%%%%%%%%%%%%%%%%%%%%%%%%%%%%%%%%%%%%%%%%%%%%%%%%%
% Step 2: Shift the data set such that the curves obey periodic boundary
% conditions. For single slice set the numframes to be equal to 1
%%%%%%%%%%%%%%%%%%%%%%%%%%%%%%%%%%%%%%%%%%%%%%%%%%%%%%%%%%%%%%%%%%%%%%%%
frametemp = size(RTdataset);
numframes = frametemp(3);

shiftedset = zeros(frametemp);
if loc(1) > 90
    for j = 1:numframes
        mod = RTdataset(:,:,j);
        xyshift = circshift(mod,(361-delta));
        for i = 1:361
            xyshift(i,1) = i-1;
        end
        shiftedset(:,:,j) = xyshift;
    end
else if loc(1) < 90
    for j = 1:numframes
        mod = RTdataset(:,:,j);
        xyshift = circshift(mod,-(361-delta));
        for i = 1:361
            xyshift(i,1) = i-1;
        end
        shiftedset(:,:,j) = xyshift;
    end
end
end
end

```

### ***B.6.3 Leadbetter Fit (used in the determination of the order parameter)***

```

function [fitresult, gof] = leadbetterfit(azimuthalangle,
normalizedintensity)
%CREATEFIT(xdata,intensity)
% Create a fit.
%
% Data for 'Leadbetter Intensity Fit' fit:
%     X Input : xdata
%     Y Output: intensity
% Output:
%     fitresult : a fit object representing the fit.
%     gof       : structure with goodness-of fit info.
%
% See also FIT, CFIT, SFIT.

```

```

%
% Auto-generated by MATLAB on 15-Nov-2013 14:35:22
% Edit Log:
% 17 November 2013, Dave Thomas (updated axes labeling)
% 21 May 2014, Dave Thomas (legend update)
% 7 July 2014, Dave Thomas (documentation)
%
% This program is a subroutine performing the numerical fit necessary for
% determining the orientational order parameter as described by Davidson,
% Petermann, and Levelut in their paper: Measurement of the Nematic Order
% Parameter by X-ray Scattering Reconsidered.
%
% The paper can be found here:
% http://dx.doi.org/10.1051/jp2:1995117
%
% The work done by Leadbetter and Norris in their paper: Distribution
% functions in three liquid crystals from X-ray diffraction measurements
% provided the foundation for the work done by Davidson et al.
%
% The paper can be found here:
% http://www.tandfonline.com/doi/abs/10.1080/00268977900101961#.U7rRrrFwVv8

%% Fit: 'Leadbetter Intensity Fit'.
% The prepareCurveData command is not common to all distributions of
% MATLAB, if you are using an older version or one without the curve
% fitting toolbox this may not work perfectly for you.

format long;
[xData, yData] = prepareCurveData( azimuthalangle, normalizedintensity );

%%%%%%%%%%%%%%%%%%%%%%%%%%%%%%%%%%%%%%%%%%%%%%%%%%%%%%%%%%%%%%%%%%%%%%%%
% The program Order_Parameter_Apr14.m calls this fit, which corresponds to
% the application of equation (4) from the Davidson et. al. papper to the
% prepared x and y data sets from realtime WAXS data. The papers show an
% expansion in powers of Cosine with the convention that the peaks are
% centered about 0 and 180, however the data as is prepared by our method
% as has the peaks centered about 90 and 270. The fit was modified by
% forcing a pi/2 shift which could have been achieved equally well with the
% same expansion in terms of powers of sine.
%%%%%%%%%%%%%%%%%%%%%%%%%%%%%%%%%%%%%%%%%%%%%%%%%%%%%%%%%%%%%%%%%%%%%%%%

% Set up fittype and options.
ft = fittype(
'a1*(2/3)*(cos(pi*((x/180)+.5))^2)+a2*(8/15)*(cos(pi*((x/180)+.5))^4)+a3*(16/
35)*(cos(pi*((x/180)+.5))^6)+a4*(128/315)*(cos(pi*((x/180)+.5))^8)+a5*(256/69
3)*(cos(pi*((x/180)+.5))^10)+a0', 'independent', 'x', 'dependent', 'y' );
opts = fitoptions( ft );
opts.Display = 'Off';
opts.Lower = [-Inf -Inf -Inf -Inf -Inf -Inf];
opts.MaxIter = 10000000;
opts.StartPoint = [0.723173479183095 0.34743764558179 0.660616824502904
0.383868601071971 0.627346502443467 0.0216498146303065];
opts.Upper = [Inf Inf Inf Inf Inf Inf];

% Fit model to data.
[fitresult, gof] = fit( xData, yData, ft, opts );

```

```

%%%%%%%%%%%%%%%%%%%%%%%%%%%%%%%%%%%%%%%%%%%%%%%%%%%%%%%%%%%%%%%%%%%%%%%%
% Plotting the fit against the normalized data. The section below is
% commented out to prevent MATLAB from opening dozens of plot windows as
% the multi frame order parameter program loops over the data set.
%%%%%%%%%%%%%%%%%%%%%%%%%%%%%%%%%%%%%%%%%%%%%%%%%%%%%%%%%%%%%%%%%%%%%%%%
% Plot fit with data.
%figure( 'Name', 'Leadbetter Intensity Fit' );
%h = plot( fitresult, xData, yData );
%legend( h, 'data', 'fit', 'Location', 'NorthEast' );
% Label axes
%xlabel( 'Azimuthal Angle' );
%ylabel( 'Normalized Intensity' );
%grid off

```

### ***B.6.4 Nematic Orientational Order Parameter Program***

```

% This program follows the method for determining the orientational order
% parameter as described by Davidson, Petermann, and Levelut in their
% paper: Measurement of the Nematic Order Parameter by X-ray Scattering
% Reconsidered. The paper can be found
% here:http://dx.doi.org/10.1051/jp2:1995117
%
% Author: Dave Thomas
% Created: 20 May 2014
%
% Edit Log
%
% 19 June 2014, Dave Thomas: Created program shift.m for inputing tilted
% multiframe datasets. See program for more details
%
% 7 July 2014, Dave Thomas: Updated incode comments and documentation
%
% This program reads in realtime X-ray scattering data as produced by the
% program Azimuthal_Apr14.m, written by prof. Peggy Cebe and returns a
% vector containing the order parameter for each frame.
%
%%
function order = Order_Parameter_Apr14(RTdataset)

%%%%%%%%%%%%%%%%%%%%%%%%%%%%%%%%%%%%%%%%%%%%%%%%%%%%%%%%%%%%%%%%%%%%%%%%
% Realtime data arrays have the following structure; <361x2xn> where n is
% the number of frames. These arrays contain the the azimuthal angle and
% corresponding intensity for each frame.
%
% Step 1: This step prepares the input data (RTdataset) and crates the
% empty arrays needed for both storing fit coefficients to be used in later
% calculations and calculated order parameter values.
%
%%%%%%%%%%%%%%%%%%%%%%%%%%%%%%%%%%%%%%%%%%%%%%%%%%%%%%%%%%%%%%%%%%%%%%%%

% Determine the number of frames in the set
frametemp = size(RTdataset);
numframes = frametemp(3);

```

```

% Create the x and y data sets from the azimuthal data arrays
    azimuthalangle = [];
    ydataraw = [];
%%%%%%%%%%%%%%%%%%%%%%%%%%%%%%%%%%%%%%%%%%%%%%%%%%%%%%%%%%%%%%%%%%%%%%%%
% Program main loop
% Step 2: Separate the x and y data (azimuthal angle, intensity) into two
% arrays which can then be passed into the fit subroutine.
%
% Step 3: Run the fit subroutine inputting the x and y data at the given
% frame and store the coefficients in the array fs.
%
% Step 4: The order parameter for the given frame is calculated from its
% corresponding coefficients stored in fs.
%
%%%%%%%%%%%%%%%%%%%%%%%%%%%%%%%%%%%%%%%%%%%%%%%%%%%%%%%%%%%%%%%%%%%%%%%%

    fs = zeros(numframes,6);
    order = zeros(numframes,1);

% Begin the main loop over all of the frames in the realtime data set
for index = 1:numframes

%%%%%%%%%%%%%%%%%%%%%%%%%%%%%%%%%%%%%%%%%%%%%%%%%%%%%%%%%%%%%%%%%%%%%%%%
% Step 2: The empty arrays for the x and y (azimuthal angle, intensity) for
% each frame are filled. This step creates arrays with the following
% structure <nx361> where the values at each column index for a given row
% contain either the azimuthal angle or the intensity. Each row is a single
% frame.
%%%%%%%%%%%%%%%%%%%%%%%%%%%%%%%%%%%%%%%%%%%%%%%%%%%%%%%%%%%%%%%%%%%%%%%%

    azimuthalangle = [azimuthalangle;RTdataset(:,1,index)'];
    ydataraw = [ydataraw;RTdataset(:,2,index)'];

%%%%%%%%%%%%%%%%%%%%%%%%%%%%%%%%%%%%%%%%%%%%%%%%%%%%%%%%%%%%%%%%%%%%%%%%
% Step 3: Solve for the expansion coefficients,  $f_{2n}$  using equation (4)
% from the paper cited above. Call the subroutine leadbetterfit.m to
% generate the fit. The subroutine leadbetterfit.m was generated from the
% MATLAB curve fitting toolbox and modified, see the program for more
% details.
%
% To successfully fit the data there are two things that must be addressed:
%
% First the y data must be bounded between zero and one - negative values
% should never be passed into the program, while the fit can still be done
% mathematically, it is not possible to have negative intensities and as a
% result the order parameter output will not be a valid result. The data is
% normalized such that every intensity value is divided by the maximum
% intensity value in the entire data set. The program works with a floating
% lower bound, again the only restriction is that there are no negative y
% intensity values (which should always be the case with real detector
% data.)
%
% Second is that the data must be symmetric about 180 with the peaks
% centered about 90 and 270.
%%%%%%%%%%%%%%%%%%%%%%%%%%%%%%%%%%%%%%%%%%%%%%%%%%%%%%%%%%%%%%%%%%%%%%%%

```

```

    azmfit =
leadbetterfit(azimuthalangle(index,:),ydataraw(index,:)/max(max(ydataraw)));
    coeff = coeffvalues(azmfit);
% This secondary loop fills the row of the array fs with coefficient values
% from the fit applied to the current frame in the loop.
    for j = 1:6
        fs(index,j) = coeff(j);
    end

%%%%%%%%%%%%%%%%%%%%%%%%%%%%%%%%%%%%%%%%%%%%%%%%%%%%%%%%%%%%%%%%%%%%%%%%
% Step 4: As detailed in the paper it is possible to construct a molecular
% distribution function, f[beta] from the coefficients obtained by
% numerically fitting to the expansion (equation (4)). This step constructs
% the molecular distribution function according to equation (3) in the
% paper. The molecular distribution function is then placed into equation
% (5) which yields the average over the second legendre polynomial - the P2
% order parameter.
%%%%%%%%%%%%%%%%%%%%%%%%%%%%%%%%%%%%%%%%%%%%%%%%%%%%%%%%%%%%%%%%%%%%%%%%
    fbeta = @(x) fs(index,1) + fs(index,2)*cos(x).^2 + fs(index,3)*cos(x).^4
+ fs(index,4)*cos(x).^6 + fs(index,5)*cos(x).^8 + fs(index,6)*cos(x).^10;

    top = @(x) fbeta(x).*sin(x).*cos(x).^2;
    bottom = @(x) fbeta(x).*sin(x);

    order(index,1) = .5*(3*quad(top,0,pi/2)/quad(bottom,0,pi/2) -1);
end

```

[1] Sbyrnes321, FTIR Interferogram, in: FTIR-interferogram.svg (Ed.) Origin, Creative Commons Attribution-Share Alike 3.0 Unported Wikimedia Commons, 2011.